

**AFRL-ML-TY-TR-2002-4522**



## **DESTRUCTION OF ENERGETIC MATERIALS IN SUPERCRITICAL WATER**

S. J. Buelow, D. Allen, G. K. Anderson, F. L. Archuleta, J. H. Atencio,  
G. T. Baca, W. D. Breshears, T. J. Butenhoff, P. C. Dell'Orco, R. B. Dyer,  
B. R. Foy, K. A. Funk, D. M. Harradine, K. C. Knutsen, J. L. Lyman,  
D. A. Masten, T. G. McGuinness, R. E. McInroy, C. J. Monahan,  
R. C. Oldenborg, J. M. Robinson, M. A. Sedillo, D. A. Counce, C. K. Rofer,  
P. E. Trujillo, Jr., R. L. Brewer, G. A. Buntain, R. L. Flesner, J. A. Sanchez,  
T. Spontarelli, L. L. Sprouse, C. A. Vecere, G. R. Brewer, R. D. McFarland,  
W. J. Parkinson, R. P. Courier, S. M. Chitanvis, C. W. Pattersen, L. R. Pratt  
Los Alamos National Laboratory  
Los Alamos, New Mexico 87545

J. C. Oxley  
Chemistry Department, New Mexico Institute of Mining and Technology  
Socorro, New Mexico 87801

Approved for Public Release; Distribution Unlimited

**AIR FORCE RESEARCH LABORATORY  
MATERIALS & MANUFACTURING DIRECTORATE  
AIR EXPEDITIONARY FORCES TECHNOLOGIES DIVISION  
139 BARNES DRIVE, STE 2  
TYNDALL AFB FL 32403-5323**

## NOTICES

USING GOVERNMENT DRAWINGS, SPECIFICATIONS, OR OTHER DATA INCLUDED IN THIS DOCUMENT FOR ANY PURPOSE OTHER THAN GOVERNMENT PROCUREMENT DOES NOT IN ANY WAY OBLIGATE THE US GOVERNMENT. THE FACT THAT THE GOVERNMENT FORMULATED OR SUPPLIED THE DRAWINGS, SPECIFICATIONS, OR OTHER DATA DOES NOT LICENSE THE HOLDER OR ANY OTHER PERSON OR CORPORATION; OR CONVEY ANY RIGHTS OR PERMISSION TO MANUFACTURE, USE, OR SELL ANY PATENTED INVENTION THAT MAY RELATE TO THEM.

THIS REPORT IS RELEASABLE TO THE NATIONAL TECHNICAL INFORMATION SERVICE  
5285 PORT ROYAL RD.

SPRINGFIELD VA 22 161

TELEPHONE 703 487 4650; 703 4874639 (TDD for the hearing-impaired)

E-MAIL [orders@ntis.fedworld.gov](mailto:orders@ntis.fedworld.gov)

WWW <http://www.ntis.gov/index.html>

AT NTIS, IT WILL BE AVAILABLE TO THE GENERAL PUBLIC, INCLUDING FOREIGN NATIONS.


THIS TECHNICAL REPORT HAS BEEN REVIEWED AND IS APPROVED FOR PUBLICATION.



**JOSEPH D. WANDER, Ph.D**  
Program Manager



**ALAN M. NEASE**  
Chief, Force Protection Branch



**DONALD R. HUCKLE, JR., Colonel, USAF**  
Chief, Air Expeditionary Forces Technologies Division

**Do not return copies of this report unless contractual obligations or notice on a specific document requires its return.**

<b>REPORT DOCUMENTATION PAGE</b>			Form Approved OMB No. 0704-0188	
Public reporting burden for this collection of information is estimated to average 1 hour per response, including the time for reviewing instructions, searching existing data sources, gathering and maintaining the data needed, and completing and reviewing the collection of information. Send comments regarding this burden estimate or any other aspect of this collection of information, including suggestions for reducing this burden, to Washington Headquarters Services, Directorate for Information Operations and Reports, 1215 Jefferson Davis Highway, Suite 1204, Arlington, VA 22202-4302, and to the Office of Management and Budget, Paperwork Reduction Project (0704-0188), Washington, DC 20503.				
1. AGENCY USE ONLY (Leave blank)		2. REPORT DATE 2002-06-25		3. REPORT TYPE AND DATES COVERED Final report, 1987-10-15–1992-04-01
4. TITLE AND SUBTITLE Destruction of Energetic Materials in Supercritical Water			5. FUNDING NUMBERS MOU: DE-AI04-79AL11812 JON: 1900 7053  PE: 62206F	
5. AUTHORS S. J. Buelow, D. Allen, G. K. Anderson, F. L. Archuleta, J. H. Atencio, G. T. Baca, W. D. Breshears, T. J. Butenhoff, P. C. Dell'Orco, R. B. Dyer, B. R. Foy, [Continued on p. ii]				
6. PERFORMING ORGANIZATION NAME(S) AND ADDRESS(ES) Photochemistry and Photophysics Group [CLS-4] Los Alamos National Laboratory Los Alamos, NM 87545			7. PERFORMING ORGANIZATION REPORT NUMBER	
8. SPONSORING/MONITORING AGENCY NAME(S) AND ADDRESS(ES) AFRL/MLQF 139 Barnes Drive, Suite 2 Tyndall AFB, FL 32403-5323			9. SPONSORING/MONITORING AGENCY REPORT NUMBER AFRL-ML-TY-TR-2002-4522	
11. SUPPLEMENTARY NOTES Technical monitor: Dr Joe Wander, AFRL/MLQF, 850-283-6240 [DSN 523-6240]				
12a. DISTRIBUTION/AVAILABILITY STATEMENT  Public release authorized. Distribution unlimited.			12b. DISTRIBUTION CODE  A	
ABSTRACT (Maximum 200 words) This effort was a survey of the compatibility of a broad series of representative energetic materials (EM) commonly used in propellants, munitions and explosives with a proposed process of controlled decomposition in water near or above the critical temperature (approximately 373 °C). Central issues, in order of consideration, are safety, environmental compatibility of decomposition products, destruction efficiency, extrapolation to compounded formulations of EM, and engineering considerations for scale-up to full-scale operation. The sequence followed in these investigations was (1) initial safety evaluation and small-scale stability tests on each of 13 individual energetic ingredients commonly used in rocket propellants, munitions, or explosives [Continued on p. ii]				
14. SUBJECT TERMS Supercritical water; hydrazine; nitroaliphatic; nitroaromatic; energetic materials; hydrolysis; explosives; propellant			15. NUMBER OF PAGES 217	
			16. PRICE CODE	
17. SECURITY CLASSIFICATION OF REPORT UNCLASSIFIED	18. SECURITY CLASSIFICATION OF THIS PAGE UNCLASSIFIED	19. SECURITY CLASSIFICATION OF ABSTRACT UNCLASSIFIED	20. LIMITATION OF ABSTRACT UL	

5. AUTHORS (CONTINUED). K. A. Funk, D. M. Harradine, K. C. Knutsen, J. L. Lyman, D. A. Masten, T. G. McGuinness, R. E. McInroy, C. J. Monahan, R. C. Oldenborg, J. M. Robinson, M. A. Sedillo, D. A. Counce, C. K. Rofer, P. E. Trujillo, Jr., R. L. Brewer, G. A. Buntain, R. L. Flesner, J. A. Sanchez, T. Spontarelli, L. L. Sprouse, C. A. Vecere, G. R. Brewer, R. D. McFarland, W. J. Parkinson, R. P. Courier, S. M. Chitanvis, C. W. Pattersen, L. R. Pratt, and J.C. Oxley

13. ABSTRACT (CONTINUED).

(all passed this stage); (2) determination of global kinetics and Destruction and Removal Efficiencies (DREs) (destruction was complete - all DREs are limited by sensitivity of detection); (3) identification of products and byproducts of the process to verify environmental compatibility (all tested passed this criterion); and (4) detailed reaction kinetics determinations and development of computational models (qualitatively successful application to nitromethane). An important result was the development of safe and practical means to deliver water-insoluble energetic materials (EM) into the supercritical region. These methods included: 1) slurried particles, 2) dissolution in an organic solvent or supercritical carbon dioxide, and 3) digestion in aqueous alkali. A pilot-scale continuous pipe reactor suitable for handling slurried, dissolved, or hydrolyzed explosives was built and tested. Results show that supercritical water is a favorable medium for decomposition of waste and off-spec EM. The process appears to be controllable, and the decomposition products are contained until they are consciously released. Oxides of nitrogen do not form in significant amounts, presumably because the medium supports their decomposition at lower temperatures than does incineration. Digestion in aqueous alkali is a safe and economical pretreatment for most EM. Nickel alloy reactors can be used for formulations that contain only carbon, nitrogen, oxygen, and hydrogen. Lined reactors are required for chlorine-containing mixtures and, in general, may be best of long term operation for all EM formulations. Useful detailed kinetic, fluid dynamic, and process modeling for SCW systems is not yet practical. Chemical reaction rates and physical properties data are needed for organic/inorganic/water mixtures at high temperatures and pressures before models can quantitatively predict reactor operation.

## EXECUTIVE SUMMARY

### Final Report on the Oxidation of Energetic Materials in Supercritical Water

#### A. OBJECTIVE

The objective of this effort was a survey of the compatibility of a broad series of representative energetic materials (EM) commonly used in propellants, munitions and explosives with a proposed process of controlled decomposition in water near or above the critical temperature (approximately 373 °C). Central issues, in order of consideration, are safety, environmental compatibility of decomposition products, destruction efficiency, extrapolation to compounded formulations of EM, and engineering considerations for scale-up to full scale operation.

#### B. BACKGROUND

Traditional methods of disposing of waste and off-spec EM (propellants, explosives, munitions, etc.) include landfilling, ocean dumping, open burning/open detonation (OB/OD), and (for rocket motors) static firing. Landfill disposal and ocean dumping have been proscribed for over a decade, and both OB/OD and static firing involve major uncontrolled release of airborne pollutants. Also, soil and ground water residues from OB/OD are sufficiently severe that sites for such disposal automatically require remediation.

Controlled incineration is a possible alternative for destruction of EM, but materials compatibility, process monitoring and control, and recovery and disposal of pollutant byproducts are technical problems remaining to be solved. Microbiological metabolism has shown promise for destruction of water-soluble EM, but this process is still in the development stage.

Destruction in supercritical water (SCW) is one of several technologies explored by the Air Force Civil Engineering Laboratory (now Airbase Technologies Directorate, Materials Laboratory, Air Force Research Laboratory) as alternatives to OB/OD and static firing of waste and off-spec solid rocket propellants. This report details work in characterizing the decomposition of EM in water at or near supercritical conditions.

## C. SCOPE

During this study, samples of 13 representative energetic components of solid and liquid rocket fuels and explosives were tested for delivery into and decomposition in water at or near supercritical conditions. The decomposition products were characterized and evaluated for environmental compatibility. For certain systems, the rates (kinetics) of disappearance of EM and of formation and disappearance of intermediates were quantified and modeled by a computational code. A high-pressure, high-temperature optical cell was developed and used for in-situ spectroscopy and for phase behavior studies. A high-pressure, high-temperature lined flow reactor was developed, tested, and used for reactions of highly corrosive mixtures. Three methods of feeding high concentrations of EM into a SCW reactor were developed and investigated. Finally, the experimentation was extended to actual propellant compositions. This report summarizes significant observations and data generated.

## D. METHODOLOGY

Several preliminary tests were conducted in small batch reactors. Most experimental work was conducted using constant-diameter flow (pipe) reactors. A gold-lined reactor was used to study ammonium perchlorate (AP), and to evaluate corrosivity of other feeds. Standard high-pressure components were used in the construction of these devices. Soluble organic products were measured by Fourier-transform infrared (FTIR) spectroscopy or by gas chromatography using flame-ionization or mass-spectrometric detection. Insoluble inorganics were identified by X-ray fluorescence. Gases were measured by gas chromatography or by a commercial NO<sub>x</sub> meter. The CHEMKIN, KIVA, and ASPEN codes were the templates upon which the kinetics fluid dynamics, and process modeling codes were based.

## E. TEST DESCRIPTION

In initial tests, small quantities of the EM in water solutions were brought up to supercritical conditions, and temperature and pressure were monitored at intervals of approximately one second to look for abrupt increases in either quantity. All equipment was required to meet explosive qualification criteria. Pipe reactor tests were run by bringing the reactor to temperature with a stream of externally heated water and, after

attainment of operating conditions, replacing the water stream with the feed stream to be tested. Electrical resistance heating was used. Depending on the test, products and unreacted EM were measured *in situ* (in a flow cell), diverted to analytical devices as described above, or collected for disposal. Small-quantity tests were conducted in an isolated facility behind blow-out walls; large-scale tests were conducted in open desert, behind bunkers.

## F. RESULTS

All of the EM tested exhibit decomposition at temperatures below the critical temperature of water. At temperatures above 250°C, they rapidly decompose to small, water-soluble molecules that can be converted into carbon dioxide, water, nitrogen, salts, and trace amounts of nitrate, nitrite and nitrous oxide by reaction in water at higher temperatures. Kinetic modeling of nitromethane (experimentally accessible, but not of consequence to solid propellant disposal), yielded semi-quantitative agreement with experiment. Corrosion of nickel alloy reactors was an extreme problem for AP, but appears to be relatively minor for halogen-free feeds. Dilution, elevated *pH* (more basic solution) and reducing agents appear to inhibit corrosion. Digestion in base (sodium hydroxide or ammonium hydroxide) or dissolution in organic solvents are satisfactory methods for pretreatment of water-insoluble feeds. The pumping of slurried explosives is problematic. Particle size may be a factor in determining the stability of slurries during pumping and transition to supercritical conditions.

## CONCLUSIONS

Results suggest that SCW is a favorable medium for decomposition of waste and off-spec EM. The process appears to be controllable, and the decomposition products are contained until they are consciously released. Oxides of nitrogen do not form in significant amounts, presumably because the medium supports their decomposition at low temperatures than does incineration. Digestion in base is a safe and economical pretreatment for most EM. Nickel alloy reactors can be used for formulations that contain only carbon, nitrogen, oxygen, and hydrogen. Lined reactors are required for chlorine-containing mixtures and, in general, may be best for long-term operation for all EM formulations. Useful detailed kinetic, fluid dynamic, and process modeling for SCW systems is not yet practical. Chemical reaction rates and physical properties data are

needed for organic/ inorganic/water mixtures at high temperatures and pressures before models can quantitatively predict reactor operation.

## H. RECOMMENDATIONS

The integrated technology demonstration should be implemented, including SCW methods as a component of the package. Additional corrosion studies are needed to identify materials of construction and to quantify corrosion rates. Close coordination should be maintained with the ongoing SCW program sponsored by DARPA.



## PREFACE

This report was prepared by Los Alamos National Laboratory, Los Alamos NM, through an Interagency Agreement under Memorandum of Understanding DE-AI0479AL11812, with the US Air Force Civil Engineering Support Agency, Civil Engineering Laboratory (AFCESA/RAVS), Tyndall Air Force Base, Florida 32403-6001.

This report summarizes work done between 15 October 1987 and 1 April 1992, under the direction of Ms Cheryl Rofer and Dr Steven J. Buelow. Dr Joseph D. Wander was the Air Force project officer for this contract.

This report has been reviewed by the Public Affairs Office (PA) and is releasable to the National Technical Information Service (NTIS). At NTIS, it will be available to the general public, including foreign nationals.

This report has been reviewed and is approved for public release.

## TABLE OF CONTENTS

Section	Title	Page
I.	INTRODUCTION .....	1
A.	OBJECTIVE .....	1
B.	BACKGROUND .....	1
	1. Need for Alternative Disposal Methods .....	1
	2. Supercritical Water Oxidation (SCWO) .....	2
	3. Results of Past SCWO Studies: Demonstrated Performance .....	4
	4. Readiness for Demonstration .....	5
	5. Comparison to Other Technology: Projected Performance .....	8
	6. Regulatory and Public Acceptance of the Technology .....	9
C.	SCOPE .....	10
D.	REPORT ORGANIZATION .....	11
II.	EXPERIMENTAL APPROACH .....	12
A.	LINEAR REACTORS .....	12
B.	FLUIDIZED SAND BATH REACTOR .....	18
C.	BATCH REACTOR .....	20
D.	TRANSPORTABLE WASTE DESTRUCTION UNIT .....	23
E.	ONE-GALLON-PER-HOUR REACTOR SYSTEM .....	26
F.	BASE HYDROLYSIS .....	34
G.	OPTICAL EXPERIMENTS .....	35
	1. Raman Spectroscopy .....	35
	2. Coherent Anti-Stokes-Raman Spectroscopy (CARS) .....	38
	3. Transient Grating Spectroscopy .....	41
H.	ANALYTICAL TECHNIQUES .....	42
	1. Gas-Phase Analysis .....	42

## TABLE OF CONTENTS (CONTINUED)

Section	Title	Page
	2. Liquid-Phase Techniques.....	45
	3. Base Hydrolysis Product Analysis.....	47
III.	REACTIONS OF ENERGETIC MATERIALS BELOW WATER-SOLUBILITY LIMITS.....	48
A.	INTRODUCTION .....	48
B.	DESTRUCTION EFFICIENCIES AND REACTION PRODUCTS UNDER HIGHLY OXIDIZING CONDITIONS .....	48
C.	REACTIONS OF AMMONIUM PERCHLORATE (AP) .....	52
D.	REACTIONS OF TRINITROTOLUENE (TNT).....	56
E.	REACTIONS OF NITROMETHANE (NM) .....	59
F.	REACTIONS OF NITRATE .....	64
G.	REACTIONS OF HYDRAZINE.....	67
	1. Introduction.....	67
	2. Experimental.....	68
	3. Hydrazine Reactions .....	69
	4. Unsymmetrical Dimethylhydrazine Reactions .....	80
	5. Conclusion .....	83
H.	REACTIONS OF NITROGLYCERIN (NG) .....	83
	1. Introduction.....	83
	2. Supercritical CO <sub>2</sub> Extraction/Injection Apparatus .....	83
	3. Supercritical CO <sub>2</sub> Extraction of Nitroglycerin .....	85
	4. SCW Processing of SCCO <sub>2</sub> Extracted Nitroglycerin .....	87
IV.	INCREASING THROUGHPUT OF EXPLOSIVES.....	90
A.	REACTIONS OF SLURRIES .....	90
	1. Small Bomb Calorimeter Experiments .....	90
	2. Slurry Flow Experiments in One-Gallon-per-Hour Reactor.....	94
	3. Particle Settling Calculations.....	98

## TABLE OF CONTENTS (CONTINUED)

Section	Title	Page
B.	INTRODUCTION OF EXPLOSIVES IN A CO-SOLVENT .....	101
C.	BASE HYDROLYSIS OF EXPLOSIVES .....	104
1.	Introduction.....	104
2.	Hydrolysis of Nitroguanidine .....	105
3.	Hydrolysis of Trinitrotoluene .....	110
4.	Hydrolysis of HMX and PBX 9404.....	111
5.	Hydrolysis of RDX .....	115
6.	Hydrolysis of M31A1E1 Propellant .....	115
7.	Hydrolysis of CYH Propellant.....	119
8.	SCWO of Hydrolysis Products .....	127
V.	SPECTROSCOPIC MEASUREMENTS IN SUPERCRITICAL WATER.....	128
A.	RAMAN MEASUREMENTS OF HYDRAZINE.....	128
B.	RAMAN MEASUREMENTS OF NITROMETHANE (NM) .....	132
C.	RAMAN MEASUREMENTS OF AMMONIUM PERCHLORATE (AP) .....	134
D.	MEASUREMENTS OF NITROMETHANE USING CARS .....	136
E.	TRANSIENT GRATING EXPERIMENTS.....	137
VI.	THERMOCHEMISTRY OF ENERGETIC MATERIALS IN SUPERCRITICAL WATER.....	139
VII.	REACTOR CORROSION .....	141
A.	REACTOR METALLURGY AND CORROSION.....	141
B.	CORROSION CAUSED BY SCWO REACTIONS OF ENERGETIC MATERIALS.....	141
1.	Corrosion by SCWO of Ammonium Perchlorate (AP) .....	141
2.	Corrosion by TNT, HMX, PETN and RDX .....	142
3.	Corrosion by Nitrate .....	143
4.	Corrosion by Hydrazine.....	144

## TABLE OF CONTENTS (CONTINUED)

Section	Title	Page
C.	CORROSION TESTING OF REACTOR MATERIALS .....	144
1.	Introduction.....	144
2.	Discussion of Corrosion Testing Methods.....	145
VIII.	SALT SOLUBILITY STUDIES .....	151
A.	INTRODUCTION .....	151
B.	PRODUCTS OF BASE HYDROLYSIS OF ALUMINUM-BEARING PROPELLANTS.....	152
1.	Composition of Aluminum-Bearing Propellants .....	152
2.	Products of Ammonium Perchlorate Hydrolysis .....	152
3.	Products of Aluminum Hydrolysis .....	152
4.	Products of Energetic Materials Hydrolysis .....	153
C.	PHASE BEHAVIOR UNDER HYDROTHERMAL PROCESSING CONDITIONS .....	154
1.	Basic Aluminate and Carbonate Solutions .....	154
2.	Solutions Below the Liquid–Vapor Critical Temperature.....	155
3.	Solutions Above the Liquid–Vapor Critical Temperature.....	155
D.	SOLUBILITY AND PHASE EQUILIBRIA MEASUREMENTS .....	156
1.	Experimental Techniques for the Study of Solubility and Phase Behavior .....	156
2.	Optical Cell Studies of Basic Aluminate and Carbonate Solution Solubilities .....	159
3.	Summary of Solubility and Phase Behavior Studies at High Density .....	162
4.	High-Temperature, Low-Density Salt Solubility Studies in the Packed-Bed Flow Apparatus .....	162

## TABLE OF CONTENTS (CONCLUDED)

Section	Title	Page
E.	CONCLUSIONS AND RECOMMENDATIONS .....	164
IX.	THEORY AND MODELING .....	165
A.	INTRODUCTION .....	165
B.	MODELING OF NITROMETHANE REACTION KINETICS .....	165
C.	STEADY STATE OXIDATION OF H <sub>2</sub> IN SUPERCRITICAL WATER .....	168
D.	MODELING OF CLUSTER DISTRIBUTIONS IN SUPERCRITICAL WATER .....	172
E.	MODELING TOOLS FOR SOLVATION FREE ENERGIES IN HYDROTHERMAL SYSTEMS .....	172
F.	REACTOR DESIGN TO MINIMIZE WALL CORROSION .....	176
	1. Basic Concept .....	176
	2. Design Considerations .....	176
	3. Numerical Calculations.....	177
G.	PROCESS EVALUATION AND OPTIMIZATION .....	180
	1. Objective .....	180
	2. The ASPEN Code .....	181
	3. Modeling Results .....	182
	4. Conclusions.....	184
X.	CONCLUSIONS .....	186
A.	SCWO CHEMISTRY .....	186
B.	INCREASING THROUGHPUT OF EXPLOSIVES .....	188
C.	REACTOR CORROSION.....	189
D.	SALT SOLUBILITY .....	189
	REFERENCES .....	191

## LIST OF FIGURES

Figure	Title	Page
1	SCWO Process Schematic .....	3
2	Simplified Schematic of Demonstration SCWO Treatment Unit.....	4
3	Schematic of linear flow reactor .....	12
4	Photograph of linear flow reactor .....	13
5	Detailed diagram of the gas–liquid separator .....	14
6	Photograph of gas–liquid separator .....	15
7	Detailed diagram of gold-lined reactor.....	16
8	Sodium concentration versus volume flowed through reactor .....	17
9	Schematic of sand bath reactor .....	18
10	Photograph of sand bath reactor .....	19
11	Schematic of the batch reactor experimental setup .....	21
12	Photograph of batch reactor .....	22
13	Transportable Waste Destruction Unit (TWDU).....	23
14	Photograph of Transportable Waste Destruction Unit.....	24
15	Photograph of 1-gal-per-hour unit .....	27
16	Photograph of wastewater feed and pressurization subsystem.....	28
17	Photograph of oxygen supply and pressurization subsystem .....	29
18	Photograph of pressure control subsystem .....	32
19	Photograph of the data acquisition and control subsystem.....	33
20	Schematic of Raman apparatus.....	36
21	Optical cell with blowup of window region .....	37
22	Photograph of the optical cell .....	38
23	Diagram of linear flow reactor with optical access .....	39
24	CARS apparatus.....	40
25	Schematic of a transient grating experiment.....	41
26	Typical FTIR calibration curve for N <sub>2</sub> O .....	44
27	FTIR spectra of the reaction products of SCWO of NQ, TNT, and RDX.....	50
28	HPLC analyses of aqueous TNT solutions .....	58
29	FTIR product analysis of SCWO of nitromethane .....	60
30	FTIR product analysis for the SCWO of NM at 600 °C.....	63
31	Nitrate removal versus temperature and residence time .....	65
32	Methanol removal versus temperature and residence time.....	66

## LIST OF FIGURES (CONTINUED)

Figure	Title	Page
33	FTIR spectrum of gas effluent from hydrazine pyrolysis.....	71
34	Proposed hydrazine decomposition mechanism in SCW. ....	72
35	Mass spectrum of products of SCWO of hydrazine with $H^{14}NO_3$ .....	76
36	Mass spectrum of products of SCWO of hydrazine with $H^{15}NO_3$ .....	77
37	FTIR spectrum of products of SCWO of hydrazine .....	78
38	Expansion of 01 <sup>1</sup> 0-00 <sup>0</sup> Q-branch region of $N_2O$ around 600 $cm^{-1}$ .....	79
39	FTIR spectrum of products of SCWO of UDMH.....	82
40	Schematic of $SCCO_2$ extraction/linear flow SCWO apparatus .....	84
41	$^1H$ NMR of M31A1E1.....	85
42	$^1H$ NMR of extracted material from $SCCO_2$ extraction of M31A1E1 .....	86
43	$^1H$ NMR of residual material from $SCCO_2$ extraction of M31A1E1 .....	87
44	Pressure rises observed due to reactions of TATB slurries in water .....	91
45	Pressure rises observed due to reactions of DBP slurries in water.....	93
46	HMX decomposition pressure as a function of temperature .....	94
47	Pumping unit and reactor inlet with and without circulating pump added.....	96
48	Predicted $V_m$ and $Q_m$ for $V_s = 0.03$ and $d = 50$ mm.....	100
49	Predicted $V_m$ and $Q_m$ for $V_s = 0.01$ and $d = 50$ mm.....	100
50	Predicted $V_m$ and $Q_m$ for $V_s = 0.1$ and $d = 50$ mm.....	101
51	Predicted $V_m$ and $Q_m$ for $V_s = 0.03$ and $d = 150$ mm.....	102
52	Predicted $V_m$ and $Q_m$ for $V_s = 0.03$ and $d = 300$ mm.....	102
53	$^{13}C$ NMR of NQ hydrolysis residue .....	107
54	$^{13}C$ NMR of NQ hydrolysis residue with excess NaOH .....	108
55	FTIR of solid NQ hydrolysis residue.....	109
56	$^{13}C$ NMR spectrum of HMX hydrolysis residue.....	113
57	Spectra of M31A1E1 in deuterated DMSO .....	117
58	$^{13}C$ NMR spectrum of the water-soluble hydrolysis products of M31A1E1 .....	118
59	Spectra of CYH in DMSO and water solution .....	122
60	Spectra of CYH hydrolysis products .....	123
61	FTIR of products of SCWO of M31A1E1 hydrolysis solution .....	126
62	Raman spectra of hydrazine in water at 270 atm.....	129
63	Decay of hydrazine Raman intensity versus average residence time .....	130
64	Arrhenius plot of effective first order decay rate for 2% $N_2H_4/H_2O$ at 350 atm ...	131



## LIST OF FIGURES (CONCLUDED)

Figure	Title	Page
65	Raman spectra of 10% nitromethane in water at 550 °C and 370 atm .....	133
66	Raman spectra for nitromethane/water mixtures .....	134
67	Arrhenius plot for nitromethane/water mixtures .....	135
68	CARS spectra of NM in water at high pressure (348 atm).....	136
69	Thermal grating decay for I <sub>2</sub> + KI + H <sub>2</sub> O solution at 400°C, 5040 psi.....	137
70	Transient grating signal from methanol/dye solution .....	138
71	General arrangement of SCWO corrosion test reactor .....	146
72	Flow schematic of SCWO corrosion test loop.....	147
73	"Static" corrosion test reactor .....	150
74	Packed-bed flow apparatus for salt solubility studies.....	158
75	Calculated species profiles for decomposition of NM in SCW.....	167
76	Steady state oxidation rate of H <sub>2</sub> .....	179
77	Steady state oxidation rate of H <sub>2</sub> versus concentration .....	171
78	Calculated potential of average force for Na <sup>+</sup> Cl <sup>-</sup> ion pair in water .....	174
79	Calculated solvation free energy of the carbonate anion in water.....	175
80	Conceptual design of flow reactor .....	177
81	Contours of CO <sub>2</sub> (product) concentration before steady state.....	179
82	Contours of CO <sub>2</sub> (product) concentration after steady state.....	180

## LIST OF TABLES

Table	Title	Page
1.	CHEMICALS TREATED BY SUPERCRITICAL WATER OXIDATION AND TYPICAL DESTRUCTION EFFICIENCIES .....	6
2.	INORGANIC COMPOUNDS PROCESSED THROUGH SUPERCRITICAL WATER OXIDATION REACTOR .....	7
3.	COMPLEX WASTES TREATED BY SUPERCRITICAL WATER OXIDATION .....	7
4.	COMPOSITION OF REACTOR MATERIALS .....	16
5.	DESTRUCTION EFFICIENCIES FOR ENERGETIC MATERIALS BELOW WATER SOLUBILITY LIMITS .....	48
6.	FTIR ANALYSIS OF GAS-PHASE PRODUCTS OF SCWO OF ENERGETIC MATERIALS .....	50
7.	ANALYSIS OF CARBON PRODUCTS IN EFFLUENT STREAMS FOR SCWO OF ENERGETIC MATERIALS .....	51
8.	ANALYSIS OF NITROGEN PRODUCTS IN EFFLUENT STREAMS FOR SCWO OF ENERGETIC MATERIALS .....	51
9.	AP SCWO PRODUCTS AS A FUNCTION OF TEMPERATURE .....	52
10.	AP SCWO PRODUCTS AS A FUNCTION OF CONCENTRATION.....	53
11.	COMPARISON OF AP SCWO REACTIONS IN C-276 AND GOLD-LINED REACTORS .....	55
12.	SCWO OF AP AND RDX MIXTURES .....	56
13.	CO <sub>2</sub> PRODUCTION IN THE SCWO OF TNT .....	57
14.	TNT SCWO PRODUCTS AS A FUNCTION OF H <sub>2</sub> O <sub>2</sub> CONCENTRATION.....	59
15.	TNT SCWO PRODUCTS AS A FUNCTION OF TEMPERATURE.....	59
16.	FTIR ANALYSIS OF NITROMETHANE DECOMPOSITION PRODUCTS .....	61
17.	MASS BALANCE FOR NITROMETHANE DECOMPOSITION .....	61
18.	CO <sub>2</sub> PRODUCTION IN THE SCWO OF NITROMETHANE .....	62
19.	ANALYSIS OF RESIDUAL CARBON IN AQUEOUS EFFLUENT FOR SCWO OF NM AT 600 °C.....	64
20.	SUMMARY OF HYDRAZINE AND UDMH SCWO REACTIONS .....	68
21.	DESTRUCTION EFFICIENCIES FOR THE SCWO OF HYDRAZINE AND UDMH .....	68
22.	HYDRAZINE NITROGEN MASS BALANCE (AS A % OF THE STARTING NITROGEN CONCENTRATION).....	69

## LIST OF TABLES (CONTINUED)

Table	Title	Page
23.	HYDRAZINE HYDROGEN MASS BALANCE, PYROLYSIS (AS A % OF THE STARTING HYDROGEN CONCENTRATION).....	70
24.	HYDRAZINE + H <sub>2</sub> O <sub>2</sub> PRODUCT RATIOS, Ø = 1 .....	73
25.	HYDRAZINE + H <sub>2</sub> O <sub>2</sub> PRODUCT RATIOS, Ø = 0.5 .....	73
26.	HYDRAZINE + HNO <sub>3</sub> PRODUCT RATIOS .....	75
27.	MASS SPECTRAL ASSIGNMENTS OF FIGURES 35 AND 36.....	77
28.	UNSYMMETRICAL DIMETHYLHYDRAZINE NITROGEN MASS BALANCE (AS A % OF STARTING NITROGEN CONCENTRATION) .....	81
29.	UNSYMMETRICAL DIMETHYLHYDRAZINE CARBON MASS BALANCE (AS A % OF STARTING CARBON CONCENTRATION) .....	81
30.	PRODUCT RATIO NORMALIZED TO THE STARTING (CH <sub>3</sub> ) <sub>2</sub> N <sub>2</sub> H <sub>2</sub> CONCENTRATION, Ø=1 .....	82
31.	PRODUCT RATIO NORMALIZED TO THE STARTING (CH <sub>3</sub> ) <sub>2</sub> N <sub>2</sub> H <sub>2</sub> CONCENTRATION, Ø=0.5 .....	83
32.	COMBINED SCCO <sub>2</sub> EXTRACTION/SCWO TREATMENT OF M31A1E1 .....	88
33.	MASS SPECTROMETRIC ANALYSIS OF HMX DECOMPOSITION PRODUCT GASES.....	93
34.	COMPOSITIONS OF FORMULATIONS USED IN BASE HYDROLYSIS EXPERIMENTS.....	104
35.	ANIONIC PRODUCTS FROM THE HYDROLYSIS OF PBX 9404 .....	114
36.	CARBON PRODUCTS FROM M31A1E1 HYDROLYSIS .....	119
37.	TOC/TIC ANALYSIS OF M31A1E1 HYDROLYSIS PRODUCTS.....	119
38.	NITROGEN PRODUCTS FROM M31A1E1 HYDROLYSIS .....	120
39.	ANIONIC PRODUCTS FROM THE HYDROLYSIS OF CYH PROPELLANT .....	121
40.	ANALYTICAL ASSAY OF HYDROLYSIS EFFLUENT .....	124
41.	INITIAL CONCENTRATIONS AND DESTRUCTION EFFICIENCIES FOR HYDROLYSIS/SCWO PROCESSES .....	125
42.	ANALYSIS OF AQUEOUS CARBON PRODUCTS IN EFFLUENT STREAMS AFTER SCWO.....	126
43.	ANALYSIS OF AQUEOUS NITROGEN PRODUCTS IN EFFLUENT STREAMS AFTER SCWO .....	127
44.	HEAT OF DECOMPOSITION OF AP IN STAINLESS STEEL CELLS .....	139

## LIST OF TABLES (CONCLUDED)

Table	Title	Page
45.	CORROSION PRODUCTS FOR SCWO OF AMMONIUM PERCHLORATE.....	142
46.	CORROSION PRODUCTS FOR SCWO OF EXPLOSIVES IN HASTELLOY C-276 ALLOY LINEAR REACTOR .....	142
47.	NOMINAL COMPOSITION OF TEST ALLOYS.....	148
48.	AVERAGE COUPON WEIGHT CHANGE .....	148
49.	SOLUTION COMPOSITION (MOLAR CONCENTRATIONS OF SUBSTITUENTS) FOR SOLUBILITY STUDIES .....	160
50.	VAPOR PRESSURES FOR SODIUM ALUMINATE SOLUTIONS IN 1.0-MOLAR SODIUM HYDROXIDE.....	160
51.	SUPERCRITICAL-PHASE SOLUBILITY OF SODIUM ALUMINATE AND SODIUM CARBONATE IN 0.1- MOLAR SODIUM HYDROXIDE .....	163
52.	PRIMARY REACTIONS FOR OXIDATION OF H <sub>2</sub> IN SUPERCRITICAL WATER.....	169

## LIST OF ABBREVIATIONS

AP	Ammonium Perchlorate
BTTN	1,2,4-Butanetriol Trinitrate
CARS	Coherent Anti-Stokes Raman Spectroscopy
CCD	Charge-Coupled Device
DA&C	Data Acquisition and Control
DAC	Digital-to-Analog Converter
DRE	Destruction and Removal Efficiency
ft	Foot
FTIR	Fourier-Transform Infrared
g	Gram
GC-MS	Gas Chromatography–Mass Spectrometry
HMX	Cyclotetramethylene Tetranitramine
HPLC	High-Performance Liquid Chromatography
id	Inside Diameter
mL	Milliliter
MPa	Megapascals
NC	Nitrocellulose
NG	Nitroglycerin[e]
NM	Nitromethane
NQ	Nitroguanidine
OB/OD	Open Burning/Open Detonation
od	Outside Diameter
PEP	Propellants, Explosives and Pyrotechnics
PETN	Pentaerythritol Tetranitrate
psia	Pounds Per Square Inch Absolute
psig	Pounds Per Square Inch Gage
RDX	Cyclotrimethylene Trinitramine
SCWO	Supercritical Water Oxidation
TNT	2,4,6-Trinitrotoluene
UDMH	1,1-Dimethylhydrazine
YAG	Yttrium Aluminum Garnet
μm	Micrometer (10 <sup>-6</sup> Meters)

## SECTION I

### INTRODUCTION

#### A. OBJECTIVE

The objective of this project was to determine the suitability of oxidation in supercritical fluids (SCO), particularly water (SCWO), for disposal of propellants, explosives, and pyrotechnics (PEPs).

The SCO studies of PEPs addressed the following issues:

- The efficiency of destruction of the substrate.
- The products of destruction contained in the effluent.
- Whether the process can be conducted safely on a large scale.
- Whether energy recovery from the process is economically practicable.

The information essential for process development and equipment design was also investigated, including issues such as practical throughput of explosives through a SCWO reactor, reactor materials and corrosion, and models for process design and optimization.

#### B. BACKGROUND

##### 1. Need for Alternative Disposal Methods

Traditional methods for disposing of PEPs have been open burning or open detonation (OB/OD); however, regulatory agencies are likely to prohibit OB/OD because of the uncontrolled air emissions and soil contaminations. Likewise, controlled incineration carries a liability for air pollution because large quantities of  $\text{NO}_x$  are produced in the conventional combustion chemistry of PEPs and because the course of combustion of PEPs is generally erratic and characterized by recurrent process upsets. Soil and groundwater have already been contaminated with PEPs through normal operations at manufacturing plants and military bases. Incineration can be used for decontamination of these soils, with the associated liability for air pollution, but few satisfactory and economic methods exist for groundwater decontamination. A clear need exists for improved disposal and destruction methods.

## 2. Supercritical Water Oxidation (SCWO)

In SCWO, the waste is generally mixed with an oxidant (oxygen, air, or hydrogen peroxide) in water at pressures and temperatures above the critical point (374 °C and 22.13 MPa). Under these conditions, water is a fluid whose densities are high enough that reasonable process throughput can be achieved, but whose transport properties are like those of a gas, allowing rapid, homogeneous chemical reactions. Supercritical water is a unique solvent medium in which oxidation can take place at lower temperatures than incineration, thus limiting the production of NO<sub>x</sub> and char. The reaction is entirely enclosed in a pressure vessel at concentrations low enough that the solvent absorbs the heat of reaction. As a result, the temperature can be maintained at any desired level (typically in the range 400–650 °C). Oxidation occurs rapidly, on the time scale of seconds to minutes, and produces simple products (ideally CO<sub>2</sub>, H<sub>2</sub>O, and N<sub>2</sub>).

In principle, any organic compound—that is, any compound composed of carbon and other elements such as hydrogen, nitrogen, phosphorus, sulfur, and the halogens—can be completely oxidized to relatively innocuous products. Because water is the reaction medium, the process can be used for a variety of organic wastes containing water, or for water contaminated with organic compounds. The optimum concentration of organics in water will vary with the heat of oxidation of the particular organic compounds present and the engineering design of the apparatus. An engineering consideration in the design of a plant is the range of organic concentrations that generates enough heat to maintain the reaction, but not more heat than can readily be removed from the processing vessel. Pure or highly concentrated organic wastes can be diluted with water, whereas fuel or other organic wastes can be added to dilute aqueous wastes. Other factors that influence the engineering design include the residence time in the reactor (determined by the chemical kinetics of oxidation of the waste), the physical state of the waste and its oxidation products, and the quantity of waste to be processed.

A schematic for the SCWO process is shown in Figure 1. The waste, oxidant, and fuel (if needed) are compressed, preheated, mixed, and injected into the reactor, in which the waste is (ideally) converted into H<sub>2</sub>O, CO<sub>2</sub>, N<sub>2</sub>, salts, and insoluble solids. Reactor pressures typically range from 25 to 35 MPa (3700 to 5100 psia). Solid, liquid, and gaseous effluents are separated, depressurized, and (if needed) postprocessed. All effluents can be contained and collected for testing before release to the environment. Unreacted oxygen can be segregated and recycled, and energy can be recovered and used to heat incoming waste.

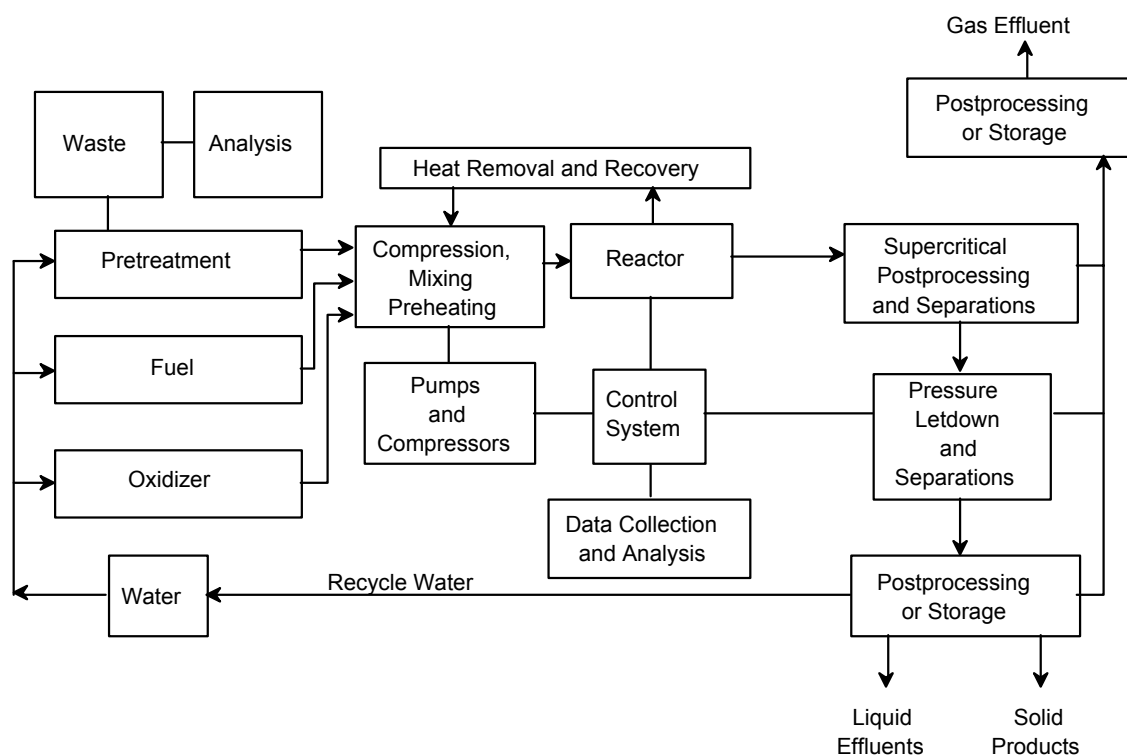


Figure 1. SCWO Process Schematic.

A great range of scale appears to be possible for supercritical water oxidation plants. Standard pressure-vessel technology can be used to provide small mobile units or permanent medium-sized surface installations for processing of laboratory or manufacturing wastes. Plants with very large capacities have also been proposed, in which a cylindrical heat exchanger and reaction vessel are placed in the ground by use of oil-field-drilling and well-completion technology.

Operation of an SCWO unit for the treatment of explosive wastes will need to be controlled remotely. The details for full-scale operation (site preparation, facility needs, utilities) will depend on the waste being treated and the particular design of the reactor (*i.e.*, tube, vessel, in-ground, etc.). A more complete description of the operation of full-scale SCWO units, including materials throughput, mass balances, and equipment design, can be found in several reports (References 7, 8).



An SCWO reactor that could be used for demonstration purposes is schematically outlined in Figure 2. Flow capacity of this unit would be 20 gallons/hour and it would process water containing up to 20 percent organic content by weight. For comparison, the capacity of a medium-sized, full-scale unit is envisioned to be 10 to 100 times larger, depending on the specific waste stream. This demonstration unit would be used to evaluate design concepts for a full-scale unit, pre- and post-processing technologies for each different waste type, and process controls. It would provide information concerning the effectiveness of the treatment process (*e.g.*, destruction efficiencies, products of SCWO, etc.), wear and useful lifetime of equipment components, health and safety considerations, and operation and maintenance requirements.

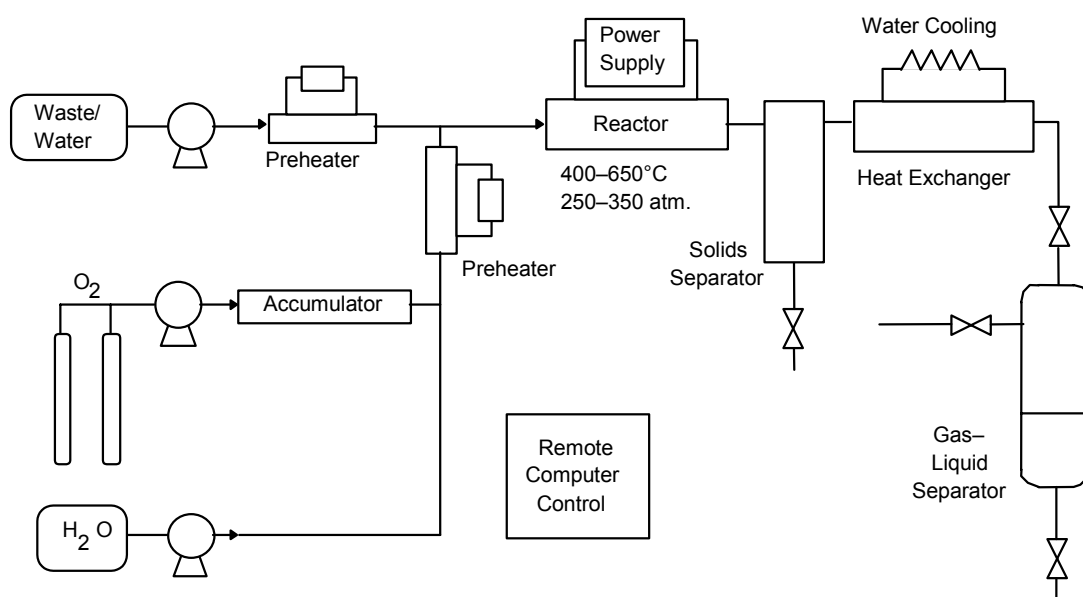


Figure 2. Simplified Schematic of Demonstration SCWO Treatment Unit.

### 3. Results of Past SCWO Studies: Demonstrated Performance

The principle of SCWO has been successfully demonstrated. Supercritical water oxidation has exhibited high destruction and removal efficiencies (DREs) for a broad range of common solid and liquid wastes, including such difficult examples as chlorinated aromatic solvents (References 1-6). These same studies have indicated that the major reaction products are water, carbon dioxide, and inorganic salts. Traces of carbon monoxide and nitrous oxide were also observed. Nitrous oxide can be efficiently converted into nitrogen and oxygen by venting through an inexpensive, commercially available catalyst. Less detailed but promising

results were also reported for 2,4-dinitrotoluene, which is structurally related to several of the substrates in this study.

A wide variety of compounds have been successfully oxidized. These include simple hydrocarbons and oxygenates, chlorinated organics and aromatics, nitro-organic compounds, pharmaceuticals and biopharmaceuticals, dioxin-contaminated soil, fermentation wastes, and municipal and industrial sludges (References 3–7). Table 1 lists a number of compounds for which destruction efficiencies have been measured. The SCWO process has been operated successfully in the presence of many inorganic compounds (Table 2) and has been used to process a number of complex wastes (Table 3). In addition, such inorganic compounds as perchlorate and nitrate salts have been destroyed in supercritical water with greater than 99.9 percent efficiency.

Although the principle of SCWO has been successfully demonstrated on many classes of wastes, it has not been (before this work) applied to energetic materials. Issues that remain unresolved include the safety of the process, kinetics of decomposition, reaction products (the nitrogen chemistry in particular is not known), effects of high salt concentrations such as aluminum and chloride salts expected to be produced with most propellant formulations, introduction of energetic materials into a SCWO reactor at practical concentrations and the effects of corrosion on reactor materials.

#### 4. Readiness for Demonstration

Industrial, governmental, and university participants at a workshop sponsored by the U. S. Air Force Engineering and Service Center, held at Los Alamos in August of 1989, decided that no fundamental impediments exist to the application of supercritical water oxidation processes to ultrahazardous materials under appropriately controlled conditions. There was, however, general agreement that several practical difficulties will require additional research and development. These areas include the handling of solids, materials problems relating to corrosive wastes, the handling of high-risk wastes (*e.g.*, highly radioactive mixed wastes), and the handling of energetic materials. Since then, progress has been made on problems associated with the handling of solids and explosives. Although work has been done on the corrosion problem, no successful solution has yet been fully demonstrated. Corrosion problems may need to be resolved for specific waste streams before a full-scale plant is implemented, although they are not severe enough to delay demonstration of the technology.

TABLE 1. CHEMICALS TREATED BY SUPERCRITICAL WATER OXIDATION  
AND TYPICAL DESTRUCTION EFFICIENCIES<sup>a</sup>

Chemical Name	Destruction Efficiency, %
Ammonia	>99.71
Ammonium Perchlorate	>99.9
Arochlors (PCBs)	>99.995
Biphenyl	99.97
Carbon Tetrachloride	>96.53
Chlorinated Dibenzo- <i>p</i> -dioxins	>99.9999
Chloroform	>98.83
2-Chlorophenol	>99.997
<i>o</i> -Chlorotoluene	>99.998
Cyclohexane	99.97
DDT	99.997
Dextrose	99.6
4,4'-Dichlorobiphenyl	99.993
1,2-Dichloroethylene	99.99
2,4-Dinitrotoluene	99.9998
Ethylene Glycol	>99.9998
Fluorescein	>99.9992
Hexachlorocyclohexane	>99.9993
Hexachlorocyclopentadiene	99.99
HMX <sup>b</sup>	>99.9
Methyl Ethyl Ketone	99.993
Nitrobenzene	>99.998
Nitroguanidine <sup>b</sup>	>99.9
Nitromethane <sup>b</sup>	>99.9
PETN <sup>b</sup>	>99.9
RDX <sup>b</sup>	>99.9
Tetrachloroethylene	99.99
TNT <sup>b</sup>	>99.9
Trichlorobenzenes	99.99
1,1,1-Trichloroethane	>99.99997
1,1,2-Trichloroethane	>99.981
<i>o</i> -Xylene	99.93

<sup>a</sup>(References. 1-6).

<sup>b</sup>This study.

TABLE 2. INORGANIC COMPOUNDS PROCESSED THROUGH SUPERCRITICAL WATER OXIDATION REACTOR<sup>a</sup>

Alumina	Magnesium Phosphate
Ammonium Chloride	Magnesium Sulfate
Ammonium Sulfate	Mercuric Chloride
Boric Acid	Potassium Bicarbonate
Bromides	Potassium Carbonate
Calcium Carbonate	Potassium Chloride
Calcium Chloride	Potassium Sulfate
Calcium Oxide	Silica
Calcium Phosphate	Sodium Carbonate
Calcium Sulfate	Sodium Chloride
Fluorides	Sodium Hydroxide
Heavy Metal Oxides	Sodium Nitrate
Hydrochloric Acid	Sodium Nitrite
Iron	Sodium Sulfate
Iron Oxide	Soil
Lithium Sulfate	Sulfur, Elemental
Magnesium Oxide	Titanium Dioxide

TABLE 3. COMPLEX WASTES TREATED BY SUPERCRITICAL WATER OXIDATION<sup>a</sup>

Adumbran	Human Waste (black and gray water)
<i>Bacillus stearothermophilus</i>	Ion Exchange Resins
(Heat-Resistant Spores)	Poly(Styrene–Divinylbenzene)
Bran Cereal	Malaria Antigen
Carbohydrates	Olive Oil
Casein Paper	
Cellulosics	Protein
Coal	Sewage Sludge
Coal Waste	Soybean Plants
Corn Starch	<i>Sulfolobus acidocaldarius</i>
Diesel Fuel	Surfactants
<i>Escherichia coli</i>	Transformer Oil
Endotoxin (Pyrogen)	Yeast

<sup>a</sup>(References. 1-6).

## 5. Comparison to Other Technology: Projected Performance

Compared to other available technologies, supercritical water oxidation is applicable to a broader range of waste types. It can be used to treat pure organics, contaminated soils and water, sludges, and some inorganics. It appears to be economically competitive with other technologies used for aqueous wastes containing 1 to 20 percent organic matter. Since the SCWO process is completely contained, emissions can be controlled and, at present, public concern should not delay obtaining operating permits. The complexity of the technology is comparable to incineration, so with proper engineering and process controls, qualified technicians should be able to operate and maintain an SCWO unit.

Incineration is a nonspecific alternate method for destroying organic materials. Incineration can be operated at a relatively low cost, but requirements for extensive emission controls and difficulties associated with controlling processes and obtaining permits can negate potential advantages. Supercritical water oxidation takes place at a much lower temperature (about 500 °C) than incineration and in a completely contained system. Almost no oxides of nitrogen are expected at these low temperatures, and the effluent is completely contained and controlled. Supercritical water oxidation can be applied to water containing 20 percent or less organic waste. By comparison, incineration is not as cost effective at these concentrations. Cost estimates for developing technologies, such as SCWO, at full scale are inherently uncertain and should be considered cautiously. The cost of SCWO of wastes has been estimated in several studies (References 6–8). For treating a ton of dry organic material, the costs are estimated to be between \$300 and \$600 per ton depending on the size of the SCWO treatment unit (Reference 8).

Other methods under development that may apply to explosive wastes include oxidation by hydrogen peroxide and/or ozone with ultraviolet (UV) radiation, electrochemical oxidation, and oxidation or thermolysis in molten salts. In two-phase systems such as these, concentration gradients across phase boundaries and mass transfer of oxygen limit the rate and extent to which compounds can be completely destroyed. A supercritical fluid is a single phase allowing complete mixing; thus, reaction rates are not diffusion limited. A preliminary cost comparison of these oxidation processes prepared by the Energy and Environmental Analysis Group at Los Alamos National Laboratory estimates the costs for the UV processes for

contaminated water at 10 to 100 times less per gallon of water than for SCWO. However, these technologies are limited to low (<1000 ppm) concentrations of organics. Concentrated wastes would need to be diluted. In addition, these methods usually require special pretreatment of the wastewater, thereby increasing costs.

#### 6. Regulatory and Public Acceptance of the Technology

The Environmental Protection Agency (EPA) has informally stated that supercritical water oxidation is not considered to be incineration. Thus it will probably be permitted under 40 CFR 264, Part X. If supercritical water oxidation units become an integral part of a manufacturing process, the EPA will not consider the unit to be a treatment facility, implying that wastewater and air discharge permits are sufficient. In a demonstration of SCWO technology in New York State, MODAR Corporation obtained a permit under the New York State Environmental Conservation Law, Article 27, Title 7, Part 360, and approval from the EPA to treat polychlorinated biphenyls (PCBs) under 40 CFR 761.60(e). The waste analysis plan and trial test plan were developed to comply with the Resource Conservation and Recovery Act (RCRA) regulations cited in 40 CFR 265.402(a)(2). A second demonstration by MODAR at a chemical plant in Pennsylvania did not require similar permits (because PCBs were not being treated) and the effluent was sent to the plant's water treatment facility.

Supercritical water oxidation has only recently come to the public's attention. Published essays presenting favorable views of the technology by the *New York Times* and Associated Press have recently appeared in newspapers nationwide. Negative public opinion is not anticipated.

## C. SCOPE

This project seeks to examine the behavior of 13 energetic substrates under conditions of SCWO to provide the DREs of the substrates, to determine the optimum conditions for maximizing the DREs, and to ensure safe operation. These substrates are

Ammonium perchlorate (AP)  
1,2,4-Butanetriol trinitrate (BTTN)  
Cyclotrimethylene trinitramine (RDX)  
Cyclotetramethylene tetranitramine (HMX)  
Nitrocellulose (NC)  
Nitroglycerin (NG)  
Nitroguanidine (NQ)  
Nitromethane (NM)  
Nitrogen tetroxide ( $\text{N}_2\text{O}_4$ )  
Pentaerythritol tetranitrate (PETN)  
2,4,6-Trinitrotoluene (TNT)  
Hydrazine ( $\text{N}_2\text{H}_4$ )  
1,1-Dimethylhydrazine (UDMH).

Products of destruction are identified and measured. Experimental results are evaluated to determine whether the reaction products are environmentally acceptable. If possible, the overall kinetics of oxidation of each substrate is quantified. Practical issues related to process development have also been explored. Corrosion studies to determine the suitability of various reactor materials are reported. Methods for achieving practical throughput of explosives through a SCWO reactor have been explored, including introducing explosives into the reactor either in a co-solvent or as a water slurry and pretreatment of explosives using base hydrolysis. Many aspects of the SCWO process have been modeled and the results are reported here, from the chemical kinetics of the oxidation reactions to fluid flow, heat transfer and process plant balance. Finally, safety studies have determined the detonation sensitivity characteristics of PEPs in supercritical water systems.

## D. REPORT ORGANIZATION

This final report summarizes the progress that has been made reaching the goals of this project. It includes

- Design, construction and operation of SCWO reactors used for explosives,
- Development of experimental procedures for determining DREs, products of destruction from SCWO reactions, and optical *in-situ* probing of SCWO reactions,
- Discussion of DREs and products of reaction for AP, RDX, HMX, NG, NQ, NM, PETN, TNT, N<sub>2</sub>H<sub>4</sub>, and UDMH,
- Examination of process techniques for introducing high concentrations of PEPs into SCWO reactors,
- Development of kinetic models for elucidating chemical reactions in supercritical fluids,
- Development of equations of state that better describe supercritical fluid properties, and
- Reaction of nitrates with organics in supercritical water.

To keep the size of this report manageable, the results of hundreds of experiments have been analyzed and summarized in the 52 tables presented in the following sections.



## SECTION II

### EXPERIMENTAL APPROACH

This section describes the reactors used to destroy high-energy materials through supercritical fluid oxidation/reduction processes, and the analytical methods used to measure product species. We constructed, tested, and operated two linear flow reactors, one of which contained a corrosion-resistant gold lining, a flow reactor heated in a fluidized sand bath, and micro-batch reactors for investigating the energetics of slurries. We present a generalized description for each of the experimental reactors and the corresponding operational procedures. The specific experimental conditions under which the destruction measurements were performed are presented in the Results and Discussion sections. The optical techniques, coherent anti-Stokes Raman spectroscopy (CARS) and normal Raman spectroscopy, to be used as probes of reaction kinetics, are also discussed in these sections.

#### A. LINEAR REACTORS

Bench-scale linear flow reactors have been developed to destroy explosives in supercritical water. Figure 3 shows a schematic and Figure 4 is a photograph of the linear reactors. Solutions of oxidizer and/or explosive were introduced at high pressure into the reactor by constant-flow, high-performance liquid chromatography (HPLC) pumps (LDC Analytical, Constametric 3200).

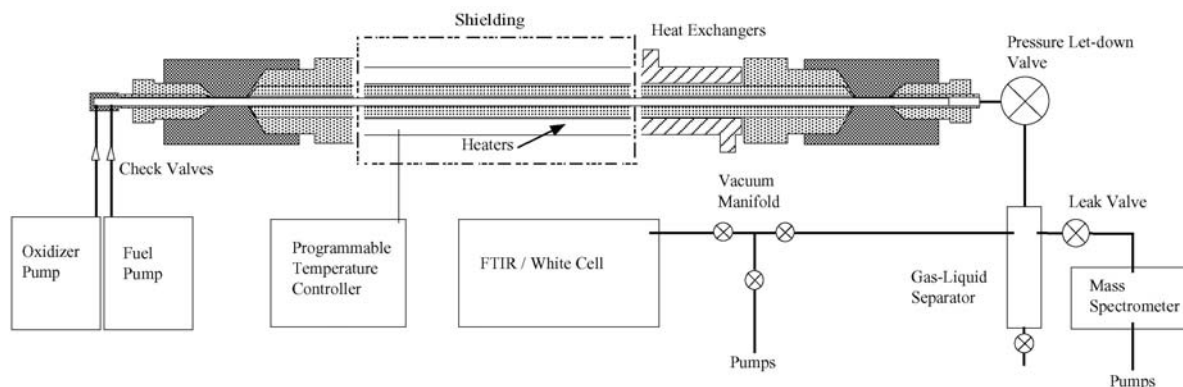


Figure 3. Schematic of linear flow reactor

The explosives were typically present in water at less than half their solubility limit or decomposed in water as the result of prior hydrolysis reactions. Check valves were placed in

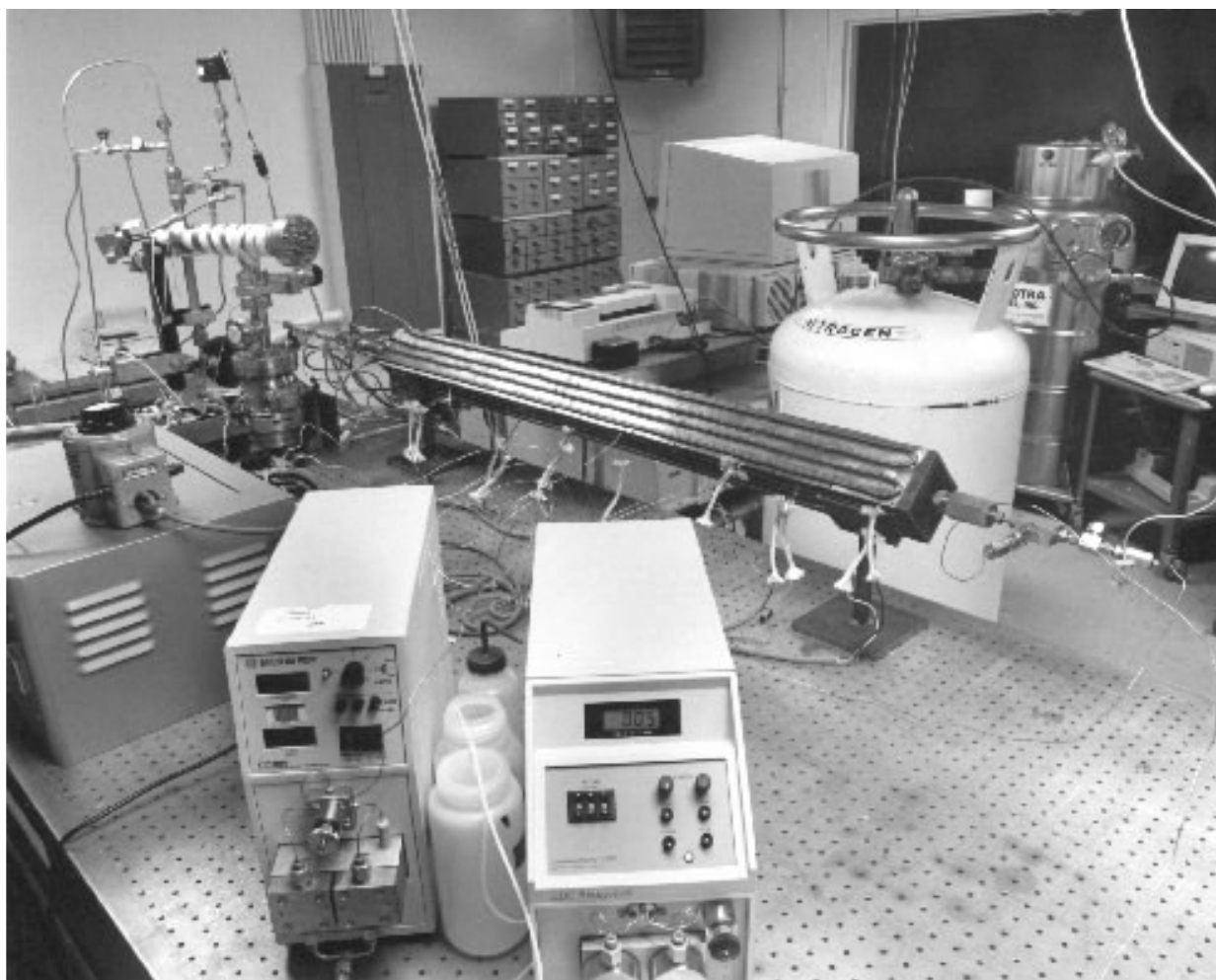


Figure 4. Photograph of linear flow reactor

each line to prevent backstreaming in case of pump failure. Fuel and oxidizer were either premixed before being pumped or were introduced separately. In either case, mixing was completed before reaching the heated section of the reactor. The central core of the reactor was heated to a controlled temperature by six heaters in parallel consisting of hollow brass tubes wrapped with MgO-insulated Nichrome<sup>®</sup> wire. The temperature was maintained by regulating the current through the heating wire with Omega CN9000 series microprocessor temperature controllers. The temperature of each of these heaters could be varied independently; however, for all experiments described in this report the temperature of each heated section was kept the same. Six K-type (chromel–nickel), sheathed thermocouples monitored the temperature in close proximity to the reactor core. A water-cooled heat exchanger at the exit cooled the reacted mixture to room temperature. The cooled effluent passed through a 7- $\mu$ m filter for removal of any particulate matter before the pressure was reduced to ambient with a letdown valve.

Gas and liquid effluents at ambient temperature and pressure then entered a gas–liquid separator (Figures 5, 6). The liquid effluent was removed from the bottom for *ex-situ* quantitative analysis as described in Section II.H.2, while the gas-phase products were expanded into a multipass White cell and analyzed with a Perkin–Elmer 1760-X Fourier-transform infrared (FTIR) spectrometer. A small portion of the gas also passed through a leak valve into a UTI quadrupole mass spectrometer for measurement of the gases N<sub>2</sub>, O<sub>2</sub>, and H<sub>2</sub>.

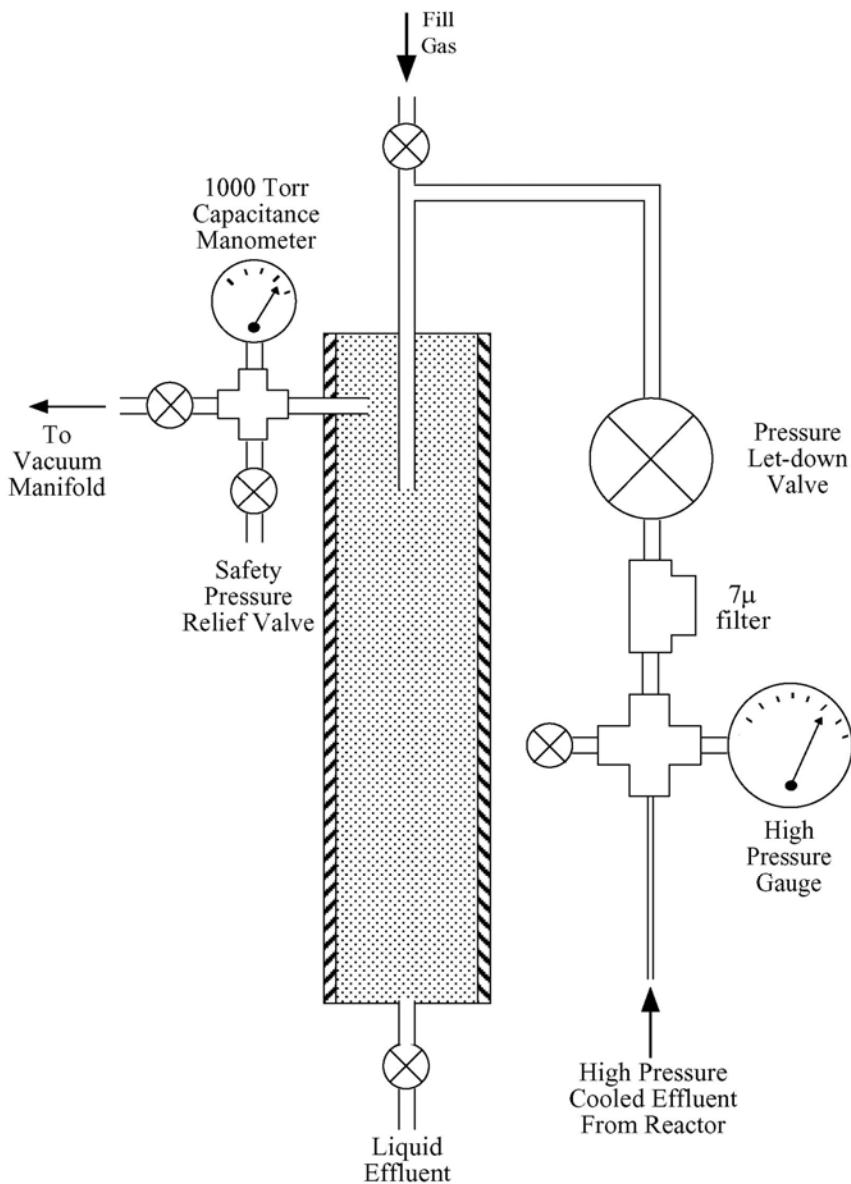


Figure 5. Detailed diagram of the gas–liquid separator. Cooled effluent is passed through a filter before pressure let-down. System is then pressurized with a buffer gas, and gaseous effluent is expanded into the White cell and mass spectrometer leak valve. The liquid effluent is removed through the bottom valve.



Figure 6. Photograph of gas-liquid separator

The high-temperature portion of one of our linear reactors was constructed of C-276, a nickel alloy. The C-276 alloy was chosen because of its known strength and resistance to corrosion at high temperatures. Even so, under some reaction conditions we saw considerable corrosion. To overcome this problem, a second reactor was constructed containing a 316 stainless steel sheath with a gold liner (Figure 7). A seal was made with the gold liner by flaring one end of the gold tube and compressing it between tapered high-pressure fittings. The liner was open at the exit of the reactor, creating a static supercritical region between the liner and stainless core. The gold liner protects all high-temperature sections of the reactor. All “taper-seal” high-pressure fittings, and most other components obtained from High Pressure Equipment Co., are manufactured from 316 stainless steel and rated to a minimum of 4080 atm. Table 4 compares the composition of 316 stainless steel, C-276, and Inconel 625 alloys.

TABLE 4. COMPOSITION OF REACTOR MATERIALS

	Ni%	Cr%	Mo%	Fe%	W%	Co%	Mn%	C%	Si%	Other%
C-276	59.5–	14.5–	15.0–	4.0–	3.0–	2.5	1.0	0.01	0.08	.048
	51.0	16.5	17.0	7.0	4.5					
Stainless Steel 316	10.0–	16.0–	2.0–	61.8–	---	---	2.0	0.08	1.0	.075
	14.0	18.0	3.0	68.8						
Inconel 625	62	21.5	9.0	5.0	---	---	---	0.1	0.5	1.9

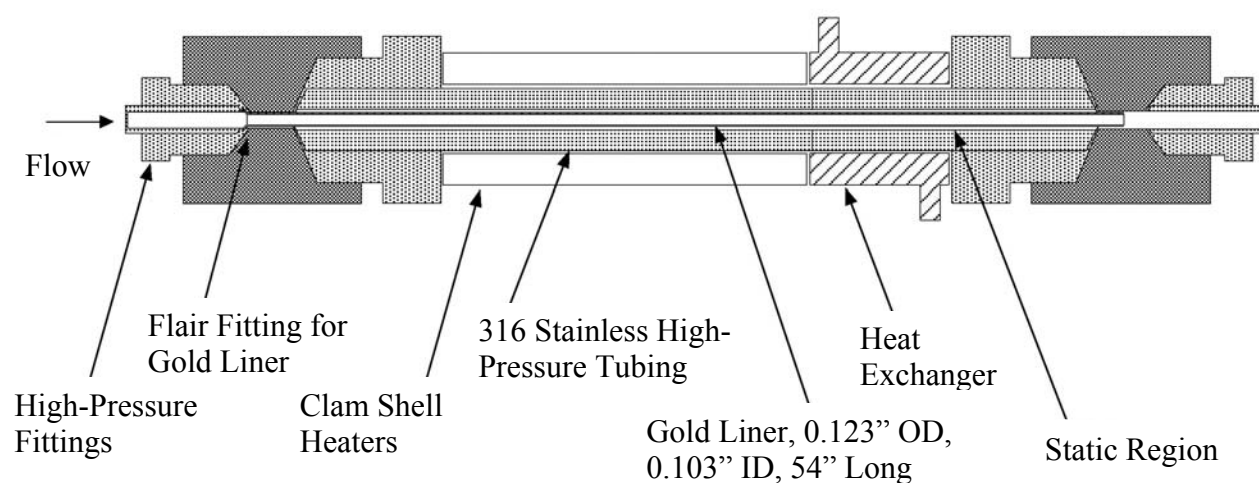


Figure 7. Detailed Diagram of gold-lined reactor. Drawing is not to scale.

The C-276 reactor core was 64 inches long by 0.083 inch inside diameter (id) (1.6 m x 0.33 mm), and the gold-lined stainless steel reactor was 55 inches x 0.103 inch (1.4 m x 0.40 mm). These dimensions provided heated volumes of 5.7 mL and 7.4 mL, respectively. Using an empirical equation of state for supercritical water (Reference 9), we estimate a 5–150-second residence time, depending on flow rate (usually 1–8 g/minute) and temperature (400–600 °C) at a

pressure of 340 atm. At higher temperatures, the density of water drops significantly, decreasing residence times. Figure 8 shows the results of an experiment used to characterize the flow through the linear reactors. A fixed volume (200 mL) of NaCl solution (2500 ppm) was pumped through the reactor at a rate of 4 mL/minute at room temperature and at 600 °C. Samples were collected every 10 minutes. The sodium ion concentration was measured by atomic absorption spectroscopy. The room-temperature trace in Figure 8 appears broader, which is typical of laminar flow with substantial axial diffusion. The narrower 600 °C trace indicates that the flow

is becoming more plug-like. Most of the broadening in the high-temperature run probably occurred in the cool regions of the reactor. However, since this reactor was not used for kinetics studies, completely developed plug flow was not critical.

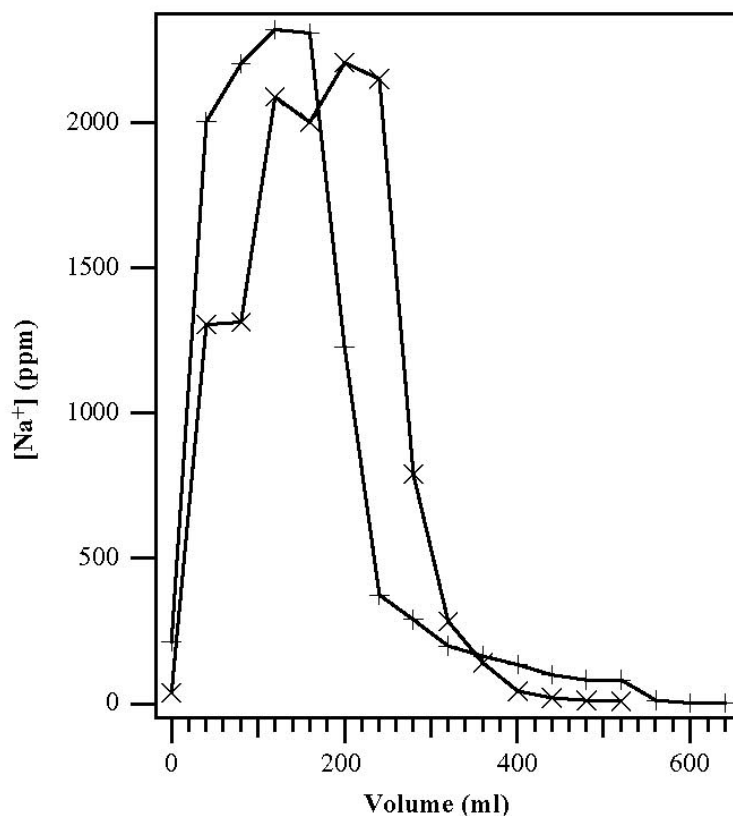


Figure 8. Sodium concentration versus volume flowed through reactor for a 200-mL aliquot of 2500 ppm NaCl solution at (x) room temperature and (+) 600 °C.

Typical experiments began by flowing deionized water through the reactor as it was brought up to temperature (400–600 °C). Solutions of explosive and/or oxidant mixtures replaced the deionized water. Aliquots of liquid effluent, including the flush, were collected continuously until the experiment was complete. The reactor was then rinsed with deionized water and the rinse effluent was also collected for analysis. Liquid effluent was analyzed for any residual explosives, inorganic and organic constituents, and corrosion products. The tracer studies suggested that for experiments with constituents that remain soluble, the volume of effluent analyzed will be only slightly greater than the volume injected into the reactor due to a slight dilution. However, if reaction products precipitate out of the SCW phase, they may appear in the effluent during the cool-down or flushing phase (see below). The gas effluent was allowed

to accumulate in the gas–liquid separator until pressures of 10–200 torr above the water vapor pressure were reached. This volume of gas was expanded into the White cell of the FTIR and pressurized to 600 torr with He for reasons discussed in Section II.H.1.a.

## B. FLUIDIZED SAND BATH REACTOR

For experiments measuring the kinetics of reactions, a coiled, tubular reactor in a fluidized sand bath was used. Figure 9 shows a schematic and Figure 10 shows a photograph of the fluidized sand bath reactor used to examine the kinetics of reactions in supercritical water. This

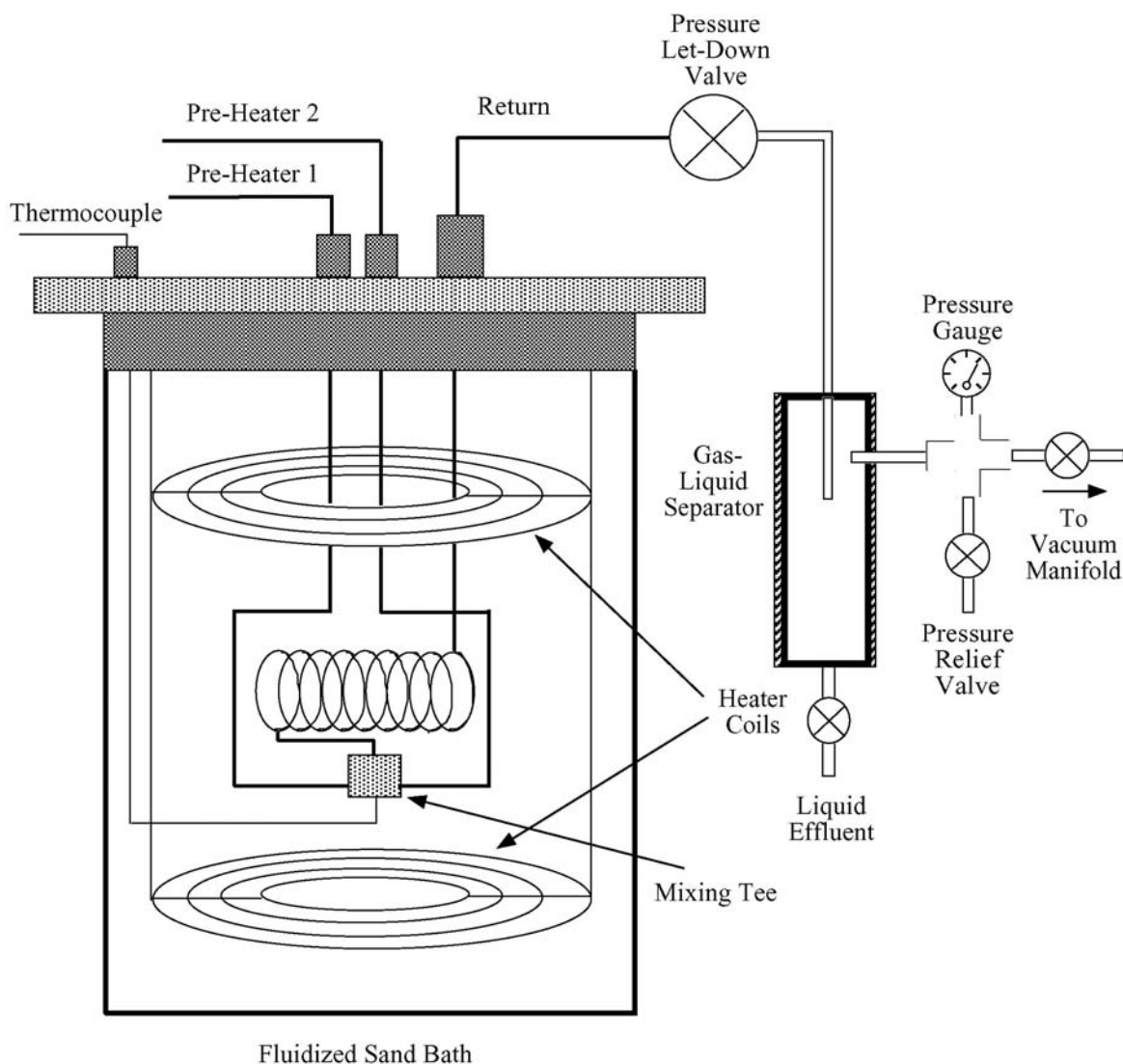


Figure 9. Schematic of sand bath reactor coupled to the gas–liquid separator.

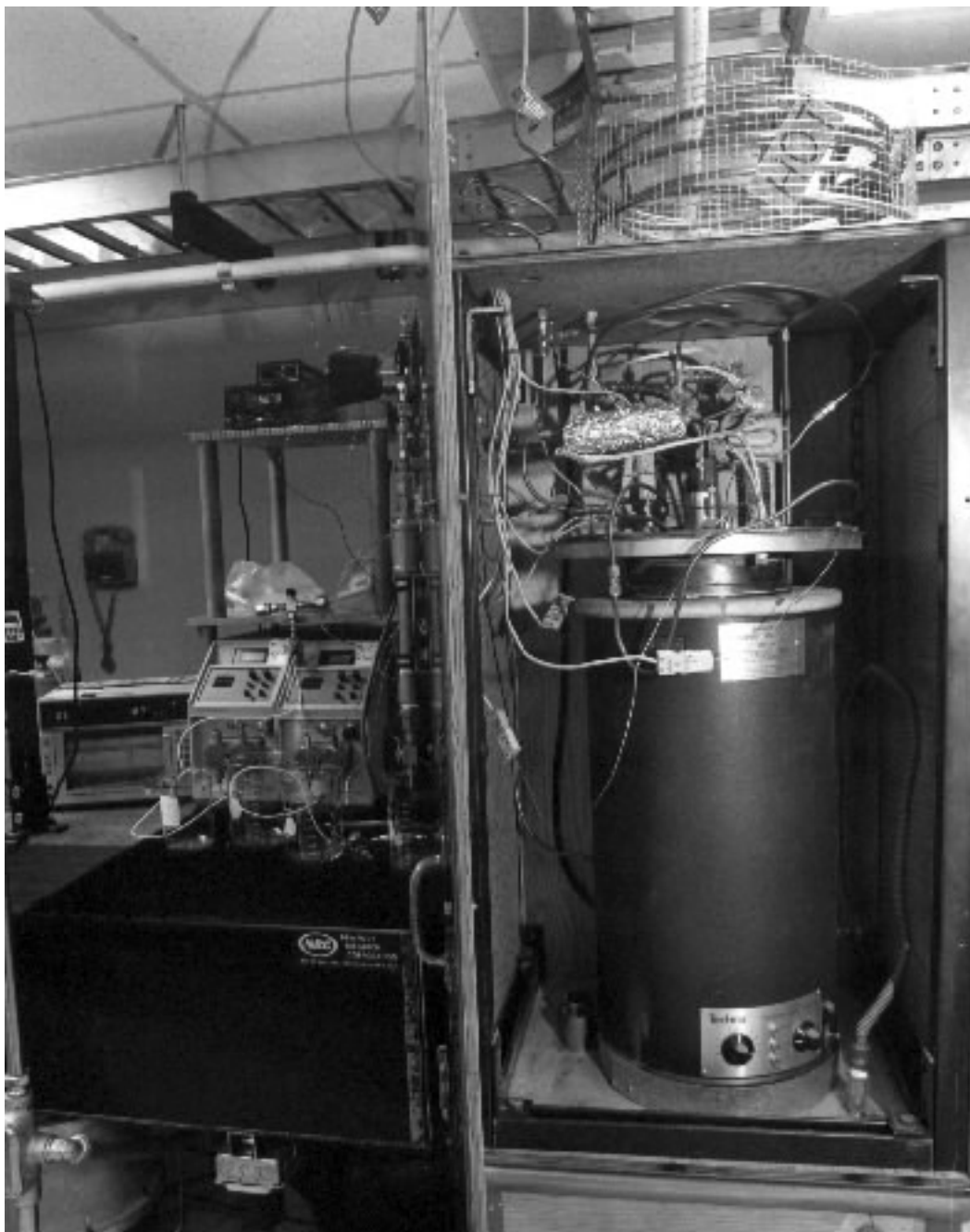


Figure 10. Photograph of sand bath reactor

reactor was used primarily for the study of nitrate reactions. The reactor consists of two preheater tubes, each having a volume of 7 mL, whose contents combine at reaction temperature in a mixing tee. The reactor tube (a C-276 alloy, 6.35 mm (od) x 2.12 mm (id), volume 13.1 mL) leads from the mixing tee to a chilled-water heat exchanger. Seven thermocouples are used to monitor surface temperatures on the preheaters and the reactor. Thermocouples are in contact



with the fluid at the mixing tee and after the chilled-water heat exchanger. Temperature profiles indicated the reactor tubing was isothermal to within 1 °C at reaction temperatures (450–525 °C).

The reaction quench was rapid, occurring within 0.25 mL of tubing. The reactor was operated in ranges where Reynolds numbers ( $> 2100$ ) indicate that flow should be turbulent. Two HPLC pumps provided flow rates up to 10 mL/minute of the oxidant and organic feed solutions. Experiments were started by circulating deionized water through the apparatus at the desired experimental pressure. While the deionized water circulated, the fluidized sand bath was brought to temperature using its internal and auxiliary heaters. The internal heaters were controlled with a feedback controller, while auxiliary heaters were controlled with a variable transformer. When the desired experimental temperature was reached, the water feed streams were changed to oxidant and fuel feed solutions. A stopwatch marked this time. After 20–30 minutes, effluent sampling was initiated. When sampling was completed at one residence time, pump flow rates were adjusted to provide a new residence time. At the new residence time, the system was allowed to equilibrate for 20–30 minutes before sampling at the new residence time was initiated. At each temperature and residence time, feed and total flow rates were measured. When all experiments were completed, the heaters to the fluidized sand bath were turned off, and a continuously recycled water rinse of the apparatus was started. This water rinse served to collect water-soluble species that adhered to apparatus walls. Water rinses were conducted for 12–16 hours.

For all temperatures and residence times, three sets of four liquid samples were collected for analyses. One sample was used for *pH* measurement, while the others were analyzed for aqueous nitrogen and carbon species, and corrosion products. Gas samples were collected for analysis by gas chromatography (GC) and Fourier-transform infrared (FTIR) spectroscopy. Ion chromatography was used to measure nitrite and nitrate concentrations. An ion-specific electrode was used to determine ammonia concentrations. Metal concentrations (Cr, Na, Mo, Fe, Ni) were measured by atomic absorption (AA) spectrophotometry, while gas chromatography was used to determine methanol concentrations.

### C. BATCH REACTOR

Two microbatch reactors were used for investigation of the dissolution of solid explosives and propellants in water during the transition through the critical point (Figures 11, 12).

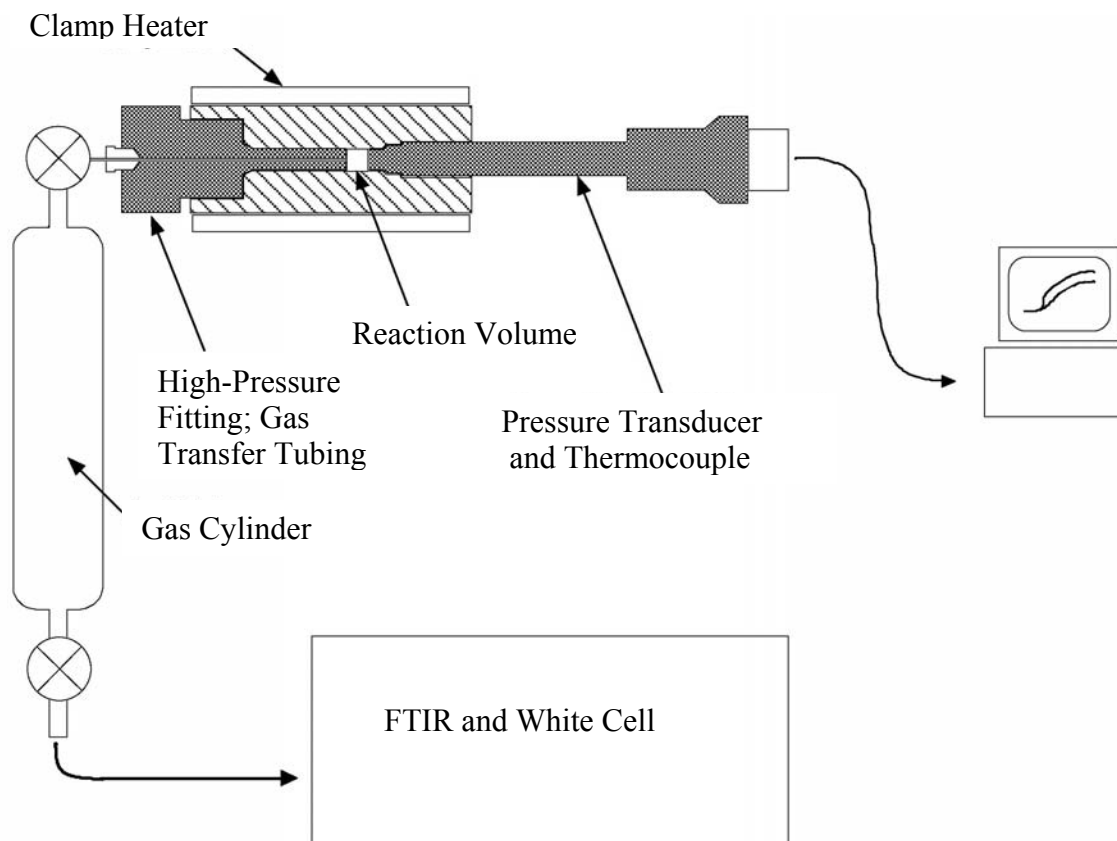


Figure 11. Schematic of the batch reactor experimental setup. The reactor volume used was 200  $\mu\text{L}$ , but it can be varied up to 2 mL. After completion of the experiment, the reactor volume was expanded into the evacuated gas cylinder

Although numerous designs were considered and tested, the two designs that proved most useful were a constant-volume reactor and an optically accessible reactor. These reactors permitted the introduction of a slurry of explosives that could be heated to 600  $^{\circ}\text{C}$  and pressurized to 10,000 psi (680 atm) in a controlled manner. The reactors were made of 316 stainless steel and had a total volume of 200  $\mu\text{L}$  each. The estimated (and observed) pressure rise was far below the maximum rating. For safety purposes, the computer, video monitor, and all experimental personnel could be located remotely behind a protective barrier. Lexan<sup>®</sup> shielding was also used to cover the reactor area during experiments.

The optically accessible reactor allowed visual inspection of the slurry as the reactor was slowly brought up to temperature and pressure and also provided the potential for the spectroscopic monitoring of SCW reactions and the dissolution of explosives. This design

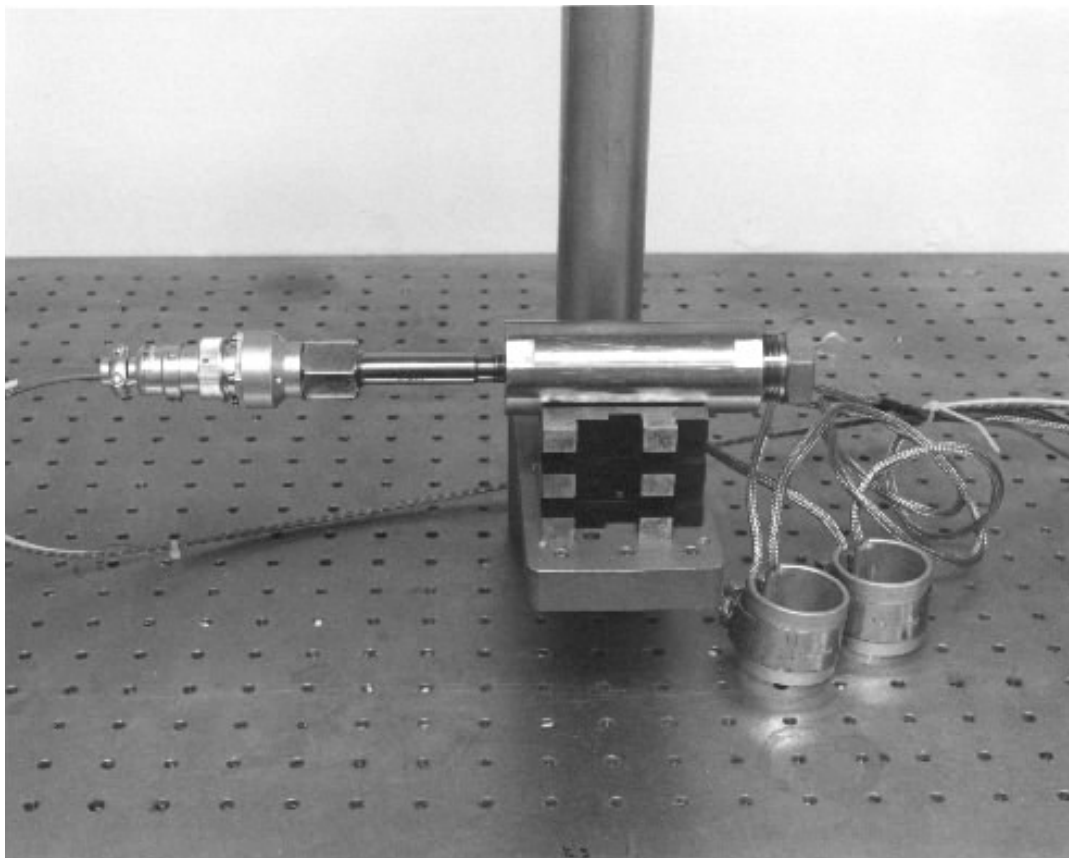


Figure 12. Photograph of the batch reactor

features two opposing diamond windows that permit backlighting of the sample and observation through the opposite window. The cell is pressurized with a pressure intensifier using water as the pressure-coupling fluid. A high-resolution, cooled charge-coupled device (CCD) camera was used to visually monitor the reactor interior.

Both cells were heated using nickel–chromium wire and a Variac® connected to line current. Temperature was measured with a K-type thermocouple placed directly in the reaction volume and pressure was monitored with a Heise pressure gauge. The pressure and temperature data were recorded on a Macintosh® computer. Gas products were expanded into a stainless cylinder and examined by FTIR spectroscopy using procedures described in Section II.H.1.a.

#### D. TRANSPORTABLE WASTE DESTRUCTION UNIT

The largest-capacity SCWO reactor we used for studying the destruction of explosives was a two-gallon-per-hour transportable waste destruction unit. A schematic of the unit is shown in Figure 13 and a photo is shown in Figure 14. The purpose of this unit was to evaluate process

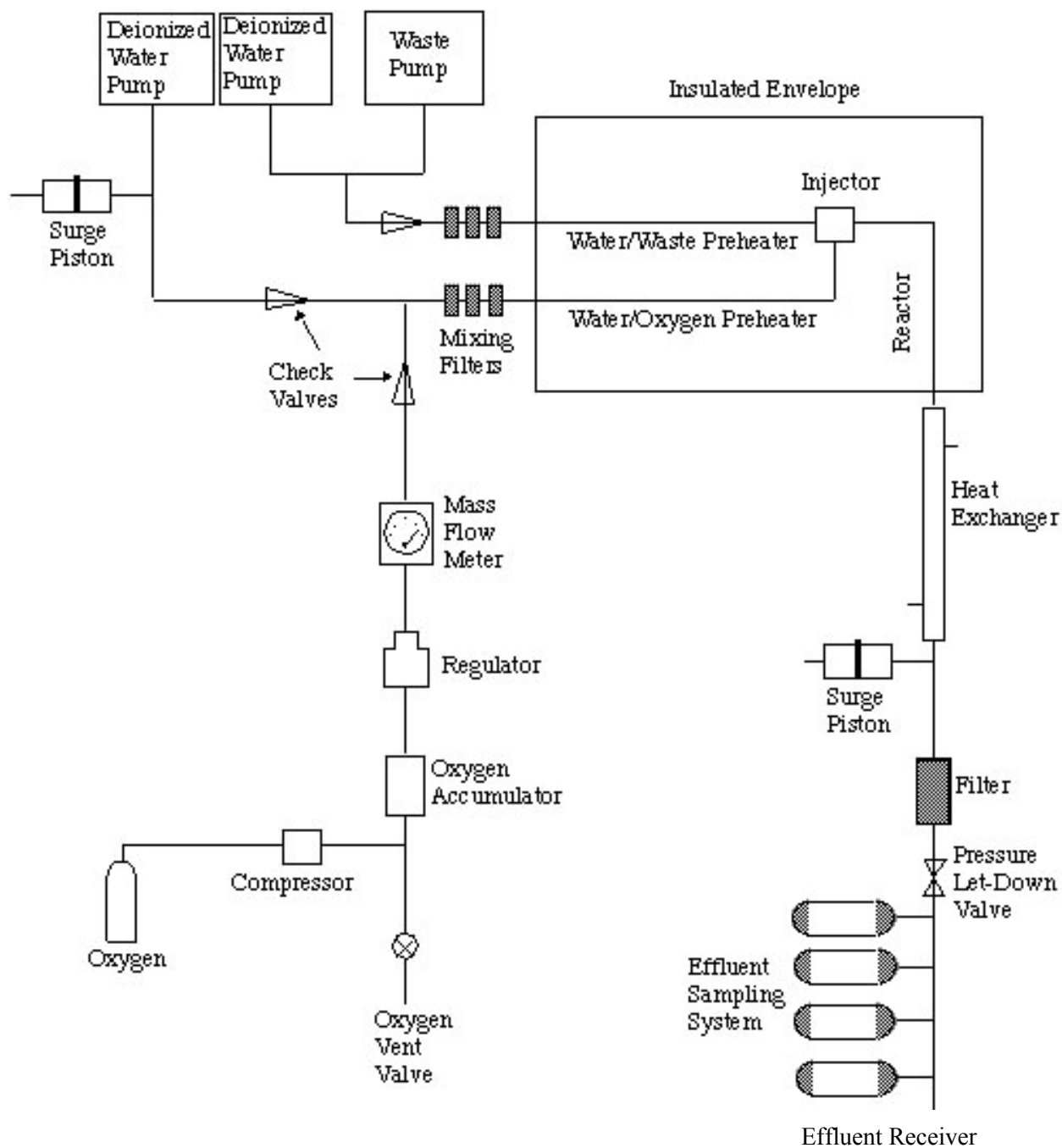


Figure 13. Transportable Waste Destruction Unit

and design issues and to develop an experience base on operability. Although not specifically designed for kinetics studies, it also had that capability. The unit could use oxygen, air, or hydrogen peroxide as the oxidant. It was designed to provide a basic system into which various reactor configurations can be inserted. The basic system uses a supply-and-mixing subsystem to



Figure 14. Photograph of the transportable waste destruction unit

provide a mixed feed for the reactor and a cooldown and pressure letdown subsystem for postprocessing the reactor effluent. The cooldown/letdown subsystems did not include solids-handling components. The unit was designed to meet or exceed ASME mechanical standards and allow all critical operations to be carried out remotely. The system fit on a framework that was roughly 5 ft. x 12 ft. x 4 ft. high (1.6 meters x 3.7 meters x 1.3 meters), and it could be picked up as a unit and transported on a truck or trailer. For initial testing with high concentrations of explosives, this feature allowed the unit to be located at an explosives firing site. The total height of the unit varied with the reactor, which was mounted on the top of the 4-

foot-high framework. The external supplies required were 120 volts AC and 220 volts AC three-phase electrical power, 160-psi compressed air, and roughly one gallon/minute of cooling water.

The supply and mixing subsystems included fluid supply reservoirs, pumps to bring the fluids to operating pressure at the desired flow rate, and devices for mixing fluids before they enter the reactor. A 50-gallon supply tank was used for water or aqueous waste feed to the system. The feed was compressed to the reactor operating pressure of about 4000 psi by a Milton Roy duplex metering pump. The maximum capacity of this pump was 2.2 gallons/hour, but the nominal operating flow was 1.1 gallons/hour. The duplex pump contained two pistons, operating 180° out of phase to reduce pulsations. There was still, however, a considerable amount of surge in the output. This surge was dampened by piston accumulators on the water line near the pump and just before the letdown valve.

A concentrated organic stream or a stream of dilute explosives was introduced into the pressurized water line by a separate Milton Roy HPLC metering pump with a maximum output of 10 mL/minute. The waste was injected into the water and passed through a filter to promote mixing. The waste/water stream was then heated before being combined with the oxidizer.

Oxygen was supplied from standard 2000-psi bottles located on the rig. The oxygen was regulated to 1500 psi and was fed into a Haskel double-acting, two-stage gas booster, in which it was compressed to the operating pressure of about 4500 psi. Oxygen from the booster was collected in a 2-liter reservoir. A high-pressure regulator controlled the oxygen pressure at 4300 psi, with a variation of 20 to 50 psi. A Linde mass flow meter was used to measure the oxygen flow rate. The output from this meter was used by the data acquisition system to control the oxygen flow via a pneumatically actuated control valve. After going through a check valve, the oxygen was injected into a water stream and was passed through a filter for further mixing. The oxygen–water stream was then heated before it was mixed with the waste.

The newest reactor was made from welded Inconel 625 tubing, 0.188-inch (0.13-mm) (id) by 0.308-inch (1.03-mm) (od). The desired operating temperature of the mixed fluids was achieved by direct electrical-resistance heating of two separate 12-foot (4-meter) preheaters. For each preheater, the heating was done in two parallel electrical circuits. Electrical power was provided to each preheater by separate Hewlett–Packard 6469-C DC power supplies rated at maximum current of 300 amps at a maximum voltage of 36 volts. The flows from the waste–

water and oxygen–water preheaters were combined. Oxidation occurred in a 6-foot (2-meter) insulated tube (Inconel 625, 0.188 inch (id) by 0.308 inch (od)) following the mixing region. Thirty-five thermocouples were attached to the outside of the preheaters and reactor to measure surface temperatures.

After leaving the reactor, the process stream was cooled using a single-pass, counterflow, coaxial-tube heat exchanger. The cooled effluent passed through a single letdown valve, where its pressure was reduced to atmospheric. The letdown valve controlled the reactor operating pressure. After the letdown valve, the effluent entered an array of sampling bottles. The entire flow could be diverted to a given bottle for a period of time. The sampling valves were controlled remotely. When the effluent was not being sampled, it passed into a product tank.

Data acquisition, control, and monitoring were accomplished with a Hewlett–Packard 3852A data acquisition and control unit and a Macintosh IIfx desktop computer. A digital voltmeter, three 20-channel multiplexers (scanners), a 4-channel digital-to-analog converter (DAC), and a 10-relay actuator were used for data acquisition and control. The DAC channels provide continuous control of the two control valves (oxygen flow and pressure let-down) and the two DC power supplies. The scanners were used to sample the voltages from the pressure transducers, thermocouples, oxygen flow meter, power supplies and two power-supply current shunt voltages. During a test all data were recorded and displayed. If needed, the data from a test could be replayed at a later time.

A more complete description of a similar version of this reactor can be found in Los Alamos report number LA-12216-MS.

#### E. ONE-GALLON-PER-HOUR REACTOR SYSTEM

The one-gallon-per-hour (1-gph) reactor system was a continuous-flow system with a tubular reactor. The system consisted of a waste/water feed-and-pressurization subsystem, an oxygen feed-and-pressurization subsystem, a preheater–reactor subsystem, a cooling subsystem, and a pressure letdown-and-sampling subsystem. For monitoring and control of the system there was a remote data-acquisition-and-control (DA&C) system. A photograph of the entire system is shown in Figure 15.

The waste/water feed-and-pressurization subsystem consisted of a pair of 6-gallon plastic feed tanks with a remotely actuated switching valve between them, a feed pump, and a pulsation dampener. A photograph of this subsystem is shown in Figure 16. In operation, one feed tank contained pure deionized water and the other contained a slurry of explosive (or explosive simulant) in water. A recirculating pump was provided for the slurry tank to keep solids from



Figure 15. Photograph of 1-gallon-per-hour unit

settling out on the tank bottom. The switching valve was used to select feed from one or the other feed tank as desired. This valve was an electric-motor-driven three-way Parker ball valve. The pressurizing feed pump was an American Lewa diaphragm pump capable of delivering up to 2 gallons/hour of liquid at pressures to 5500 psia. The pump was driven by a 220-Vac, three-phase electric motor, which was remotely actuated by a 110-Vac relay. Pump capacity control was accomplished with a manual stroke adjustment, although a remotely controlled stroke actuator was available. The surge suppressor was a cylindrical accumulator with a floating piston. One end of the accumulator was attached to the process fluid downstream of the main feed pump, and the other end was charged with a trapped volume of nitrogen. The gas end was charged to about one-half of anticipated system operating pressure when there was no system pressure and was then valved off so that the piston was roughly in the mid position during



operation. The system was essentially undamped until the system pressure reached the nitrogen charging pressure. All fittings and lines between the pump and the preheater were high-pressure-rated 316 stainless steel components. The lines were 0.250-inch (od) by 0.083-inch (id) and were kept as short and straight as possible to prevent appreciable accumulation of solids.



Figure 16. Photograph of wastewater feed and pressurization subsystem

The oxygen supply-and-pressurization system comprised a bank of conventional 2200-psi oxygen bottles with a regulator, a remotely-actuated oxygen supply shutoff valve, an oxygen compressor, an oxygen accumulator, an oxygen-feed shutoff valve, an oxygen-feed pressure regulator, an oxygen flow meter, an oxygen flow control valve and a check valve. A photograph of this subsystem is shown in Figure 17. Oxygen feed pressure was supplied by a double-acting, two-stage, intercooled Haskel Gas Booster, which could boost the oxygen from bottle pressures as low as 200 psi up to 4500 psi at flow rates of 20 slm (standard liters per minute) or more. Typical oxygen flow rates in operation were 5–10 slm. The gas booster was driven by

compressed nitrogen gas from a standard 50,000-scf trailer, but any clean compressed air or nitrogen at about 100 psig or higher could have been used. In operation, the oxygen supply pressure was not allowed to drop below about 1100 psia to prevent excessive use of drive gas. The booster was equipped with a pilot valve, which turned the booster on when the outlet pressure dropped below 4350 psia and turned it off when the outlet pressure went above 4500



Figure 17. Photograph of oxygen supply and pressurization subsystem

psia. These limits were adjustable, but it was difficult to reduce the "deadband" below this 150-psi level. Since it was not feasible to obtain a steady flow from the booster, a 2-liter oxygen accumulator was provided at the booster exit. This capacity resulted in booster operation about every 3–5 minutes for nominal oxygen flow rates.

Booster operation resulted in a rapid increase in accumulator pressure from 4350 psia to 4500 psia followed by a slow decay in pressure back to 4350 psia. Since this rapid increase in

oxygen pressure made oxygen flow control difficult, a Tescom pressure regulator was provided downstream of the accumulator to even out the oxygen pressure. Ideally, the regulator could keep the pressure at a steady 4350 psia. Experience had shown that we must keep the regulator outlet pressure at or below about 4100 psi to avoid excessive pressure pulses at the flow control valve when the booster operates. At this setting the pressure pulses are 40 psi or less. The regulator was provided with an automatic controller that used the output from a pressure transducer just downstream of the regulator. This signal was compared to an outlet pressure setpoint signal sent by the DA&C system. Following the regulator were a Linde mass flow meter and a Research Control pneumatically actuated flow control valve with a Moore Products I/P transducer. Oxygen flow control was accomplished by a 4–20 mA signal sent from the DA&C system, which was converted into a proportional 3–15 psi pneumatic signal to the valve by the I/P transducer. The signal from the DA&C system could either be set "manually" at the control panel or (more usually) determined "automatically" using the difference between the flow rate measured by the mass flow meter and a setpoint value set on the control panel. Downstream of the control valve the oxygen was fed through a check valve into the waste/water stream. Oxygen flow control was therefore affected by the system pressure as well as the oxygen feed pressure. For this reason it was desirable to keep a fairly large pressure drop across the oxygen flow control valve—about 400 psi in this case. All lines and fittings in the oxygen feed subsystem were high-pressure-rated 316 stainless steel.

Maximum system operating pressure is generally limited by the maximum *allowable* oxygen pressure, which is 5000 psi. Haskell (for one) recommends against the use of pure oxygen at pressures above 5000 psi even with an "oxygen clean" system such as this one. This means that the maximum *operating* pressure should be no higher than 4500 psi. The required pressure drops through the pressure regulator and the flow control valve dictate a maximum system pressure of about 3700 psia.

The primary feature of the preheater/reactor subsystem was a straight Inconel 625 tube, 19 feet long by 0.308 inch (od) by 0.188 inch (id). This tube served as both the preheater and reactor sections of the subsystem. In the preheater section (the first 8 ft of the tube) the tube was spiral-wrapped with nine Watlow cable heaters, each 95 inches long by 0.125 inch (od), and each capable of producing 1000 W of heating at 220 V. This was actually a tighter wrapping (0.308 inch (id)) than is recommended for these heaters, but we observed no problems. The heater power was controlled by a 220-Vac, three-phase SCR power controller wired in a delta configuration with three heaters, wired in parallel with each other, on each of the three legs.

Proportional power control was provided by a 0–10 V signal from the DA&C system. This signal could be set either manually at the DA&C system control panel, or automatically using the difference between a measured maximum preheater temperature and a setpoint temperature set on the control panel. The purpose of the preheater was to bring the mixture of water, waste and oxygen to operating temperature.

Maximum operating temperature for this system was 650 °C (1200 °F). Of course, since all of the reactants were premixed, some, if not most, of the reaction occurred in the preheater. The "reactor" section (the last 11 feet of tube) was wrapped with low-power strip heaters to offset heat loss through the insulation. This was an attempt to keep the reactor section as near to isothermal as possible and to obtain a residence time at temperature. These heaters were controlled by another SCR power controller in a manner similar to the preheater, but using much less power. Roughly 30 thermocouples were attached to the outside of the preheater/reactor tube with glass tape. These thermocouples were used for power control and for display. A real-time plot of temperature vs. distance along the preheater/reactor was displayed on the control panel. The preheater/reactor tube and heaters were placed inside a concentric 10-inch (od) by 0.250-inch wall aluminum tube, and Saffil® alumina-fiber insulation was lightly packed into the intervening space. The aluminum tube was split longitudinally for installation of the tube, heaters and insulation, and was held together with steel bands.

Cooldown of the process fluid was accomplished by putting a concentric 316 stainless steel cooling jacket around a 6-foot extension of the Inconel 625 preheater/reactor tube. The total preheater/reactor/cooler length was 25 feet, all enclosed in the 10-inch aluminum tube. Water, with ethylene glycol added as a rust inhibitor, was circulated through the cooling jacket annulus counter-current to the process flow. The water was then circulated through an industrial water-to-air forced-convection heat exchanger (actually an air heater) and back to the cooling jacket using a low-pressure 5-gpm centrifugal water pump.

After going through the cooler the process fluid passed through a Research Control valve to drop and control the system pressure. A photograph of this subsystem is shown in Figure 18. This valve was similar to the oxygen flow control valve, and had an attached I/P transducer to transform the electronic control signal into a proportional pneumatic signal for valve actuation. The 4–20 mA signal from the DA&C system to the I/P transducer could be set manually on the DA&C system control panel, or automatically by the control program using the difference between the system pressure, measured by a transducer just upstream of the control valve, and a

setpoint pressure set on the control panel. Several remotely actuated, three-way ball valves in the low-pressure, low-temperature line downstream of the control valve were used for sampling. These valves were plumbed in series so that, in normal operation, all of the process effluent passed through all of the valves before going into the catch tank. When a sample of the effluent was desired, one ball valve was switched and the entire effluent flow was diverted to an attached



Figure 18. Photograph of pressure control subsystem

sample bottle for a period of time. The effluent contained dissolved gas due to excess oxygen in the feed and gas production during processing, so the period of sampling must be limited. For the standard 300-mL sample containers and a flow rate of 1 gph, the sampling period was limited to about 2 minutes to prevent significant buildup of pressure in the sampling system.

The heart of the DA&C system was a Mac II fx computer running a LabVIEW®-based DA&C program written specifically for this application. A photograph of the DA&C subsystem is

shown in Figure 19. The computer was mated to a Hewlett–Packard HP-3852A DA&C unit via a GPIB interface bus. The HP-3852A has a voltmeter board; three 20-channel analog-to-digital multiplexer ("scanner") boards for monitoring of temperatures, pressures, flow rates, voltages, etc.; and two four-channel digital-to-analog (DAC) boards for sending control signals to the various control devices (I/P transducers, power controllers, etc.). The DAC channels may



Figure 19. Photograph of data acquisition and control subsystem

be configured to send either 4–20 mA or 0–10 Vdc. An eight-channel relay actuator board was also available for computer-controlled on/off functions, although we did not use it.

The DA&C program was run on a 5-second cycle. In each cycle raw voltage data were read in from the scanners, converted into "engineering" units using predetermined calibration factors (the scanner boards were capable of automatically converting thermocouple mV values into temperature values), and logged into a random access data file. On specified data channels the measured value was checked against specified high and low limits, and if the channel was out

of limits the reactor was shut down. Computer-controlled shutdown consists of turning off the preheater power, fully opening the pressure-letdown control valve and fully closing the oxygen flow control valve. Control DAC values were generated for the two power controllers, the pressure-letdown and oxygen flow control valves and the oxygen pressure regulator. In case the pump stroke adjustment drive was installed, this also required a DAC control signal. The values of the DAC signals to be sent could be set on the control program front panel or could be determined in a control subprogram by comparing the value of a control-channel measurement with a setpoint value specified on the control program front panel. The latter method is referred to as "automatic" control, and was optionally available for operation of the two power controllers and the two control valves. For the power controllers and the pressure-letdown control valve a proportional-derivative control scheme was used, and for the oxygen flow control valve a proportional-only control is used. These control subprograms were "home-built" and PID control subprograms are now available from National Instruments (makers of LabVIEW).

Besides the control settings and switches, measured and converted data were also displayed for on-line monitoring. These displays included an  $X$ - $Y$  plot of reactor tube wall temperature versus distance along the preheater/reactor and strip charts of value versus time for various data channels, all updated each scanning cycle (*i.e.*, every 5 sec). The channels displayed on the strip charts were varied, but typically included the system pressures, oxygen flow rate, some measure of preheater power, specific (or maximum) reactor temperatures, and/or some DAC signal values.

## F. BASE HYDROLYSIS

All chemicals used were of reagent grade. Base solutions were prepared with deionized water. The volume and concentration of base solution depended on the material being hydrolyzed. In general, an excess of base was used over that required to match the molar equivalents of nitro groups in the material. Reactions of sodium hydroxide with energetic materials were normally performed in an open beaker or in a flask fitted with a condenser. When open beakers were used, evaporated water was replaced as needed. When analysis of the gaseous hydrolysis products was desired, the reaction was performed in a stainless steel pressure vessel rated to 1000 psi. Hydrolysis reactions with aqueous ammonia were also performed in a sealed pressure vessel. In all cases, an appropriate blast shield was employed during the hydrolysis. Reactions were usually done at the boiling point of the solution, approximately 93°C at Los Alamos elevation. In some cases, a temperature controller was used to obtain a constant

temperature below or above (pressure vessel) the solution boiling point. Hydrolysis reactions were considered complete when solid material and gas evolution were no longer visible in the mixture. Runs in the sealed pressure vessel were terminated when the gas pressure leveled off. For some reactions foaming was found to be a problem and was counteracted with an antifoam agent, Hercules Defoamer #4.

## G. OPTICAL EXPERIMENTS

### 1. Raman Spectroscopy

While end product analyses of effluents from our flow reactors allowed more-comprehensive analysis of products and precise assessment of process efficiency, the use of optical spectroscopic methods allowed us to probe reactions *in situ*, and yields additional insight into chemical interactions. We report here the use of *in-situ* Raman spectroscopy to monitor reactants, products and reaction rates of energetic materials at supercritical and near-critical conditions. Raman spectroscopy is a versatile diagnostic tool that measures the vibrational spectrum of a molecule, and has been applied widely in gas, liquid and solid media. Compared to other optical techniques, Raman spectroscopy is well suited to supercritical fluids because it is immune to quenching at high pressures (or densities) and because it allows easy access to broad spectral ranges. Solvated molecules can usually be identified by their distinct Raman shifts.

A number of experimental setups were used, all similar to Figure 20. Raman measurements were made with an argon-ion laser source, tuned to 488 nm. The polarization of the laser output proportional-only control was used. These control subprograms were "home-built" and PID control subprograms are now available from National Instruments (makers of LabVIEW).controlled by a double-rhomb, half-wave retarder, then focused with a 20-cm focal length lens, exciting the sample with about 2 W of cw power. Raman scattering was collected at 90° with a collection lens and sent to a three-stage monochromator (Spex Triplemate), where the light was dispersed by a 600-line/mm grating and detected with a CCD camera. The CCD was a 516 X 516 pixel array; vertical columns were summed electronically to generate a one-dimensional array for Raman spectra. Signals were collected typically for 60 seconds.

The sample was passed through an optical cell that could withstand high pressures (>600 atm) and high temperatures (600 °C). One of the optical cell designs used is shown in Figure 21 and its photograph in Figure 22. This cell was constructed from a 316 stainless steel



high-pressure "cross" fitting, machined to accept three diamond windows. Diamond (Type II) was chosen as a window material because of its ability to withstand high pressures and its broad spectral transmission, from the ultraviolet to the infrared. We have also built optical cells using sapphire windows. The diamonds shown in the figure are "anvil-type" windows with flat optical faces providing an aperture of 0.6 mm on the inside and 3 mm on the outside. The high-pressure

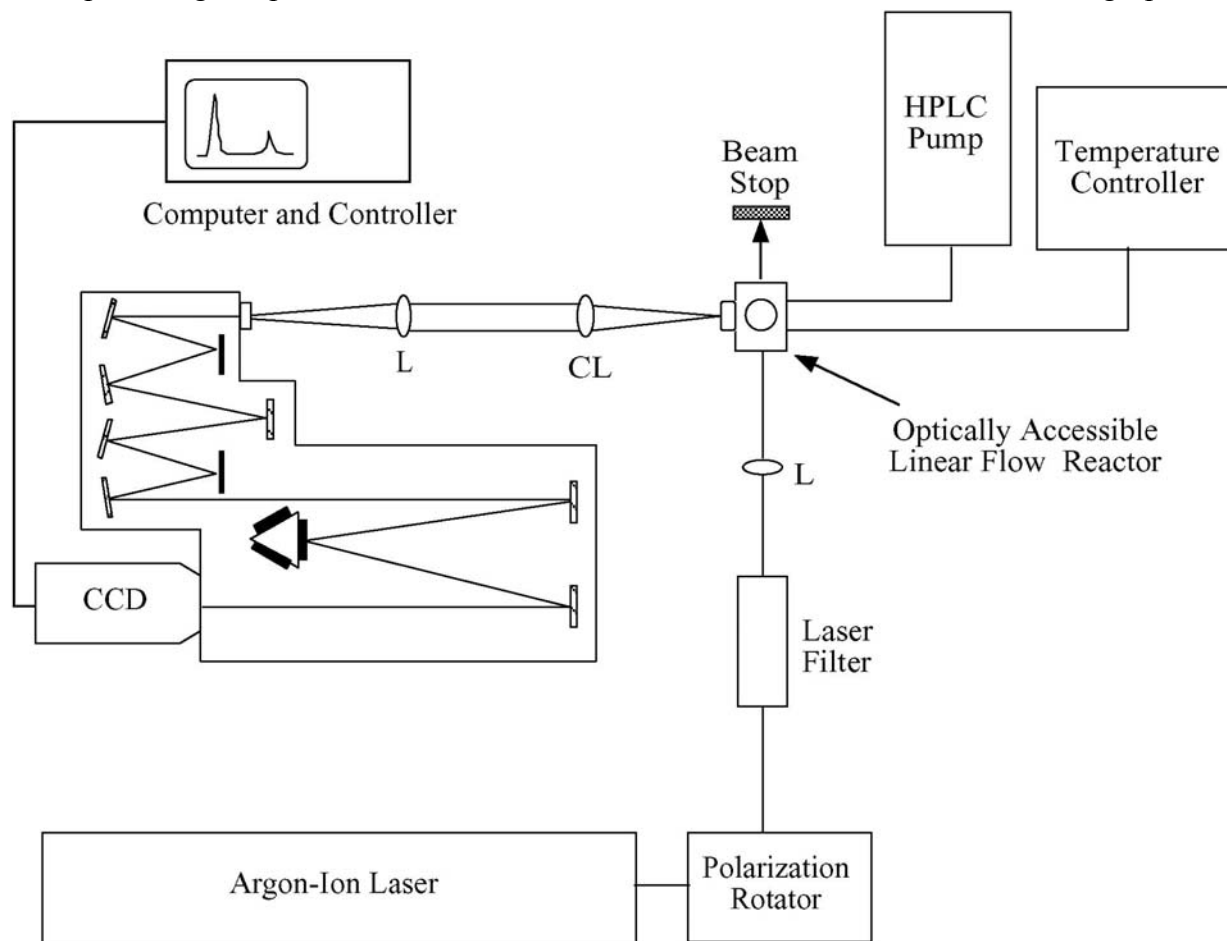


Figure 20. Schematic of Raman apparatus. Polarization rotator: double rhomb, half-wave half-wave retarder; Laser filter: small monochromator; L: lens; CL: collection lens; CCD: charge-coupled device camera for detection. Data collection using Macintosh II computer.

seal is aided by an inert gold gasket between the diamond and the cell wall. Two windows are used to pass the laser beam through the cell, with entrance and exit faces 1.6 mm apart. A third window, oriented at  $90^\circ$  with respect to the laser axis, was used to collect Raman scattered light. By positioning the collection window very close to the laser axis, a collection aperture of  $f/2$  is

achieved. Another cell was used that included two inlet ports allowing separate feed and oxidizer streams.

The reaction mixture was introduced into the optical cell with a standard HPLC solvent pump, which was rated to a pressure of 6000 psi (400 atm) and regulated solvent flow

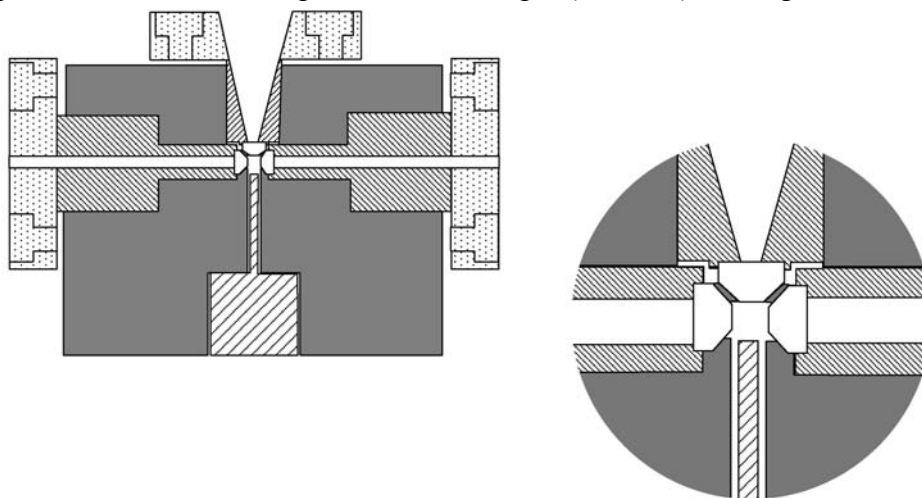


Figure 21. Optical cell with blowup of window region

rates of 0–10 mL/min. High-pressure fittings rated to 60000 psi at room temperature were used at all of the heated plumbing ports. Heat was supplied to the cell by four 150-W cartridge heaters imbedded in a brass shell surrounding the stainless steel cell. The fluid temperature was measured with a K-type thermocouple inside an Inconel sheath. The thermocouple was in direct contact with the fluid at a point close to the optically viewed region. Pressure was measured after the optical cell with a standard transducer. The reaction mixture flowed through a cylindrical volume in the cell with dimensions of 1.57 mm (id) and 51 mm length, yielding a volume of 0.10 mL. The optical window was located at the midpoint of this heated length, and the central portion (about one-third) of the flow was imaged optically. Experiments were performed with fluid flow rates in the range 0.05–3 g/min, yielding corresponding residence times of 0.5–30 seconds.

A second reactor, shown in Figure 23, is much like the linear reactors described previously. It measures 10 inches (25 cm) by 0.0625 inch (1.56 mm) (id), providing a volume of 0.50 mL. This reactor was used both as a flow reactor with HPLC pumps and as a batch reactor with a pressure intensifier.

## 2. Coherent Anti-Stokes Raman Spectroscopy (CARS)

Coherent anti-Stokes Raman spectroscopy (CARS) is a technique that is also well suited to noninvasive, *in-situ* optical diagnostics. In CARS two tunable lasers operating at

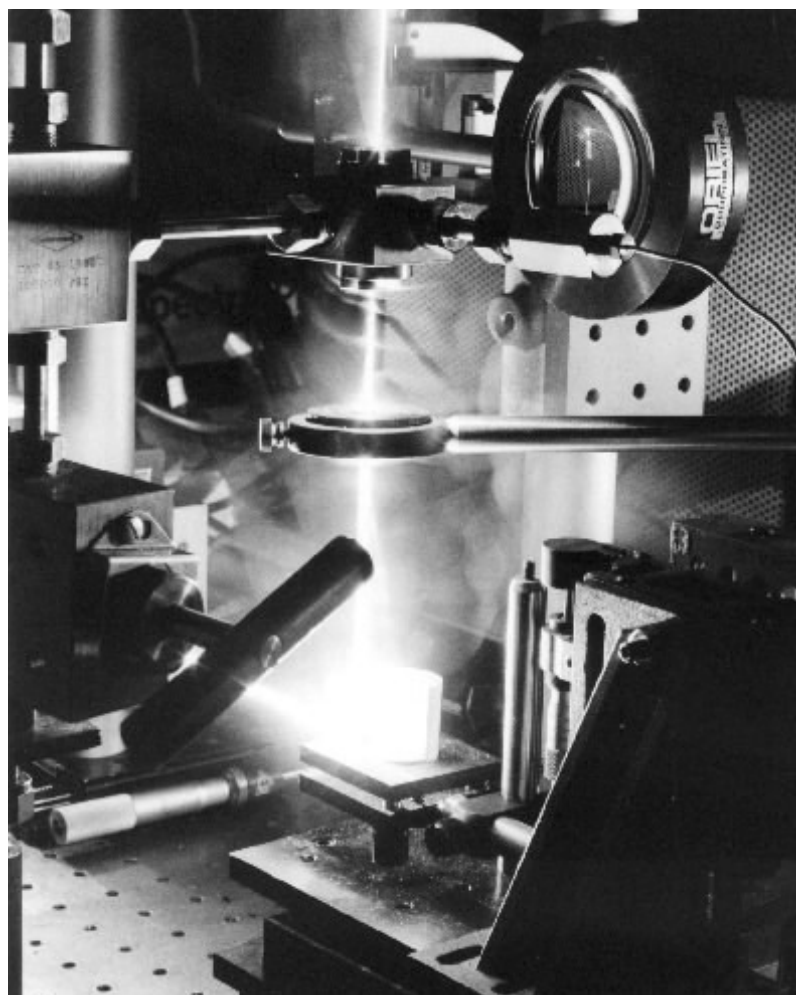


Figure 22. Photograph of the optical cell

frequencies  $\omega_1$  and  $\omega_2$  are used to excite a Raman-active vibrational mode of a molecule at the frequency  $\omega_1 - \omega_2$ . A coherent output beam with laser-like characteristics is produced at the frequency  $2\omega_1 - \omega_2$ . By sweeping  $\omega_2$  and monitoring the signal intensity, the shape of the CARS spectrum is mapped out. In addition to the CARS signal generated by the molecular transition (the "resonant" signal), there is a weaker signal generated by the sample at every value of  $\omega_2$ , the "nonresonant" signal. Because of the nonlinear nature of the CARS process, the resonant and

nonresonant signals combine in a complex way to produce a spectrum having a shape different from that of an ordinary Raman spectrum.

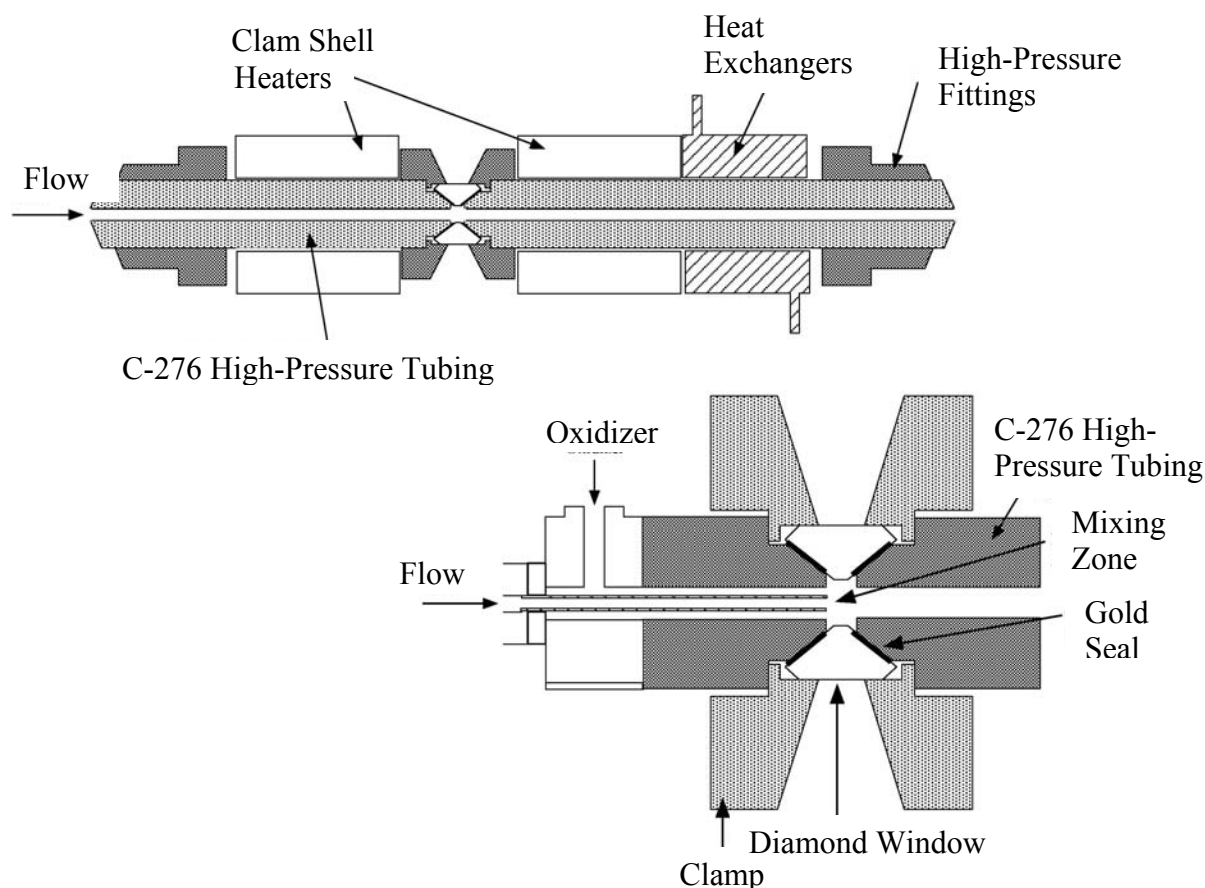


Figure 23. Diagram of linear flow reactor with optical access and details of diamond window seals. Also shown is an injector for introduction of oxidizer and fuel allowing mixing just before the diamond windows.

In our experiments, picosecond lasers (pulses of  $\sim 20$  psec duration) generated the CARS spectrum. A schematic of the CARS setup is shown in Figure 24. A Nd:YAG laser was used to pump two dye lasers at  $\lambda_1 = 577$  nm and  $\lambda_2 = 609$  nm. These were directed to the larger optical cell described previously. Instead of sweeping the frequency of one of the lasers, we operated the laser at 609 nm in a broadband mode, so that the resulting CARS beam was broadband. The beam was sent to a monochromator, which dispersed the CARS beam and sent it to a CCD camera that was operated as a linear array detector, registering a broad portion of the spectrum on each laser shot. The lasers were fired at a repetition rate of 500 pulses/second, and the CARS signal was averaged (typically for a few minutes) until satisfactory signal-to-noise ratios were obtained.

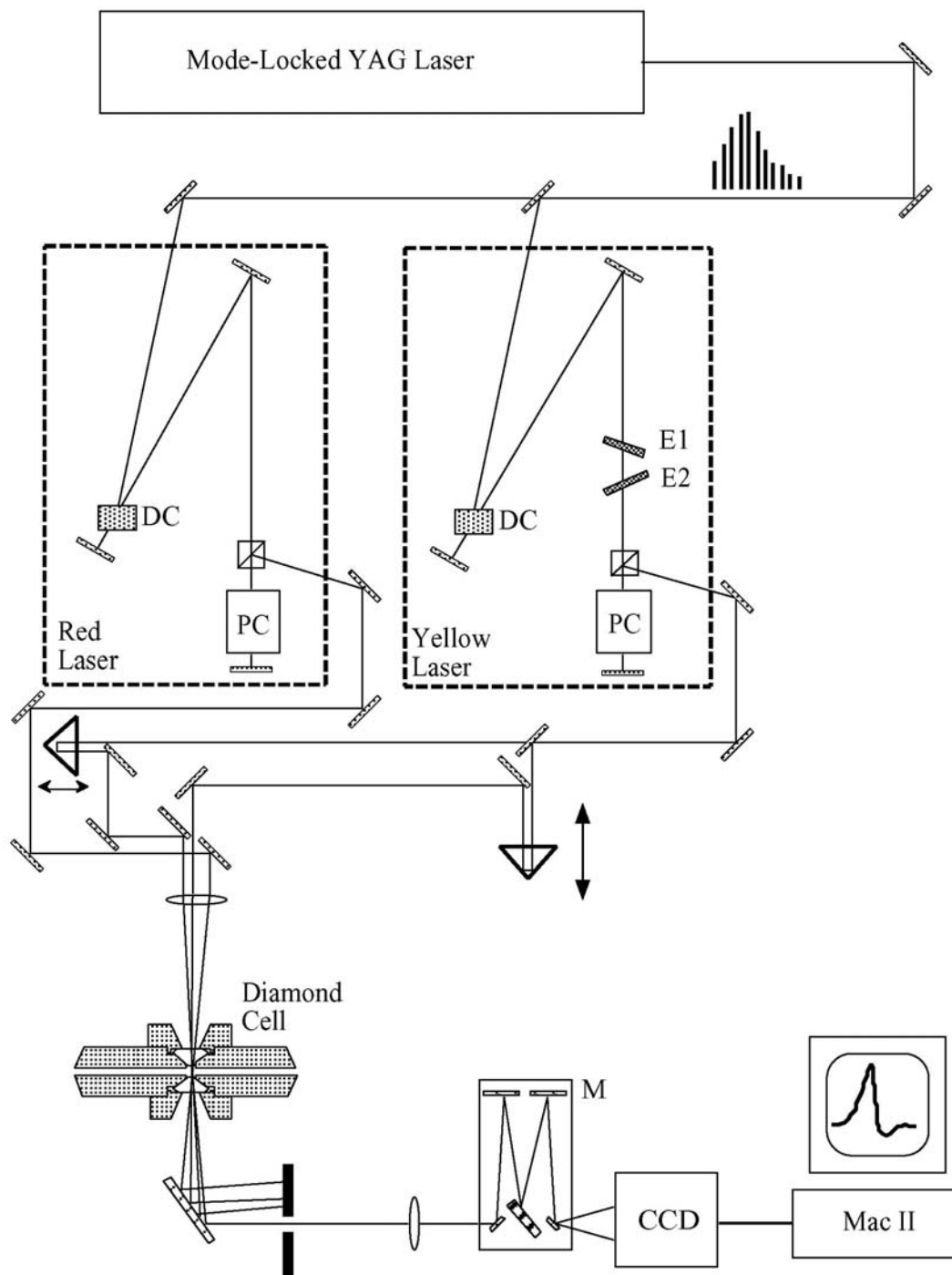


Figure 24. CARS apparatus. DC: dye cell, containing Sulforhodamine 640 for the red laser and Rhodamine 610 for the yellow laser. PC: Pockel's cell used to fire the dye laser pulse. M: monochromator used to disperse the broadband CARS beam. CCD: charge-coupled device camera to detect CARS beam. Mac II: computer for data acquisition, display, and analysis.

### 3. Transient Grating Spectroscopy

The transient grating technique is a non-invasive optical method that can be used to measure thermal diffusion constants and the speed of sound of a fluid. Both thermal diffusion constants and speed-of-sound measurements can be used as sensitive tests for potential equations of state of hydrothermal solutions. Figure 25 shows a schematic of the transient grating experiment. In this experiment, two laser pulses of the same wavelength  $\lambda_1$  are crossed at an angle  $\theta$  in the hydrothermal solution, thereby creating a sinusoidal interference pattern of fringe spacing  $\Lambda = \lambda_1/[2 \sin(\theta/2)]$  in the overlap region. When the sample absorbs the pump light, the excited molecules quickly relax and deposit their energy into the bath molecules, which produces a spatial modulation in the temperature of the sample. This temperature modulation results in a spatial modulation of the index of refraction and is a volume diffraction grating. This type of grating is called a thermal grating. The grating is probed by Bragg diffraction of a third laser pulse at  $\lambda_2$ , which produces a coherent signal beam also with wavelength  $\lambda_2$ . Thermal diffusion causes the temperature grating to smear out and the diffracted signal intensity as a function of the pump-probe delay time is

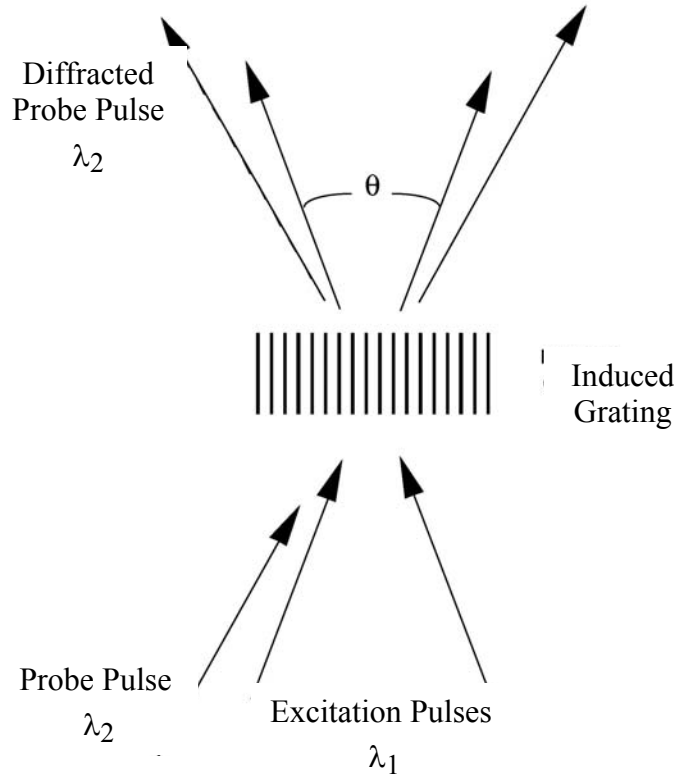


Figure 25. Schematic of a transient grating experiment.

described by the equation  $S(t) = C \exp[-8\pi^2 D_t t / \Lambda^2]$ , where  $S(t)$  is the time-dependent diffracted signal and  $D_t$  is the thermal diffusion constant. In addition, if the pump pulses are short enough, they can produce counterpropagating acoustic waves that appear as large undulations in the transient grating decay spectrum. The speed of sound in the sample is simply the fringe spacing divided by the undulation period.

The sample cell used in the transient grating experiments had two diamond windows for optical access and was very similar to the cell used for the phase behavior (see Section III.C) and Raman optical studies of hydrothermal solutions. The pump light (532 nm, 10 ns pulse width,  $\sim 200 \mu\text{J}/\text{pulse}$ , 10 Hz) was produced from the second harmonic of a Nd:YAG laser. A beam splitter split the light into two beams of equal energy, which were focused and overlapped in the sample with a small crossing angle ( $< 3^\circ$ ). The probe beam (585 nm, 10 ns pulse width,  $\sim 10 \mu\text{J}/\text{pulse}$ , 10 Hz) was produced by a Nd:YAG pumped dye laser and was focused into the interaction volume of the sample at the Bragg angle. A digital delay generator controlled the time delay between the pump and probe pulses. The diffracted signal beam was spatially and spectrally filtered to reduce scattered pump and probe beam light. The signal was detected with a photomultiplier tube, amplified, integrated with a gated integrator, and sent to a computer where data averaging and acquisition take place.

## H. ANALYTICAL TECHNIQUES

Many analytical and spectroscopic techniques were needed to identify and quantify the effluent products and reactants resulting from the SCWO process. Our goal was to achieve a mass balance between waste reactant and product species. For purposes of this discussion, these techniques are divided into gas-phase analyses and liquid analyses. Brief descriptions are given of each.

### 1. Gas-Phase Analysis

#### a. Fourier-Transform Infrared Spectroscopy (FTIR)

A procedure was developed to quantify the concentration (and thus number of moles) of  $\text{CO}_2$  and  $\text{N}_2\text{O}$  (the primary gas-phase products) produced using FTIR. Calibration

curves for CO<sub>2</sub> and N<sub>2</sub>O were obtained by measuring the fraction of infrared light absorbed by a series of known concentrations of CO<sub>2</sub> or N<sub>2</sub>O in the range expected to occur in SCWO reactions. The unknown concentration is then determined by measuring the fraction of infrared light absorbed by the unknown sample (*i.e.*, the volatile components of the reactor effluent). The dependence on concentration of the integrated absorbance of each of the two major CO<sub>2</sub> IR absorptions (asymmetric OCO stretch, 2350 cm<sup>-1</sup>, and OCO bend, 630 cm<sup>-1</sup>) was nonlinear, exhibiting distinctive saturation behavior over the range of pressures (concentrations) from 0.1 to 10 torr. Another observation was that, for a given pressure of CO<sub>2</sub>, the observed absorption intensity increased with increasing total pressure. Pressure broadening of absorption lines is a well-understood phenomenon. As total pressure is increased, some molecules will absorb light further from the center of each rotational line, causing a decrease in the center intensity and a concomitant broadening of the peak. The integrated absorbance should remain constant. The reason for the apparently anomalous behavior of our initial results is that the rotational linewidths of most small molecules (including CO<sub>2</sub>) are much narrower than the resolution limit of FTIR (maximum resolution = 0.5 cm<sup>-1</sup>). The observed lines are a convolution of the instrument resolution function and the actual line shape and thus appear to be optically thick to the FTIR, meaning that essentially all the radiation at center frequency appears to be absorbed, resulting in a "saturated" absorbance. As the pressure is increased, more light is absorbed away from the center frequency while the center continues to absorb essentially all the incident radiation. Since the lines are not fully resolved by the spectrometer, absorption of additional light in the wings of the narrow line, but still within the instrument resolution, results in a higher apparent absorbance. This effect can be eliminated by decreasing the concentration of the absorbing species or the path length until the line centers are no longer saturated, or by increasing the total pressure until the linewidths are comparable to the instrument resolution. The White cell we used did not have the capability to operate at pressures higher than atmospheric, so the nonlinearity of our calibration curves was not completely corrected for. The calibrations and unknown pressure determinations were made at a total pressure of 600 torr, using N<sub>2</sub> or He as a buffer gas. The resulting calibration data were fit to a saturation function,  $y=a(1-e^{-bP})+cP$  where  $P$  is the partial pressure of the absorbing gas. A typical calibration curve is shown in Figure 26. This technique enabled us to measure the gas pressure with a relative standard deviation of 3 percent.



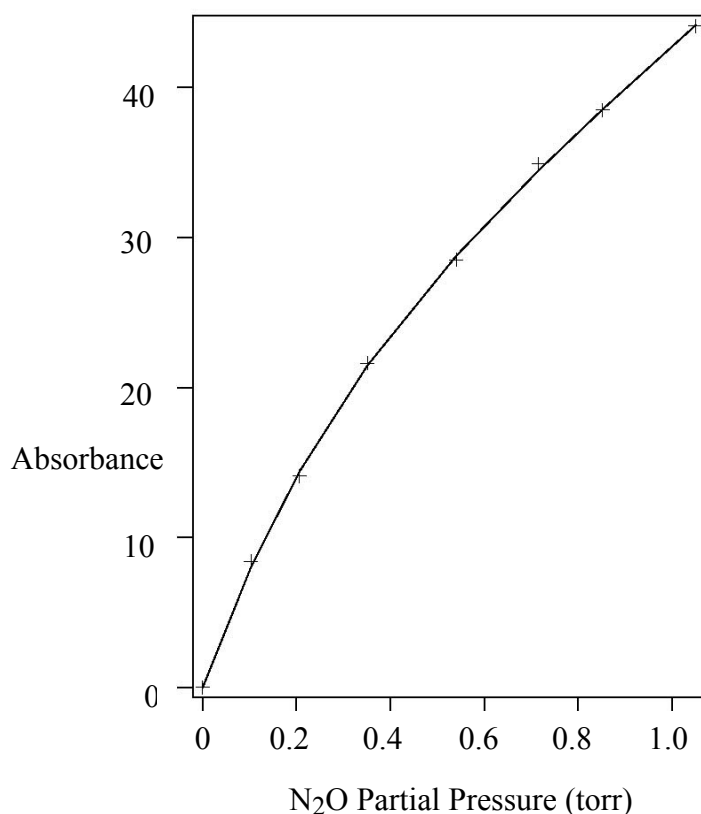


Figure 26. Typical FTIR calibration curve for N<sub>2</sub>O, quantity measured in the integrated absorbance for the symmetric N–O stretch versus pressure of N<sub>2</sub>O.

b. GC–Mass Spectrometry

The GC technique is complementary to FTIR, because it is capable of detecting H<sub>2</sub>, O<sub>2</sub>, and N<sub>2</sub>, in addition to all other gases. Three gas chromatographs (GC) were set up to analyze the gaseous effluent from the reactor: an HP 5890A Series II with capillary injection ports operated with HP ChemStation software control from a 386-based IBM-compatible computer, and two Perkin–Elmer Model 8410 units. A 10-port gas sampling valve was used to inject gas samples of ~0.1 mL into the capillary column. The carrier gas was He except for one of the gas chromatographs, in which Ar was used for the detection of H<sub>2</sub>. Thermal conductivity detectors were installed for quantitative detection of the eluting gases. The column (30 meters x 0.53 mm (id)) used for separating O<sub>2</sub>, N<sub>2</sub>, H<sub>2</sub>, CO, CO<sub>2</sub>, CH<sub>4</sub> and CH<sub>3</sub>OH was a Chrompack CarboPLOT with carbon molecular sieve adsorbent. A molecular sieve 5A column was run in the isothermal mode at -40 °C for H<sub>2</sub> and an Alltech CTR-1 column with a temperature ramp program from -10 °C to 180 °C was used for the other gases. A mass spectrometer (HP 5971

MSD) is also available for detection of gases and liquids that elute from the column. In addition, a GC–FTIR interface is installed to a Mattson 500 series FTIR spectrometer, which can be used to characterize the separated compounds.

c. Quadrupole Mass Spectrometry (QMS)

A UTI quadrupole mass spectrometer was also used to detect H<sub>2</sub>, N<sub>2</sub>, and O<sub>2</sub>. Gaseous products are sampled online through a leak valve. To obtain a steady leak rate, a constant backing pressure of sample plus He buffer gas (600 torr total) was maintained. The pressure in the quadrupole region was typically in the 10<sup>-5</sup> torr range. Calibration of this technique has so far proved difficult due to constantly changing backgrounds.

2. Liquid-Phase Techniques

a. Metals

The metals analyzed for include sodium, chromium, nickel, iron, molybdenum and gold. In most cases these were done on a Perkin–Elmer inductively coupled plasma spectrophotometer (ICP) using indium as an internal standard for all the metals except sodium, for which a lanthanum internal standard was used. If very low detection limits were required, the samples were analyzed using a graphite furnace or flame atomic absorption.

b. Total Organic Carbon (TOC) and Total Inorganic Carbon (TIC)

Total organic carbon (TOC) and total inorganic carbon (TIC) were analyzed using a Rosemount Dohrmann Model DC-190 Carbon Analyzer. Calibrations were done with each set of samples using different concentrations of standardized potassium acid phthalate solution.

c. Inorganic Anions

Inorganic anions, particularly nitrate, nitrite and chloride, were analyzed with a Dionex 4500i Series ion chromatograph using a Dionex IonPac AS4A column with an eluent consisting of 1.5mM NaHCO<sub>3</sub> and 2.2mM Na<sub>2</sub>CO<sub>3</sub>. In most cases conductivity detection was used, but a UV/visible detector set at 215 nm was used for low levels of nitrate and nitrite.

d. Ammonium Ion

Ammonium ion concentration was determined by an Orion Model 95-12 ammonia electrode using an ionic strength adjuster (ISA) containing 5M NaOH, 0.05M ethylenediaminetetraacetic acid (EDTA), and 10 percent methanol. The ISA converted the ammonium ion into dissolved ammonia gas, which was detected by the electrode.

e. TNT, PETN, HMX, NQ, RDX, Hydrazine, and UDMH.

Trace amounts of these explosives were analyzed by reverse-phase liquid chromatography on the Dionex 4500i. The liquid chromatograph used a Waters 490E Programmable Multiwavelength Detector that allows for simultaneous detection at several wavelengths. This feature is particularly useful if interferences are present, since interferences usually give different signals at different wavelengths. All these compounds were analyzed using a 150 mm x 2.1 mm (id) C8 narrow-bore column that was slightly heated for temperature stability. Trinitrotoluene was measured at 240 and 260 nm using an eluent of 35 percent methanol (MeOH) and 4.5 percent tetrahydrofuran (THF) in water at 0.3 mL/minute in a 6.7- $\mu$ L sampling loop; PETN was measured using 48 percent MeOH at 0.3 mL/minute in a 27- $\mu$ L loop at 215 and 230 nm; RDX and HMX were both measured using 32 percent MeOH and 4.8 percent THF at 0.3 mL/minute in a 15- $\mu$ L loop at 235 and 245 nm; and NQ was analyzed using 4 percent MeOH at 0.3 mL/minute in a 9.5- $\mu$ L loop at 263 and 275 nm. UDMH was measured at 294 nm using 65 percent MeOH and monobasic sodium phosphate ( $\text{NaH}_2\text{PO}_4$ ) as a buffer at a pH of 2.5. Before analysis, nitrosalicylaldehyde was added to the sample to concentrations of 50 ppm and the sample was heated in a water bath for 5 minutes to form a color complex. Hydrazine was measured at 458 nm using 90 percent MeOH and 10 percent  $\text{NaH}_2\text{PO}_4$  buffer. One mL of dimethylaminobenzaldehyde (DAMB) reagent was added to 5 mL of sample to form a color complex. Both UDMH and hydrazine used a 15- $\mu$ L sampling loop.

f. Methanol

Methanol was analyzed using an SRI Model 8610 gas chromatograph by direct injection on a 30-meter x 0.53-mm J&W Scientific DB-Wax column at 60 °C.

### 3. Base Hydrolysis Product Analysis

Products from the hydrolysis reactions were analyzed by a number of different methods. Nuclear magnetic resonance (NMR) spectrometry was used to identify the major hydrolysis products. A JEOL GSX-270 multi-nuclear spectrometer was used to obtain proton, carbon, nitrogen, and phosphorus NMR spectra. Analyses were performed on the hydrolysis solution with a small amount of deuterated water added to provide a lock signal. Mass spectrometry was used to analyze gaseous hydrolysis products (DuPont model 104) and, in some cases, for solid residue analysis (Finnigan–MAT model 8200). Quantitative analysis for inorganic and organic anions was performed with a Dionex model 2000i ion chromatograph using a conductivity detector. Solid residues from dried hydrolysis solutions were tested for energetic material by observing their burning characteristics in a flame and by differential thermal analysis (DTA) using a DuPont model 910 thermal analyzer.

## SECTION III

### REACTIONS OF ENERGETIC MATERIALS BELOW WATER-SOLUBILITY LIMITS

#### A. INTRODUCTION

Much of our effort focused on reactions of solutions having concentrations less than half of their solubilities at room temperature. We have obtained destruction efficiencies and product analyses for the SCWO of AP, NM, PETN, HMX, RDX, TNT, NG, N<sub>2</sub>H<sub>4</sub>, UDMH and NQ. In some cases, Cl, N, and C mass balances have been obtained. In addition, for the AP and NM reactions we have obtained kinetic data for limited ranges of temperature and concentration.

#### B. DESTRUCTION EFFICIENCIES AND REACTION PRODUCTS UNDER HIGHLY OXIDIZING CONDITIONS

The destruction efficiencies for the SCWO of five explosive compounds, PETN, HMX, RDX, TNT, and NQ are given in Table 5. These reactions were run at high temperatures (near 600 °C) and with a large excess of oxidant. Numerous reactions were run at lower temperatures and with varying amounts of oxidant, and these are discussed in subsequent sections. In addition, N<sub>2</sub>H<sub>4</sub>, UDMH, AP and NM, which are unique in their high solubilities and their chemistry, will be discussed in separate sections.

TABLE 5. DESTRUCTION EFFICIENCIES FOR ENERGETIC MATERIALS BELOW WATER-SOLUBILITY LIMITS<sup>a</sup>

Substrate	PETN	HMX	RDX	TNT	NQ
Initial conc. (ppm)	3.8	2.6	35.2	65.5	1700
Destruction efficiency	>0.9825	>0.9900	>0.9992	>0.9998	>0.9999

<sup>a</sup>Conditions: 600 °C, 5500 psi; excess H<sub>2</sub>O<sub>2</sub>; 11-s residence time; gold-lined reactor.

The initial concentrations of the explosives were kept at less than half their room-temperature solubilities to prevent precipitation and accumulation of explosive material in the feed lines leading to the reactor. Hydrogen peroxide was used as the oxidizer and was mixed

with the feedstock containing explosives before the fluids were heated. In all cases the oxidizer was in 30-fold excess of the stoichiometry required to convert the explosive into CO<sub>2</sub>, H<sub>2</sub>O, and N<sub>2</sub>. The experimental conditions for each of these explosives were nearly identical: pressure, 340 atm; reactor temperature, 600 °C; and residence time, 11 seconds. The reactions were run primarily in the gold-lined reactor to minimize the heterogeneous chemistry that might occur at the reactor walls. The only compound for which any reactor-dependent chemistry was observed is AP. No significant difference in DREs or products chemistry was observed for reactions of TNT, HMX, and RDX in the C-276 and the gold-lined reactors. We conclude from these observations that reactions with the C-276 and 316 stainless walls must not be significant for these energetic materials.

For these “extreme” conditions, the aqueous effluent contained no detectable amounts of explosives. The detection limit of the HPLC/UV–visible analysis ranges from 20 to 50 parts per billion (ppb) depending on the compound. Consequently, the measured destruction efficiencies represent lower limits defined by the low starting concentrations and the detection limits.

Gaseous and liquid effluents from these reactions have been analyzed to determine the products of reaction. Typical FTIR spectra of the gaseous effluent from the reactions of NQ, TNT, and RDX with excess oxidant are shown in Figure 27. These spectra show IR absorptions corresponding to CO<sub>2</sub>, N<sub>2</sub>O, and H<sub>2</sub>O. Qualitative FTIR analyses of gas-phase products of SCWO of energetic materials with and without oxidant are summarized in Table 6. It is clear from these analyses that the extreme conditions of high temperature and excess oxidant produce only CO<sub>2</sub> and N<sub>2</sub>O in the gaseous effluent. Other possible products such as CO, CH<sub>4</sub>, NO, and NO<sub>2</sub> were not detected and were, therefore, below part-per-million (ppm) levels (generally below 0.1 percent of the starting C and N). Additional products that were likely to be produced in these reactions, but which cannot be quantified by FTIR, include N<sub>2</sub>, O<sub>2</sub> (no infrared-active vibrations), and H<sub>2</sub>O (swamped by large water background absorption). In addition, quantitative measurements of the CO<sub>2</sub> and N<sub>2</sub>O produced are summarized in Tables 7 and 8.

The reactor effluents were analyzed for carbon content and the results are summarized in Table 7. The final two columns list the percentage of the starting C that is observed in the aqueous effluent (as organic and inorganic C) and as CO<sub>2</sub> in the gaseous effluent. For PETN and HMX, both the TIC and TOC quantities are below detection limits (0.1 ppm). Detectable quantities of organic carbon were found for RDX, TNT, and NQ. Since in all of these cases the substrate was destroyed to levels well below the detection limits of the HPLC analysis (10 ppb)

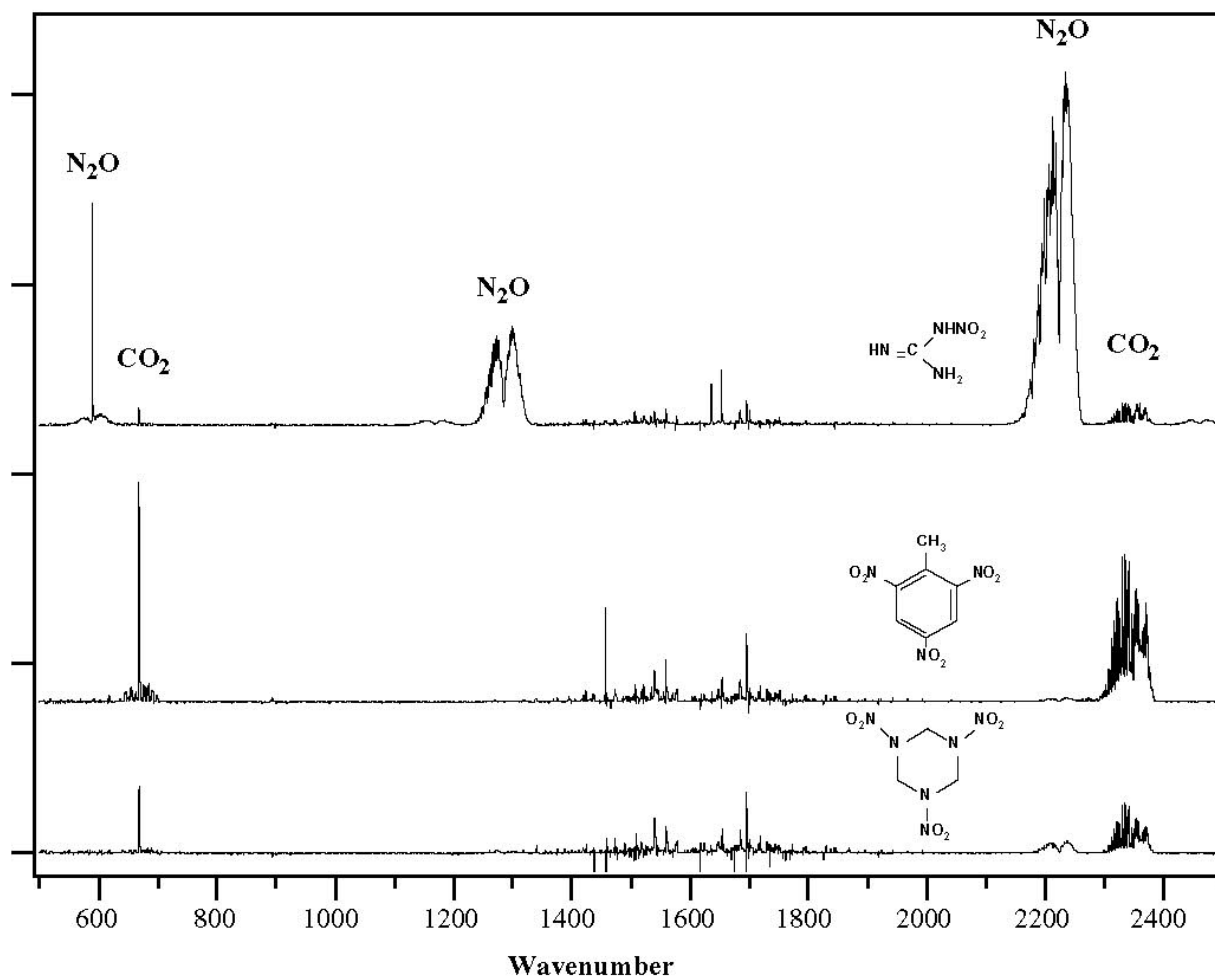


Figure 27. FTIR spectra of the reaction products of SCWO of NQ, TNT, and RDX

TABLE 6. FTIR ANALYSIS OF GAS-PHASE PRODUCTS OF SCWO OF ENERGETIC MATERIALS<sup>a</sup>

Substrate	Without oxidant	With oxidant
PETN	CO <sub>2</sub> , CO	CO <sub>2</sub>
HMX	CO <sub>2</sub> , N <sub>2</sub> O	CO <sub>2</sub> , N <sub>2</sub> O
RDX	CO <sub>2</sub> , CO, N <sub>2</sub> O	CO <sub>2</sub> , N <sub>2</sub> O
TNT	CO <sub>2</sub> , CO, CH <sub>4</sub> , NO	CO <sub>2</sub> , N <sub>2</sub> O
NQ	CO <sub>2</sub> , N <sub>2</sub> O	CO <sub>2</sub> , N <sub>2</sub> O

<sup>a</sup>Conditions: 600 °C, 5500 psi; 11-s residence time; gold-lined reactor.

TABLE 7. ANALYSIS OF CARBON PRODUCTS IN EFFLUENT STREAMS FOR SCWO OF ENERGETIC MATERIALS<sup>a</sup>

Substrate	[C] <sub>i</sub> <sup>b</sup> (ppm)	TIC (ppm) <sup>c</sup>	TOC (ppm) <sup>c</sup>	% C <sub>aqueous</sub>	% C <sub>CO<sub>2</sub></sub>
PETN	2	d	d	d	81
HMX	2	d	d	d	87
TNT	24	0.2	1.7	8	98
RDX	5.7	<0.1	<0.1	<4	98
NQ	195	152	10	83	21

<sup>a</sup>Conditions: 600 °C, 5500 psi; excess H<sub>2</sub>O<sub>2</sub>; 11-s residence time; gold-lined reactor; <sup>b</sup>Initial carbon concentration; <sup>c</sup>TIC, Total inorganic carbon, TOC, Total organic carbon; <sup>d</sup>Initial concentrations of PETN and HMX are ~2-3ppm, the analyses for TOC and TIC are below detectable limits.

and since no volatile organics were observed in the FTIR analyses, the observed organics must be nonvolatile reaction products such as formate or acetate. For the TNT reactions, greater than 94 percent of the C was detected as CO<sub>2</sub>, with the remainder detected as nonvolatile organics in solution. The only substrate to give significant TIC (carbonate or bicarbonate) quantities is NQ. In this case, 83 percent of the C was detected as CO<sub>3</sub><sup>2-</sup> or HCO<sub>3</sub><sup>-</sup> while 21 percent was detected as gaseous CO<sub>2</sub>, accounting for most of the C.

Reactor effluents were analyzed for nitrogen content and the results are summarized in Table 8. For PETN, HMX, and RDX, some N<sub>2</sub>O was observed in the FTIR spectra, but quantitative analysis showed the amounts to be less than 0.5 percent of the initial N. With excess oxidant, significant amounts of nitrite and nitrate were observed for all substrates except NQ. Most of the detected N from NQ was determined to be N<sub>2</sub>O. Trinitrotoluene (TNT) yielded the greatest fraction (65 percent) of NO<sub>x</sub><sup>-</sup>. As NO<sub>x</sub><sup>-</sup> is an undesirable product, some effort was

TABLE 8. ANALYSIS OF NITROGEN PRODUCTS IN EFFLUENT STREAMS FOR SCWO OF ENERGETIC MATERIALS<sup>a</sup>

Substrate	PETN	HMX	RDX	TNT	NQ
% NO <sub>3</sub> <sup>-</sup>	18.7	12.4	10.1	36.6	0.03
% NO <sub>2</sub> <sup>-</sup>	6.0	5.3	14.1	28.5	0.04
% N <sub>2</sub> O	b	b	b	4.0	35

<sup>a</sup>Conditions: 600 °C, 5500 psi; excess H<sub>2</sub>O<sub>2</sub>; 11-s residence time; gold-lined reactor. <sup>b</sup>Less than 0.5%.



made to determine conditions for which its production can be minimized in the case of TNT. These results are summarized in Section III.D. In all cases examined, a large fraction of the initial nitrogen remained undetected by our analytical techniques. We interfaced a mass spectrometer to the gas–liquid separator on the gold-lined reactor, which enabled us to obtain on-line analyses of the effluent gases. We have observed formation of  $N_2$  in the SCWO oxidation of TNT. In addition, we have a gas chromatograph interfaced to the gas–liquid separator of the sand bath reactor, with the appropriate column and detector for separation and detection of  $N_2$ . Experiments on SCWO of nitromethane with this setup indicated the formation of  $N_2$ ; however, we did not obtain quantitative analysis for  $N_2$  for any of the very-low-concentration experiments.

### C. REACTIONS OF AMMONIUM PERCHLORATE (AP)

This section summarizes the data for the SCWO reactions of AP. Because of corrosion problems, most of these reactions were performed in the gold-lined reactor. Some results in the C-276 reactor are included for comparison. Sodium hydroxide was always added to the AP solutions in a 1:1 stoichiometry to ensure a net  $pH$  balance. This was particularly important for the gold-lined reactor, where the presence of a high  $Cl^-$  ion concentration together with a low  $pH$  and highly oxidizing conditions might have resulted in the oxidation of the gold liner to  $AuCl_4^-$  (see Section VII.B.1).

Data describing the dependence of destruction efficiencies and reaction products on temperature and concentration are summarized in Tables 9 and 10, respectively. The products containing Cl and N are given as a percentage of the initial Cl and N concentration, respectively. No decomposition of AP was observed at temperatures lower than 400 °C. Most of the ammonia

Table 9. AP SCWO Products as a Function of Temperature<sup>a</sup>

T (°C)	% $ClO_4^-$	% $Cl^-$	% $NO_2^-$	% $NO_3^-$	% $N_2O$	% $NH_4^+$
400	100	0.0	0.3	0.0	0.0	95.0
450	95.5	6.9	0.8	0.3	1.3	85
500	46.0	16.0	0.0	2.0	13.6	40.0
550	3.5	17.0	0.0	2.0	23.1	0.0
600	0.4	5.0	0.2	0.2	23.3	0.0

<sup>a</sup>Conditions: 0.1 M AP; equimolar NaOH; residence time varied from 11–52 s (600–400 °C); flush between runs not analyzed; gold-lined reactor.

TABLE 10. AP SCWO PRODUCTS AS A FUNCTION OF CONCENTRATION<sup>a</sup>

[AP] (M)	% ClO <sub>4</sub> <sup>-</sup>	% Cl <sup>-</sup>	% NO <sub>2</sub> <sup>-</sup>	% NO <sub>3</sub> <sup>-</sup>	% N <sub>2</sub> O
0.001	0.3	108.1	7.1	1.9	0.0
0.01	12.5	95.0	1.1	1.0	13.7
0.1	0.4	69.1	0.0	3.8	23.0

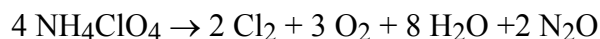
<sup>a</sup>Conditions: 600 °C; equimolar NaOH; 11-s residence time; flush between runs included in analyses; gold-lined reactor.

and all of the perchlorate were recovered. The small ammonia loss was likely due to the evolution of ammonia gas from the feed solution and effluent. AP begins to react at 450 °C and is nearly completely destroyed (99.6 percent) after 11 seconds at 600 °C. The effect of concentration on destruction efficiency appears to be less straightforward, since results at the intermediate concentration (0.01M) indicated a lower destruction efficiency of 87.5 percent. This result is inconsistent with the results at higher and lower concentrations, and we suspect there was a problem with the analyses of these data.

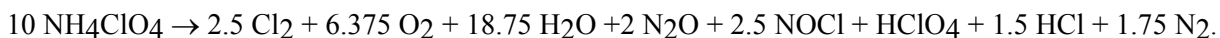
Almost all the chlorine from the perchlorate appeared in the effluent as sodium chloride (NaCl). Although salt solubility decreases in supercritical water, the sodium chloride product remained in solution at low concentrations or temperatures. However, when the concentration and/or temperature were raised, the Cl mass balance was degraded, probably due to precipitation of Cl<sup>-</sup> salts in the reactor. We found that our mass balances improved when the reactor was cooled and flushed between runs and the flushing solutions were included in the analysis. With this procedure a burst of Cl<sup>-</sup> was generally observed in the first or second flush sample as the reactor was cooled.

The liquid effluent also contained a small amount (< 2 percent) of nitrogen as nitrite (NO<sub>2</sub><sup>-</sup>) and nitrate (NO<sub>3</sub><sup>-</sup>). The mass spectra indicated that both nitrous oxide (N<sub>2</sub>O) and oxygen (O<sub>2</sub>) were produced. The amount of N<sub>2</sub>O produced was quantified using the FTIR/White cell and appears to increase with increasing temperature and AP concentration. Most of the N was not detected (for the best case, 600 °C, only 25 percent is detected) and likely occurs as N<sub>2</sub>. The FTIR and mass-spectrometric analyses of the gaseous effluent did not detect the presence of chlorine (Cl<sub>2</sub>), nitrosyl chloride (NOCl), or nitrogen dioxide (NO<sub>2</sub>).

Previous studies of the thermal decomposition of solid ammonium perchlorate show that a variety of products are possible (Reference 10). Below 300 °C, the equation



represents the majority of the products. At higher temperatures, more nitric oxide (NO) formed. Gas analysis of the products of thermal decomposition Between 350 °C and 450 °C gives



Thus the decomposition of AP in supercritical water avoids the formation of the hazardous products (Cl<sub>2</sub>, NOCl) formed in thermal decomposition.

Above 450 °C, AP detonates. The possibility of explosive energy release was investigated. Concentrated solutions of ammonium perchlorate (1.0 M, 117.5 g/L) were rapidly heated to temperatures over 600 °C at pressures near 340 atm in a small batch reactor. Neither pressure nor temperature transients indicative of rapid energy release were observed. These results indicate SCWO is, therefore, better controlled (*i.e.*, safer) than thermal decomposition.

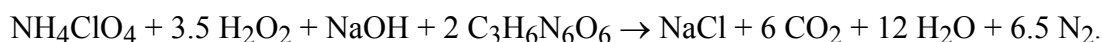
One interesting observation in the gold-lined reactor was a lower destruction efficiency for AP compared to that found for the C-276 reactor. Comparisons of the destruction efficiencies in the two reactors at various temperatures are summarized in Table 11. The conditions for these reactions were roughly equivalent except that the residence time in the C-276 was approximately 80 percent that in the gold-lined reactor. Despite the longer residence times in the latter reactor, the destruction efficiencies were always poorer at a given temperature. AP was 99.95 percent destroyed at 500 °C in the C-276 reactor while the best destruction efficiency achieved in the gold-lined reactor is 99.6 percent at a higher temperature, 600 °C. We attribute this difference to the absence of reactions with the reactor walls in the case of the gold-lined reactor. The extensive corrosion of the C-276 reactor by AP reactions supports this conclusion (see Section VII.B.1).

TABLE 11. COMPARISON OF AP SCWO REACTIONS IN C-276 AND GOLD-LINED REACTORS<sup>a</sup>

Destruction Efficiency(%)	400 °C	450 °C	475 °C	500 °C	550 °C	600 °C
C-276 Reactor	0	40	86	99.95	-	-
Gold-Lined Reactor	0	4.5	-	54.0	96.5	99.6

<sup>a</sup>Conditions: 0.1M AP; equimolar NaOH; residence time varied from 11–52 s (600–400 °C); flush between runs not analyzed.

A series of experiments was run on mixtures of AP and RDX in an attempt to model the complex mixtures actually found in a rocket motor. Ammonium perchlorate, NaOH and RDX were mixed in a 1:1:2 molar ratio. This ratio yields a slight oxygen deficiency if the reaction goes to completion, according to



Experiments were performed with and without additional oxidant (H<sub>2</sub>O<sub>2</sub>) and at temperatures ranging from 500 to 600 °C (Table 12). The oxidant was added in a 2:1 molar ratio with RDX, to yield an oxygen balance as defined by the equation above. The best possible comparison to the chemistry of pure RDX is with SCWO reactions at the same concentration, at 600 °C and with a large excess of oxidant (Tables 5, 7, 8, pages 48 and 51). The destruction efficiency of RDX was the same in both cases (99.92 percent). Only one-third of the C was recovered as CO<sub>2</sub> for the mix, compared to nearly 100 percent for the pure RDX under these conditions. The nitrogen chemistry was also significantly different. While the percent N converted into nitrite was similar for both the pure and mixed cases, no formation of nitrate was observed in the case of the mix whereas 10 percent of the N in pure RDX was converted to nitrate. Another puzzling observation is that the percent N converted to nitrite dropped by a factor of two to three upon the addition of oxidant. It is likely that the differences in both the C and N chemistry are due to the difference in the oxygen balance in these reactions. The large excess (30 equivalents) of oxidant used in the reactions of the pure RDX solutions appears to have resulted in better conversion of all the C into CO<sub>2</sub> with the negative side effect of causing the formation of nitrate.

TABLE 12. SCWO OF AP AND RDX MIXTURES<sup>a</sup>

T (°C)	[H <sub>2</sub> O <sub>2</sub> ] added (ppm)	% Cl <sup>-</sup>	% ClO <sub>4</sub> <sup>-</sup>	% NO <sub>2</sub> <sup>-</sup>	% NO <sub>3</sub> <sup>-</sup>	% N <sub>2</sub> O	%CO <sub>2</sub>
500	0	100.0	5.0	44.0	1.0	0.3	23
500	11	89.0	20.0	15.0	1.0	0.4	27
550	0	96.0	3.0	45.0	1.0	0.4	28
550	11	86.0	10.0	18.0	0.0	10.1	28
600	0	98.0	3.0	30.0	0.0	10.5	34
600	11	86.0	9.0	18.0	0.0	15.2	33

<sup>a</sup>Conditions: 18.3 ppm AP; equimolar NaOH; 34.6 ppm RDX; residence time varied from 11–16 s (600–500 °C); flush between runs included in analysis; gold-lined reactor.

The best possible comparison with the chemistry of pure AP is to reactions run at slightly higher concentration ( $1.00 \times 10^{-3} M = 118$  ppm) and at 600 °C (Table 10, page 53). The chemistry yielded a slightly smaller destruction efficiency of ClO<sub>4</sub><sup>-</sup>. Addition of oxidant (H<sub>2</sub>O<sub>2</sub>) caused the destruction efficiency of ClO<sub>4</sub><sup>-</sup> to decrease from greater than 97 percent to less than 91 percent. This observation suggests that better destruction of ClO<sub>4</sub><sup>-</sup> may be achieved by adding more reducing agents (fuels). This is consistent with the higher destruction efficiencies observed in the C-276 reactor, where the reactor itself was acting as a source of reductant.

#### D. REACTIONS OF TRINITROTOLUENE (TNT)

This section discusses the SCWO reactions of TNT in greater detail, particularly the effects of temperature and oxidant concentration on observed destruction efficiencies and reaction products. Data for CO<sub>2</sub> production from the SCWO of TNT in the linear reactor at 600 °C, 5400 psi, 4 g/min flow rate and a large excess (~30-fold) of H<sub>2</sub>O<sub>2</sub> are summarized in Table 13.

Expected pressures of CO<sub>2</sub> are calculated from initial concentrations of TNT and the volume of effluent collected—using the ideal gas law and assuming complete conversion of the TNT into CO<sub>2</sub>—according to the following equation:

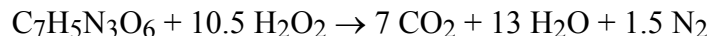


TABLE 13. CO<sub>2</sub> PRODUCTION IN THE SCWO OF TNT

Exp.	P <sub>meas</sub> <sup>a</sup> (mtorr)	P <sub>calc</sub> <sup>b</sup> (mtorr)	%C detected
1	260	259	100
2	245	272	90
3	314	303	104
4	232	244	95
5	258	261	99

<sup>a</sup>Determined from integrated FTIR band intensities and CO<sub>2</sub> calibration curves.

<sup>b</sup>Calculated from the ideal gas law assuming complete oxidation.

The average percent C detected as CO<sub>2</sub> in these experiments was 98 percent. The residual C could have been tied up in the nonvolatile product observed in the HPLC analysis shown in Figure 28 (identity and concentration unknown). It is possible that this product is a small nonvolatile organic acid such as formic acid. Nitrogen balances for these reactions were not complete. Detected products, including N<sub>2</sub>O, NO<sub>3</sub><sup>-</sup> and NO<sub>2</sub><sup>-</sup> accounted for about 69 percent of the starting N, (Table 8, page 51). The remaining N presumably occurred as N<sub>2</sub> or ammonia.

A large number of experiments were conducted on TNT to determine the SCWO chemistry as a function of reaction temperature and oxidant concentration. All of these experiments were performed using TNT solutions near one-half the solubility limit in water (65 ppm). In all cases, the TNT was destroyed to below detectable limits of ~10 ppb, yielding a destruction efficiency of greater than 99.98 percent. The product analyses are summarized in Tables 14 and 15. The values listed in these tables represent averages of at least 10 runs each. The NO<sub>2</sub><sup>-</sup> and NO<sub>3</sub><sup>-</sup> values are listed as a percentage of the starting nitrogen concentration. Similarly, the total inorganic carbon (TIC) and total organic carbon (TOC) values are listed as a percentage of the starting carbon concentration. The ratio of H<sub>2</sub>O<sub>2</sub> to TNT represents a stoichiometric ratio based on complete reaction of TNT with H<sub>2</sub>O<sub>2</sub> to form CO<sub>2</sub>, H<sub>2</sub>O, and N<sub>2</sub>.

The most efficient conversion of TNT into CO<sub>2</sub>, as determined by FTIR analysis of the gas production and by the TIC and TOC analyses of the aqueous effluents, occurred at the highest temperature (600 °C) and the highest H<sub>2</sub>O<sub>2</sub> concentration. These conditions also yielded the highest concentrations of NO<sub>2</sub><sup>-</sup> and NO<sub>3</sub><sup>-</sup>. In general, at lower temperatures and lower ratios of H<sub>2</sub>O<sub>2</sub>:TNT, less NO<sub>2</sub><sup>-</sup> and NO<sub>3</sub><sup>-</sup> were observed. While these conditions do not compromise the destruction efficiency of TNT, they tend to leave more carbon in the aqueous effluent. Much of this carbon appears as carbonate, however, which can be removed by lowering the pH. The best

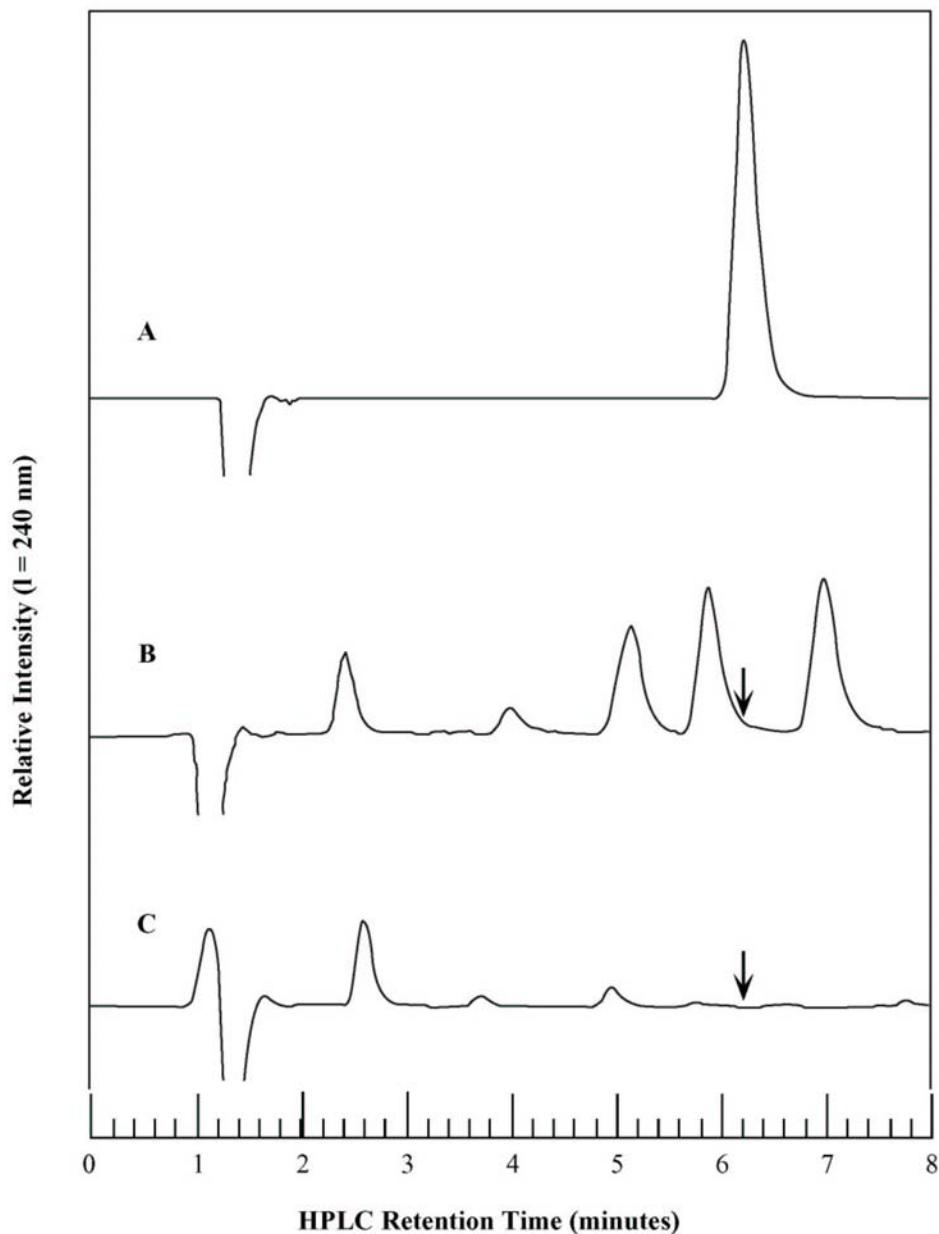


Figure 28. HPLC analysis of aqueous TNT solutions: (A) TNT standard, 32.4 ppm; (B) SCWO reaction (550 °C) without added oxidant; (C) SCWO reaction (550 °C) with excess  $\text{H}_2\text{O}_2$ . The arrows indicate where the TNT peak should occur.

conditions for the destruction of TNT and any organic byproducts with minimum  $\text{NO}_2^-$  and  $\text{NO}_3^-$  formation appear to be 600 °C and a 1:1 stoichiometric (as defined on page 57) ratio of  $\text{H}_2\text{O}_2$ :TNT.

TABLE 14. TNT SCWO PRODUCTS AS A FUNCTION OF H<sub>2</sub>O<sub>2</sub> CONCENTRATION

Exp.	Temp (°C)	H <sub>2</sub> O <sub>2</sub> :TNT <sup>a</sup>	%NO <sub>2</sub> <sup>-</sup>	%NO <sub>3</sub> <sup>-</sup>	Total %NO <sub>x</sub> <sup>-</sup>	%TIC	%TOC	%Total C
1	600	0:1	18	0	18	12	34	46
2	600	1:1	11	6	17	15	0	15
3	600	2:1	6	6	12	14	0	14
4	600	5:1	33	38	71	9	0	9
5	600	20:1	25	49	74	4	0	4

<sup>a</sup>Stoichiometric ratio based on equation on page 56.

TABLE 15. TNT SCWO PRODUCTS AS A FUNCTION OF TEMPERATURE

Exp.	Temp (°C)	H <sub>2</sub> O <sub>2</sub> :TNT <sup>a</sup>	%NO <sub>2</sub> <sup>-</sup>	%NO <sub>3</sub> <sup>-</sup>	Total %NO <sub>x</sub> <sup>-</sup>	%TIC	%TOC	%Total C
1	500	0:1	18	0	18	14	28	42
2	600	0:1	18	0	18	12	34	46
3	400	20:1	11	30	41	4	18	22
4	500	20:1	26	51	77	4	11	15
5	600	20:1	25	49	74	4	0	4

<sup>a</sup>Stoichiometric ratio based on equation on page 56.

## E. REACTIONS OF NITROMETHANE (NM)

This section summarizes experiments on the SCWO of nitromethane. These experiments were conducted primarily in either the C-276 linear flow reactor or in the shorter optical cell configured as a linear flow reactor. The destruction of nitromethane was monitored using the FTIR/White cell, by the intensity of the N–O stretching band at 1590 cm<sup>-1</sup>. The integrated intensity of this band indicates that the nitromethane was greater than 98 percent destroyed at 550 °C and in the short residence time (< 1 second) of the optically accessible reactor (Figure 23, page 39). The FTIR spectrum of the 550 °C run is compared to the spectrum at 300 °C in Figure 29. It is clear from these data that little of the NM reacted at 300 °C, but most was



destroyed at 550 °C. All the peaks in the 550 °C spectrum have been assigned to vibrations of the residual  $\text{CH}_3\text{NO}_2$  and volatile reaction products, including  $\text{CO}_2$ ,  $\text{CO}$ ,  $\text{CH}_4$ ,  $\text{N}_2\text{O}$ ,  $\text{NO}$ , and  $\text{HCN}$ . These are indicated in Figure 29. Expected reaction products that were not detected included  $\text{N}_2$  and  $\text{O}_2$  (no infrared absorptions),  $\text{NO}_3^-$  and  $\text{NO}_2^-$  (not volatile species) and  $\text{H}_2\text{O}$  (obscured by large  $\text{H}_2\text{O}$  background). Other possible products that are detectable under these conditions at levels above 1 ppm but were not observed include  $\text{NH}_3$  and  $\text{NO}_2$ .

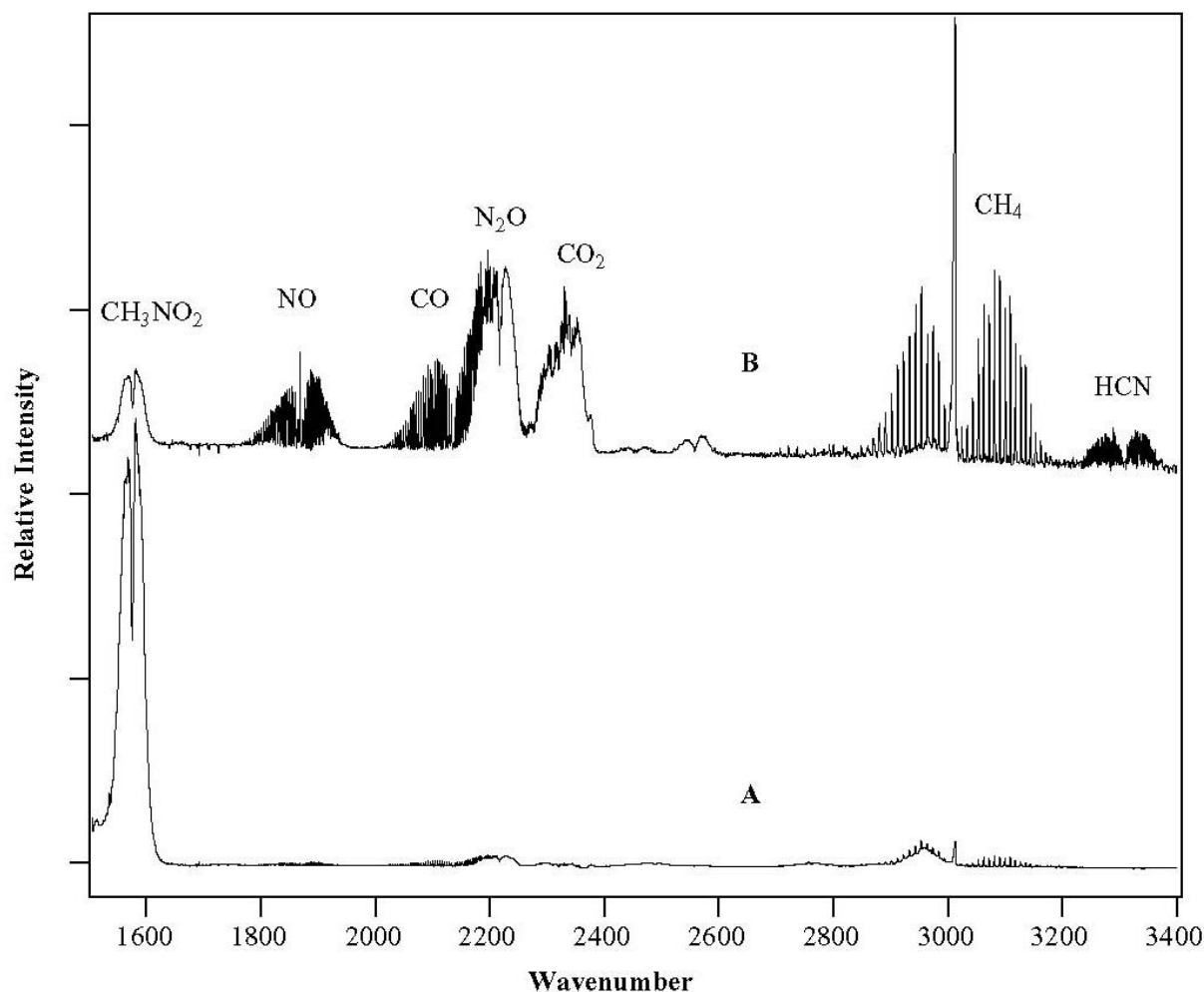


Figure 29. FTIR product analysis of SCWO of nitromethane. (A)  $\text{CH}_3\text{NO}_2$  in  $\text{H}_2\text{O}$ , 300 °C, 5000 psi; (B)  $\text{CH}_3\text{NO}_2$  in  $\text{H}_2\text{O}_2$ , 550 °C, 5000 psi

Quantitative analyses of the reaction products were obtained from these spectra. The infrared assignments and number densities (molecules per  $\text{cm}^3$  in the White cell) calculated from literature values of the absorption cross sections are summarized in Table 16. The starting number density of the  $\text{CH}_3\text{NO}_2$  was measured to be  $5.7 \times 10^{16}$  molecules/ $\text{cm}^3$ . The number

TABLE 16. FTIR ANALYSIS OF NITROMETHANE DECOMPOSITION PRODUCTS<sup>a</sup>

Product	$\nu$ (cm <sup>-1</sup> )	Absorbance	$\sigma \times 10^{19}$ (cm <sup>2</sup> /molecule) <sup>b</sup>	$N \times 10^{-15}$ (molecules/cm <sup>3</sup> ) <sup>c</sup>
CH <sub>3</sub> NO <sub>2</sub>	1590	0.022	2.82	0.8
CO <sub>2</sub>	2360	0.039	1.05	3.7
CO	2120	0.025	0.08	27.0
CH <sub>4</sub>	3020	0.126	0.46	27.0
N <sub>2</sub> O	2235	0.052	0.48	11.0
NO	1875	0.028	3.16	0.9
HCN	3312	0.009	?	?

<sup>a</sup>Reaction conditions: 550 °C, 4800 psi, 2-s residence time.

<sup>b</sup>Absorption cross section, estimated from Sadtler Commercial Spectra of Gases and Vapors, 1972.

<sup>c</sup>Calculated number density,  $N = (A/\sigma l)$ .

density for HCN could not be calculated because the absorption cross section was not available, but a reasonable estimate yields a number density of less than  $2.0 \times 10^{14}$  molecules/cm<sup>3</sup>. The mass balance for the reaction was calculated from these measured number densities and is summarized in Table 17. The carbon is completely accounted for. It is almost evenly distributed

TABLE 17. MASS BALANCE FOR NITROMETHANE DECOMPOSITION IN SCW AT 550 °C

PRODUCT <sup>a</sup>	%C (±1%)	%N (±1%)	%O (±1%)	%H (±1%)
CH <sub>3</sub> NO <sub>2</sub>	1	1	1	1
CO <sub>2</sub>	6	-	6	-
CO	47	-	24	-
CH <sub>4</sub>	47	-	-	63
N <sub>2</sub> O	-	38	10	-
NO	-	2	1	-
H <sub>2</sub> O <sup>b</sup>	-	-	27	36
TOTAL	101	41	69	100

<sup>a</sup>Based on number densities of products detected by FTIR. Number density of CH<sub>3</sub>NO<sub>2</sub> before reaction,  $N_0 = 5.7 \times 10^{16}$  molecules/cm<sup>3</sup>. Undetected products include NO<sub>3</sub><sup>-</sup> and NO<sub>2</sub><sup>-</sup>. N<sub>2</sub> and O<sub>2</sub> not detectable.

<sup>b</sup>Calculated from undetected H.

between CO and CH<sub>4</sub>, with a small amount occurring as CO<sub>2</sub>. Only 41 percent of the nitrogen was detected, mostly as N<sub>2</sub>O. Nitrogen dioxide (NO<sub>2</sub>) and NH<sub>3</sub> were not detected and if present are below our 1 ppm detection limit. Based on previous experiments, we expected a small amount (~4 percent) of the nitrogen to occur as NO<sub>3</sub><sup>-</sup> and NO<sub>2</sub><sup>-</sup>. The remaining 55 percent likely occurred as N<sub>2</sub>, which is not detectable by FTIR analysis. The undetected hydrogen (36 percent) most likely occurred as H<sub>2</sub>O. Given this reasonable assumption and the ~4 percent of the oxygen that occurred as NO<sub>3</sub><sup>-</sup> and NO<sub>2</sub><sup>-</sup>, 27 percent of the oxygen remains unaccounted for. It is possible that the decomposition produced O<sub>2</sub>, which would not be detected in the FTIR analysis.

Measurements can be made as a function of residence time and temperature, yielding kinetic information for reactant destruction and product formation. Additional analysis using the GC–mass spectrometer would enable the determination of N<sub>2</sub> and O<sub>2</sub> as well as the validation of other volatiles detected by the FTIR. While this would allow more complete mass balances, the impossibility of detecting the small quantities of H<sub>2</sub>O produced in these reactions remains as an intrinsic barrier to a complete mass balance.

The addition of H<sub>2</sub>O<sub>2</sub> as an oxidant in the SCWO of nitromethane radically changed the product composition and the destruction efficiency. The reaction of NM with a 30-fold excess of oxidant under similar conditions (600 °C, 5400 psi) resulted in > 99.9 percent destruction of NM and produced only CO<sub>2</sub> and small amounts of N<sub>2</sub>O. These results are dramatically illustrated in the FTIR spectrum shown in Figure 30. Quantitative data for CO<sub>2</sub> production are summarized in Table 18. The measured and expected CO<sub>2</sub> values were determined as described for TNT, assuming complete conversion of the NM into CO<sub>2</sub> according to the following equation:



TABLE 18. CO<sub>2</sub> PRODUCTION IN THE SCWO OF NITROMETHANE

Exp.	P <sub>meas</sub> <sup>a</sup> (torr)	P <sub>calc</sub> <sup>b</sup> (torr)	%C detected
1	0.69	1.09	63
2	0.70	1.08	65
3	0.82	1.06	77
4	0.80	1.06	75

<sup>a</sup>Determined from integrated FTIR band intensities and CO<sub>2</sub> calibration curves.

<sup>b</sup>Calculated from the ideal gas law assuming complete oxidation.

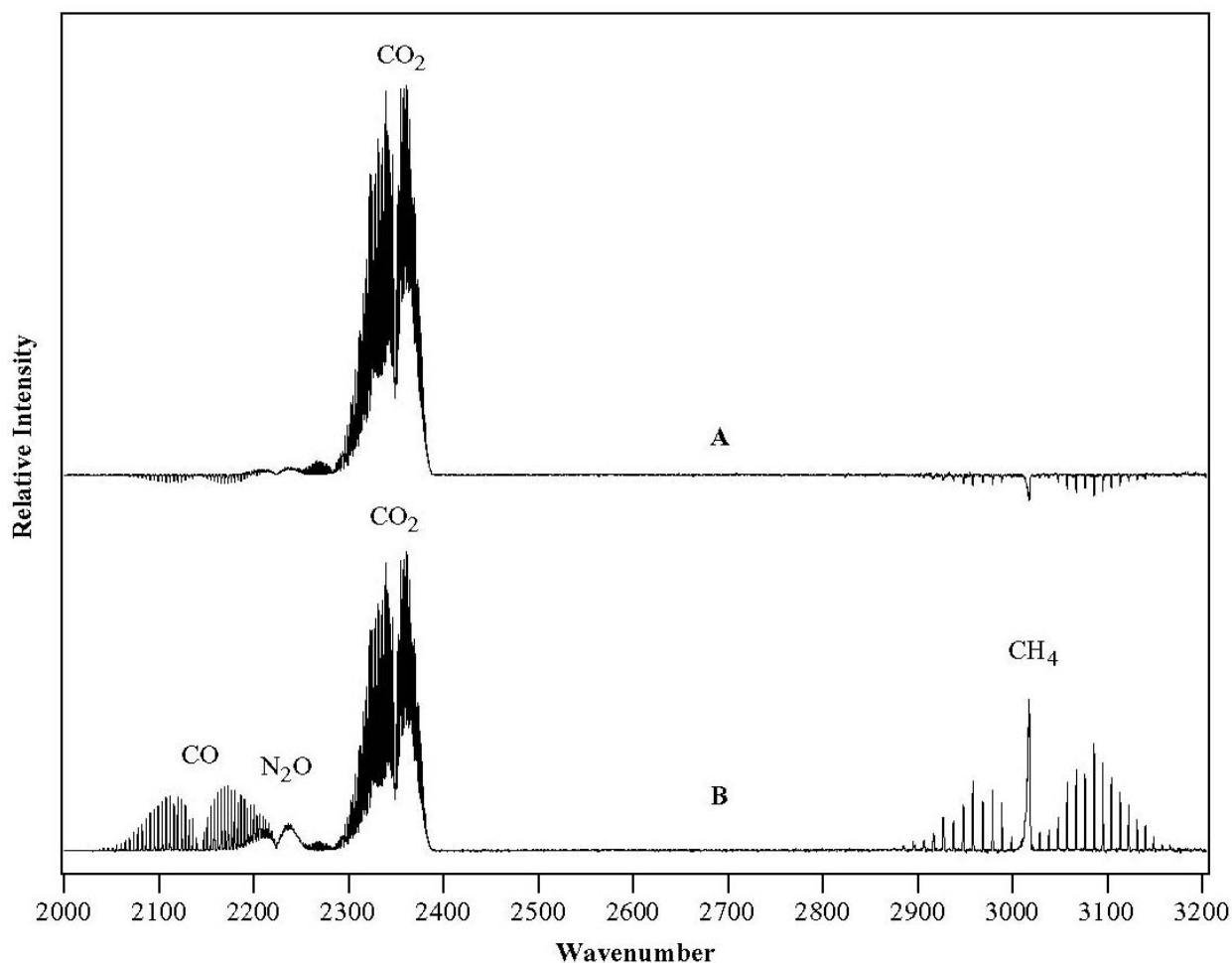


Figure 30. FTIR product analysis for the SCWO of NM at 600 °C. (A) NM plus Oxidant ( $\text{H}_2\text{O}_2$ ); (B) NM without oxidant.

The first two experiments were performed with a 3-day-old solution of NM in water whereas a freshly prepared solution was used for the latter two. Evaporation is the presumed cause for the difference in the two sets of experiments. No other volatile products (*i.e.*,  $\text{CH}_4$  or  $\text{CO}$ ) were detected. If such components were present they comprised less than 0.1 percent of the total carbon. The percentage of the nitrogen detected as  $\text{N}_2\text{O}$  was 4.5 percent. The remaining N likely occurred as  $\text{N}_2$ .

The carbon remaining in the aqueous effluent was analyzed and these results are summarized in Table 19. Under these conditions, very little of the initial carbon remained in the aqueous effluent. For reactions of NM with oxidant, greater than 80 percent of the C was detected as  $\text{CO}_2$ , while only one percent was detected in solution. Without oxidant, 64 percent

TABLE 19. ANALYSIS OF RESIDUAL CARBON IN AQUEOUS EFFLUENT FOR SCWO OF NM AT 600 °C

Solution	No. of Runs	$[C]_i$ (ppm)	TIC (ppm) <sup>‡</sup>	TOC (ppm) <sup>†</sup>	%C
NM + H <sub>2</sub> O <sub>2</sub>	4	85	0.2	0.8	1.2
NM + H <sub>2</sub> O <sub>2</sub>	10	75	<0.1	0.5	0.8
NM	4	79	0.2	2.9	4

of the C was detected in the gas phase as CO<sub>2</sub>, CO, and CH<sub>4</sub> and four percent of the C was detected in solution. We cannot account for the "missing" C, but we suspect volatilization of the NM from the stock solution lowered starting concentrations.

#### F. REACTIONS OF NITRATE

Nitrates are formed when explosives decompose in supercritical water. As discussed in previous sections, the amount of nitrogen converted into nitrate and nitrite depends upon the substrate and the reaction conditions. The chemistry of nitrogen appears to be more complicated than that of carbon in supercritical water. To produce an effluent that is free of NO<sub>x</sub><sup>-</sup>, the nitrogen chemistry needs to be understood. To gain a better understanding, we studied the reactions of nitrates with simple organics in supercritical water. This work, partly sponsored by DOE's Office of Technology Development, has relevant to the treatment of nitrate-containing radioactive wastes stored in underground tanks at the Hanford Reservation in Washington. In this section we discuss the reactions of nitrate with methanol in supercritical water.

Experiments were conducted in which nitrate was reacted with methanol. A 1:1 stoichiometry was assumed for the reaction. Experiments were conducted at 25-degree intervals from 450 °C to 525 °C, and at 30.9 MPa (4500 psi). Residence times ranged from 5 to 18 seconds. Figures 31 and 32 display nitrate and methanol decomposition as a function of temperature and residence time. Reaction conditions resulted in observed methanol destruction efficiencies ranging from 31% at 450 °C to 85% at 525 °C. Corresponding nitrate removals ranged from 15% to >99%. At 500 °C and above, ammonia appeared to be the predominant nitrogen species. Below 500 °C, nitrite was the predominant nitrogen species. Gas-phase analysis (by GC) indicated the production of N<sub>2</sub>, N<sub>2</sub>O, and O<sub>2</sub>. Gas-phase analysis by FTIR showed that some samples contained trace amounts of NO. Carbon was recovered as an

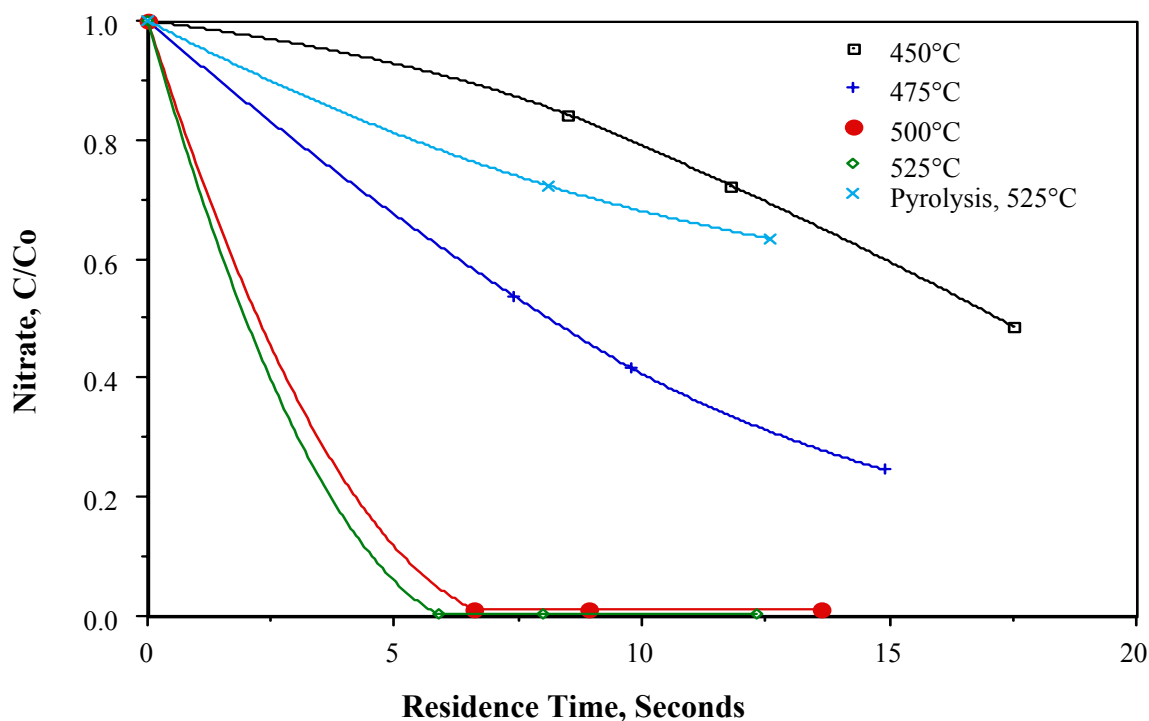


Figure 31. Nitrate removal as a function of temperature and residence time.

Lines drawn to aid in viewing.

inorganic species, as determined by TIC analysis. This species was either carbonate or bicarbonate, depending on the *pH* of the effluent stream. Effluent *pH* values were neutral to basic (7–10). No carbon products of incomplete combustion ( $\text{CO}$ ,  $\text{CH}_4$ ) were detected in the gas phase. Trace amounts of  $\text{CO}_2$  were detected by FTIR in several gas samples.

A nitrate pyrolysis run was also conducted. At 525 °C and a 12.6-second residence time, a maximum nitrate conversion (to nitrite) of 36% was observed. No ammonia was detected in nitrate pyrolysis at 525 °C. For all experiments, mass recoveries for nitrogen and carbon were been  $100 \pm 10\%$ .

In addition to carbon and nitrogen species, aqueous effluent and reactor rinse samples were also analyzed for sodium (present in the sodium nitrate feed) and corrosion products (Fe, Cr, Mo, and Ni). Trace amounts of corrosion products were recovered in all experiments. While iron and nickel appeared only at sub-ppm levels in all experiments, chromium and molybdenum were present in both effluent and rinse water samples. At temperatures above 500 °C, these species were recovered primarily in reactor rinse water samples. These samples, which were yellow tinted, are believed to contain the hexavalent forms of chromium ( $\text{CrO}_4^{=}$ ) and molybdenum

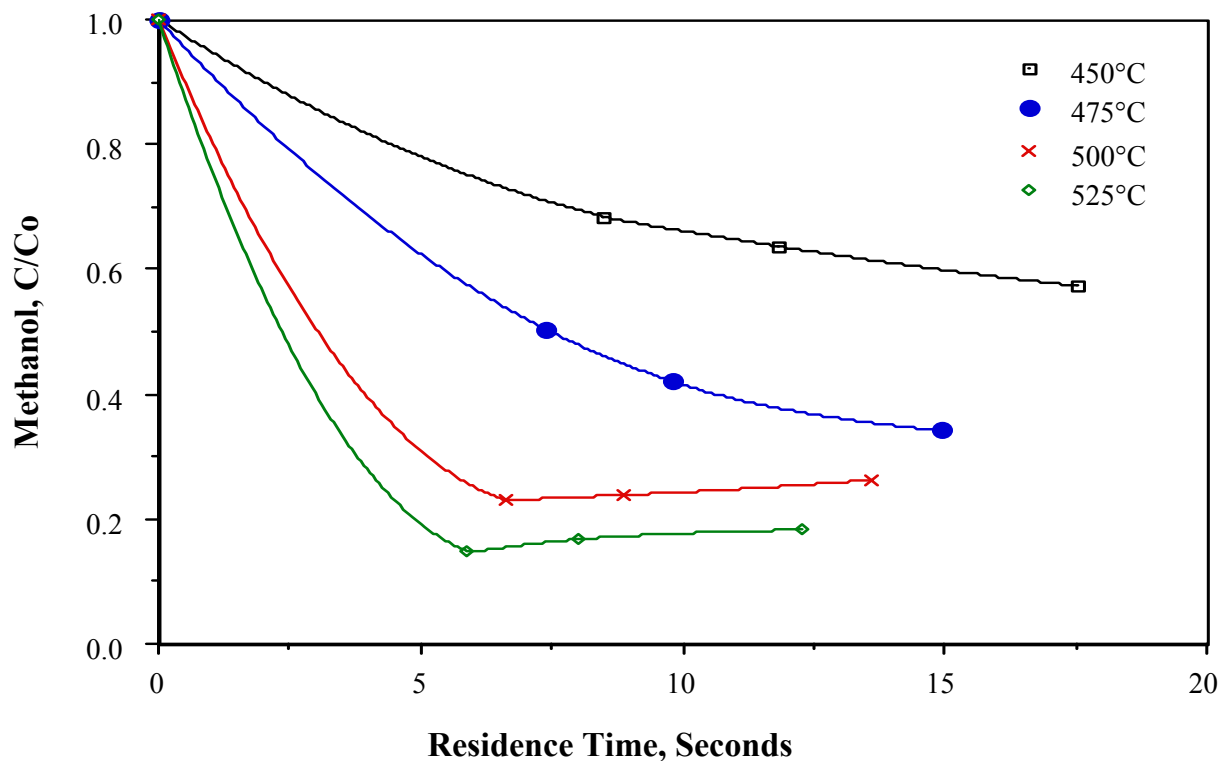


Figure 32. Methanol removal as a function of temperature and residence time.  
Lines drawn to aid in viewing.

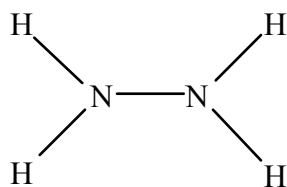
( $\text{MoO}_4^{=}$ ). These species likely deposited on the reactor walls as sodium precipitates. Sodium also precipitated substantially with carbonate species. These precipitation reactions were supported by ion balances performed on reactor rinse samples. Such balances were successful in predicting measured  $p\text{H}$  values to within one  $p\text{H}$  unit. Effluent concentrations of sodium, bicarbonate, chromium, and molybdenum decreased with increasing temperatures, which indicated decreasing solubilities with increasing temperatures. The absence of iron and nickel indicated that these metals formed a passivating oxide film on the reactor surface, which was insoluble in water rinses.

Studies projected by DOE at the completion of this project were to investigate the kinetics of the  $\text{MeOH} / \text{NO}_3^-$  reaction in more detail. These were to include additional experiments at different residence times and temperatures, and different stoichiometries. Further studies of nitrate and methanol pyrolysis were also projected, together with other experiments, such as reactions of sodium nitrite with methanol, and reactions of nitrate with a different organic compound, designed to elucidate the kinetic mechanisms.

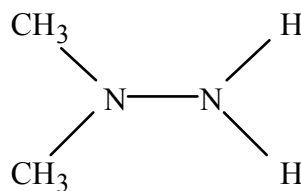
## G. REACTIONS OF HYDRAZINE

### 1. Introduction

This section summarizes the experiments on the supercritical water reactions of hydrazine and unsymmetrical (1,1-)dimethylhydrazine (UDMH). Hydrazine and UDMH are important rocket propellants, whose structures are given below. In particular they find use as flight control thrusters, which can be actuated for short periods of time. With special catalysts they can decompose in milliseconds providing very precise attitude control. Both these propellants present special hazards in handling and disposal. Neat solutions may spontaneously ignite in air and both are suspect carcinogens. The breakdown products of UDMH using conventional destruction techniques are undesirable (Reference 11). In particular, dimethyl nitrosamine, which is a carcinogen, is produced by incineration of UDMH.



Hydrazine



UDMH

Hydrazine and UDMH are both clear liquids and completely miscible in water at all temperatures. In water, the auto-ignition problem is abated and the resultant mixture is very suitable for destruction using the hydrothermal processing techniques described in this report. The favorable solubility characteristics avert the throughput problems associated with solid explosives such as HMX, RDX and TNT. Thus, even with our bench-scale reactors we demonstrated large processing capabilities using up to 1-wt% solutions.

We studied the pyrolysis and oxidation reactions of hydrazine and UDMH in supercritical water using both hydrogen peroxide and nitric acid or sodium nitrate as oxidants. Table 20 summarizes the product formation for these reactions. Under oxidizing conditions the primary products are relatively innocuous, consisting of various amounts of nitrogen, nitrous oxide and also CO<sub>2</sub> in the case of UDMH (see following discussions). Under fuel-rich conditions, incomplete combustion products resulted.



TABLE 20. SUMMARY OF HYDRAZINE AND UDMH SCWO REACTIONS

Reaction	Major Products	Minor Products
$\text{N}_2\text{H}_4 + \text{no oxidizer}$	$\text{N}_2, \text{H}_2, \text{NH}_3, \text{NH}_4^+$	
$\text{N}_2\text{H}_4 + \text{H}_2\text{O}_2$	$\text{N}_2$	$\text{N}_2\text{O}, \text{NH}_4^+, \text{NO}_3^-, \text{NO}_2^-$
$\text{N}_2\text{H}_4 + \text{HNO}_3$	$\text{N}_2, \text{N}_2\text{O}$	$\text{NH}_4^+, \text{NO}_3^-, \text{NO}_2^-$
$\text{N}_2\text{H}_4 + \text{NaNO}_3$	$\text{N}_2, \text{N}_2\text{O}, \text{NaOH}$	$\text{NH}_4^+, \text{NO}_3^-, \text{NO}_2^-$
$(\text{CH}_3)_2\text{N}_2\text{H}_2$ (fuel rich)	$\text{CO}_2, \text{N}_2$	$\text{N}_2\text{O}, \text{CO}, \text{CH}_4, \text{NH}_4^+, \text{amines}$
$(\text{CH}_3)_2\text{N}_2\text{H}_2$ (fuel lean)	$\text{CO}_2, \text{N}_2$	$\text{N}_2\text{O}, \text{NO}_3^-, \text{NO}_2^-, \text{CO}_3^{2-}$

Destruction of the parent compound was essentially complete. In every experiment the destruction efficiency exceeded 99.999%, with or without oxidizer. Table 21 shows the measured destruction efficiency for hydrazine and UDMH. These numbers, for the destruction of a 0.5-wt% solution, represent lower limits due to our limits of detection (0.01 ppm).

TABLE 21. DESTRUCTION EFFICIENCIES FOR SCWO OF HYDRAZINE AND UDMH

Species	Destruction (%)
$\text{N}_2\text{H}_4$	>99.9998
$(\text{CH}_3)_2\text{N}_2\text{H}_2$	>99.9998

## 2. Experimental

All results reported in this section are from experiments conducted in the gold-lined reactor described in Section II.A. Some experiments were conducted in a similar reactor constructed of C-276, but severe corrosion was observed when  $\text{HNO}_3$  or  $\text{NaNO}_3$  was used as the oxidizer. (See section VII.B.4.) For our purposes, the gold liner minimizes chemistry due to wall reactions. For these experiments the reactor was kept at a constant temperature of  $600^\circ\text{C}$ , 340 atm, and a total flow rate of 4 mL/min. This provided a reaction residence time of approximately 11 seconds. The fuel and oxidizer were mixed cold using two HPLC pumps running at 2 mL/min. For mass balance calculations and to ensure desired fuel:oxidizer ratios the weight loss of the fuel and oxidizer mixtures was monitored continuously using Precisa 3000D top-loading balances.

Both hydrazine and UDMH solutions were prepared at concentrations of 1 weight-percent (wt%) for all runs except the isotopic comparisons with  $\text{H}^{14}\text{NO}_3$  and  $\text{H}^{15}\text{NO}_3$ , which were prepared at 0.25 wt%. When mixed with the oxidizer stream in the reactor, the effective concentration was halved. This relatively high loading caused high rates of gas production, necessitating redesign of the gas–liquid separator to accommodate larger volumes.

The gas-phase effluent was analyzed using the combination of gas chromatography, set up to quantify  $\text{N}_2$ ,  $\text{N}_2\text{O}$ ,  $\text{O}_2$ ,  $\text{CO}_2$ ,  $\text{CO}$ ,  $\text{H}_2$ , and  $\text{CH}_4$ , FTIR spectroscopy with  $0.5\text{ cm}^{-1}$  resolution, and mass spectroscopy. The liquid effluent was routinely analyzed for nitrates, nitrites, ammonium, and TIC and TOC in the case of UDMH. Metals analysis was performed, but very few corrosion products were observed.

### 3. Hydrazine Reactions

Several experiments investigating the destruction of hydrazine were conducted. These included hydrazine pyrolysis (no oxidizer), and reaction with an oxidizer, either hydrogen peroxide or nitric acid. Based on our previous results with explosives, a large excess of oxidizer will lead to a high concentration of nitrate and nitrite in solution. Therefore, the oxidizer in these experiments did not exceed twice stoichiometric as defined by the reaction equations to follow. Tables 22 and 23 show the product analysis of these experiments. The equivalence ratio ( $\phi$ ) is given by the ratio of the stoichiometric oxidizer concentration to the actual concentration as defined by the equation corresponding to the specified reaction.

TABLE 22. HYDRAZINE NITROGEN MASS-BALANCE (AS A % OF THE STARTING NITROGEN CONCENTRATION)

Species	Pyrolysis	$\text{H}_2\text{O}_2\ \phi=1$	$\text{H}_2\text{O}_2\ \phi=0.5$	$\text{HNO}_3\ \phi=1$
$\text{N}_2$	60	98	94	78
$\text{N}_2\text{O}$	0	0.1	0	21
$\text{NH}_3$	not quantified	0	0	0
$\text{NH}_4^+$	29	1.0	0	0.2
$\text{NO}_3^-$	0	0.1	0.1	0.0
$\text{NO}_2^-$	0	0.1	0	0.2
Total	89	99.3	94.1	99.4

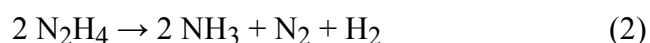
TABLE 23. HYDRAZINE HYDROGEN MASS-BALANCE, PYROLYSIS (AS A % OF THE STARTING HYDROGEN CONCENTRATION)

Species	pyrolysis	pyrolysis
H <sub>2</sub>	19	19
NH <sub>3</sub>	not quantified	16 (estimated)
NH <sub>4</sub> <sup>+</sup>	44	44
Total	63	79

a. Hydrazine Pyrolysis

Hydrazine was effectively destroyed (Table 21, page 68) in hot, high-pressure water in less than 11 seconds. However, without oxidizer present, large amounts of NH<sub>3</sub>/NH<sub>4</sub><sup>+</sup> and H<sub>2</sub> were observed. Ammonia was probably the major product of the pyrolysis of hydrazine and was in equilibrium with NH<sub>4</sub><sup>+</sup> through the reaction  $\text{H}_2\text{O} + \text{NH}_3 \rightarrow \text{NH}_4^+ + \text{OH}^-$ . Nitrogen and NH<sub>4</sub><sup>+</sup> were detected in nearly equal molar ratios. Ammonia is observed in the FTIR spectrum shown in Figure 33. A small background of CH<sub>4</sub>, which was due to reduction of char left over from previous experiments, has been subtracted from this spectrum. Because NH<sub>3</sub> appeared to be sticking to the wet walls of our manifold we were unable to quantify this species, and thus unable to achieve a nitrogen or hydrogen mass balance. If we assume that all undetected nitrogen is NH<sub>3</sub>, then the hydrogen mass balance becomes 79%.

Typical global models for hydrazine pyrolysis are represented by reaction 1 and 2 (References 13–19).



However, since we did not obtain a mass balance for the hydrazine pyrolysis, we cannot determine a global reaction stoichiometry, but it probably is a combination of reactions 1 and 2. In hydrazine the N–N bond is weaker than the N–H bond (70.8 Kcal/mole and >100 Kcal/mole, respectively) (Reference 12), so the first elementary step in the pyrolysis of hydrazine is most likely to be (References 13–19)



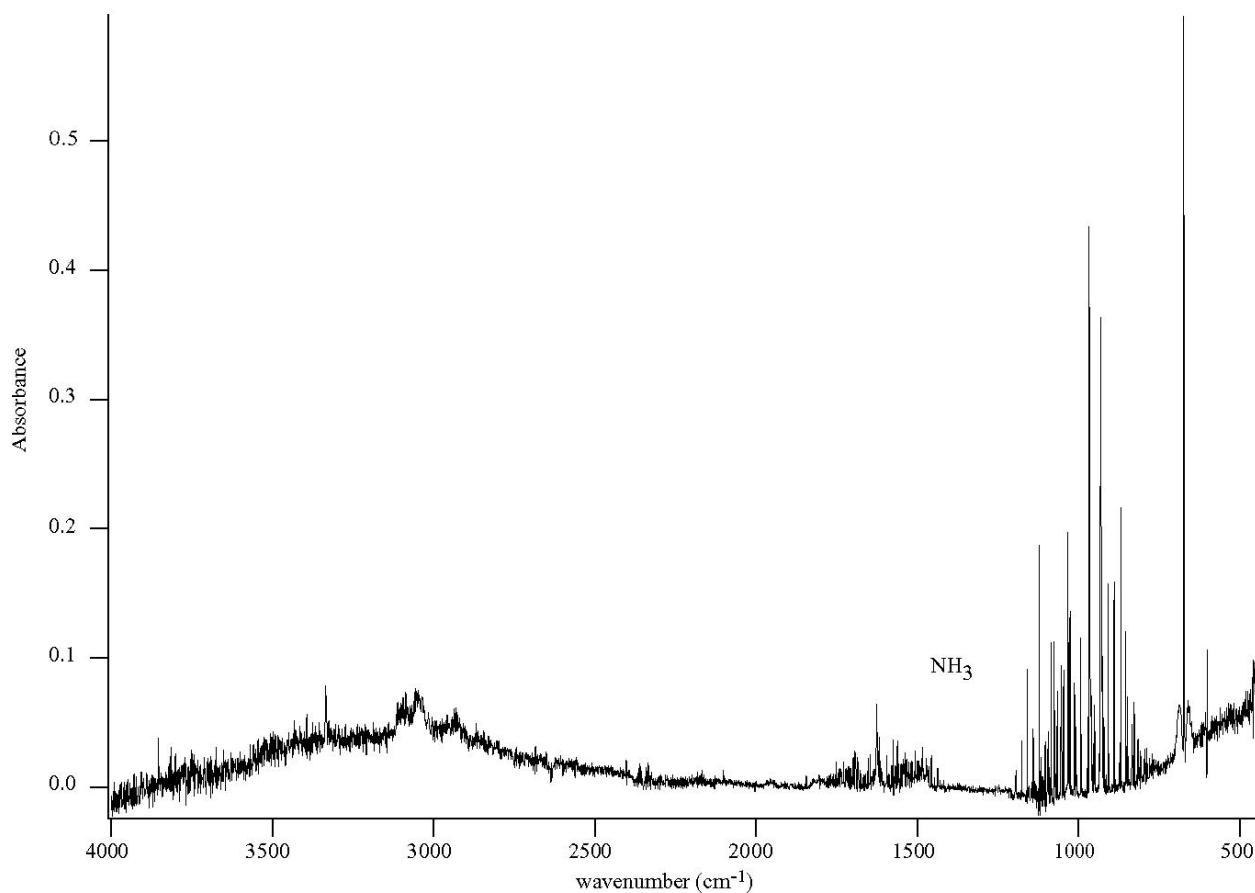
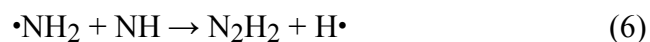
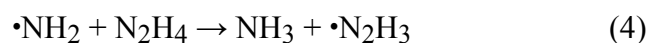


Figure 33. FTIR spectrum of gas effluent from hydrazine pyrolysis, primarily ammonia (NH<sub>3</sub>).

followed by such elementary steps as



These and related radical reactions are likely to dominate the chemistry under the low-density conditions employed. At 600°C and 340 atm the water density is approximately 0.15 g/cc. Higher densities may support ionic chemistry leading to different products. The nitrogen chemistry is quite complex. Many of the postulated intermediates have not been observed nor have the reaction rates been measured in previous gas phase studies (References 13–20). Based on current understanding of gas-phase reaction mechanisms (Reference 20), we postulate a simplified mechanism as shown in Figure 34.

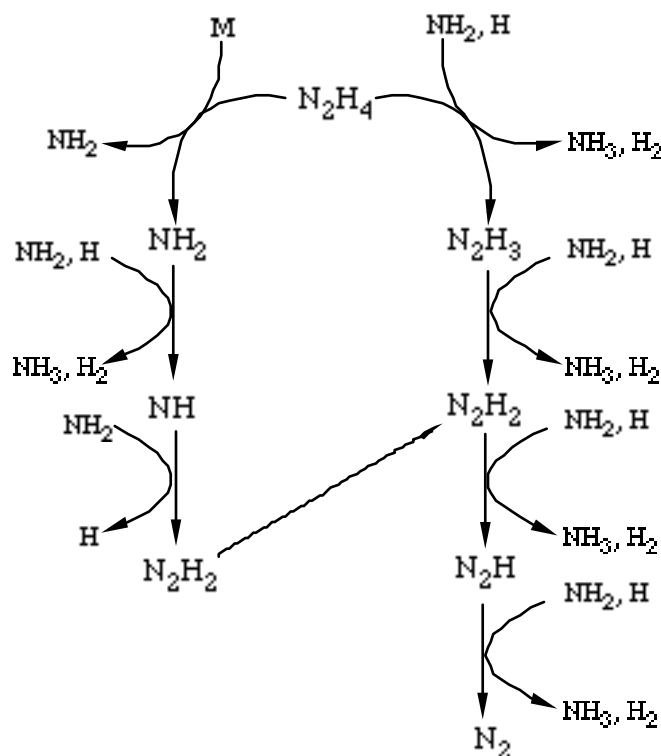


Figure 34. Proposed hydrazine decomposition mechanism in supercritical water.

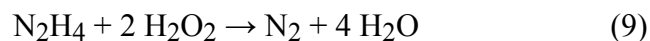
Each step is a hydrogen abstraction accomplished by reactions such as 7 and 8 leading to observed final products  $NH_3$ ,  $H_2$  and  $N_2$ .



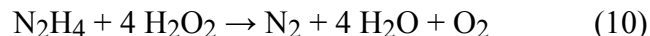
We observed virtually no oxygenated products of nitrogen leading us to believe that water plays little role in the decomposition of hydrazine under these conditions.

#### b. Hydrazine Reaction with Hydrogen Peroxide

With the addition of an oxidizer in the form of hydrogen peroxide no incomplete combustion products were observed. The only major product was nitrogen (Table 22, page 69). The amount of nitrate and nitrite in the liquid effluent and of  $N_2O$  in the gas produced were more than two orders of magnitude smaller than the amount of  $N_2$  produced. Two fuel-to-oxidizer ratios were run based on a stoichiometric case given in reaction equation 9.



Reaction equation 10 is an equivalence ratio of 0.5 and represents a fuel-lean case.



By normalizing the moles of product obtained to the number of moles of hydrazine reactant we can show that these global reactions (9 and 10) are consistent with reality (see Tables 24 and 25). Other than releasing excess oxygen, the addition of excess oxidizer to hydrazine had essentially no effect or benefit. The FTIR spectrum had only trace amounts of  $\text{N}_2\text{O}$  in the  $\phi = 1$  case and no infrared-active products in the  $\phi = 0.5$  case. In both cases the nitrogen mass balance obtained (Table 22, page 69) was quite reasonable.

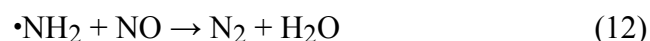
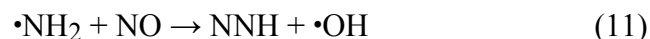
TABLE 24. HYDRAZINE +  $\text{H}_2\text{O}_2$  PRODUCT RATIOS,  $\phi = 1$

	$\text{N}_2$	$\text{O}_2$
expected	1	0
actual	0.98	0.03

TABLE 25. HYDRAZINE +  $\text{H}_2\text{O}_2$  PRODUCT RATIOS,  $\phi = 0.5$

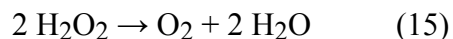
	$\text{N}_2$	$\text{O}_2$
expected	1	1
actual	0.94	1.05

Miller, in his paper on the oxidation of ammonia in flames (Reference 20), shows NO as an important intermediate (and product) leading to the formation of  $\text{N}_2$ . For example, such reactions as

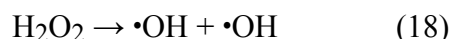
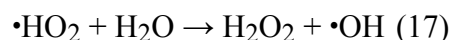


all play a major role in the formation of the nitrogen final product. In our study we never

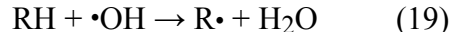
observed NO as an end product in the oxidation of N<sub>2</sub>H<sub>4</sub>. The lower temperatures in the SCWO reactor vs. that of a flame do not promote the formation of NO. We therefore postulate that N<sub>2</sub>H<sub>4</sub> oxidizes primarily by OH radical abstraction of hydrogen atoms. The oxidizer, hydrogen peroxide, supplies O<sub>2</sub> to the reaction by quickly reacting in warm water by reaction 15



The initiation step is probably reaction 2, the cleavage of the weak N–N bond of hydrazine. The following three elementary steps are responsible for the formation of a large hydroxyl radical pool:



These hydroxyl radicals proceed to abstract hydrogen atoms from nitrogen-containing intermediates, eventually forming nitrogen. The abstraction reaction is



where R is N<sub>2</sub>H<sub>3</sub>, N<sub>2</sub>H<sub>2</sub>, N<sub>2</sub>H, etc., as seen in Figure 34, page 72. Since neither H<sub>2</sub> nor NH<sub>3</sub>/NH<sub>4</sub><sup>+</sup> was observed in this reaction, the OH radical abstraction of hydrogen atoms from all radicals is probably the dominant pathway. Formation of H<sub>2</sub> and NH<sub>3</sub> is suppressed by reaction of •NH<sub>2</sub> and H• with •OH. Hydroxyl radical abstraction of hydrogen atoms may also be faster than H<sub>2</sub>N–NH<sub>2</sub> bond cleavage, suppressing NH<sub>2</sub> radical formation. The oxidation of hydrazine with hydrogen peroxide in SCW reactors appears to be an excellent method for its destruction, producing only the benign products N<sub>2</sub> and H<sub>2</sub>O.

#### c. Hydrazine Reactions with Nitric Acid

Nitrogen tetroxide (N<sub>2</sub>O<sub>4</sub>) is an oxidizer typically used with hydrazine and UDMH in liquid-fueled rockets. It would be convenient to use N<sub>2</sub>O<sub>4</sub> as the oxidizer in the SCWO process since it is stored close proximity to the fuel. However, nitrogen tetroxide disproportionates into nitric and nitrous acids (HNO<sub>3</sub> and HNO<sub>2</sub>) when placed in water. Therefore, the use of nitric and nitrous acid as oxidizers in reactions with hydrazine is essentially equivalent to the use of

N<sub>2</sub>O<sub>4</sub> as the oxidizer in aqueous solution. This section describes our results using nitric acid (HNO<sub>3</sub>) and isotopically labeled nitric acid (H<sup>15</sup>NO<sub>3</sub>) to oxidize hydrazine in SCW.

Table 22, (page 69) shows the mass balance results when using normal HNO<sub>3</sub> as the oxidizer for the destruction of hydrazine in SCW. All the conditions were identical with the previous experiments discussed (600°C, 340 atm, 11-sec residence times) except that in this case we used only a 0.25-wt% hydrazine feed solution. A major difference in the HNO<sub>3</sub> combustion chemistry was immediately noticed. Nitrous oxide gas was produced in large quantities (approximately 20% of the gas-phase effluent) in stark contrast to oxidation with hydrogen peroxide, where the only product was nitrogen. The nitrogen mass balance obtained was good (Table 22, page 69) and hydrazine was destroyed with >99.9992% efficiency. Virtually no NO<sub>3</sub><sup>-</sup> remained in the liquid effluent and only 0.2% of the starting nitrogen ended up as NO<sub>2</sub><sup>-</sup>. Equimolar mixtures of N<sub>2</sub>H<sub>4</sub> and HNO<sub>3</sub> were used in this experiment. The results show that this case is slightly fuel lean. We might expect much higher liquid effluent concentrations for fuel:oxidizer ratios less than one. However, since hydrazine was destroyed to relatively benign products, excess oxidizer is unnecessary.

A global reaction equation that comes close to predicting the product distribution is given in equation 20. Table 26 shows the actual product distributions normalized to the starting hydrazine concentration.



TABLE 26. HYDRAZINE + HNO<sub>3</sub> PRODUCT RATIOS

	N <sub>2</sub>	N <sub>2</sub> O	O <sub>2</sub>
expected	1.2	0.3	.1
actual	1.17	0.31	0.03

To investigate further this new chemistry with the NO<sub>3</sub><sup>-</sup> oxidizer, an identical experiment was run using the <sup>15</sup>N isotopically substituted HNO<sub>3</sub>. This compound was obtained from Aldrich at a concentration of 40 wt% in water and 98% isotopic purity. Since the objective of this experiment was to follow the nitrogen, we did not attempt to measure mass balance. Mass spectroscopy and FTIR spectroscopy provided the definitive diagnostics for comparison between the H<sup>14</sup>NO<sub>3</sub> and H<sup>15</sup>NO<sub>3</sub> experiments.



Figure 35 is the mass spectrum between  $m/z$  0 and 50 of the gas effluent from the  $\text{H}^{14}\text{NO}_3$  experiment. This spectrum can easily be simulated using known cracking patterns for  $\text{N}_2$  and  $\text{N}_2\text{O}$  (which are instrument dependent) and the measured  $\text{N}_2:\text{N}_2\text{O}$  gas ratio. Table 27 presents a qualitative analysis of the mass spectra.

Figure 36 is the mass spectrum for the  $\text{H}^{15}\text{NO}_3$  experiment. Table 27 also assigns these peaks. First note that the  $^{14}\text{N}:^{15}\text{N}$  ratio in this experiment was 2:1, from the equimolar starting ratio of hydrazine and isotopic nitric acid. As expected, this 2:1 ratio was preserved in the mass spectrum of the products as seen from the ratios of mass numbers 14 and 15 ( $^{14}\text{N}:^{15}\text{N}$ ) or the mass numbers 28 and 29 ( $^{14}\text{N}^{14}\text{N}:^{14}\text{N}^{15}\text{N}$ ). Second, almost all of the nitrous oxide formed was labeled with one  $^{15}\text{N}$  ( $m/z$  45), *i.e.*, one of the nitrogens came from nitric acid. Third,  $m/z$  28 and 29 have nearly the same integrated area when the small contribution from  $^{14}\text{N}^{15}\text{NO}$  cracking is subtracted. This implies two reaction pathways of comparable magnitude leading to the formation of nitrogen.

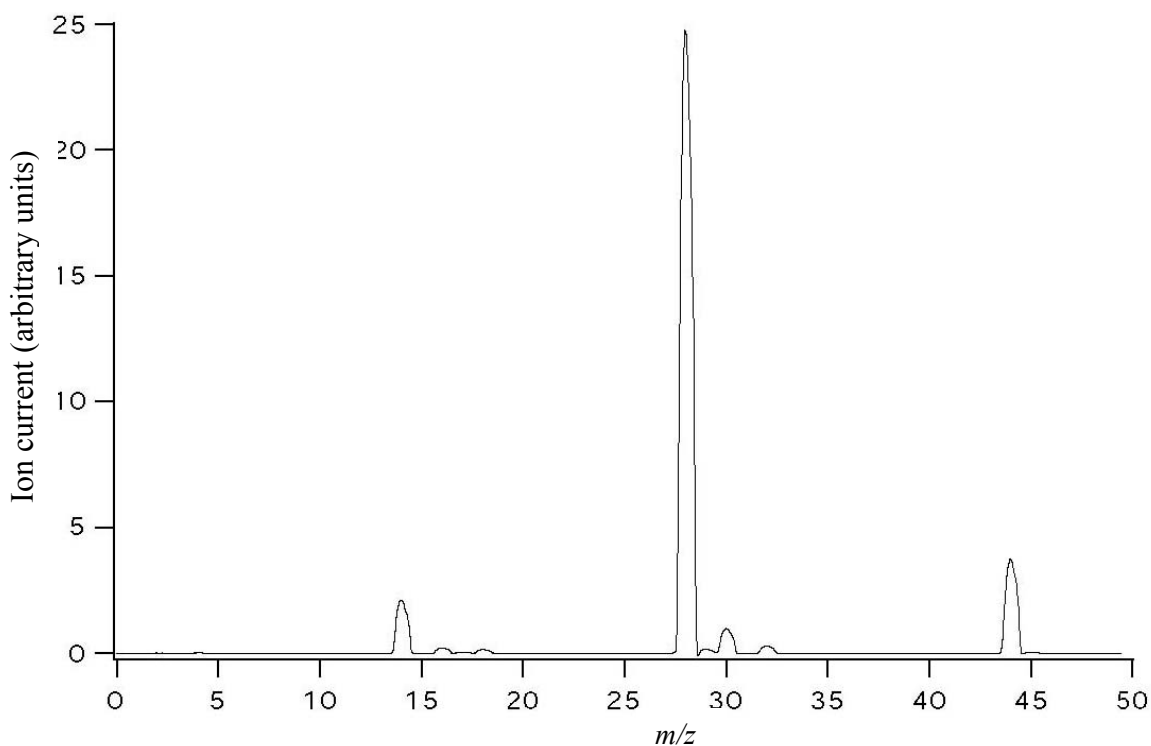
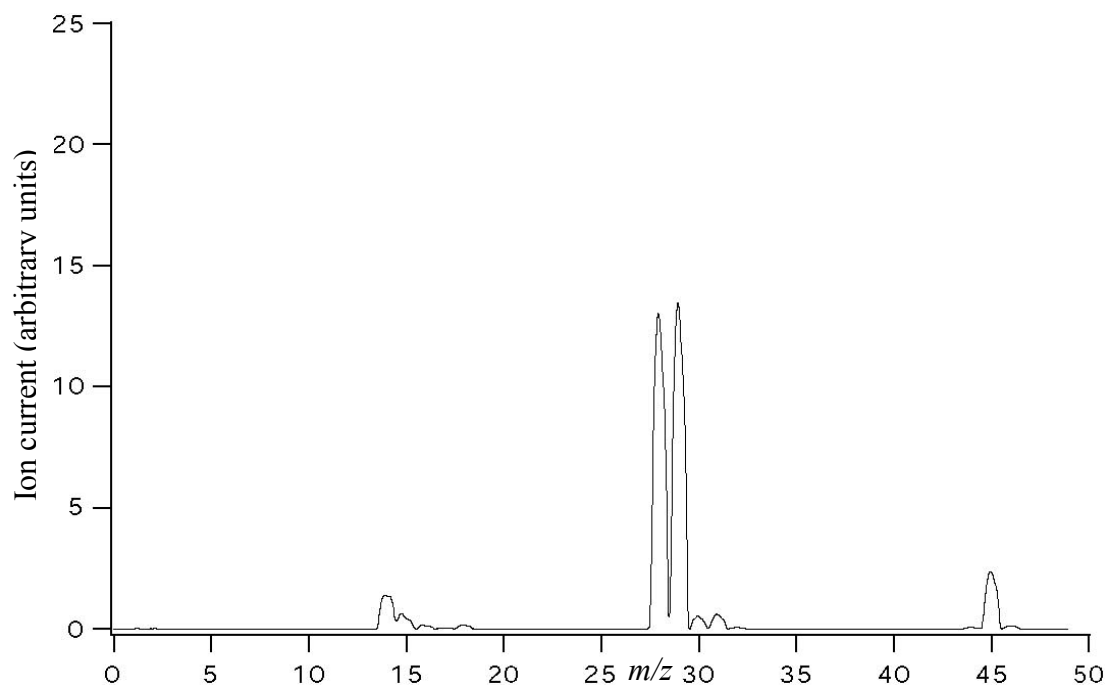


Figure 35. Mass spectrum of gas effluent resulting from SCWO of hydrazine with  $\text{H}^{14}\text{NO}_3$

TABLE 27. MASS SPECTRAL ASSIGNMENTS OF FIGURES 35 AND 36

Mass Number	Assignment N = $^{14}\text{N}$	Comments
14	N	Cracking from $\text{N}_2$ and $\text{N}_2\text{O}$
15	$^{15}\text{N}$	Isotopic N cracking from $\text{N}_2$ and $\text{N}_2\text{O}$
16	O	Cracking from $\text{O}_2$
17	OH	Cracking from water
18	$\text{H}_2\text{O}$	Residual reactor water
28	$\text{N}_2$	$\text{N}_2$ parent peak and cracking from $\text{N}_2\text{O}$
29	$\text{N}^{15}\text{N}$	Isotopic $\text{N}_2$ and cracking from $\text{N}_2\text{O}$
30	$\text{NO}$ , $^{15}\text{N}_2$	Cracking from $\text{N}_2\text{O}$ or isotopic $\text{N}_2$
31	$^{15}\text{NO}$	Isotopic NO cracking from $\text{N}_2\text{O}$
32	$\text{O}_2$	Excess oxygen from reactor
44	$\text{N}_2\text{O}$	$\text{N}_2\text{O}$ parent peak
45	$\text{N}^{15}\text{NO}$ / $^{15}\text{NNO}$	Isotopic $\text{N}_2\text{O}$
46	$^{15}\text{N}_2\text{O}$	Isotopic $\text{N}_2\text{O}$

Figure 36. Mass spectrum of the gas effluent resulting from the SCWO of hydrazine with  $\text{H}^{15}\text{NO}_3$ .

We can determine explicitly that we have  $^{14}\text{N}^{15}\text{N}^{16}\text{O}$  and not  $^{15}\text{N}^{14}\text{N}^{16}\text{O}$  from the FTIR spectra, Figures 37 and 38. Figure 37 covers the entire infrared spectrum of the gas effluent and compares the SCWO of hydrazine with  $\text{H}^{14}\text{NO}_3$  (a) and  $\text{H}^{15}\text{NO}_3$  (b). The only infrared-active gas was  $\text{N}_2\text{O}$  after subtraction of trace quantities of  $\text{CO}_2$  due to the combustion of char from previous experiments. Each vibrational mode in Figure 37b exhibits an isotopic shift consistent with a  $^{14}\text{N}^{15}\text{N}^{16}\text{O}$  molecule (Reference 21). Figure 38a is the spectrum expanded around the  $01^10-00^00$  Q-branch region of  $\text{N}_2\text{O}$ . If any  $^{15}\text{N}^{14}\text{N}^{16}\text{O}$  existed it would appear near the arrow drawn in the bottom trace. This implies that the N–O bond in nitric acid stays intact during the formation of nitrous oxide. There are small amounts of  $^{14}\text{N}^{14}\text{N}^{16}\text{O}$  and  $^{15}\text{N}^{15}\text{N}^{16}\text{O}$  in the mass and FTIR spectra, indicating that other minor reaction channels do exist.

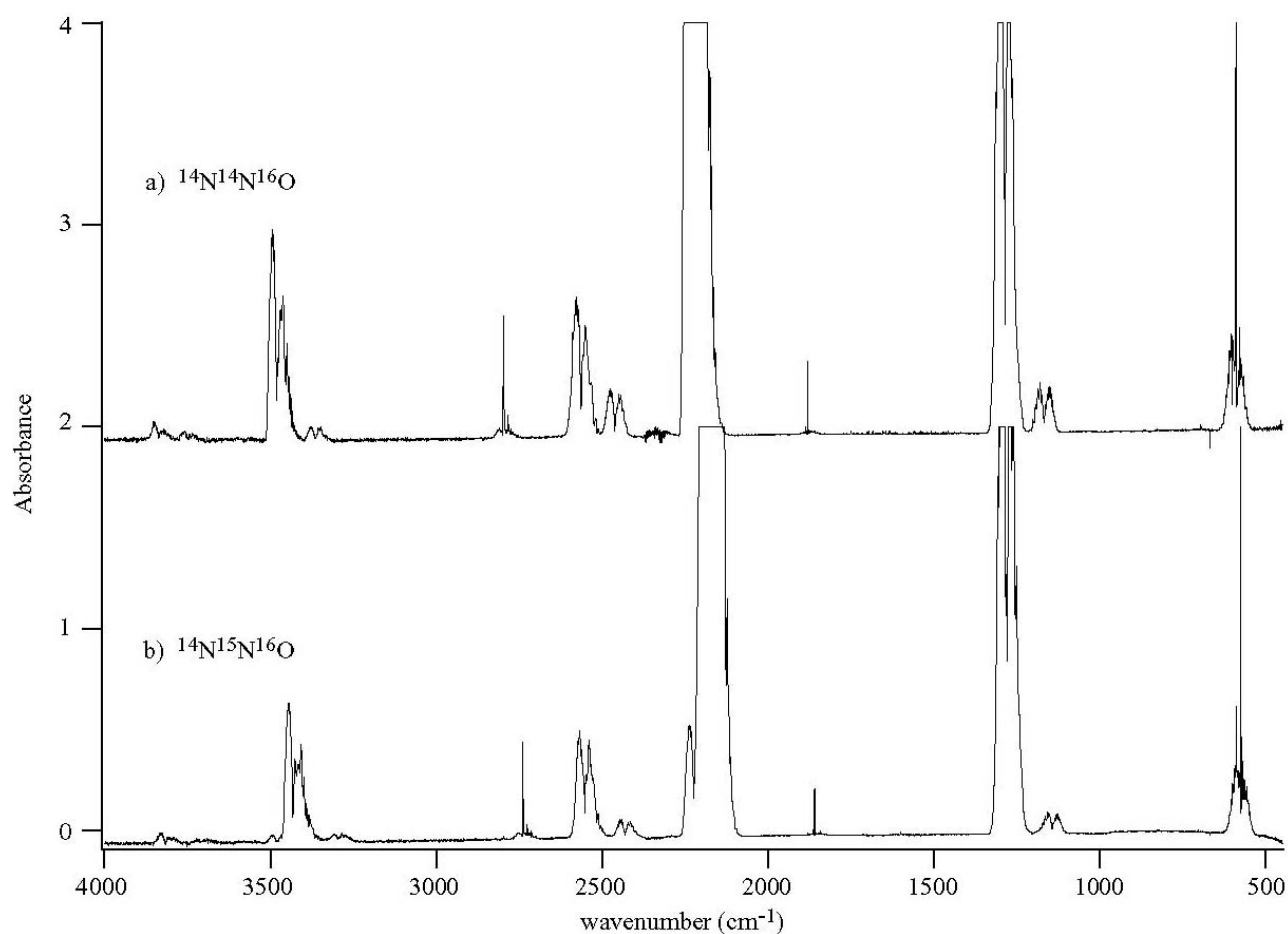
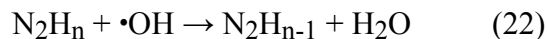
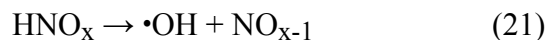


Figure 37. FTIR spectrum of gas effluent from a) SCWO of hydrazine with  $\text{H}^{14}\text{NO}_3$  and b) SCWO of hydrazine with  $\text{H}^{15}\text{NO}_3$ . These spectra show only nitrous oxide ( $\text{N}_2\text{O}$ ).

The oxidation of hydrazine with nitric acid seems to be very complex. One possible explanation for the observed reaction products may be a reaction scheme such as



where the sequence would start with  $\text{HNO}_3$  producing hydroxyl radicals and  $\text{NO}_2$ . The hydroxyl radicals would feed into the  $\text{N}_2\text{H}_4$  oxidation mechanism as discussed previously, again inhibiting the  $\text{H}_2\text{N}-\text{NH}_2$  bond cleavage favoring hydrogen abstraction leading to the formation of  $\text{N}_2$  [in this case  $^{14}\text{N}^{14}\text{N}$ ]. The  $\text{NO}_2$  could either react as in reaction 23, or go into a different reaction loop that also acts to abstract the hydrogen

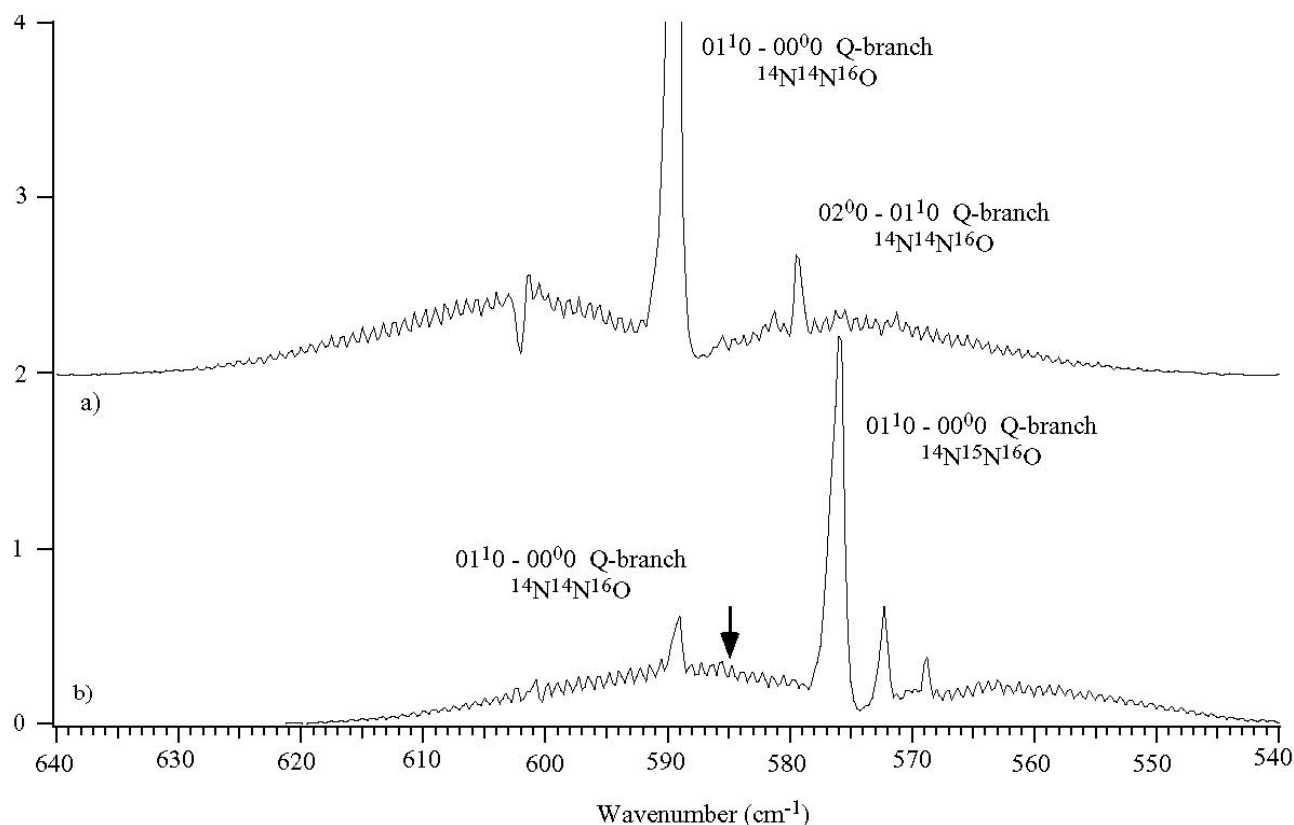
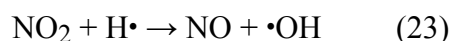
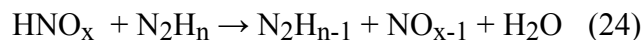
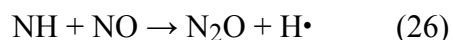


Figure 38. Expansion of  $01^{10}-00^{00}$  Q-branch region around  $600\text{ cm}^{-1}$  of Figure 37. The arrow indicates where  $^{15}\text{N}^{14}\text{N}^{16}\text{O}$  species would appear if it were present in the sample.

atoms from hydrazine (reaction 25). Summing reactions 21 and 22 gives the general reaction 24. The chemical cycle represented by reactions 24 and 25 would ultimately



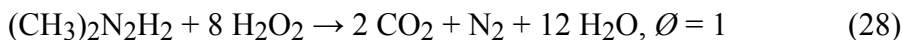
produce  $^{15}\text{NO}$  and again  $^{14}\text{N}^{14}\text{N}$ . The labeled NO would form the  $^{14}\text{N}^{15}\text{N}$  and  $^{14}\text{N}^{15}\text{NO}$  products observed in the mass spectrum by reactions such as



Nitrous oxide may also react by numerous pathways to form  $^{14}\text{N}^{15}\text{N}$ . If this reaction had been carried out for longer times it is possible that all the  $\text{N}_2\text{O}$  would have been converted to  $\text{N}_2$ . This oxidizer (and therefore  $\text{N}_2\text{O}_4$ ) may also be an excellent choice for the conversion of hydrazine into benign products. Experiments reacting hydrazine with nitrous acid ( $\text{HNO}_2$ ) have yet to be explored.

#### 4. Unsymmetrical Dimethylhydrazine Reactions

Experiments investigating the destruction of UDMH in SCW included UDMH added to hydrogen peroxide at different stoichiometric ratios. One pyrolysis experiment (no oxidizer) was done, but unidentified, and perhaps undesirable products resulted, so these experiments were discontinued. As with hydrazine, these experiments did not exceed twice stoichiometric as defined by the following reaction equations.



Tables 28 and 29 summarize the product analyses of these experiments. Figure 39 compares the FTIR spectra of these two experiments. Apparently the reaction as written in equation 28 is not sufficient to cause complete combustion. Although the carbon was oxidized to  $\text{CO}_2$  with good efficiency (Table 29), the nitrogen balance was very low. We suspect, based on the cation HPLC analysis, that there may also be mono or dimethyl amines remaining in the liquid effluent, in

TABLE 28. UNSYMMETRICAL DIMETHYLHYDRAZINE NITROGEN MASS BALANCE (AS A % OF STARTING NITROGEN CONCENTRATION)

Species	H <sub>2</sub> O <sub>2</sub> , Ø = 1	H <sub>2</sub> O <sub>2</sub> , Ø = 0.5
N <sub>2</sub>	60.8	100.3
N <sub>2</sub> O	0.3	1.1
NH <sub>3</sub>	not quantified	0
NO	detected (FTIR)	0
NH <sub>4</sub> <sup>+</sup>	0.8	0
NO <sub>3</sub> <sup>-</sup>	0.7	1.8
NO <sub>2</sub> <sup>-</sup>	0.2	0.5
Total	62.8	103.7

TABLE 29. UNSYMMETRICAL DIMETHYLHYDRAZINE CARBON MASS-BALANCE (AS A % OF STARTING CARBON CONCENTRATION)

Species	H <sub>2</sub> O <sub>2</sub> , Ø = 1	H <sub>2</sub> O <sub>2</sub> , Ø = 0.5
CO <sub>2</sub>	96.1	91.7
CO	0.2	0
CH <sub>4</sub>	0.5	0
TIC	1.7	1.2
TOC	<0.03	<0.03
Total	98.5	92.9

addition to unquantified ammonia gas. With the addition of excess oxidizer the reaction is driven to completion, the major products being N<sub>2</sub> and CO<sub>2</sub>. Tables 30 and 31 show the exact product ratios. An important point is that dimethyl nitrosamine ((CH<sub>3</sub>)<sub>2</sub>NNO<sub>2</sub>) was not observed in any oxidation runs of UDMH. Destruction efficiencies were 99.9998% or better (Table 21, page 68).

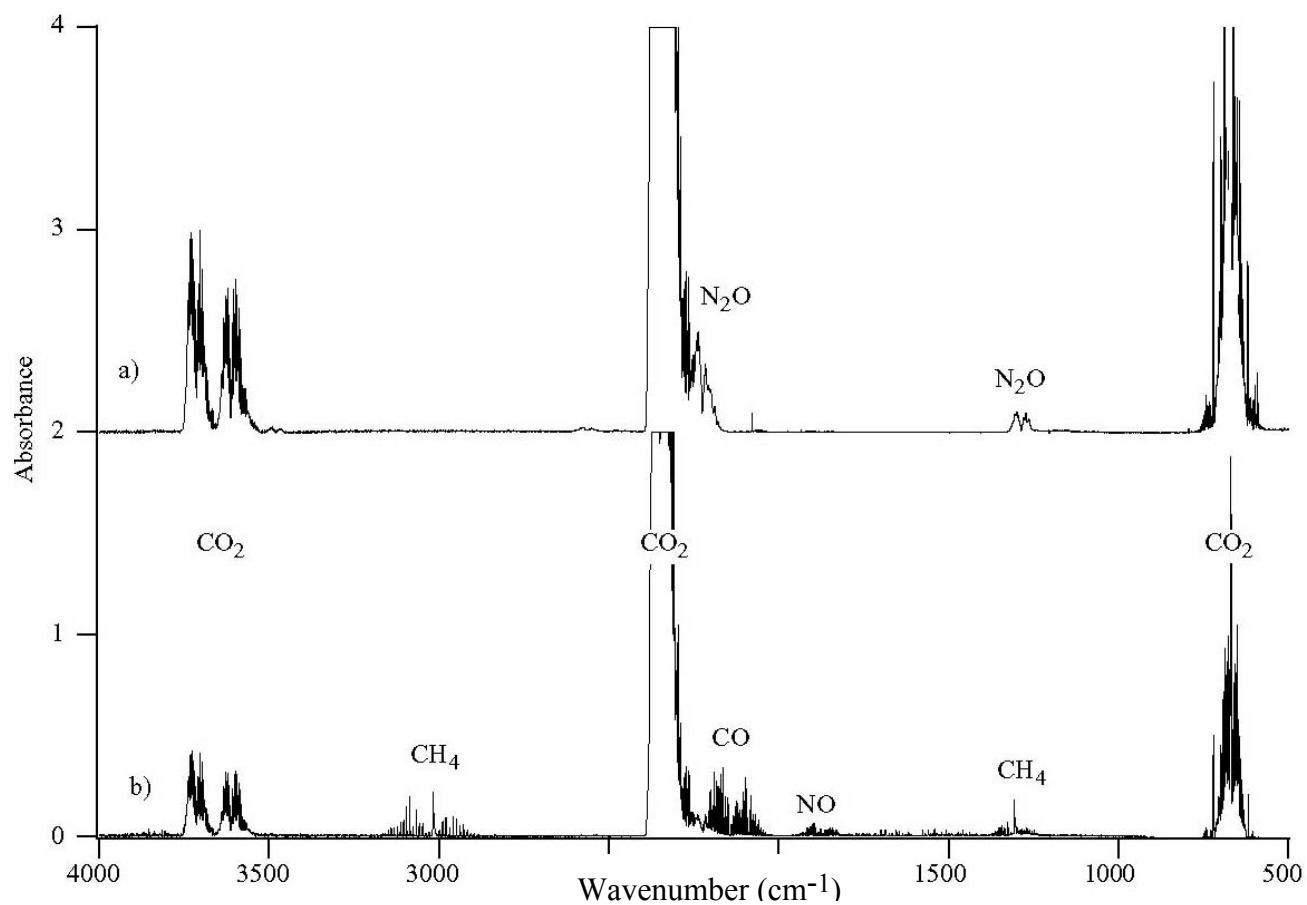


Figure 39. FTIR spectrum of gas effluent from a) SCWO of UDMH with  $\text{H}_2\text{O}_2$  based on reaction equation 29 (fuel lean), and b) SCWO of UDMH with  $\text{H}_2\text{O}_2$  based on reaction equation 28.

TABLE 30. PRODUCT RATIO NORMALIZED TO THE STARTING  $(\text{CH}_3)_2\text{N}_2\text{H}_2$  CONCENTRATION,  $\phi = 1$

	$\text{CO}_2$	$\text{N}_2$
expected	2	1
actual	1.92	0.61

TABLE 31. PRODUCT RATIO NORMALIZED TO THE STARTING  $(\text{CH}_3)_2\text{N}_2\text{H}_2$  CONCENTRATION,  $\phi = 0.5$

	$\text{CO}_2$	$\text{N}_2$	$\text{O}_2$
expected	2	1	4
actual	1.83	1.01	4.06

## 5. Conclusion

Supercritical water oxidation techniques are ideally suited for destroying hydrazine and UDMH hazardous wastes. Destruction efficiencies better than 99.999% were routinely observed, and with the addition of suitable oxidizers the major products were environmentally benign, ( $\text{N}_2$ ,  $\text{CO}_2$  and water). No hazardous or carcinogenic products were produced. Because of their miscibility with water in all proportions, large throughput may easily be obtained, making scaleup easier. Plugging and corrosion were not a problem in the gold-lined reactor.

## H. REACTIONS OF NITROGLYCERIN (NG)

### 1. Introduction

Safety regulations at LANL forbid the handling of neat nitroglycerin (NG). Consequently, we studied the reactions of NG in supercritical water by means of an extraction process that did not require the direct handling of pure NG. Our approach was to use supercritical  $\text{CO}_2$  ( $\text{SCCO}_2$ ) as an inert solvent to extract NG from a triple-base propellant, M31A1E1. This propellant is 18% (by weight) NG, 22% nitrocellulose (NC) and 55% nitroguanidine (NQ). We have shown that NG can be preferentially extracted from M31A1E1 in  $\text{SCCO}_2$ , leaving the insoluble NC and NQ behind. After extraction into supercritical  $\text{CO}_2$ , the NG was directly injected into a SCW reactor for processing.

### 2. Supercritical $\text{CO}_2$ Extraction/Injection Apparatus

The apparatus used for supercritical  $\text{CO}_2$  extraction and subsequent injection into the supercritical water reactor is shown in Figure 40. A cylinder of  $\text{CO}_2$  equipped with a liquid delivery tube supplied the  $\text{CO}_2$ . A heat exchanger cooled the high-pressure liquid (1000 psi) to approximately  $0^\circ\text{C}$ . The pressure was then boosted to operating levels (4000–6000 psi, well above the critical pressure of 1073 psi) in a constant-flow, high-performance liquid



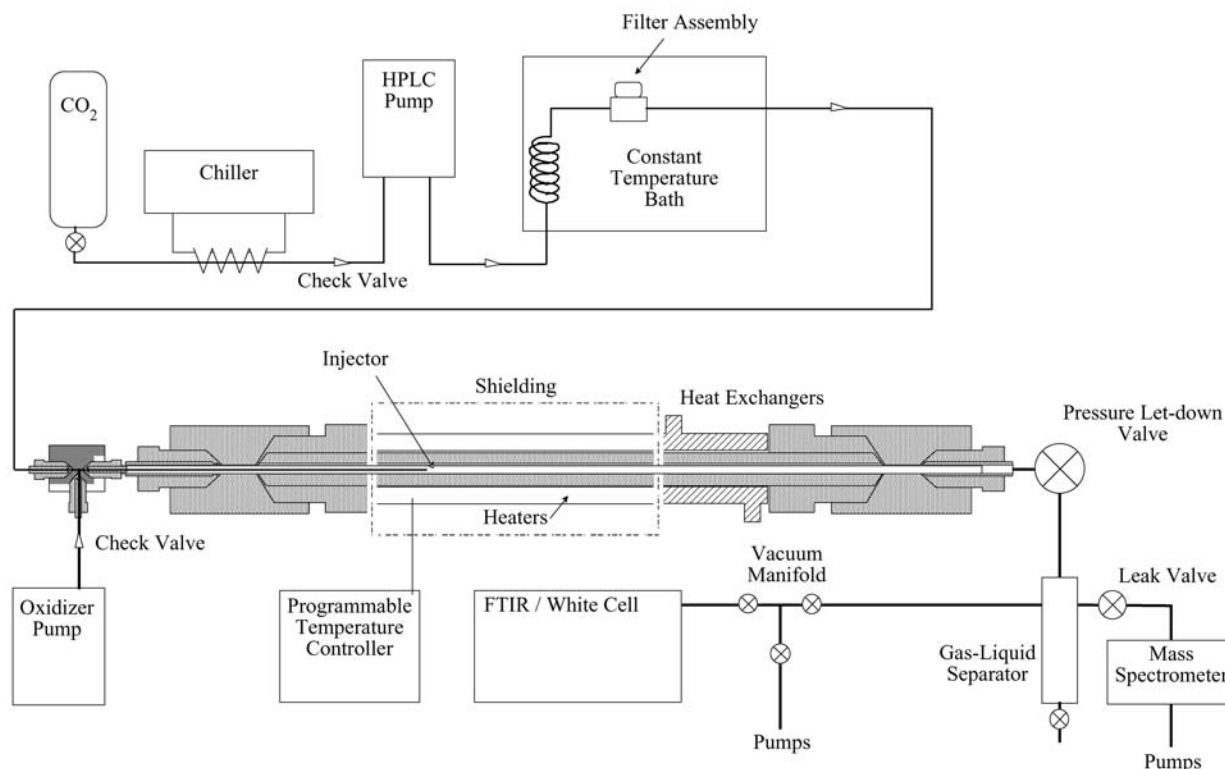


Figure 40. Schematic of SCCO<sub>2</sub> extraction apparatus coupled to the linear flow reactor.

chromatography pump (LDC Analytical, Constametric 3200) with cooled heads. The high-pressure CO<sub>2</sub> was pumped through a heat exchanger submerged in a constant-temperature bath held above the critical temperature of CO<sub>2</sub> (31°C), typically at 44 °C. The supercritical CO<sub>2</sub> passed through a filter assembly containing the material to be extracted, approximately 200 mg of the propellant. This solution was then injected into the SCW reactor. A check valve between the extractor and SCW reactor prevented backflow of water. Water and oxidizer were pumped separately so that the relative concentrations of all components could be varied independently.

Solubility experiments were performed with an apparatus having essentially the same front end, but with a pressure-letdown valve and a trap instead of a SCWO reactor on the back end. Liquid CO<sub>2</sub> was pumped with a HPLC pump through a heat exchanger that heated it above the critical temperature. The pressure from the pump to the pressure letdown valve was held above the critical pressure (1073 psi). The SCCO<sub>2</sub> was pumped through the extraction cell, a metal thimble with a 7- $\mu$ m frit, that contained approximately 200 mg of the propellant. The pressure was reduced to less than 100 psi at the valve, and dissolved material precipitated in the trap. A steel-ball float flowmeter monitored flow rate of gaseous CO<sub>2</sub> as it exited the system.

### 3. Supercritical CO<sub>2</sub> Extraction of Nitroglycerin

The solubility of nitroglycerin in supercritical CO<sub>2</sub> was examined by extraction of M31A1E1 and subsequent analysis of the soluble and insoluble components. A 207-mg sample of propellant flakes was extracted for about 6 hours with SCCO<sub>2</sub> at a temperature of 40 °C and a pressure of approximately 3700 psi. The liquid CO<sub>2</sub> was pumped at a rate of 0.45 mL/min. When the experiment was terminated, the extraction cell contained 164 mg of propellant residue, indicating that 21% by weight had been extracted. The yellow liquid extract was found to have collected mostly in the tubing between the pressure letdown valve and the trap.

The identities of the extracted and unextracted components were determined by proton nuclear magnetic resonance (<sup>1</sup>H NMR). Each organic component of M31A1E1 is clearly identifiable in the spectrum of M31A1E1 shown in Figure 41:  $\delta$  7.66 (singlet), NQ;  $\delta$  7.0 (two triplets), EC;  $\delta$  5.77 (septet), NG;  $\delta$  4.9 (quartet), NG;  $\delta$  4.20 (triplet), DBP;  $\delta$  4.0 (broad singlet), NC;  $\delta$  1.6, 1.35 (two multiplets), DBP;  $\delta$  0.89 (multiplet), EC, DBP. The <sup>1</sup>H NMR spectrum of the extracted material is shown in Figure 42. It is clear from this spectrum that supercritical CO<sub>2</sub> preferentially extracts nitroglycerin and the two binder materials DBP and EC. These components comprise 22.5% by weight of M31A1E1, consistent with the weight fraction extracted. The <sup>1</sup>H NMR spectrum of the undissolved residue is shown in Figure 43. This

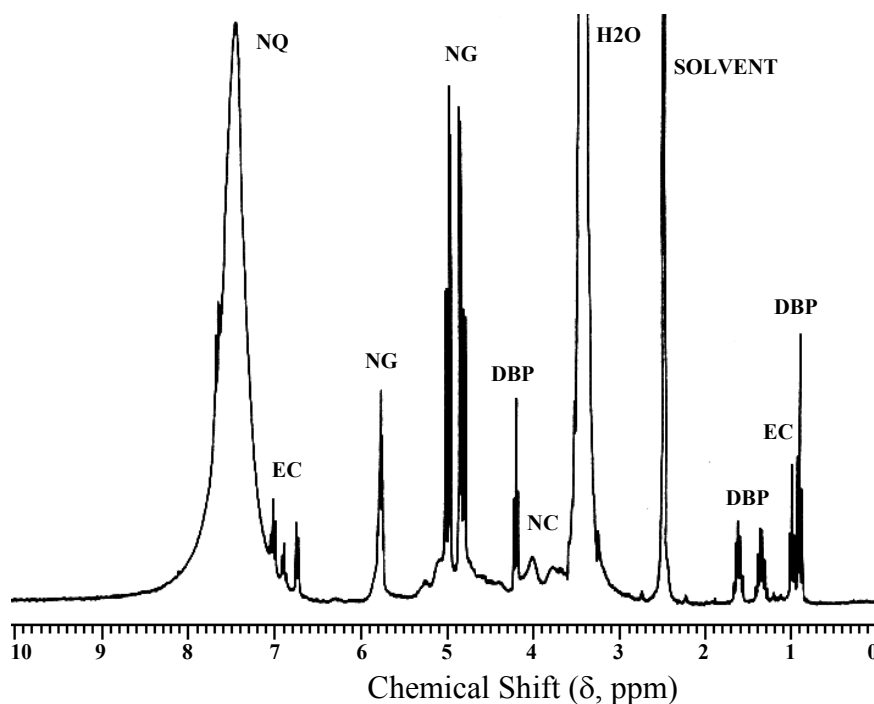


Figure 41. <sup>1</sup>H NMR of a solution of M31A1E1 in DMSO-*d*<sub>6</sub>.

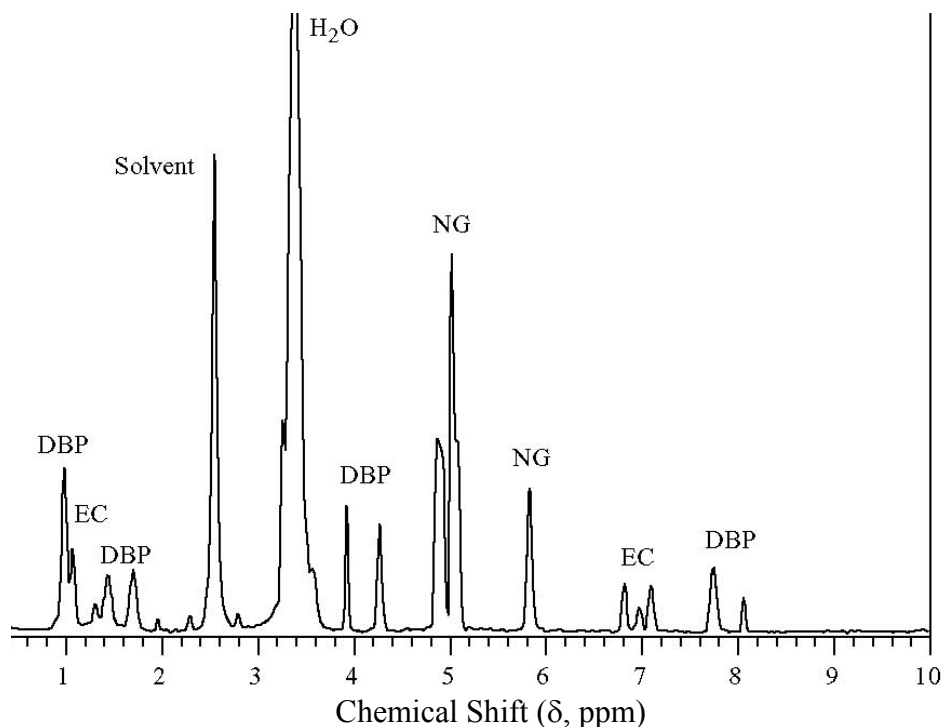


Figure 42.  $^1\text{H}$  NMR of extracted material from supercritical  $\text{CO}_2$  extraction of M31A1E1.

spectrum accounts for all of the organic components that were not extracted, including nitrocellulose and nitroguanidine.

These data show that nitroglycerin and the EC and DBP binders are quantitatively extracted in  $\text{SCCO}_2$ . The actual solubilities of the extracted components in  $\text{SCCO}_2$  could not be determined from these experiments because the rate of extraction was not measured.

Experiments on the combined  $\text{SCCO}_2$  extraction/SCWO of nitroglycerin, however, indicate that these components are very soluble and are extracted very rapidly (less than 10 minutes under the conditions employed). It is not surprising that the major components of M31A1E1 are not soluble in  $\text{SCCO}_2$ . Nitroguanidine is highly polar and not likely to be soluble in the relatively nonpolar solvent  $\text{SCCO}_2$ . Nitrocellulose is a medium-molecular-weight polymer that also requires a more-polar solvent such as DMSO to solubilize it.

A potential safety hazard was observed in these extraction experiments. Extracted nitroglycerin tends to drop out of solution and accumulate in the tubing between the pressure letdown valve and the trap. This is the region of the extractor where the pressure is decreased

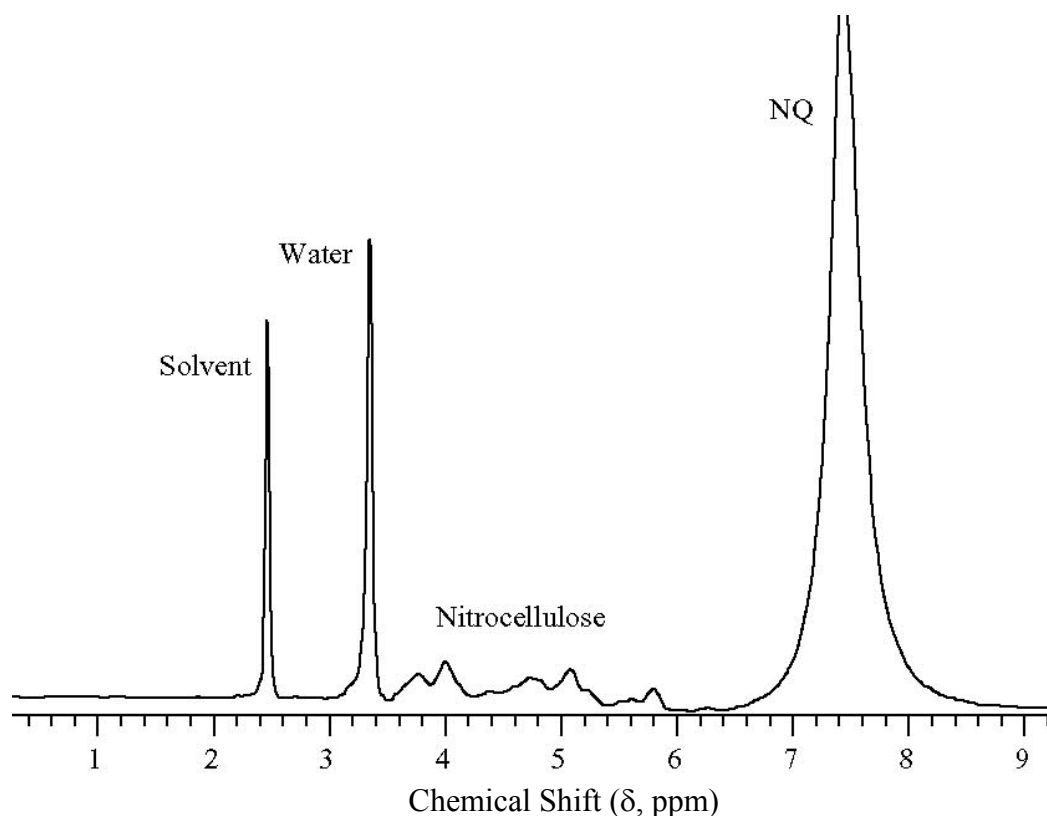


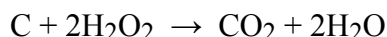
Figure 43.  $^1\text{H}$  NMR of residual (unextracted) material from supercritical  $\text{CO}_2$  extraction of M31A1E1.

below the critical pressure.  $\text{CO}_2$  expands rapidly in this region, probably producing substantial cooling. Hence, NG may accumulate in this tube near the letdown valve. The tube attaches at both ends with threaded high-pressure fittings. Accumulation of NG in the tube could lead to contamination of the threads or sealing cones and possible detonation during assembly/disassembly. Because of the unpredictable nature and sensitivity of NG, we determined that this extractor was unsafe and performed no further extraction experiments with this apparatus.

#### 4. SCW Processing of $\text{SCCO}_2$ -Extracted Nitroglycerin

Nitroglycerin extracted from M31A1E1 in  $\text{SCCO}_2$  was processed in supercritical water using the apparatus shown in Figure 40, page 84. The nitroglycerin was extracted as described previously, then injected directly into the heated region of a linear flow SCW reactor. All reactions were conducted in a gold-lined reactor to prevent interferences from corrosion reactions. Reactions were conducted at  $550^\circ\text{C}$ , 5000 psi and 4 mL/min flow rate (11-s residence time), conditions which were known from previous results in our laboratories to result in complete oxidation of all carbon present. Hydrogen peroxide was used as the oxidant; a dilute

solution was pumped independently and mixed in the cold region prior to injection into the reactor. A 30-fold excess of oxidant was used based on the following chemical reaction:



The carbon concentration was calculated from the composition of the extracted material determined from previous extraction experiments.

Data obtained for runs with two different flow rates of a solution of the SCCO<sub>2</sub> extract are presented in Table 32. Analytical results for carbon and nitrogen products were obtained from TOC/TIC, ion chromatography and FTIR analyses. Gaseous products were analyzed by FTIR. One of the major nitrogen products, N<sub>2</sub>, has no infrared-active vibration; it was qualitatively observed by gas chromatography. The major C product, CO<sub>2</sub>, was concealed by solvent CO<sub>2</sub> introduced during the extraction step. Undetected species (below detection limits, typically <100 ppb) include NO, NO<sub>2</sub> and CO. An observation not reported in the data in Table 32 is the rate of appearance of these products in the reactor effluents. Approximately 90% of each of the products in the aqueous effluent was observed in the first 40-mL sample taken subsequent to initiation of the extraction/SCWO process. This indicates that the extraction occurs very rapidly, primarily within the first 10 minutes (10–30 mL of CO<sub>2</sub> flowed through the extractor). This corresponds to a concentration of NG in SCCO<sub>2</sub> of up to 4 mg/mL.

TABLE 32. COMBINED SCCO<sub>2</sub> EXTRACTION/SCWO TREATMENT OF M31A1E1

Product	3mL/min <sup>a</sup>	1mL/min <sup>a</sup>
	mg (%) <sup>b</sup>	mg (%) <sup>b</sup>
TOC	0.7 (9)	0.02 (0.2)
TIC	4.4 (59)	0.7 (9)
NO <sub>3</sub> <sup>-</sup>	24.4 (36)	15.2 (21)
NO <sub>2</sub> <sup>-</sup>	2.3 (4)	1.5 (3)
N <sub>2</sub> O	10.6 (43)	na

<sup>a</sup>CO<sub>2</sub> flow rate; other reaction conditions: gold-lined reactor, 550 °C, 5000 psi, 4 mL/min H<sub>2</sub>O flow, 30-fold excess H<sub>2</sub>O<sub>2</sub>.

<sup>b</sup>Percent of initial carbon or nitrogen occurring as specified product; starting weight of M31A1E1 ~200 mg; extracted N ~ 16 mg; extracted C ~ 8 mg.

It is clear from the results presented in Table 32 that the extracted nitroglycerin was destroyed in the SCW reactor. The organic carbon content of the reactor effluent is reduced to 9 and 0.2% of the starting C concentration for the two flow rates, respectively. In other words, 91 and 99.8% of the starting C present as NG is converted into  $\text{CO}_2$  or  $\text{CO}_3^-$ , depending on the flow rate. It is interesting that at the faster  $\text{CO}_2$  flow rate (*i.e.*, shorter reaction time), the reaction does not go to completion, leaving about 9% of the organic carbon incompletely oxidized. In addition, more of the C is left in solution as inorganic carbon (carbonate or bicarbonate) at faster flow rates. The major nitrogen products are  $\text{N}_2\text{O}$  and  $\text{NO}_3^-$ .

These results are consistent with previous results for the supercritical water oxidation of such energetic materials as HMX, RDX and TNT. NG was completely destroyed and the carbon was converted into  $\text{CO}_2$  or inorganic carbon. The nitrogen was primarily converted into  $\text{N}_2\text{O}$  and  $\text{NO}_3^-$ . The high nitrate content of the products is a consequence of the strongly oxidizing nature of these reactions, given the large (30-fold) excess of oxidant. With other energetic materials we have shown that nitrate production can be reduced by using a 1:1 stoichiometry of oxidant to carbon.

## SECTION IV

### INCREASING THROUGHPUT OF EXPLOSIVES

Three approaches were explored for increasing the throughput of bulk explosives in a SCWO reactor. These include the introduction of the explosive as a slurry, the use of a cosolvent, and the pretreatment of explosives by hydrolysis.

#### A. REACTIONS OF SLURRIES

One of the simplest methods to continuously feed high concentrations of explosives into a supercritical water reactor is as a slurry of small particles ( $< 100\ \mu\text{m}$ ) in water. This method presents potential safety hazards because it requires mechanical pumping and heating of comparatively large amounts of solid explosive entrained in water. An explosion could occur if sufficient material collects or settles in the reactor feed tubes. In addition, the operation of the SCWO reactor could be difficult to control if the rate of reaction of the explosive depends strongly on particle size or morphology. In this section, we report on experiments and calculations designed to characterize the behavior of small particles in high-temperature water and to help evaluate the hazards associated with processing slurries of explosives.

##### 1. Small Bomb Calorimeter Experiments

Initial experiments with the optically accessible reactor studied slurries of 1,3,5-triamino-2,4,6-trinitrobenzene (TATB), chosen for its inertness and high deflagration temperature,  $T_d = 384\ ^\circ\text{C}$ , which is above the critical temperature of water. Slurries of TATB, 5 to 20 percent by weight, were loaded by syringe into the reactor, which was then sealed and pressurized to about 200 atmospheres. The temperature was then slowly ramped ( $\sim 200\ ^\circ\text{C}/\text{hour}$ ) up to a maximum of  $600\ ^\circ\text{C}$ . A total of five such experiments were conducted with no sudden temperature or pressure surges (our sampling rate is 10 per second) that would characterize deflagration. Calculations based on the known volume of gases produced in a TATB detonation suggest that the expected magnitude of the pressure rise for a deflagration would have been observable in these experiments. In general, the images obtained during these runs were somewhat obscured by the high light scattering of the slurry. In all of the runs, however, the TATB was observed to disappear gradually as the temperature approached  $300\ ^\circ\text{C}$ , well below

the deflagration and critical temperatures. It is possible that the TATB is dissolving at this temperature. At higher temperatures, the TATB appears to decompose, leaving only a slight (insoluble) tar and other organics dissolved in the aqueous effluent upon cooling.

Quantitative measurements of temperature and pressure changes caused by reactions of slurries as they were heated were made in the batch reactor (Figure 11, page 21). The reactor volume was adjusted to 200  $\mu\text{L}$  to permit the use of small quantities of material. Milligrams of explosive were added to 100  $\mu\text{L}$  of water to make a slurry of 5–20 percent explosive by weight. The balance of the reactor volume was air. A computer recorded the pressure and temperature of the reactor at one-second intervals as the reactor temperature was increased in a controlled ramp. The pressure rise due to reaction of the explosive was determined by obtaining a baseline pressure rise using an equal quantity of water with no explosive. This pressure difference gives a measure of both the extent and rate of reaction of the explosive. Figure 44 shows results

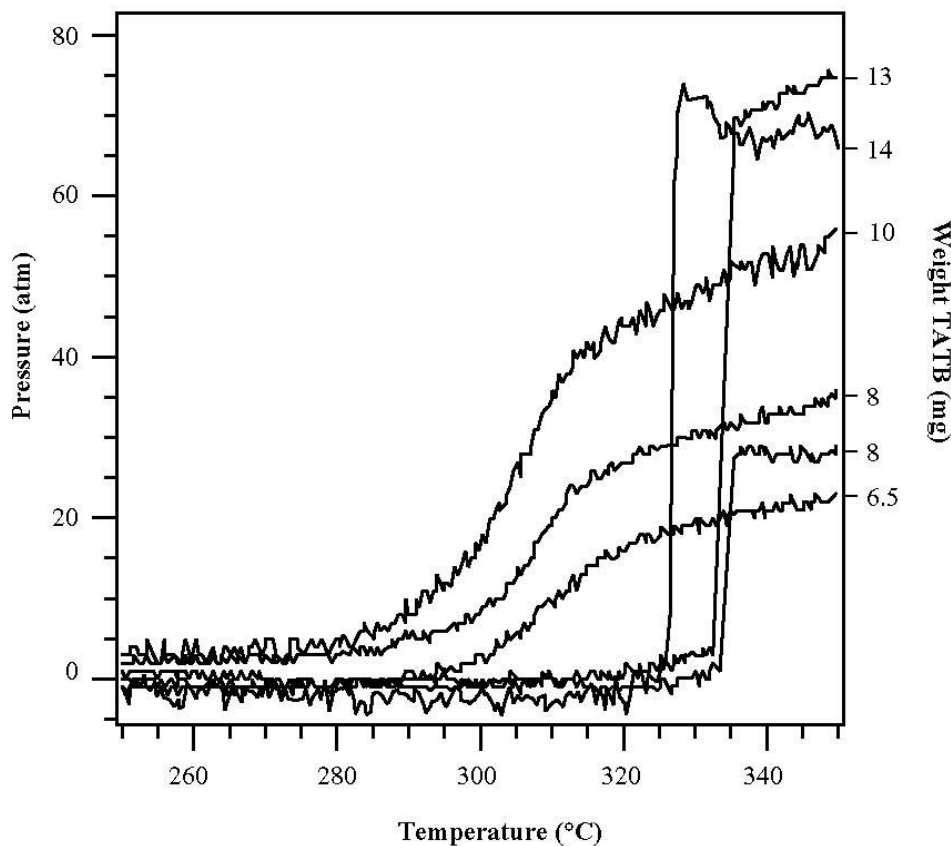


Figure 44. Pressure rises observed due to reactions of TATB slurries in Water as a function of temperature and starting concentration. Background pressures have been subtracted.



for the behavior of TATB as it is heated. It is interesting to note that while the deflagration temperature of TATB is 384 °C, reaction begins at significantly lower temperatures (300-330 °C). These measurements are in agreement with the qualitative observations made in the optically accessible reactor. For quantities of TATB less than 10 mg (10 percent by weight), the reaction is generally slow, requiring more than 30 seconds to reach a constant pressure (complete reaction). Quantities greater than 13 mg always yielded a sudden pressure rise, which occurred in less than our one-second time resolution. One exception was a run with 8 mg of TATB that also showed a sudden pressure rise. This behavior may depend on the degree of dispersion of the solid in the water. The slurry was not stirred, and some settling or clumping of the "wet" TATB could have occurred. These results indicate that the behavior of slurries may be unpredictable and that above certain concentrations the slurry can react very rapidly. Such uncertainties raise concerns about using slurries in supercritical water reactors.

In contrast, similar experiments performed with a double-base propellant (DBP, nitroglycerin/nitrocellulose), shown in Figure 45, show no unpredictable behavior. Reactions were performed with slurries composed of up to 16 percent by weight of the DBP. Slow pressure releases (reactions) were observed in every case; however, further studies are required to insure that this is generally true. A run made without the addition of water is also shown to demonstrate the rapid reaction (deflagration) that occurs under these conditions.

A series of experiments was also carried out on HMX slurries in a 1-mL constant-volume reactor. The cell pressure was monitored as the temperature was gradually increased. The results of these experiments with HMX are shown in Figure 46. For a 1% HMX slurry in water, the pressure started to increase as the temperature approached 200°C and then stabilized near 240°C. For 5% HMX in water, the pressure also sharply increased as temperature was increased above 200°C, followed by a similar plateau region. However, near the critical temperature, the pressure exhibited a second sharp increase, as shown in Fig. 46. For both these runs, the pressure contribution due to water was subtracted to reflect the effect of HMX decomposition and subsequent heat up of product gases in the supercritical water environment.

For comparison, the decomposition of dry HMX in air in the same cell is also shown in this figure. Near 260°C, HMX undergoes an extreme pressure increase from 200 to 650 psi. This reflects the spontaneous decomposition of HMX. Clearly the HMX decomposition reaction is moderated by the presence of water as reflected in the more moderate pressure increases from 200 to 400°C. Reaction products are also different for the two reactions as shown in Table 33.

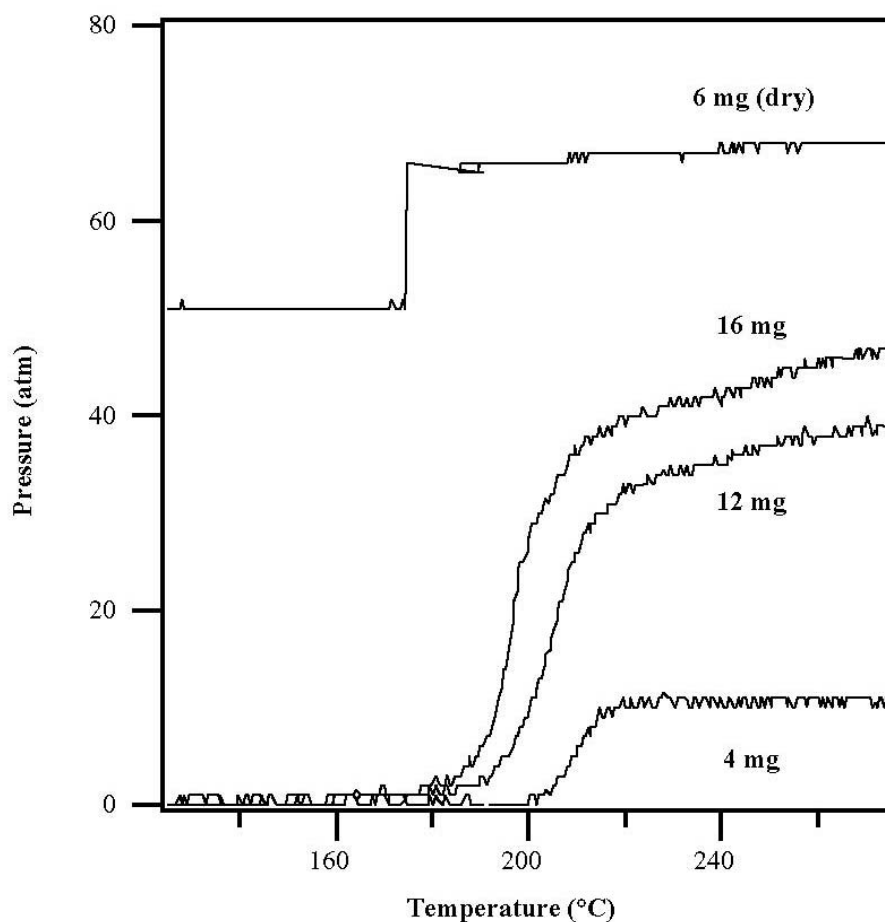


Figure 45. Pressure rises observed due to reaction of DBP slurries in water, as a function of temperature and starting concentration. Background pressure rises have been subtracted

TABLE 33. MASS SPECTROMETRIC ANALYSIS OF HMX DECOMPOSITION PRODUCT GASES

Dry HMX (wt/wt %)		5% HMX in H <sub>2</sub> O (wt/wt %)	
N <sub>2</sub>	73%	N <sub>2</sub>	62%
O <sub>2</sub>	18%	CO <sub>2</sub>	27%
CO <sub>2</sub>	3.8%	N <sub>2</sub> O	7.6%
H <sub>2</sub>	2.8%	O <sub>2</sub>	2.3%
CO	1.4%	H <sub>2</sub>	1.0%

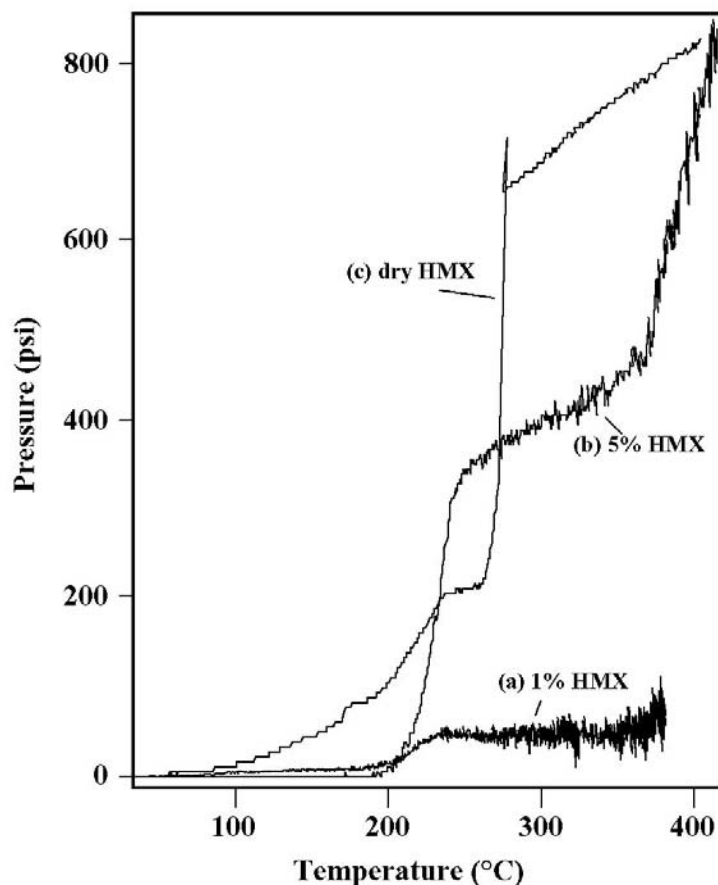


Figure 46. HMX decomposition pressure as a function of temperature. 1% HMX in water, (b) 5% HMX (80 mg) in water, and (c) 80 mg HMX dry.

As seen in Table 33, the dry decomposition of HMX produces primarily nitrogen and oxygen in the gas phase, with a trace of  $\text{CO}_2$ ,  $\text{H}_2$ , and  $\text{CO}$ . In contrast, the wet decomposition yields a significant amount  $\text{CO}_2$  and  $\text{N}_2\text{O}$  in place of much of the oxygen, and virtually no  $\text{CO}$  forms.

## 2. Slurry Flow Experiments in One-Gallon-per-Hour Reactor

A series of tests were initiated to evaluate the effectiveness of the one gallon per hour reactor system, described in Section II.E, for pumping explosive slurries. For safety reasons, initial tests were done with melamine in place of the explosive. The melamine simulates many of the physical properties of the granular explosive, but without the high chemical reactivity. Like HMX, melamine is relatively insoluble in water and has a density of  $1.6 \text{ g/cm}^3$ , which is similar to that of HMX,  $1.8 \text{ g/cm}^3$ .

Water slurries containing 1 to 10 percent by weight melamine were pumped through this reactor, both under ambient conditions and at nominal process conditions (550°C, 3700 psi, and an oxygen flow of 4 slm) that are more typical for chemical destruction. The reactor tube remained free flowing throughout all the runs. However, using the initial pump and reactor inlet configuration shown in Figure 47 (a), significant plugging was observed at both the pump inlet and the pressure letdown valve. The settling of particles in the pump clogs the check valves (both inlet and outlet). With these check valves inoperative, the slurry pumping rate dropped to virtually zero. To alleviate plugging at the pump inlet, a second small recirculating pump was added to the system, as shown in Figure 47 (b). The Little Giant pump recirculated the feed at a flow rate of approximately 3 gal/min. Even with the recirculating pump, slurries of 100  $\mu\text{m}$  melamine still plugged the pump inlet. However, decreasing the particle size to 50  $\mu\text{m}$  alleviated this problem. Decreasing the particle size decreases their overall settling rate. However, even with the decreased particle size, plugging at the pressure letdown valve was still observed. Because the melamine is far less reactive than typical explosive compounds, the required reactor residence time is probably longer than our present design allows. Consequently, we do not believe that plugging of the letdown valve will be a problem when HMX or other explosive slurries are used, since the explosive particles should all be destroyed before reaching this valve.

We also explored the use of viscosity enhancers to slow the settling rate of particles in the slurries. Sodium carboxymethylcellulose (CMC) was chosen as a suitable viscosity enhancer for these experiments. The first questions to be addressed involved whether the CMC could be pumped through the system, and whether it would be destroyed by the SCWO process. A 1% solution of CMC was successfully pumped through our reactor system under cold conditions, indicating that increased viscosity would not limit the overall system flow rate. Under SCWO conditions at approximately 400°C, the CMC gum was not completely mineralized, as the effluent stream was brown and had a bad odor. Higher temperatures of 580 °C appeared to destroy all of the CMC additive, but no comprehensive product analysis was performed. We attempted to pump 10% melamine in a 1% CMC–water mixture under cold conditions. The letdown valve closed up very fast (within 4 minutes). Significant settling occurred at the inlet. The effective settling rate is difficult to accurately quantify. Nevertheless, based on our observations, the settling rate for 10% melamine in 1% CMC gum/99% water appeared to be approximately half as bad as the 3% melamine mixture in water.

Experiments were also conducted to determine if an actual HMX slurry could be safely and effectively pumped using our present apparatus. A 3-percent by weight slurry of fine

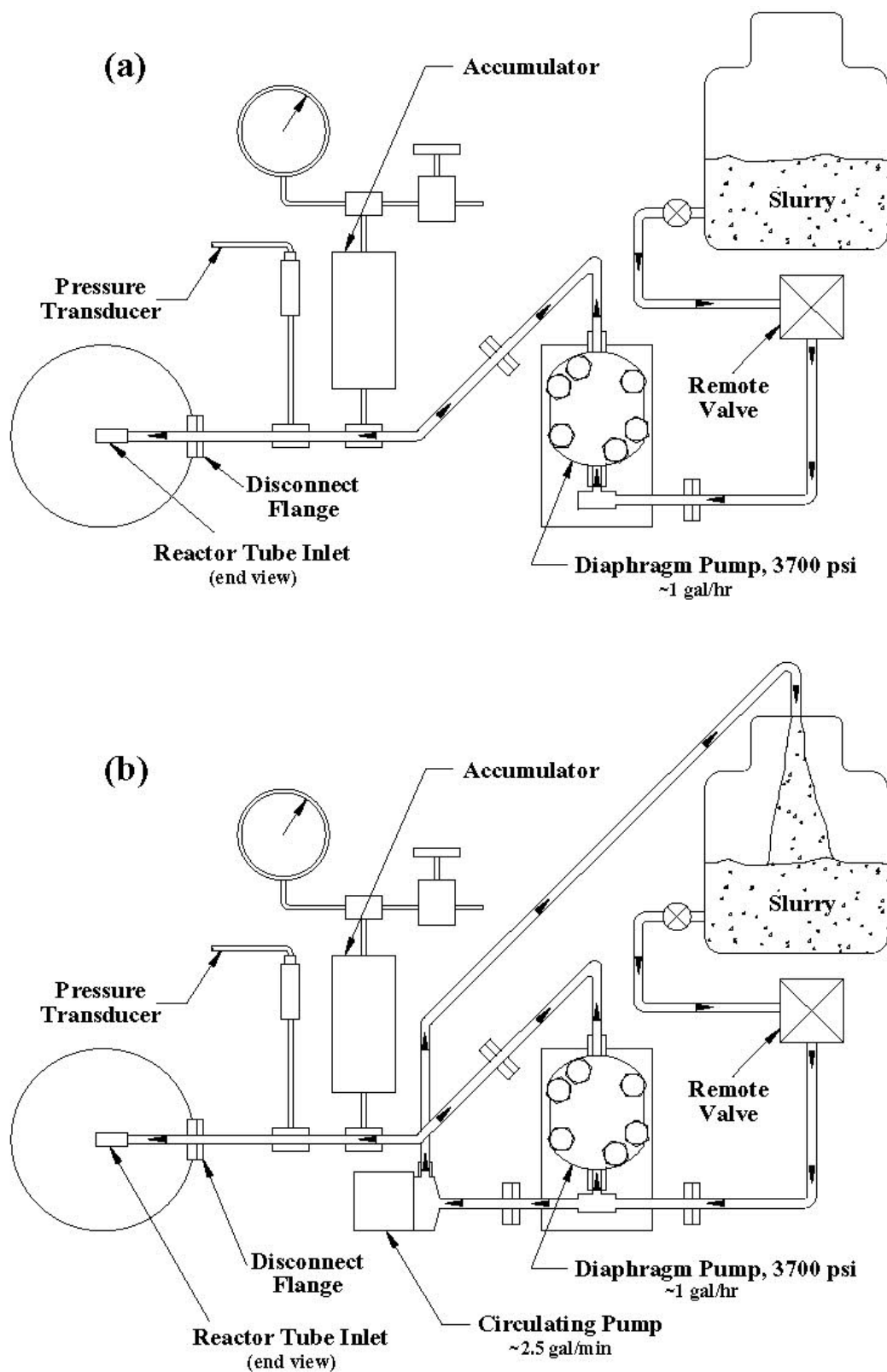


Figure 47. Pumping unit and reactor inlet. (a) original configuration;  
(b) with circulating pump added.

HMX (98 % of the particles are smaller than 44  $\mu\text{m}$ ) was employed in these experiments. The apparatus was the same as used for the melamine experiments discussed above, except that the heated reactor tube was replaced with a filter manifold, since the purpose of these experiments was to evaluate the pumping system rather than to measure the destruction efficiency. This filter manifold, which consisted of six filters, each 5  $\mu\text{m}$  in size, was placed directly upstream of the letdown valve to prevent contamination of the letdown valve. The previous studies with melamine had shown that the letdown valve would plug if any solids were to reach this valve. In addition, a system vent valve was placed upstream of both the filter manifold and letdown valve. This valve allowed remote venting of the system from high to ambient pressure if either the letdown valve or the filter manifold was plugged. Special flanges were also designed and added to allow the disconnection of the system in a potentially HE contaminated environment. These flanges were of conflat-type design, except that two concentric viton *O*-rings were used as the sealing surface instead of a copper gasket and a knife edge on the flange.

In the actual test, deionized water was pumped for  $\sim 30$  minutes to establish steady state conditions. The Lewa diaphragm pump was pressurized to 3700 psi and the flow was set at 1 gal/hour. The flow was then switched from deionized water to a two-gallon slurry reservoir of 3 percent HMX in deionized water. A small Giant pump recirculated the slurry at the pump inlet, as was done with the melamine slurry, to prevent plugging at the inlet. When flow was switched to the 3 percent HMX slurry, the pressure remained steady, indicating smooth flow of the slurry. Approximately seven minutes after switching to the HMX slurry, however, pressure began to build up. The letdown valve was opened up to compensate for the increased pressure, but this proved to be ineffective, indicating that the filter manifold or the letdown valve was fully plugged. To further demonstrate that indeed either the letdown valve or the filter manifold (or both) had plugged, flow was then switched through the system vent. The HMX slurry flowed freely through the system vent, but was not under pressure since the letdown valve was bypassed.

In previous experiments, the melamine slurry used to simulate HMX plugged the filter manifold in approximately 18 minutes. Two possible scenarios exist to explain why HMX plugged sooner than melamine. First, since the same filter manifold was used in the HMX experiment and the previous melamine experiment, some residual melamine may have remained. The second explanation is that the particle size of HMX was smaller than the melamine, and a small amount of HMX of less than 5  $\mu\text{m}$  in size may have passed through the filters to plug the

letdown valve. However, in either case, this experiment demonstrated that an HMX slurry can be effectively and safely pumped using our present Lewa pump system.

### 3. Particle Settling Calculations.

For a suspension of solids of size large enough to settle under gravity in a static fluid, horizontal transport in a pipe may involve any one of three flow regimes. These may be identified as: (1) saltation flow, in which the solid particles form dunes at the bottom of the conduit. At low fluid velocities, only the particles on the surface may be swept along in a bouncing motion called "saltation." This regime can result in unsteady or periodic behavior and plugging in worst cases. The dunes can move along the bottom if the fluid shear forces are large enough; (2) "heterogeneous" flow, in which settling occurs to some degree so that particles are not uniformly distributed over the flow field. Thus a solid density gradient may exist from top to bottom within the pipe. The minimum flow velocity required to sustain heterogeneous flow is designated as  $V_m$ ; (3) "homogenous" flow, in which fluid turbulence is high enough so that solids are uniformly distributed. The mixture can then often be treated as a single-phase non-Newtonian fluid. The fluid velocity required for homogenous flow is referred to as the critical velocity,  $V_c$ . Variables influencing the hydrodynamics of the suspension include particle shape, volume fraction of solids, particle size, and particle size distribution. In addition, solids wettability, surface charge, the ionic nature of the fluid, and the degree of turbulence will all play a role. While rigorous treatment of solids transport in the hydrothermal system is not feasible, empirical correlations can be employed to estimate  $V_m$ .

Most empirical correlations for  $V_m$  have a basis in dimensional analysis and give the Froude number (ratio of inertial to gravitational forces) as a function of the Reynolds number (ratio of inertial to viscous forces), ratio of particle to tube diameter, solid to fluid density ratio, and volume fraction of solids. Correlations may or may not include corrections to account for particle shape and size distributions. Of the many correlations available in the literature, only a few were selected for the present calculations. Emphasis was placed on widely used correlations and those which were regressed to data taken in relatively small diameter pipes and involving particle sizes in the range expected for slurried propellants. Perhaps the most widely used correlation for  $V_m$  is due to Durand (Reference 22) and is of the form

$$V_m = F [2 g D (s - 1)]^{0.5} \quad (1)$$

where  $g$  is the acceleration due to gravity,  $D$  is the nominal pipe diameter and  $s$  is the ratio of solid to fluid density. The parameter  $F$  is given graphically as a function of particle size and volume fraction solids. Spells' correlation (Reference 23) is of the form

$$\frac{V_m^2}{gd_{85}} = K \left( \frac{\rho_m V_m D}{\mu} \right)^{0.775} (s - 1) \quad (2)$$

with  $K = 0.0251$  and  $\rho_m = \rho[1 + V_s(s-1)]$ . Here  $\rho$  is the density of the carrier fluid,  $\mu$  the fluid viscosity, and  $V_s$  is the volume fraction solids. The quantity  $d_{85}$  is the particle diameter such that 85% by weight of the solid is smaller than  $d_{85}$ . Spells found that  $V_c$  was approximately 2.4 times greater than  $V_m$  and both could be estimated using the functional form of eq. (2), provided the constant  $K$  was suitably adjusted. Cairns et al. (Reference 24) focused on particle diameters in the 240–380  $\mu\text{m}$  range, in pipes of 1.9 to 5 cm diameter. Their correlation is of the form

$$\frac{V_m^2}{gd_{50}} = 9.8 \left( \frac{V_s D V_m \rho}{\mu} \right)^{0.3} (s - 1)^{0.6} \quad (3)$$

Here  $d_{50}$  is defined analogously to  $d_{85}$  above. When compared to other correlations, Durand's predictions were generally conservative, *i.e.*, they estimated a higher  $V_m$ . In virtually all cases examined, the data used in the regressions showed significant amounts of scatter. Thus, as a caveat, the correlations should not be regarded as highly accurate. Errors of  $\pm 25$ –30% can routinely be expected. Use of the correlations for gas-like carrier fluid densities may also be suspect, as the correlations were developed for liquid suspensions. Correlations for pneumatic transport of solids may be more accurate in such cases. Also, pipe diameters for the cases examined here are at the low end of those used in data correlation.

Calculations were performed using eqs. (1–3) for several particle sizes and loadings. For a selected particle size, the same value was used for  $d_{50}$  and  $d_{85}$  in the above correlations. This gives some indication of the effects of particle size distribution. Physical properties of the carrier fluid were assumed to be those of water at 450 °C and 3700 psia. Thus, the values  $\rho = 0.113 \text{ g/cm}^3$  and  $\mu = 3 \times 10^{-4} \text{ g/cm-sec}$  were used. Furthermore, the solid density was assumed to be  $\rho_s = 1.8 \text{ g/cm}^3$ , which is reasonable for HMX. For a fixed particle size of 50  $\mu\text{m}$  (*i.e.*,  $d_{50}$  or  $d_{85}$ ), calculations were performed for solids loadings of  $V_s = 0.03, 0.01$ , and 0.10. The predicted  $V_m$  values for these cases are shown in Figures 48–50 as a function of pipe diameter. Also shown



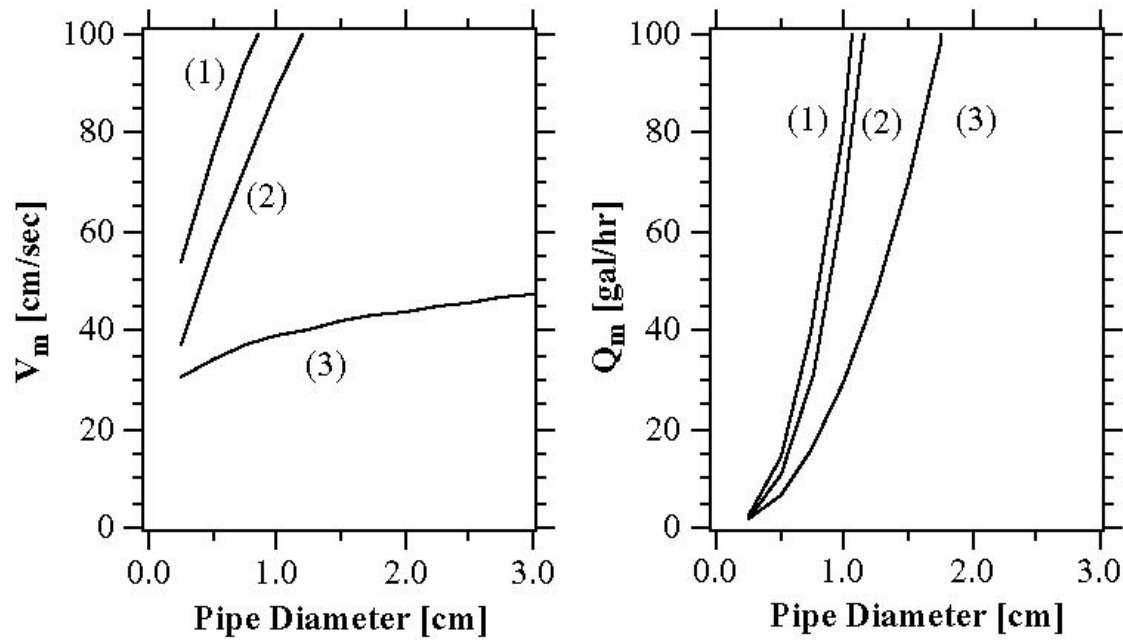


Figure 48. Predicted  $V_m$  and  $Q_m$  for  $V_s = 0.03$  and  $d = 50$  mm. The labels (1-3) correspond to eqs. (1-3).

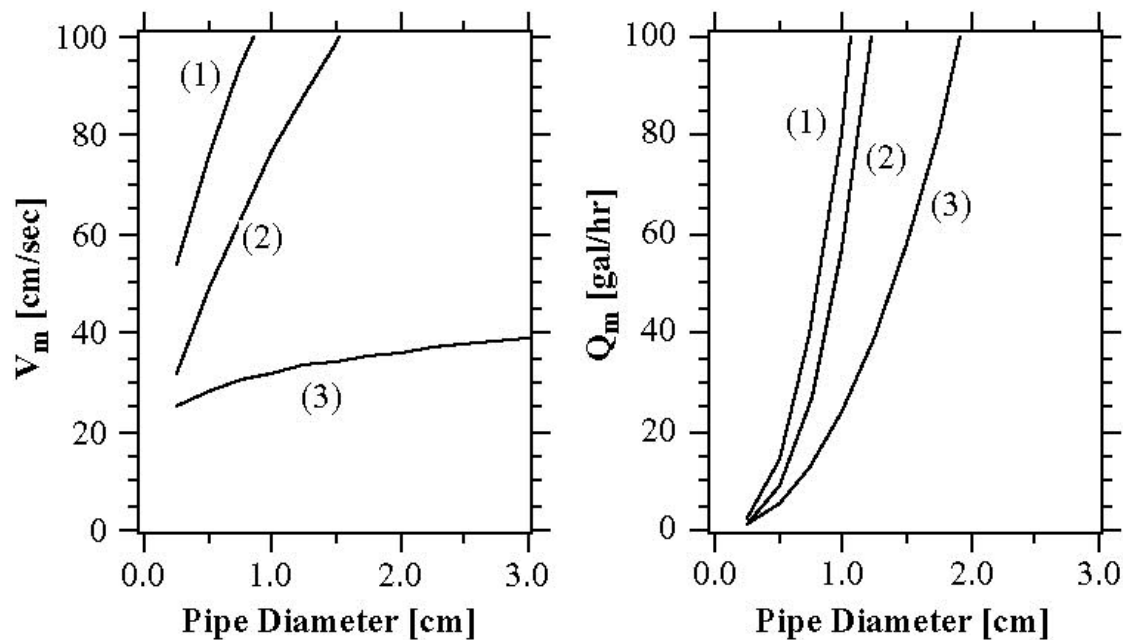


Figure 49. Predicted  $V_m$  and  $Q_m$  for a solids volume fraction of 0.01 and particle size of 50 mm. The labels (1-3) correspond to eqs. (1-3).

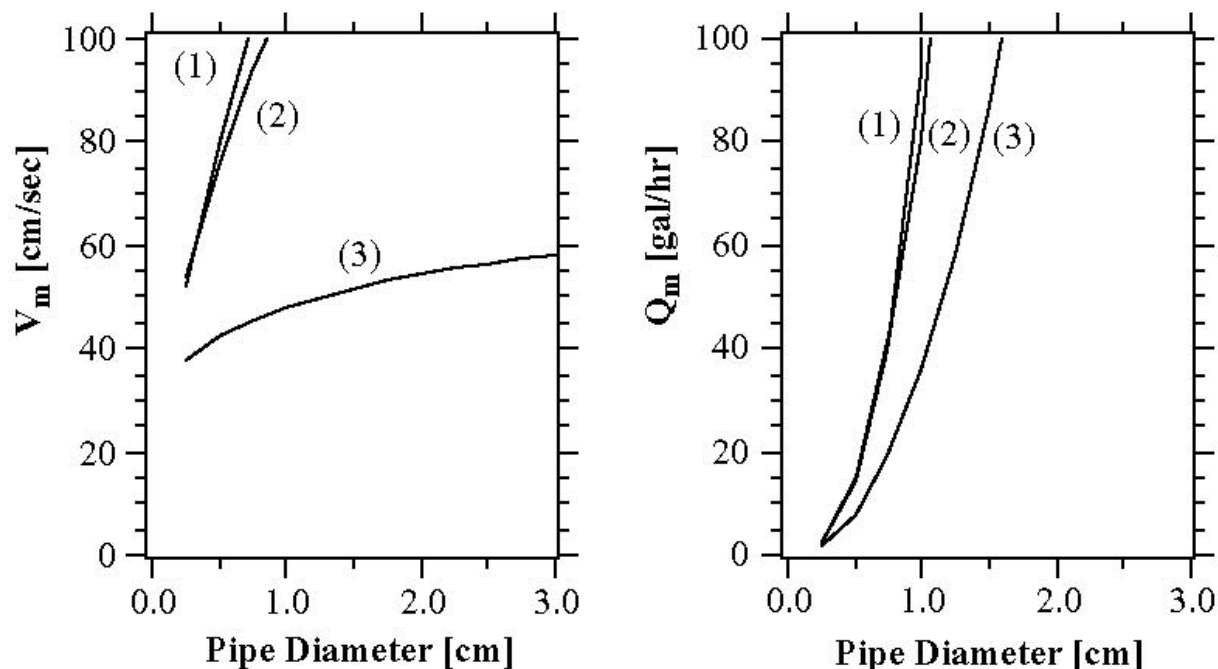


Figure 50. Predicted  $V_m$  and  $Q_m$  for  $V_s = 0.10$  and  $d = 50$  mm. The labels (1-3) correspond to eqs. (1-3).

is the corresponding volumetric flow rate,  $Q_m$ , in gallons per hour (gph). From these figures, we see that the required minimum flow velocity increases less than a factor of two for an order of magnitude increase in solids loading. Figures 51 and 52 show results obtained using a solids volume fraction of 0.03 and particle sizes of 150 and 300  $\mu\text{m}$ . A comparison of Figures 48, 51, and 52 shows that particle size is a more important parameter than solids loading. For a constant solids loading, a factor-of-six increase in particle size increases the required minimum flow velocity by roughly a factor of three. For the slurry pumping experiments discussed above, the particle size was 100  $\mu\text{m}$  and solids loading up to 0.10 were employed. For the reactor pipe id of 0.188 in. (0.5 cm), we estimate from the figures that a flow velocity of 40–90 cm/sec would be required to insure that the particles will not settle out of the flow in the reactor region. The actual flow velocity employed in these experiments was roughly 50–55 cm/sec in the reactor.

## B. INTRODUCTION OF EXPLOSIVES IN A CO-SOLVENT

The feasibility of dissolving explosives in a cosolvent for introduction at higher concentrations into the reactor was investigated. The linear reactor (Figure 15, page 27) allowed delivery of water-insoluble reactants that can be dissolved in a cosolvent and injected directly

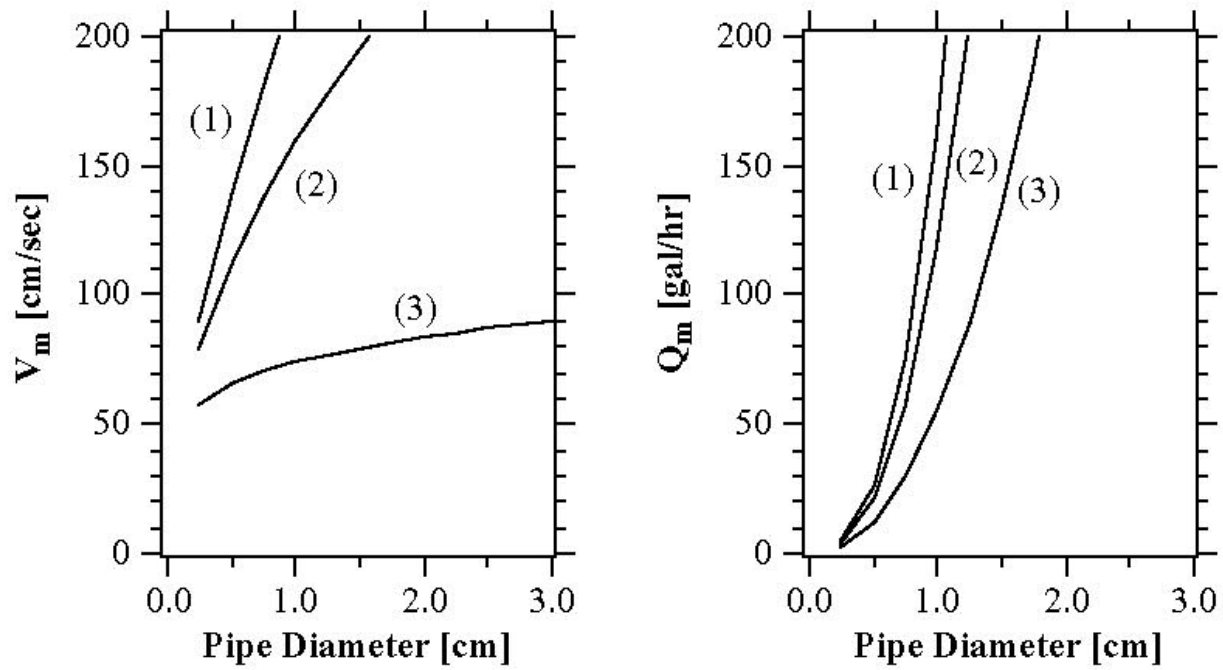


Figure 51. Predicted  $V_m$  and  $Q_m$  for  $V_s = 0.03$  and  $d = 150$  mm. The labels (1-3) correspond to eqs. (1-3).

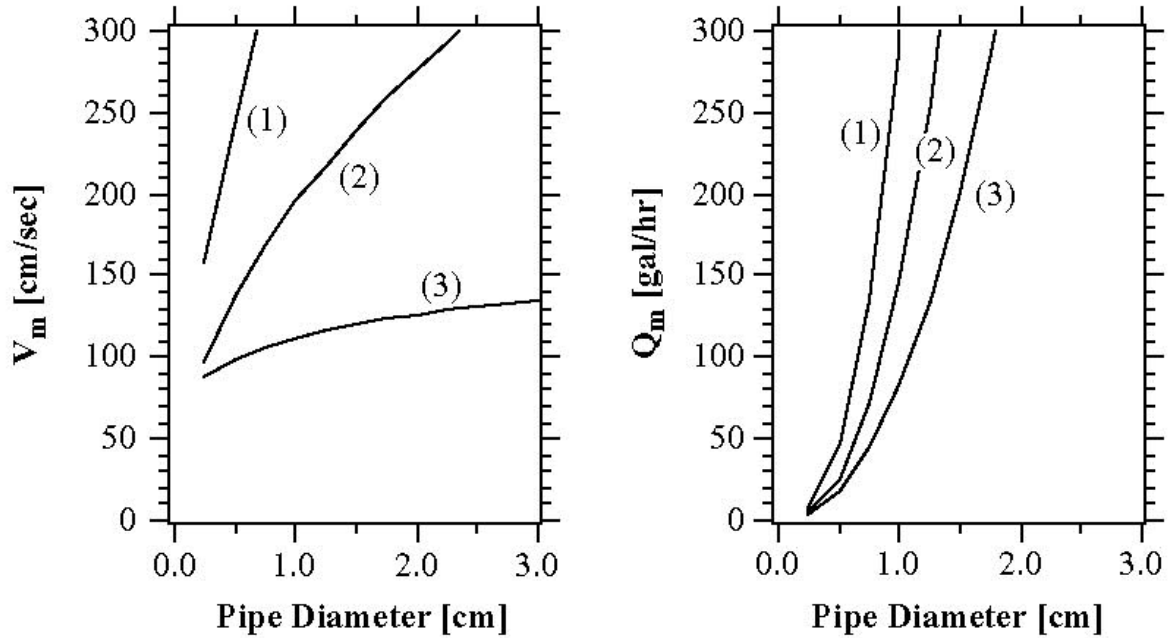


Figure 52. Predicted  $V_m$  and  $Q_m$  for  $V_s = 0.03$  and  $d = 300$  mm. The labels (1-3) correspond to eqs. (1-3).

into the supercritical region of the reactor. Separate pumps were employed to flow the water (reaction medium) through the main (outer) reactor tube and the reactants through the inner injector tube. The flow rate of each pump was adjusted to give the desired concentration of reactant in the water. The mixing region was observable through optical (diamond) windows. The modified reactor was tested in a series of experiments in which a one-percent solution of HMX in methyl ethyl ketone (MEK) was injected into water in varying ratios under supercritical conditions. No oxidant was added in these experiments. Temperatures at the injector were varied from 100 °C to 400 °C while the pressure was maintained between 290 and 375 atm. For most experiments the water flow rate, 3 mL/minute, was kept about 7.5 times greater than the HMX/MEK flow rate, 0.4 mL/minute. For a few experiments the flow rates of the two solutions were set equal at 3.0 mL/minute. These injection rates yield very high concentrations of HMX, ranging from 0.1 percent to 0.5 percent. The injection and subsequent mixing were observed through the optical window using a TV camera and magnifying optics, and recorded with a VCR. Under these conditions we did not observe a solid phase of HMX (due to precipitation of insoluble material) forming near the opening of the injector.

When the reactor was operated under the conditions described, less than 10 percent of the MEK was destroyed. A large number of organic products were observed in the HPLC analyses, most likely from the thermal decomposition of the MEK. The identity of these products has not been determined. The HMX was completely destroyed for all concentrations employed. The highest HMX concentration employed was 5000 ppm, yielding a detection-limited destruction efficiency of 99.9996 percent. The effluent contained low concentrations of nitrite (0.3 to 6 ppm) and nitrate (0.1 to 0.6 ppm). Less than 0.5 percent of the nitrogen in the HMX is converted into  $\text{NO}_x^-$ . This result differs from experiments in which HMX is the only organic present in solution. The high concentration of MEK and low level of oxidizer produces a smaller percentage of nitrogen as  $\text{NO}_x^-$ .

Dissolving HMX in MEK is convenient for introducing high concentrations of HMX into the reactor. However, this approach produces significant quantities of MEK decomposition products. Although thermal decomposition of the MEK is relatively low at temperatures at which most of the HMX decomposes, these products not only interfere significantly with the analysis of the HMX reaction products, but are themselves likely to be undesirable waste. It would be possible to separate the remaining MEK for reuse and to destroy the MEK decomposition products in a second SCWO step. The extra energy and oxidant required for these steps are likely to be significant.

## C. Base Hydrolysis of Explosives

### 1. Introduction

The instability of energetic materials to strong bases is well known. The three classes of explosive compounds, namely nitroaromatics, nitrate esters and nitramines, can all be decomposed under alkaline conditions (References 25–29). Our experiments indicate that the hydrolysis of certain explosives in basic solutions produces water-soluble products that can be processed by SCWO. Our experiments show that NQ, RDX, HMX, TNT, NC, and NG can be hydrolyzed at low temperatures ( $< 150\text{ }^{\circ}\text{C}$ ) and low pressures ( $< 60\text{ psi}$ ) to produce water-soluble, nonexplosive products. In addition, the following formulations were subjected to base hydrolysis: PBX 9404, tritonal, triple-based gun propellant M31A1E1, and CYH class 1.1 rocket propellant. Compositions of the formulations that were studied are listed in Table 34.

TABLE 34. COMPOSITIONS OF FORMULATIONS USED IN BASE HYDROLYSIS EXPERIMENTS

Component / Weight Percent	9404	Tritonal	M31A1E1	CYH
Aluminum		20.0		19.8
Ammonium perchlorate				10.8
Carbon black			0.05	
Dibutylphthalate (DBP)			3.0	
Ethyl Centralite (Diethyldiphenylurea)			1.5	
Glycerol triacetate (triacetin)				5.3
HMX	94.0			10.8
3-Hydroxyphenol (resorcinol)				1.1
Nitrocellulose (NC)	3.0		21.5	21.6
2-Nitrodiphenylamine				1.0
Nitroglycerin (NG)			18.0	29.6
Nitroguanidine (NQ)			54.7	
Potassium sulfate			1.25	
Tris(2-chloroethyl) phosphate	3.0			
TNT		80.0		

Although experiments were performed on all of the materials mentioned above, the work focused on HMX, PBX 9404, and the propellant formulations. With the exception of

PETN, all of the energetic materials studied decomposed completely to non-energetic products. PETN only partially decomposed due to its higher resistance to base hydrolysis and problems with its wettability in aqueous solution. In this section we discuss hydrolysis experiments for NQ, TNT, HMX, PBX 9404, RDX, M31A1E1, and CYH. These materials were hydrolyzed under basic conditions. Experiments were conducted using both open and sealed containers, and using both small and large pieces of explosives. The products of hydrolysis were analyzed by the following techniques: Fourier-transform nuclear magnetic resonance spectrometry (FTNMR); Fourier-transform infrared spectroscopy (FTIR); gas chromatography (GC); mass spectrometry (MS); and ultraviolet spectroscopy (UV). The hydrolysis of the energetic materials NC and NG was not studied directly. However, the results of their hydrolysis can be inferred from our study of the triple base propellant, M31A1E1, which contains these components. We complete this section with a discussion of the SCWO of the hydrolysis products.

## 2. Hydrolysis of Nitroguanidine

Hydrolysis of nitroguanidine (NQ) was studied under a variety of experimental conditions in an open container. In several experiments, flaked NQ samples weighing approximately 200 mg each were placed in beakers and mixed with sodium hydroxide solution at a 1:1 molar ratio of Base:NQ. Although some of the NQ dissolved in the aqueous solution, no reaction was evident upon mixing at room temperature. The mixtures were heated on a steam table to approximately 74 °C over a period of 5 minutes, maintained at 74 °C for 30 minutes, and then cooled. During heating, vigorous evolution of gaseous products was observed. At the solution boiling point, some foaming occurred but did not require the addition of a defoaming agent. The resulting solutions were analyzed for starting material and products. In this case, gaseous effluents were not captured or analyzed, although the odor of ammonia could be detected in several experiments. After the reaction was complete, a golden-yellow, homogeneous solution remained. In one experiment, the aqueous solution resulting from the hydrolysis was diluted from 2.0 mL to 1.0 liter, and the diluted solution was analyzed for unreacted NQ by UV spectroscopy. A standard solution of NQ in water was prepared and found to have an absorbance maximum at 263 nm, with a molar absorptivity of  $14,500 \text{ cm}^{-1}\text{M}^{-1}$ . Analysis of the diluted hydrolysis solution from experiment 1 showed that 99.97 percent of the NQ had reacted. The destruction of NQ may have been even greater since no attempt was made to separate reaction products that could contribute to the UV absorbance at 263 nm and thereby cause a greater apparent NQ concentration. Similar experiments were conducted in which distilled water alone was used without any sodium hydroxide. After heating for 30 minutes, it

was observed that most of the NQ remained undissolved, indicating that the heating in water alone is not sufficient for the hydrolysis to occur.

Larger-scale open-container tests were also conducted. These large-scale hydrolysis experiments involved 500-gram pressed charges and were performed at a firing site. The explosive charge, a 2.5-inch-by-2.5-inch-diameter cylinder of pressed NQ, was placed in an open container with 4 liters of sodium hydroxide solution. The mixture was heated to a final temperature of 74 °C. Total heating time averaged about 3 hours, including the time required to reach the final temperature. The progress of the reaction was monitored remotely using a video camera and recorder. During heating, gas evolution was visible from the sides and top of the cylinder. The color of the solution gradually changed from clear to dark yellow. Flakes of NQ could be observed peeling from the charge. The resulting mixture was filtered to remove unreacted explosive, and the aqueous phase was analyzed and processed in an SCWO reactor. In the first large-scale experiment, the sodium-hydroxide-to-NQ mole ratio used was relatively low, *i.e.*, NQ was in excess. When the test was terminated, a 16-gram piece of NQ remained. Analysis of the hydrolysis solution by UV spectroscopy showed it to be saturated with NQ. The solution was also analyzed for hydrolysis products by  $^{13}\text{C}$  NMR and found to contain four different carbon species (Figure 53). The peaks between 0 and 60 ppm in Figure 53 are due to an NMR reference compound. An aliquot of the solution was evaporated to dryness and the solid residue was analyzed by GC/MS. By matching the mass spectra obtained to a spectral library, we the following products identified: ammonium carbamate; sodium carbonate; urea; and guanidine carbonate. The products were verified by acquiring additional NMR spectra of the sample spiked with the suspected materials.

A second large-scale NQ hydrolysis experiment was performed with a higher sodium-hydroxide-to-NQ mole ratio of 1.25. UV spectroscopic analysis of the hydrolyzed solution showed no detectable amount of NQ. The  $^{13}\text{C}$  NMR spectrum of the solution in this case showed three carbon species (Figure 54). Spiking the sample identified two of the products as carbonate and urea, but the  $^{13}\text{C}$  chemical shift of the third product did not match that of guanidine, carbamate, or nitroguanidine. The splitting of the peak indicates that the carbon is bonded to nitrogen. Splitting of  $^{13}\text{C}$  peaks by  $^{14}\text{N}$  is uncommon but can occur if the molecule is highly symmetric. Examination of  $^{13}\text{C}$  NMR correlation charts shows that the chemical shift of the unknown is close to that of nitriles and isocyanates. Further evidence for the presence of a nitrile or isocyanate is found in the infrared spectrum of the sample (Figure 55). Although the

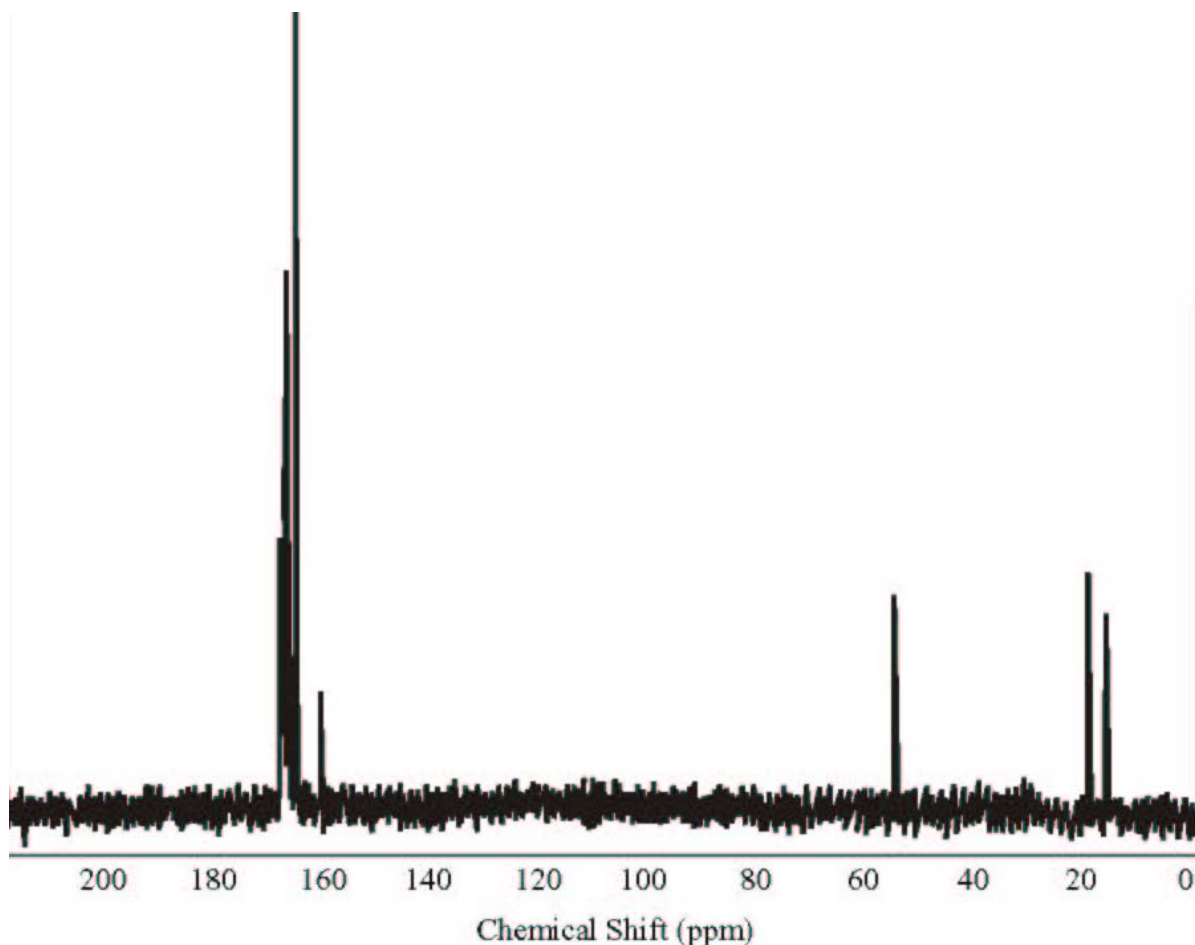


Figure 53.  $^{13}\text{C}$  NMR spectrum of NQ hydrolysis residue. Peak assignments are 167.51, carbamate; 166.38, carbonate; 164.69, urea; and 160.31, guanidine.

spectrum in Figure 55 is of the carbonate/urea/unknown mixture, the absorbance near 2200 wavenumbers is consistent with a nitrile or isocyanate. Based on the starting material, NQ, possible candidates for the unknown were cyanamide and the cyanate anion. By comparison with known samples of cyanamide and cyanate, the unknown was identified as cyanate. Additional small scale experiments were conducted to determine if the NQ hydrolysis could be driven to completion (*i.e.*, all the NQ converted to carbonate). In these experiments, the sodium hydroxide-to-NQ mole ratio was increased to 2.6 and the mixture was maintained at the final temperature for 3 hours. NMR analysis of the hydrolysis solution showed the same three products as before, with the major product being cyanate.



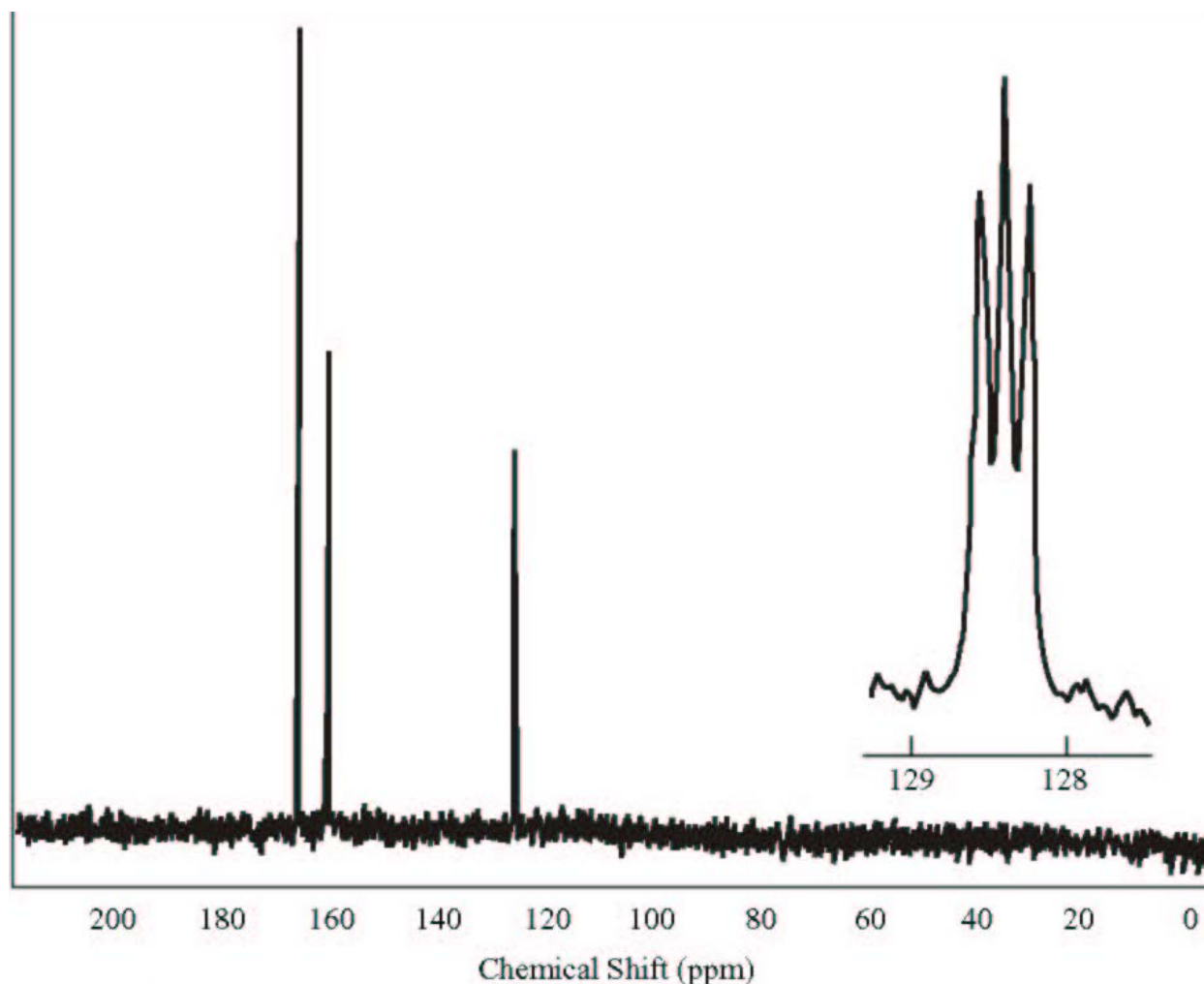


Figure 54.  $^{13}\text{C}$  NMR spectrum of NQ hydrolysis residue with excess NaOH. Peak assignments are 168.16, carbonate; 162.65, urea; and 128.44, cyanate or cyanamide.

A closed-container NQ hydrolysis was performed to identify the gaseous reaction products. In this experiment, 3.0 g. of NQ was mixed with sodium hydroxide solution with a base:NQ ratio of 1.25:1, sealed in a 50-mL pressure vessel, and heated to approximately 80 °C. After the pressure leveled off, heating was terminated and the vessel cooled to room temperature. The pressure of the cooled vessel was found to be 110 psi. Analysis by MS showed the major gaseous product to be nitrous oxide, with a small amount of ammonia. NMR analysis of the liquid phase gave the same three products as described above.

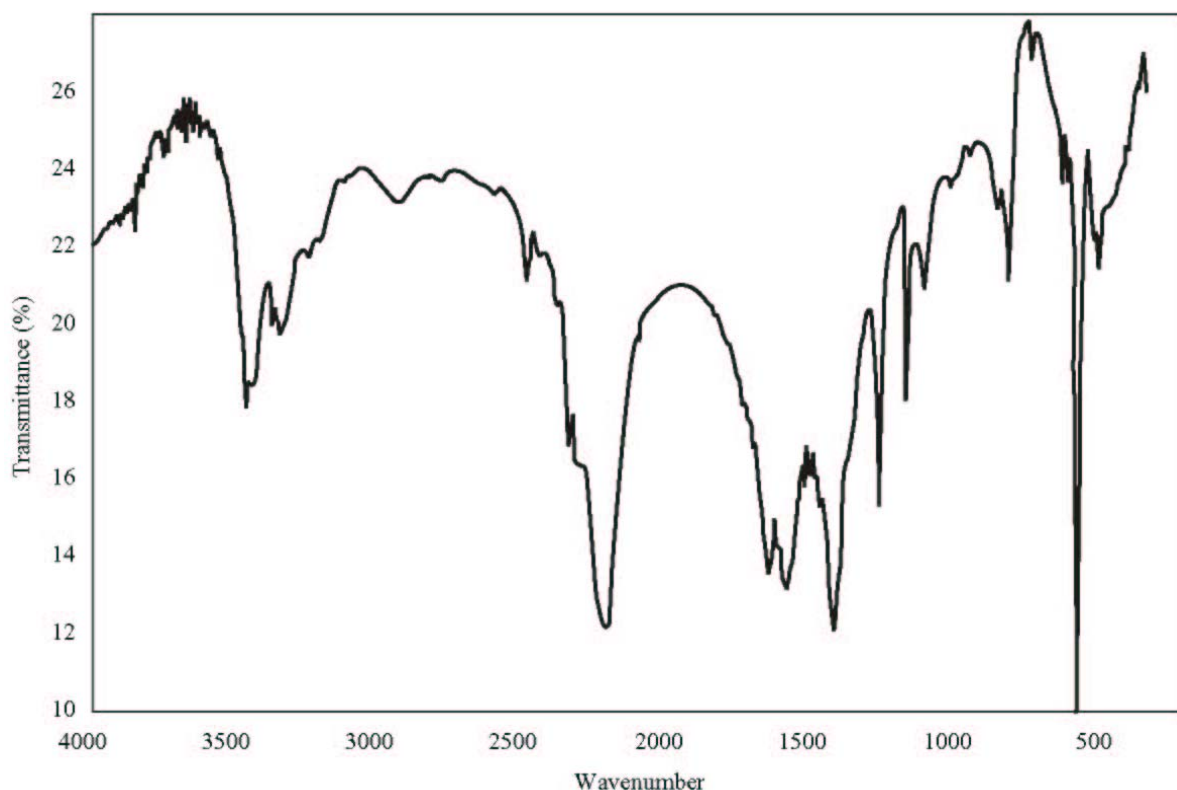
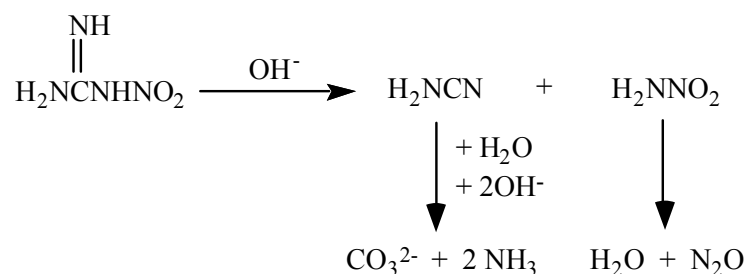


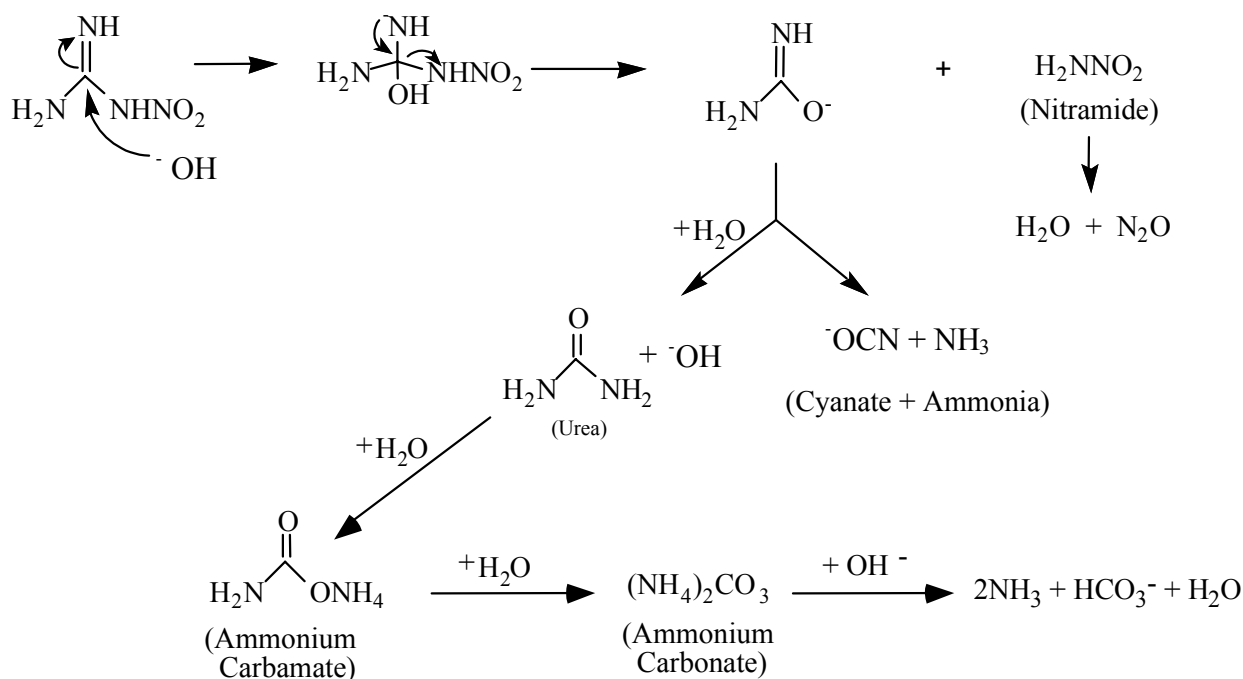
Figure 55. FTIR spectrum of NQ hydrolysis residue.

NQ hydrolysis is thought to proceed by decomposition to give cyanamide and nitramide (Reference 27), whence cyanamide further decomposes to ammonia and carbon dioxide (carbonate in basic media) and nitramide to water and nitrous oxide.



However, in addition to nitrous oxide, ammonia, and carbonate, we detected urea, ammonium carbamate, and sodium cyanate as major products. This simple mechanism does not account for this product distribution. We also found that hydrolysis of ammonium carbamate and urea under the same conditions as used for NQ, affords carbonate as the only product. When

cyanamide is subjected to base hydrolysis, urea and sodium carbonate are produced. From this information we propose a more-comprehensive mechanism for NQ hydrolysis.



In the above mechanism, one equivalent of base is consumed per mole of starting C to convert that C into a mixture of cyanate and carbonate (sodium salts). In general, however, we found that an excess of base (1.25:1 molar ratio) was needed to complete the hydrolysis reaction.

### 3. Hydrolysis of Trinitrotoluene

Trinitrotoluene (TNT) experiments were performed only on a small scale in a closed container. When TNT was mixed with NaOH solution at a base:TNT molar ratio of 1.25:1, the solution turned a clear, pale red. The mixture was heated to 150 °C and the pressure leveled off at 64 psi after 109 minutes of heating. A control run that did not contain TNT was found to develop a pressure of 61 psi, indicating that minimal gaseous products formed from TNT hydrolysis. The gases were analyzed by MS and the major gaseous product was CO<sub>2</sub>. The liquid phase was dark black with a suspension of tar-like material. Attempted analysis of products was unsuccessful due to clogging of filters and insolubility of the material. As pH of the solution was no longer basic after the hydrolysis, it was evident that more base should be employed.

In a subsequent experiment, the NaOH-to-TNT mole ratio was six. The mixture was sealed in a 100-mL vessel and heated to 150 °C, under which conditions the pressure leveled off at 54 psi after 73 minutes. Upon cooling, the residual pressure was too low to measure. The liquid phase appeared dark black and homogeneous, consistent with the earlier literature (Reference 25). Analysis by  $^{13}\text{C}$  NMR gave a single carbon species having a chemical shift that corresponds to a carbonyl group, and no  $^{13}\text{C}$  peaks matching those of TNT. It appears that TNT is completely hydrolyzed to a nonexplosive, water-soluble product that we have not identified.

#### 4. Hydrolysis of HMX and PBX 9404

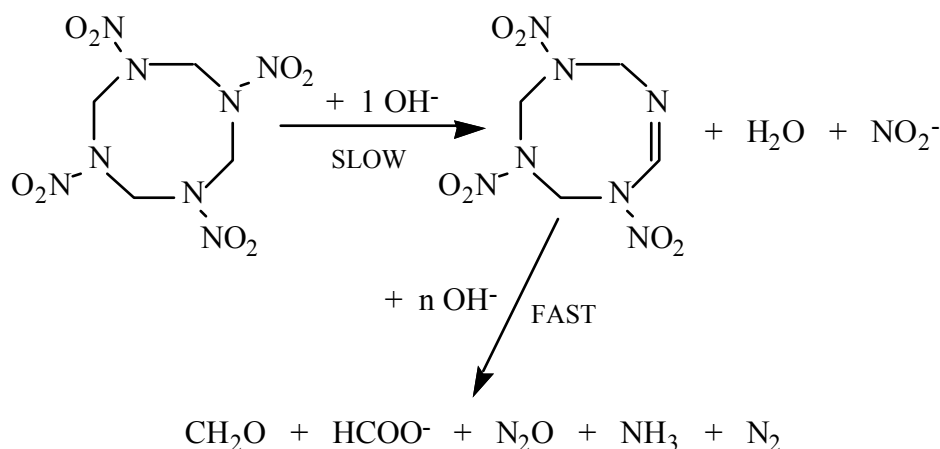
Because HMX is a major component in both DOE and DoD formulations, we have performed a large number of hydrolysis experiments on it. We have also done many experiments with PBX 9404, which is 94.0 weight percent in HMX. The experiments on PBX 9404 were conducted in conjunction with our DOE program, but the results will be included here because of the obvious relevance to this project. The complete composition of PBX 9404 is shown in Table 34 (page 104). Base hydrolysis has been done on the PBX in the form of molding powder, 1- inch-by-1-inch pressed pellets (23 g), 5.125-inch diameter hemispheres (1.1 kg), and 1.625-inch- by-1-inch pieces (63 g) encased in 1/8-inch steel. The amount of sodium hydroxide used in the reactions was 6 moles per mole of HMX contained in the PBX. Four moles are required for complete reaction with HMX and a two-mole excess was added for reaction with the binder and plasticizer. Upon mixing PBX 9404 and sodium hydroxide solution at ambient temperature, there was no visible reaction. When the mixture was heated to temperatures above 60 °C, the NC binder decomposed quickly, leaving behind HMX powder. In the 70 to 80° range, vigorous gas evolution was observable and the mixture began to foam. When the solution boiling point was reached, 93 °C, the foaming was severe enough that a defoaming agent had to be added. During the reaction, the odor of ammonia was detected. Upon completion of the reaction, the resulting homogeneous solution was clear brown and had a *pH* of approximately 13. Titration of the solution to determine the amount of hydroxide consumed showed that 4.4 moles was used per mole of HMX in the PBX 9404.

We have observed that the time required for complete destruction of the HMX depends on temperature, stirring efficiency, particle size of the material, and volume of the hydrolysis solution. Mixtures in which the solution volume was 4 mL per gram of PBX did not react completely after many hours of heating. When the volume was increased (keeping the total amount of NaOH reactant the same) to 15 mL/g PBX 9404, reaction was complete after several

hours of boiling. Subsequent experiments were carried out with volumes of 7 and 10 mL/g of PBX. In most cases, a solution volume of 10 mL/g was used to effect complete decomposition of PBX 9404 in a reasonable amount of time. Typically, the reaction is finished after 2 hours of boiling with constant stirring. The rate of HMX hydrolysis appears to become progressively slower as the reaction proceeds. This may be due to "salting-out" of the HMX from the hydrolyzing solution as the concentration of the product salts increases. The solubility of HMX in water is very low, 5 ppm at 20 °C, and is likely to be lower in concentrated salt solution. To compensate for this problem, experiments were performed with dimethyl sulfoxide (DMSO), a good solvent for HMX, added to the hydrolysis solution. The time required for hydrolysis of HMX in 100 % aqueous solution was compared to that in 10 % by volume DMSO solution. The reaction time was found to decrease by a factor of three. Presumably, the rate enhancement is due to a solubility effect but the reactivity of DMSO in base may also contribute.

The rate-limiting step of the alkaline hydrolysis of HMX is postulated (Reference 12) to be a bimolecular elimination reaction producing nitrous acid. The intermediate produced in the slow step of the reaction is very unstable to base, and quickly decomposes to the products shown.

Of the gaseous products shown above, we have found that nitrous oxide is produced in much larger quantity than is ammonia or nitrogen. A trace of hydrogen was also detected. Although formaldehyde is shown as one of the products, we have not detected it under the reaction conditions we have used. Formaldehyde itself is unstable in strong bases, producing the formate ion by the Cannizzaro reaction (Reference 30).



Quantitative analysis was performed on the product solution from the hydrolysis of 5.05 grams of PBX 9404 in 50 mL of 2M sodium hydroxide. The hydrolysis solution was analyzed by  $^{13}\text{C}$  NMR (Figure 56). None of the peaks corresponds to PBX 9404 components, and the major peak at 171.01 ppm has a chemical shift typical of a carbonyl group. Subsequent NMR analyses identified the major product as the formate anion. However, the carbon NMR

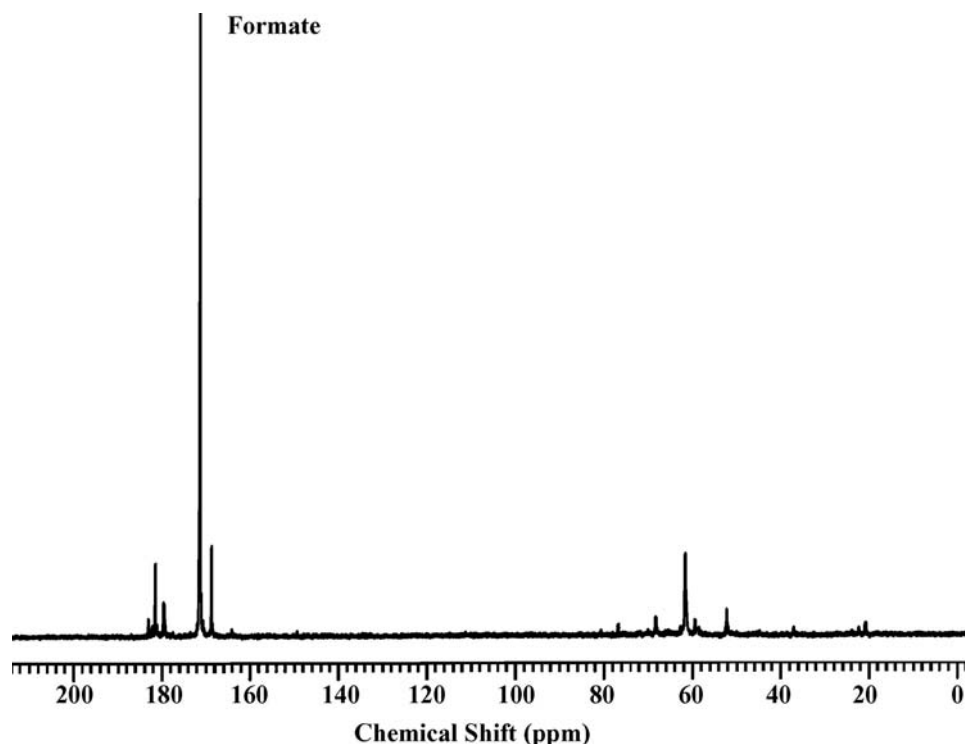


Figure 56.  $^{13}\text{C}$  NMR spectrum of HMX hydrolysis residue.

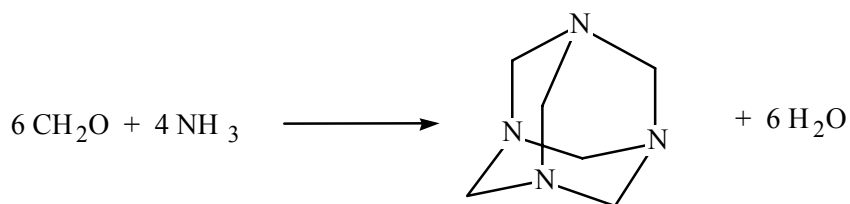
spectrum shows at least 15 minor carbon species in addition to the formate. The hydrolysate was also analyzed by ion chromatography for formate, nitrite, nitrate, and chloride. Table 35 lists the results of the analysis. The weight percentages of carbon, nitrogen, and chlorine in PBX 9404 are 16 %, 36 %, and 1.1 %, respectively. As shown in Table 35, 35 % of the total carbon was converted into formate. The balance of the carbon remained in solution as unidentified, water-soluble products. Of the starting nitrogen 19% was converted into nitrite, and 0.4 % ended up as nitrate. Most of the remaining nitrogen formed nitrous oxide ( $\text{N}_2\text{O}$ ) gas, but the exact fraction was not determined. The chlorine from the PBX 9404 plasticizer, tris(2-chloroethyl) phosphate (CEF) is almost completely converted into chloride ion; 80 % is accounted for. Phosphorus NMR analysis of the hydrolysis products indicates that the CEF phosphorus is not converted into inorganic phosphate, but remains an organic species, possibly a hydroxyethyl phosphate. Also shown in Table 35 are the mole ratios of the products to the starting moles of HMX or CEF.

TABLE 35. ANIONIC PRODUCTS FROM THE HYDROLYSIS OF PBX 9404

Anion	Conc. (g/liter)	Total Moles	Wt. % of Total	Mole Ratio
Formate	22.5	0.024	35 % of C	1.5 / HMX
Nitrite	22.5	0.024	19 % of N	1.5 / HMX
Nitrate	0.633	0.52 e-3	0.4 % of N	0.032 / HMX
Chloride	0.891	1.3 e-3	80 % of Cl	2.4 / CEF

Several experiments were conducted that examine the use of ammonium hydroxide in place of sodium hydroxide. In one experiment, sodium hydroxide and HMX were mixed in a mole ratio of 5 to 1 and sealed in a 100-mL pressure vessel. After 59 minutes' heating at 160 °C, the pressure leveled off at 87 psi. A control was run without HMX and the maximum pressure was 76 psi. When the vessel was cooled, the residual pressure was 12 psi. The major gaseous product was N<sub>2</sub>O. The NMR spectrum of the clear, yellow liquid phase was almost identical to that of the PBX 9404 hydrolysis products discussed above. Formate was the major nonvolatile product. For comparison, a similar HMX hydrolysis was done using ammonium hydroxide instead of sodium hydroxide. The 5:1 ammonium hydroxide/HMX mixture was heated to 150 °C, reaching a final pressure of 104 psi after 60 minutes (compared to the control, which gave a final pressure of only 56 psi). When the vessel was cooled to room temperature, the residual pressure was 34 psi. Analysis of the gaseous products again gave N<sub>2</sub>O as the major product and significantly more nitrogen than produced in the sodium hydroxide experiment. The nitrogen formation may be due to decomposition of ammonium nitrite. NMR and MS analyses of the liquid phase showed the major product to be hexamethylenetetramine instead of formate.

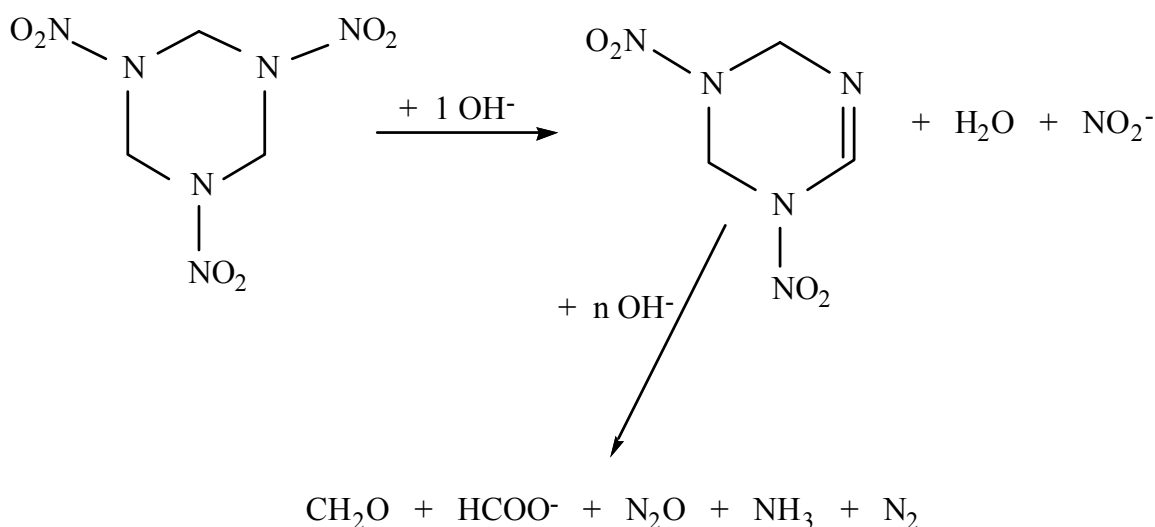
When HMX was hydrolyzed with aqueous ammonia as the base, much less formate ion was found and a significant amount of hexamethylenetetramine was formed. Interestingly, hexamethylenetetramine can be used as a starting material for HMX and RDX syntheses. Its production can be explained by the reaction of ammonia and formaldehyde as follows:



## 5. Hydrolysis of RDX

RDX was hydrolyzed using ammonium hydroxide as the base in a 1-liter pressure vessel that was heated to 150 °C. After 49 minutes, system pressure was stable at 70 psi. Upon cooling, the residual pressure was found to be 15 psi; however, gaseous products were not analyzed. The liquid phase was analyzed by  $^{13}\text{C}$  NMR, which showed two carbon species. The major product is identified as hexamethylenetetramine and the other product is probably formate.

References 25 and 26 present a mechanism for base hydrolysis of RDX:



Hydrolysis of the product formed by the first step proceeds very rapidly, making isolation of the first product difficult. The kinetics of this process has been previously investigated (References 31–33). When ammonium hydroxide is used for the base hydrolysis, the major product is hexamethylenetetramine. Its production can be explained by the reaction of ammonia and formaldehyde, as was discussed in the section on HMX.

## 6. Hydrolysis of M31A1E1 Propellant

M31A1E1 is a gun propellant manufactured at the Radford Army Ammunition Plant in Radford, Virginia. The hydrolysis and SCWO of this propellant were conducted in conjunction with our project sponsored by the U. S. Army Corps Of Engineers Construction Engineering Research Laboratory. We received the M31A1E1 propellant in the form of tubular sticks of dimensions 29 by 0.275 inches with a 0.098-inch-diameter perforation. For small-scale



hydrolysis reactions of less than a gram, the propellant was ground to a powder. Larger-scale reactions of up to a quarter pound were performed on the propellant stick as received. Normally, 10–15 mL of 2M sodium hydroxide was used per gram of M31A1E1. This translates to a two-to-threefold molar excess over the moles of nitro groups in the propellant, assuming the nitrocellulose was 13% nitrated. No reaction was visible upon mixing at ambient temperature. When the mixture was heated above 60 °C, gas evolution was observed, and at boiling a small amount of foaming occurred. Completion of the reaction occurred on the same general time scale as described for NQ. The resulting solution was dark brown with a suspension of carbon black, which is a minor component (0.05%) of the propellant.

Analysis of the M31A1E1 hydrolysis products was performed by mass spectrometry,  $^1\text{H}$  and  $^{13}\text{C}$  NMR spectrometry, and by ion chromatography. Figure 57 shows the  $^1\text{H}$  and  $^{13}\text{C}$  NMR spectra of a solution of the propellant in deuterated dimethyl sulfoxide. Resonances due to nitroguanidine (NQ), nitroglycerin (NG), nitrocellulose (NC), ethyl centralite (EC), and dibutyl phthalate (DBP) can be seen in the proton NMR. Because NC is polymeric, the peaks due to it are very broad. The largest resonances seen in the  $^{13}\text{C}$  NMR are due to NQ and NG. The small peaks are EC and DBP, and the carbons of NC do not show up at all. Figure 58 is the  $^{13}\text{C}$  NMR spectrum of the water-soluble hydrolysis products. The major peaks from the spectrum have been identified as sodium carbonate, urea, and sodium cyanate ( $\text{NaOCN}$ ), which are the same products as for the NQ hydrolysis. In addition, sodium formate was detected and at least ten minor products that contain carbon. One of the minor products was identified as sodium oxalate. Previous studies (Reference 26) of nitroglycerin hydrolysis have identified nitrate, nitrite, acetate, and formate as the primary products. These products have also been detected from nitrocellulose hydrolysis, along with many others such as ammonia, cyanides, and modified cellulose. The  $^1\text{H}$  and  $^{13}\text{C}$  NMR spectra of the hydrolysis products showed no detectable amount of any of the propellant components.

A small-scale experiment was performed to obtain a quantitative analysis of some of the M31A1E1 hydrolysis products. A 120-mg piece of propellant was hydrolyzed in excess NaOH solution for 30 minutes at 93 °C. The gases evolved were collected and analyzed by mass spectrometry. The mass spectrometric data identified the major gaseous product as nitrous oxide ( $\text{N}_2\text{O}$ ). The amount of nitrous oxide gas evolved was found to be approximately 200  $\text{cm}^3$  per gram of propellant hydrolyzed. The aqueous solution of hydrolysis products was analyzed by ion chromatography. Anions detected and quantified by ion chromatography include nitrite, nitrate, carbonate, cyanate, and oxalate. In addition, at least ten minor products, including

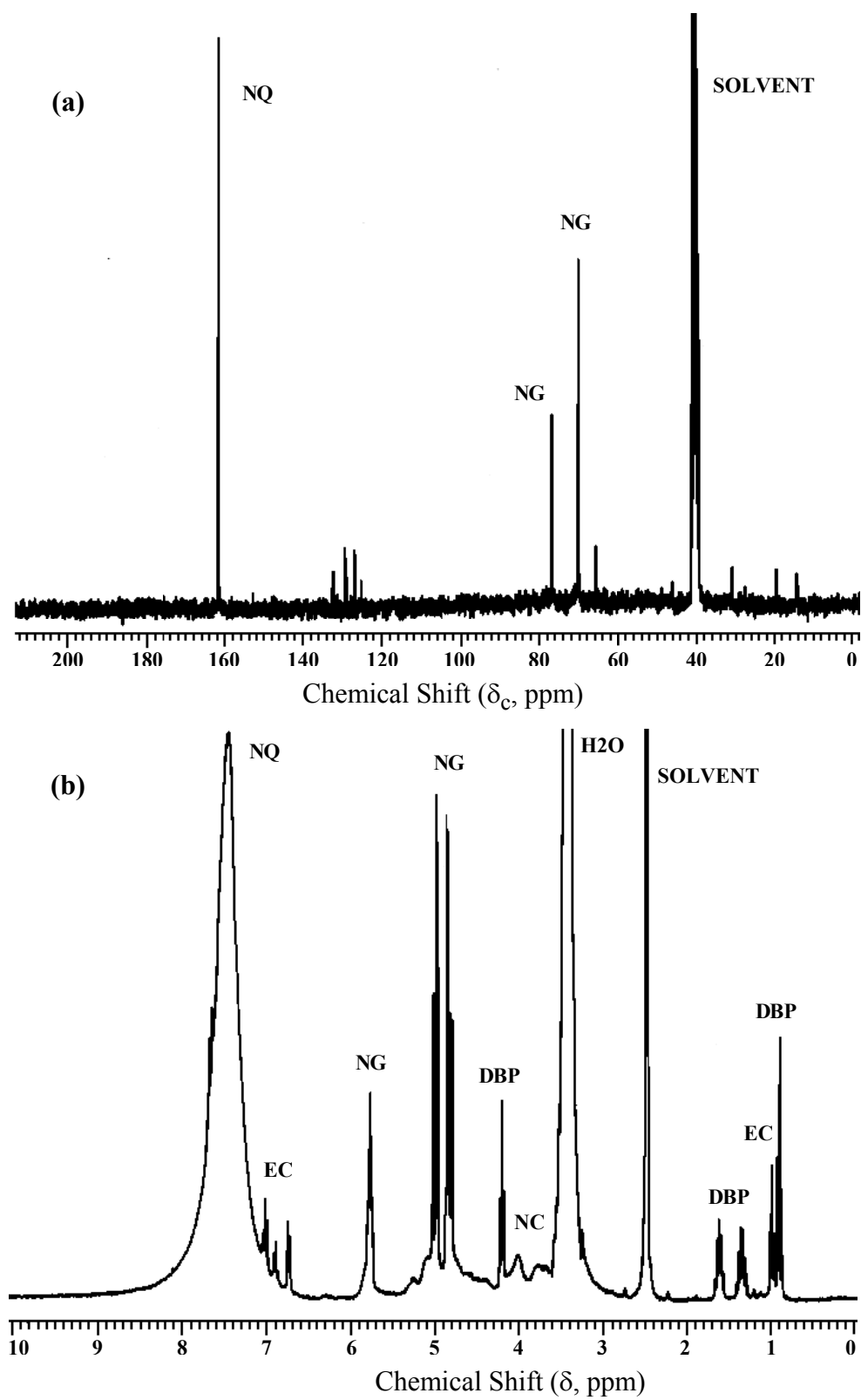


Figure 57. Spectra of M31A1E1 in deuterated DMSO: (a)  $^{13}\text{C}$  NMR and (b)  $^1\text{H}$  NMR.

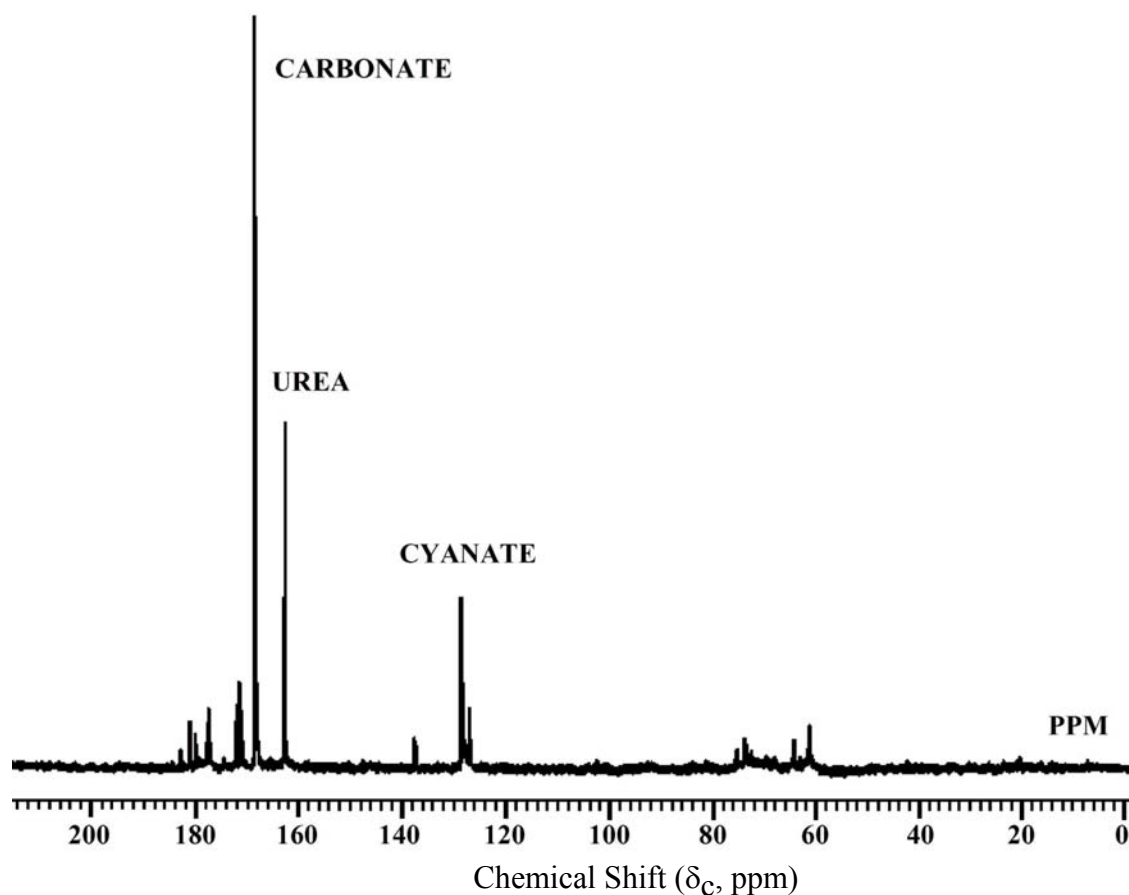


Figure 58.  $^{13}\text{C}$  NMR spectrum of the water-soluble hydrolysis products of M31A1E1.

formate, were detected but could not be quantified. The carbon was also quantified by TOC and TIC analyses. The concentration of urea was estimated from the integrated  $^{13}\text{C}$  NMR. Although  $^{13}\text{C}$  peak intensities are very dependent on relaxation times, this approach was found to be self-consistent by comparing the concentrations of carbonate and cyanate estimated from  $^{13}\text{C}$  peaks to the concentrations determined by independent analytical techniques. These results are summarized in Tables 36, 37, and 38.

Calculated mass balances for carbon are shown in Tables 36 and 37. A comparison of these tables shows that a considerable fraction of the organic carbon is contained in molecular forms that could not be quantified with the analytical techniques employed. The calculated mass balance for nitrogen is shown in Table 38. In contrast to the carbon analysis, all of the nitrogen is accounted for, within the experimental error of the analytical procedures. The bulk of the nitrogen is converted into  $\text{N}_2\text{O}$  and lost from solution. The nitrogen remaining in solution is primarily urea and nitrite.

TABLE 36. CARBON PRODUCTS FROM M31A1E1 HYDROLYSIS

Product	[Product] ppm <sup>a</sup>	[C] ppm(%) <sup>b</sup>
Cyanate (OCN <sup>-</sup> )	3565	1019 (12)
Oxalate (O <sub>2</sub> CCO <sub>2</sub> <sup>2-</sup> )	1145	312 (3)
Urea (OC(NH <sub>2</sub> ) <sub>2</sub> )	5729	1146 (13)
TIC (CO <sub>3</sub> <sup>2-</sup> , HCO <sub>3</sub> <sup>-</sup> )	2504	2504 (29)
Total C		4981 (57)

<sup>a</sup>Determined by Ion Chromatography except for urea, which is estimated from <sup>13</sup>C NMR peak intensities

<sup>b</sup>[C] is the percent of total C occurring as specified product; the initial concentration of C was 8750 ppm

TABLE 37. TOC/TIC ANALYSIS OF M31A1E1 HYDROLYSIS PRODUCTS

	ppm	% carbon <sup>a</sup>
TOC	5853	67
TIC	2504	29
Total C	8357	96

<sup>a</sup>% carbon is the percent C occurring as the specified product

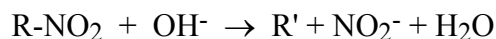
## 7. Hydrolysis of CYH Propellant

CYH is a DoT class 1.1, double-base rocket propellant that contains 19.8 wt % aluminum. The material was received in the form of large chunks, approximately 50 g in weight, and was processed to smaller particles for the hydrolysis experiments. Reactions with NaOH were first performed on a very small scale, 100 mg, and later scaled up to as much as 5 g. The amount of NaOH used was at least a factor of two greater than that required for complete reaction with all components of the propellant, according to the following analysis. The components of the propellant that react with base are the organic explosives, the aluminum and the ammonium perchlorate (AP). Our work on the hydrolysis of pure explosives has revealed that generally one unit of base is consumed per nitro group in the explosive:

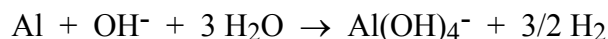
TABLE 38. NITROGEN PRODUCTS FROM M31A1E1 HYDROLYSIS

Product	[Product] ppm	[N] ppm (%) <sup>a</sup>
Ammonium (NH <sub>4</sub> <sup>+</sup> )	309	240 (1)
Nitrate (NO <sub>3</sub> <sup>-</sup> )	4225	954 (5)
Nitrite (NO <sub>2</sub> <sup>-</sup> )	5940	1808 (10)
Cyanate (OCN <sup>-</sup> )	3565	1188 (7)
Urea (OC(NH <sub>2</sub> ) <sub>2</sub> )	5729	2674 (15)
Nitrous Oxide (N <sub>2</sub> O)	(gas)	(gas) (64)
Total N		(102)

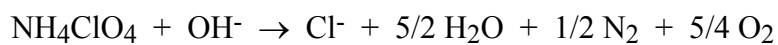
<sup>a</sup>Percent N occurring as specified product



The reaction of aluminum metal (Al) with base consumes one mole of base per mole of Al:



Finally, the reaction of AP with base consumes one mole of base per mole of AP:



The amount of N, Al and AP in CYH (1.1) propellant is 0.011, 0.0074 and 0.001 moles per gram of propellant, respectively. From the above analysis, the sum of the number of moles of N, Al and AP per gram of propellant yields the number of moles of OH<sup>-</sup> required (0.0194 moles or 0.8 g NaOH) per gram of propellant. Typically, 20 mL of 2M NaOH solution (1.6 g NaOH) per gram of propellant was used. Upon mixing the propellant with the sodium hydroxide solution at ambient temperature, reaction was observed as gas evolution from the particles. Presumably, the gas was hydrogen from the reaction of aluminum metal with base.

During the reaction of 5 g of CYH with 100 mL of base solution, the temperature of the solution rose slightly from the aluminum reaction and, after approximately 10 minutes, leveled off at 3 °C above ambient. Heat was applied to the mixture, causing more-vigorous gas

evolution as the temperature increased. Near the boiling point of the solution, foaming became a problem and was counteracted with a defoaming agent. After approximately 30 minutes of boiling, no solids or gas evolution were visible and the reaction was considered complete.

The hydrolysis products were analyzed by NMR spectrometry. Figure 59 shows  $^{13}\text{C}$  and  $^1\text{H}$  NMR spectra of a DMSO extract of CYH; corresponding spectra for the hydrolyzed solution are shown in Figure 60. No CYH component was observed in the hydrolysis solution, and the major carbon-containing products were identified as acetate and formate anions. A small amount of carbonate was detected along with at least ten unidentified minor products. In another experiment, ion-chromatographic analysis was performed on a product solution in which 520 mg of CYH was reacted with 20 mL of 2M NaOH. The results are presented in Table 39. From the composition of CYH listed in Table 34 (page 104), the total carbon and nitrogen contents of the propellant can be calculated as 16 and 14 percent, respectively. The ion chromatogram accounts for 44 % of the total carbon and 45 % of the total nitrogen. Analysis of the gaseous products from CYH hydrolysis found hydrogen, nitrous oxide and a trace of nitrogen.

TABLE 39. ANIONIC PRODUCTS FROM THE HYDROLYSIS OF CYH PROPELLANT

Anion	Conc. (g/liter)	Total Moles	Wt. % of Total
Acetate	3.40	1.2 e-3	34 % of C
Formate	1.55	0.69 e-3	10 % of C
Nitrite	3.69	1.6 e-3	32 % of N
Nitrate	2.10	0.68 e-3	13 % of N

## 8. SCWO of Hydrolysis Products

Several solutions resulting from the hydrolysis experiments were processed in the gold-lined supercritical water reactor. These included TNT, RDX, NQ, HMX, and the triple-base propellant M31A1E1. The chemical composition of these effluents has been discussed; they contained only organic decomposition products from the explosives. Table 40 presents the results from analysis of these effluents for nitrites, nitrates, ammonia, TIC and TOC.

Except for NQ, the hydrolysis effluent typically contained more  $\text{NO}_2^-$  than  $\text{NO}_3^-$ . This is not surprising since hydrolysis is not an oxidative process. The unusually large  $\text{NH}_4^+$  concentration found in RDX resulted from the ammonium hydroxide ( $\text{NH}_4\text{OH}$ ) that was used to

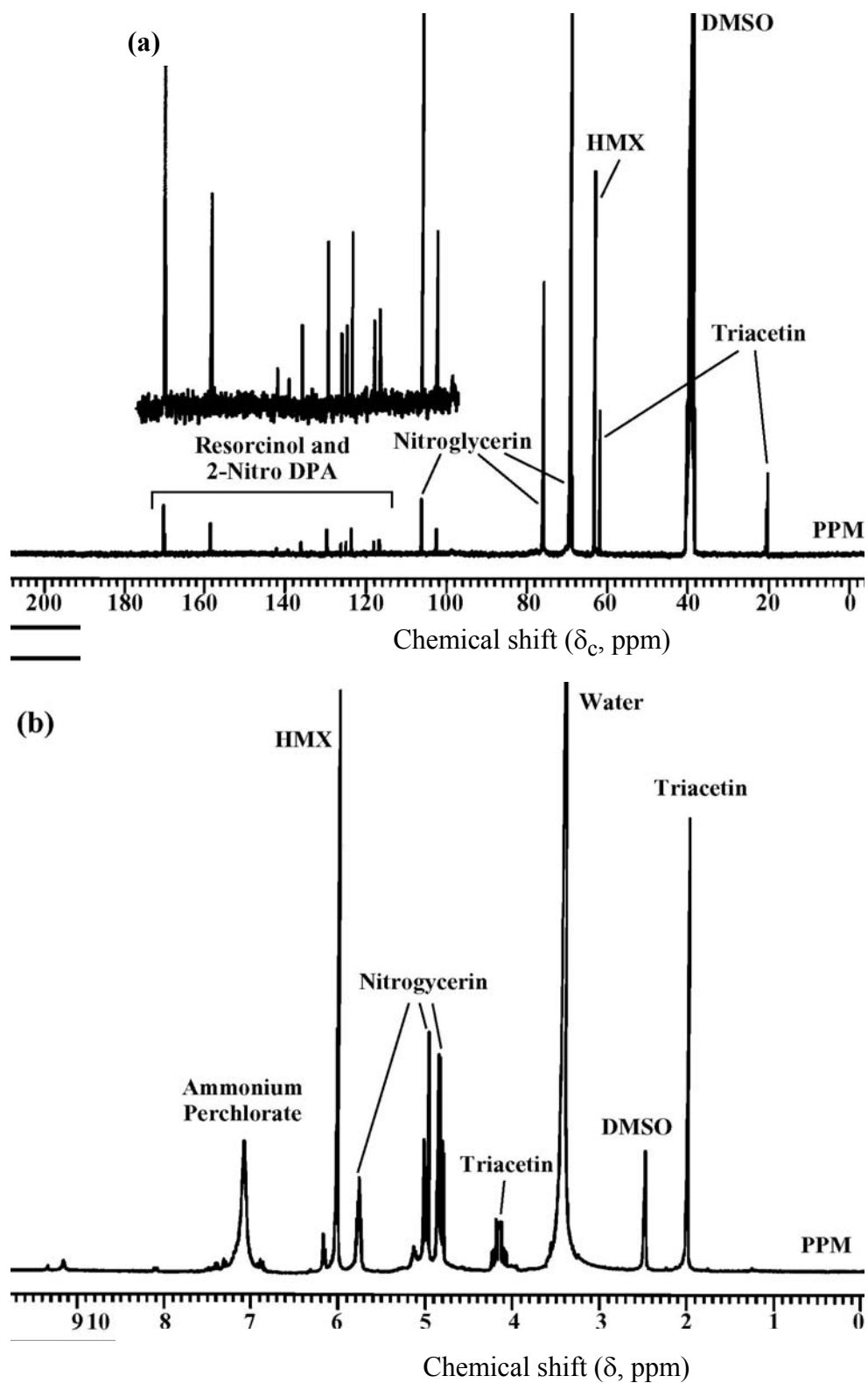


Figure 59. Spectra of CYH in deuterated DMSO–water solution: (a)  $^{13}\text{C}$  NMR and (a)  $^1\text{H}$  NMR.

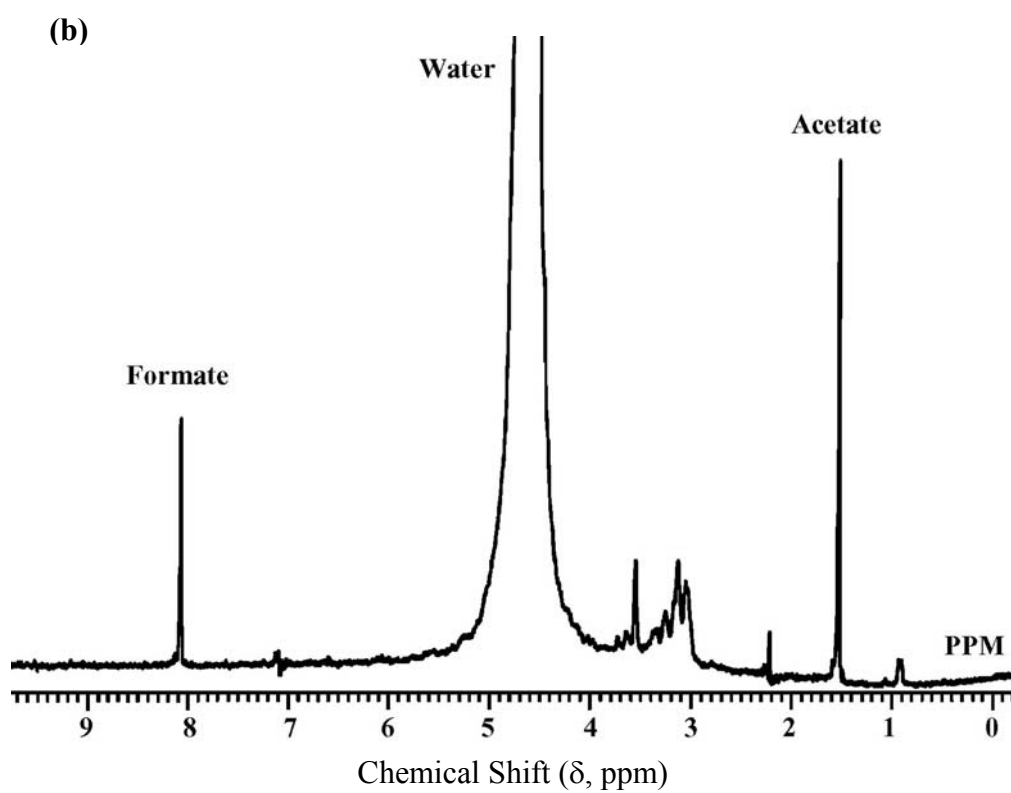
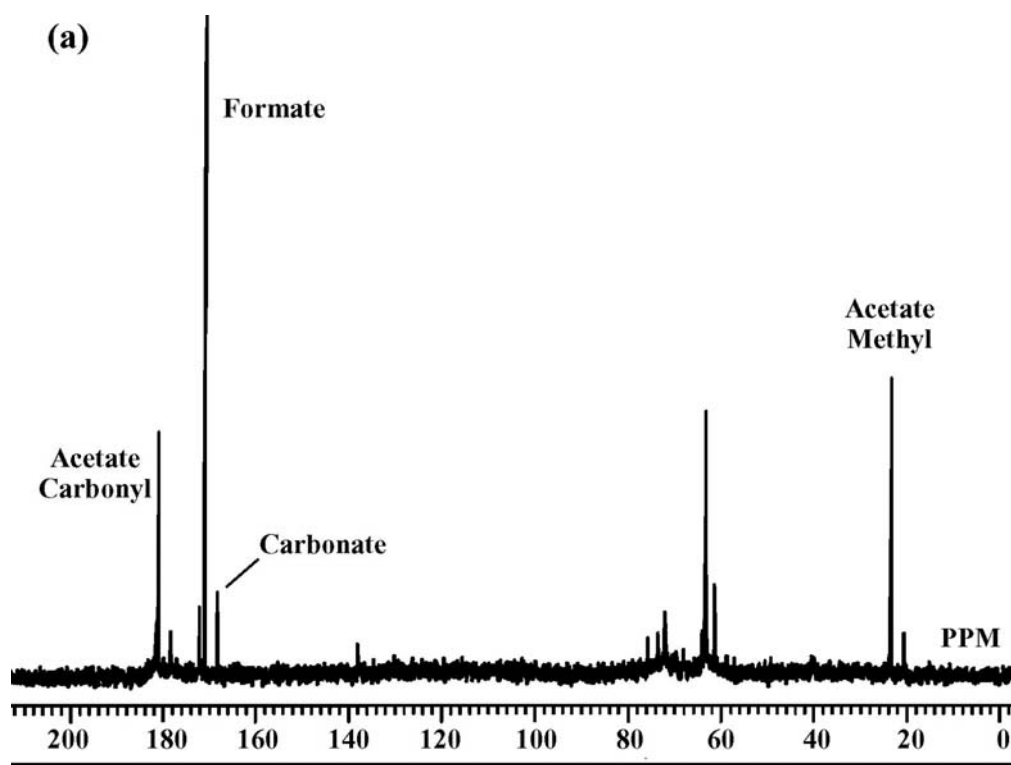


Figure 60. Spectra of CYH hydrolysis products. (a)  $^{13}\text{C}$  NMR and (b)  $^1\text{H}$  NMR.



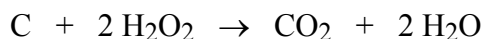
TABLE 40. ANALYTICAL ASSAY OF HYDROLYSIS EFFLUENT

Substrate	NO <sub>2</sub> <sup>-</sup> (ppm)	NO <sub>3</sub> <sup>-</sup> (ppm)	NH <sub>4</sub> <sup>+</sup> (ppm)	TIC (ppm)	TOC (ppm)	Substrate (ppm)
TNT	2577	5.06	185	1080	3380	<2
RDX	1476	111	2325	34.7	1777	2.6
NQ	5.1	57.1	a	a	a	1886
HMX	605	355	a	<0.5	10255	22.5
M31A1E1	5940	4225	309	2504	5853	a

a: not analyzed

initiate hydrolysis. Sodium hydroxide was the base used in the other cases. Although the NQ hydrolysis effluent was not analyzed for NH<sub>4</sub><sup>+</sup>, the odor of NH<sub>3</sub> was apparent. The total carbon analysis exhibited high organic concentrations indicative of the breakdown products. The effluents were also analyzed for any remaining explosive and we saw efficient destruction as a result of the hydrolysis (>98 % in all cases, and >99.9 % for TNT and RDX).

These effluents were processed through an SCWO reactor at 600 °C at a residence time of 11 seconds. The hydrolysis solutions were processed directly, except for the M31A1E1 solution, which was diluted a factor of 10 prior to injection into the SCW reactor, to yield an initial carbon concentration of 836 ppm. Attempts to run the undiluted M31A1E1 hydrolysis mixture resulted in clogging of the reactor, probably due to precipitation of sodium carbonate. In each case, the amount of oxidant, H<sub>2</sub>O<sub>2</sub>, was in excess of the stoichiometric ratio. In addition, for the M31A1E1 mixture, two different oxidant concentrations were examined. In this case, the concentration of the oxidant was varied from a stoichiometric ratio to a 10-fold excess based on the following chemical reaction:



The results are presented in Tables 41, 42, and 43. We demonstrated extremely high destruction efficiencies for the combined hydrolysis / SCWO processes, ranging from > 99.99 % to > 99.9999 %. The residual explosive concentrations were all below detectable limits after processing through the SCWO reactor.

The major gas-phase products as determined by FTIR spectra taken during the SCWO process were N<sub>2</sub>O and CO<sub>2</sub>. Figure 61 shows a typical FTIR spectrum, which was obtained

TABLE 41. INITIAL CONCENTRATIONS AND DESTRUCTION EFFICIENCIES FOR HYDROLYSIS / SCWO PROCESSES

Substrate	Oxidant concentration	Initial concentration (ppm)	Destruction Efficiency (%)
TNT	excess	11350	>99.9971
RDX	excess	11200	>99.9996
NQ	excess	125000	>99.99992
HMX	excess	15000	>99.9995
M31A1E1	stoichiometric (1:1)	836	>99.9909
M31A1E1	10:1	836	>99.9989

during the SCWO of the M31A1E1 hydrolysis mixture. It was not possible to obtain a mass balance on the hydrolysis / SCWO procedure because the gas effluent was not completely accounted for during the hydrolysis step.

The analysis for the carbon content of the aqueous reactor effluent is shown in Table 42. The data are presented in both parts per million and as a percent of the total initial carbon content. Appreciable quantities of TIC remained in solution for all explosives except HMX. Inorganic carbon was probably present as HCO<sub>3</sub><sup>-</sup> or CO<sub>3</sub><sup>-2</sup>. The TOCs were very low and, for TNT, below detection limits. In the solubility-limited studies of NQ (*i.e.*, those with no hydrolysis pretreatment), the aqueous carbon accounted for 83 percent of the total. With hydrolysis the aqueous carbon is less than one-half of one percent. This result may be due to the different chemical pathways of the oxidation of the hydrolysis products rather than for NQ itself. The remaining carbon product for all cases (at least through the SCWO reactor) was present in the form of CO<sub>2</sub>.

The nitrogen content of the SCWO reactor effluent was analyzed and is presented in Table 43. Again, the data are presented as ppm and as a percent of total initial nitrogen. The trends are similar to the straight SCWO of these explosives. The total concentration of nitrites and nitrates in the aqueous effluent was much higher, but the starting explosive concentrations were two orders of magnitude higher than in the solubility-limited experiments. The actual percent of starting nitrogen converted into NO<sub>2</sub><sup>-</sup> and NO<sub>3</sub><sup>-</sup> was lower for TNT, RDX and HMX

and about the same for NQ. Trinitrotoluene (TNT) continued to show the highest  $\text{NO}_x^-$  production rates. Nitrous oxide ( $\text{N}_2\text{O}$ ) and nitrogen ( $\text{N}_2$ ) were found in the FTIR and the mass spectra as the only detectable gas-phase nitrogen species.

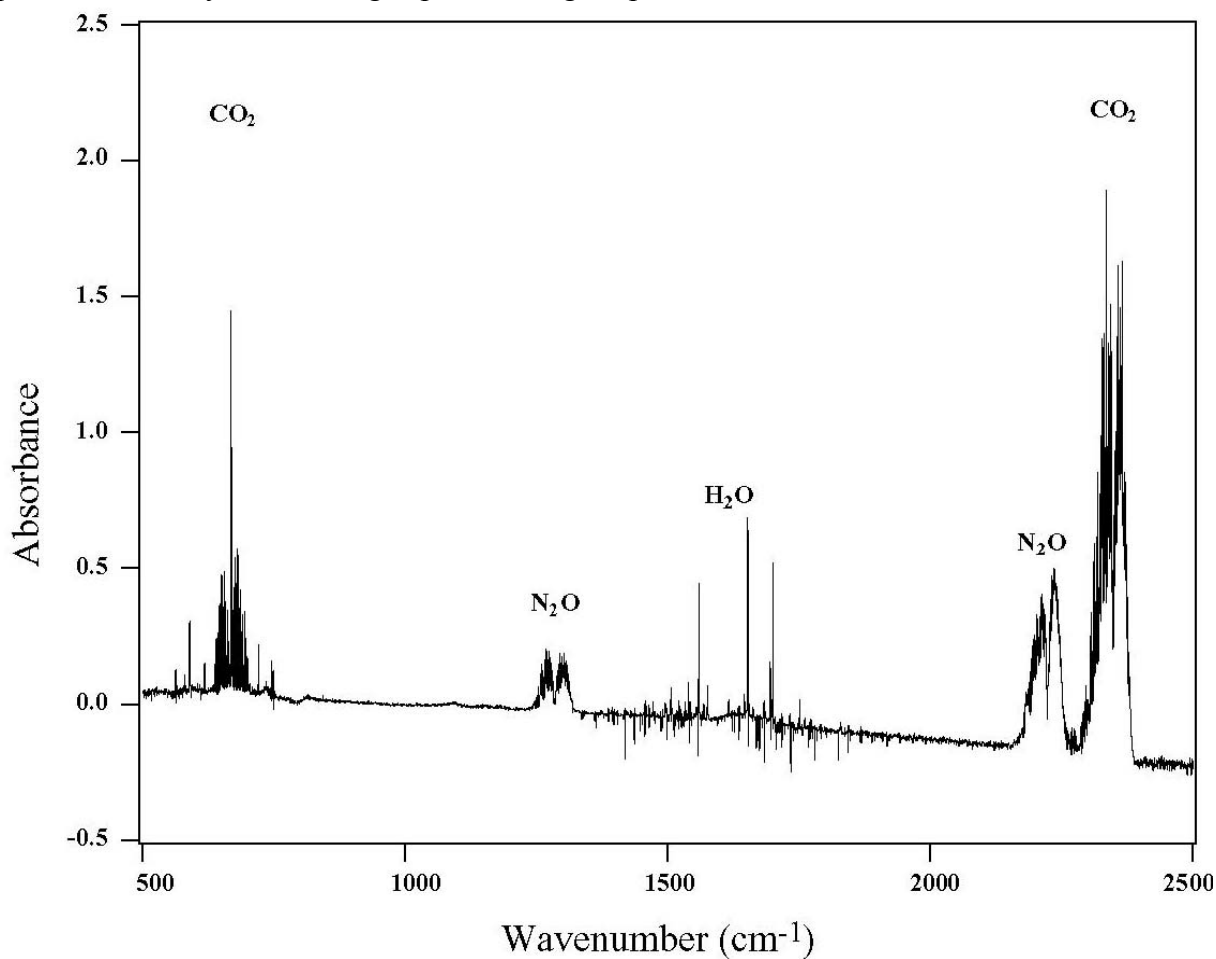


Figure 61. FTIR spectrum of gas-phase products from SCWO of M31A1E1 hydrolysis solution.

TABLE 42. ANALYSIS OF AQUEOUS CARBON PRODUCTS IN EFFLUENT STREAMS AFTER SCWO

Substrate	TIC		TOC	
	(ppm)	(% of Initial C)	(ppm)	(% of Initial C)
TNT	9.63	9.51	<0.2	<0.01
RDX	37.89	3.72	0.46	0.07
NQ	22.42	0.31	0.49	0.01
HMX	0.20	0.06	0.70	0.09
M31A1E1 (1:1)	33.3	3.98 <sup>126</sup>	0.08	0.009
M31A1E1 (10:1)	30.6	3.66	0.01	0.001

TABLE 43. ANALYSIS OF AQUEOUS NITROGEN PRODUCTS IN EFFLUENT STREAMS AFTER SCWO

Substrate	NO <sub>2</sub> <sup>-</sup>		NO <sub>3</sub> <sup>-</sup>	
	(ppm)	(% of Initial N)	(ppm)	(% of Initial N)
TNT	28.22	7.56	89.95	17.05
RDX	18.11	0.23	2.32	0.022
NQ	8.54	0.01	166.59	0.11
HMX	2.93	0.09	133.99	2.88
M31A1E1 (1:1)	2.77	0.05	0.95	0.01
M31A1E1 (10:1)	13.2	0.23	97.2	1.28

## SECTION V

### SPECTROSCOPIC MEASUREMENTS IN SUPERCRITICAL WATER

A number of optical diagnostics were developed as part of the effort to better understand the hydrothermal destruction processes. These *in-situ*, non-invasive diagnostics are useful in the investigation of fundamental properties of supercritical fluids, including phase equilibria and chemical kinetics. The Raman and coherent anti-Stokes Raman Spectroscopy (CARS) diagnostics were utilized to identify intermediate and product species, yield information on their state, such as solvation, and measure reaction rates. Transient grating spectroscopy was applied to the measurement of diffusivity and fluid sound speed, which yield state information. Further, the real-time nature of the diagnostics may be exploited for the development of process monitoring and control.

#### A. RAMAN MEASUREMENTS OF HYDRAZINE

The Raman spectrum of a mixture of 2 wt% hydrazine ( $\text{N}_2\text{H}_4$ ) in water at 270 atm is shown in Figure 62. Spectra are shown over a range of temperatures from room temperature to just above the critical temperature of water ( $T_c=374^\circ\text{C}$ ). The broadest feature in these spectra is the O–H stretching band of water. One of the N–H stretching bands of hydrazine is indicated at  $3300\text{ cm}^{-1}$ . (There are also two smaller bands at  $3220\text{ cm}^{-1}$  and  $3361\text{ cm}^{-1}$ .) (Reference 34) As the temperature increases, this band disappears and a new band grows in at  $3314\text{ cm}^{-1}$ , which we assign (Reference 35) to  $\text{NH}_3$ . The intensity of this band suggests that ammonia is a major product of hydrazine decomposition.

The integrated area of the Raman peak at  $3300\text{ cm}^{-1}$  serves as a measure of the hydrazine concentration. By using the optical cell as a steady-state flow reactor, the kinetics of the decomposition may be determined. This was done by setting the flow rate to some constant value and allowing the system to equilibrate. From the known water density and heated volume, we calculate the residence time of the fluid from the entrance of the cell to the optical window, with the fluid flow in a steady-state condition. The Raman intensity then gives the fraction of hydrazine remaining at this residence time. By repeating this for various flow rates, the decay of the concentration is measured as a function of residence time. Figure 63 shows the decay of the

hydrazine Raman signal as a function of residence time at 400 °C. At times longer than those shown, the intensity decays to zero, as expected. For each data point, the Raman intensity of

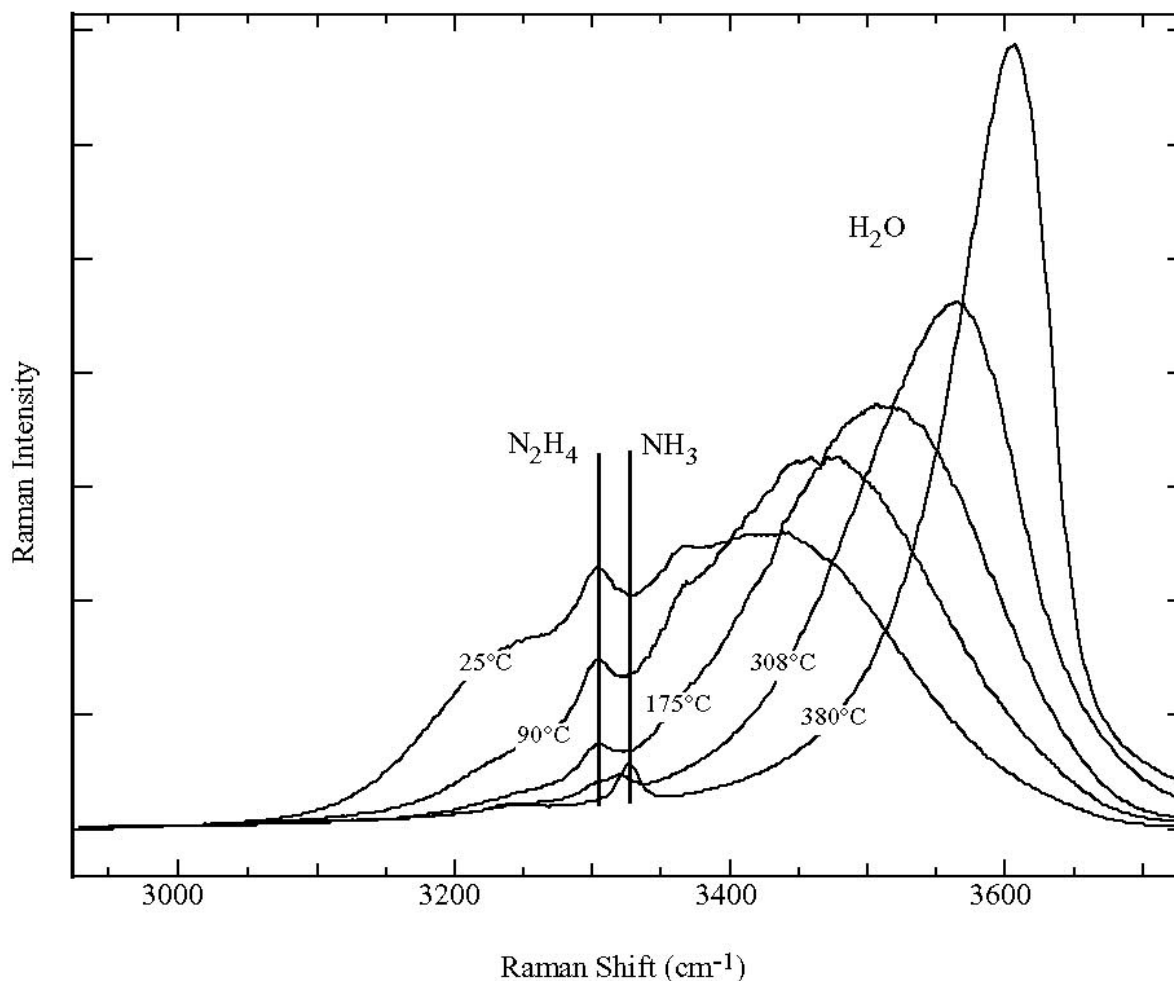


Figure 62. Raman spectra of hydrazine in water at 270 atm in the region of the N–H stretching vibrations. Spectra are shown from 25–380 °C. Curves are scaled to the same total area.

hydrazine was normalized to the peak area of the water band to correct for signal fluctuations. Although the limited signal-to-noise ratio does not permit us to rule out non-exponential decay of the concentration, we can at least assign an effective first-order rate constant for decomposition,  $k(400\text{ °C}) = 0.32\text{ sec}^{-1}$ .

An alternative analysis was made by following the hydrazine concentration while heating the optical cell. At each temperature, we calculate the residence time in the reactor, measure the

extent of decomposition from the Raman intensity and deduce the effective first-order rate constant. At several temperatures throughout the range depicted, the decay was followed as a

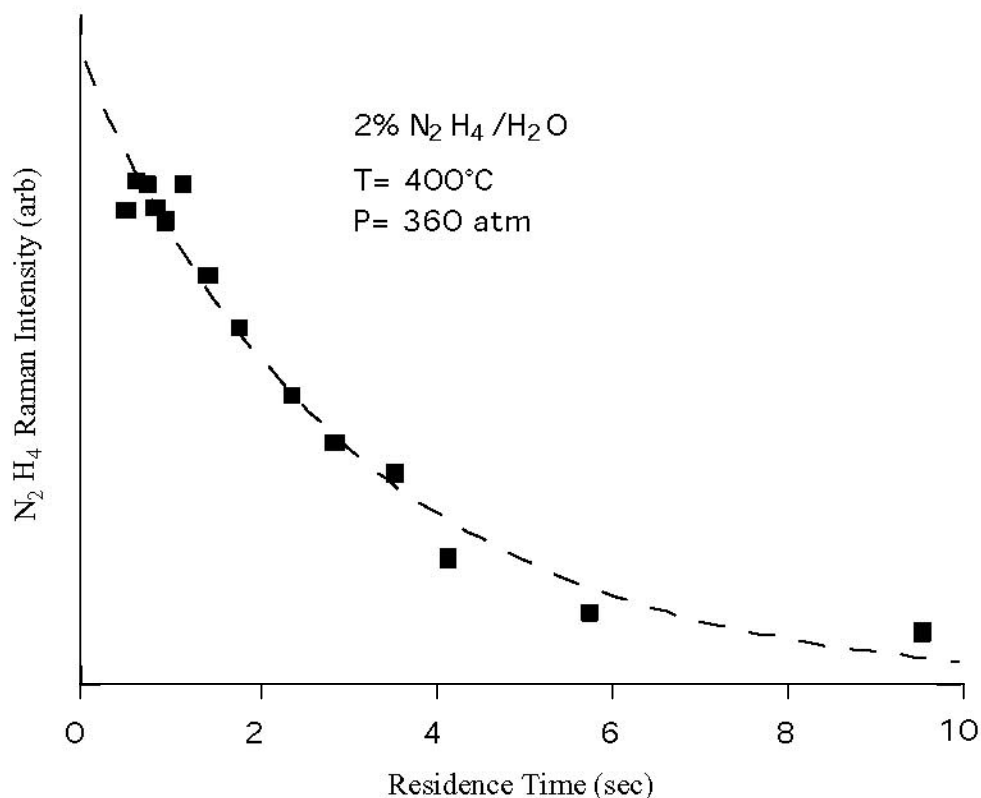


Figure 63. Decay of hydrazine Raman intensity as a function of average residence time in the optical cell. The dashed line is an exponential fit to the data.

function of residence time to verify that it was approximately exponential. Agreement between the two methods was excellent. In this way, an Arrhenius plot for the rate is generated, as shown in Figure 64. We derive the rate expression  $k(\text{sec}^{-1}) = 5.2 \times 10^8 \exp(-14220/T)$ . It is interesting to note that the critical temperature of water (647 K, or  $1000/T_c = 1.55$ ) is situated in the middle of the range of our measurements shown in Figure 64. There does not appear to be any anomalous or discontinuous behavior of the rate as one passes through the critical temperature.

Tsang (Reference 38) has analyzed the available data on the elementary hydrazine decomposition reaction and used RRKM theory to derive the high-pressure limit,  $k_\infty$ . Pressure-dependent measurements suggest that this reaction should be at the high-pressure limit under our conditions. Tsang gives a rate of  $k_\infty(\text{sec}^{-1}) = 10^{16.25} \exp(-32300/T)$  in the temperature range

840–1150 °C. It is probably not appropriate to extrapolate this rate down to 400 °C, but it is interesting to note that the extrapolation gives a rate in our temperature range that is much smaller than what we observe, by a factor of  $10^4$ . There are several possibilities for this

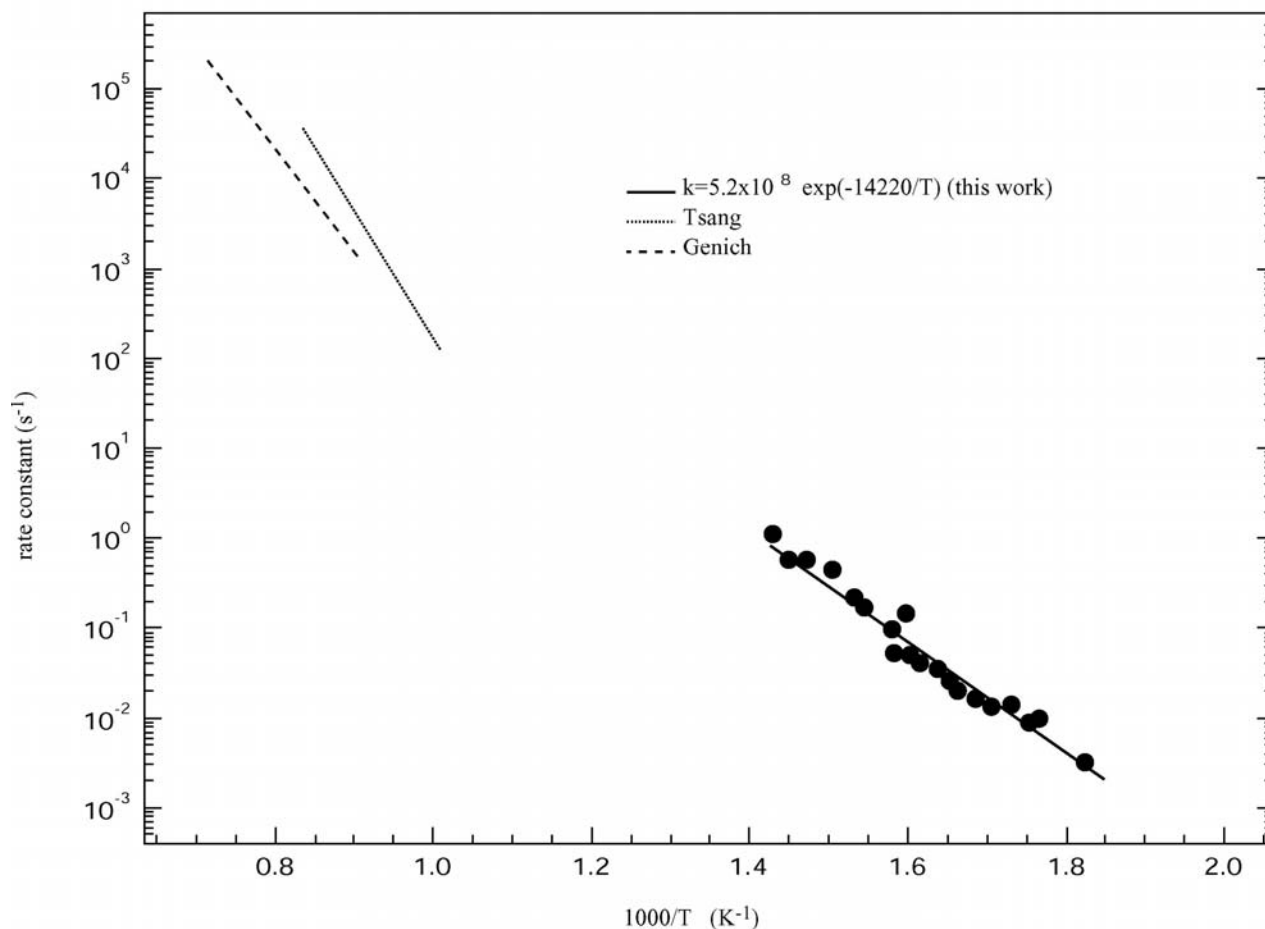


Figure 64. Arrhenius plot of effective first-order decay rate for 2%  $\text{N}_2\text{H}_4/\text{H}_2\text{O}$  at 350 atm. Rates were determined by monitoring Raman intensity as a function of temperature, shown as circles. Also shown are rates for reaction (1) in the gas phase (references 15, 19).

difference: (1) our disappearance rate could be influenced by chain-reaction processes; (2) the decomposition in our optical cell might be surface-catalyzed at the reactor walls (Reference 15); (3) the reaction mechanism in near-critical and supercritical water may be different from that in gases. Melius (Reference 39) has presented calculations relevant to the last possibility, which indicate that solvation can reduce activation barriers to reaction. In addition, uncertainties in reactor residence time and temperature may be important, as discussed below.



We measured the relative Raman cross sections of  $\text{N}_2\text{H}_4$  and  $\text{NH}_3$  in water for the bands near  $3300\text{ cm}^{-1}$  to quantify the amount of ammonia produced. We found that the  $\text{N}_2\text{H}_4$  cross section is greater by a factor of  $1.3 \pm 0.1$ .

Comparison of the intensity of the unreacted  $\text{N}_2\text{H}_4$  peak to the  $\text{NH}_3$  peak after reaction gives the conclusion that  $1.5 \pm 0.2$  moles of  $\text{NH}_3$  were produced per mole of  $\text{N}_2\text{H}_4$  consumed. This is greater than the 0.9–1 mole of  $\text{NH}_3$  produced in the gas phase (References 13–14) and close to the 1.3 moles of  $\text{NH}_3$  observed for heterogeneous decomposition. (Reference 15) We also expect to produce  $\text{N}_2$  and  $\text{H}_2$  in this reaction. (References 13–19) These products were not observed, probably due to their smaller Raman cross sections and the limited sensitivity of our measurements.

These experiments were carried out at low flow rates, where the Reynolds number for the fluid flow is fairly small (in the range 10–1000). In the absence of disturbances, this would give rise to laminar flow, in which the reactor has a distribution of residence times rather than a single, well-defined residence time. Also, it is possible that a radial temperature gradient could exist in the fluid. These uncertainties make it difficult to derive reliable decomposition rate constants from the data. Although the plug-flow approximation can be used at low Reynolds numbers if certain criteria are satisfied, (Reference 37) those conditions were not always met in these experiments. In addition, the heat-up time of the fluid in the reactor was not measured and was a function of flow rate. However, preliminary fluid dynamics calculations that we have carried out using the code FLUENT (Fluent, Inc., Lebanon, N.H.) suggest that the heat-up time is much shorter than the 3 seconds reaction time shown in Figure 63, page 130. The calculated radial temperature distributions in the fluid are fairly narrow. In addition, natural (gravity-induced) convective heating effects and obstructions in the flow tube may disrupt the flow patterns and impart some degree of turbulence to the fluid, which is desirable for use of the plug-flow approximation. Therefore, one must exercise care in interpreting the results in a more quantitative fashion.

## B. RAMAN MEASUREMENTS OF NITROMETHANE (NM)

Raman spectra of 0.15–10% nitromethane/water mixtures were collected at temperatures from 500–560 °C at pressures near 5500 psi. The flow rates of the solutions through the reactor were varied from 0.1 to 2 g/minute, corresponding to reactor residence times of 0.2 to 3 seconds. The evolving concentration of the nitromethane was determined by integration of the Raman

scattering intensity of the methyl stretching peak near  $2980\text{ cm}^{-1}$ . The C–N stretching peak at  $900\text{ cm}^{-1}$  was also monitored. Decomposition of NM and formation of product  $\text{CH}_4$  ( $2914\text{ cm}^{-1}$ ) was observed at temperatures above  $520^\circ\text{C}$ . An example at  $554^\circ$  is shown in Figure 65.

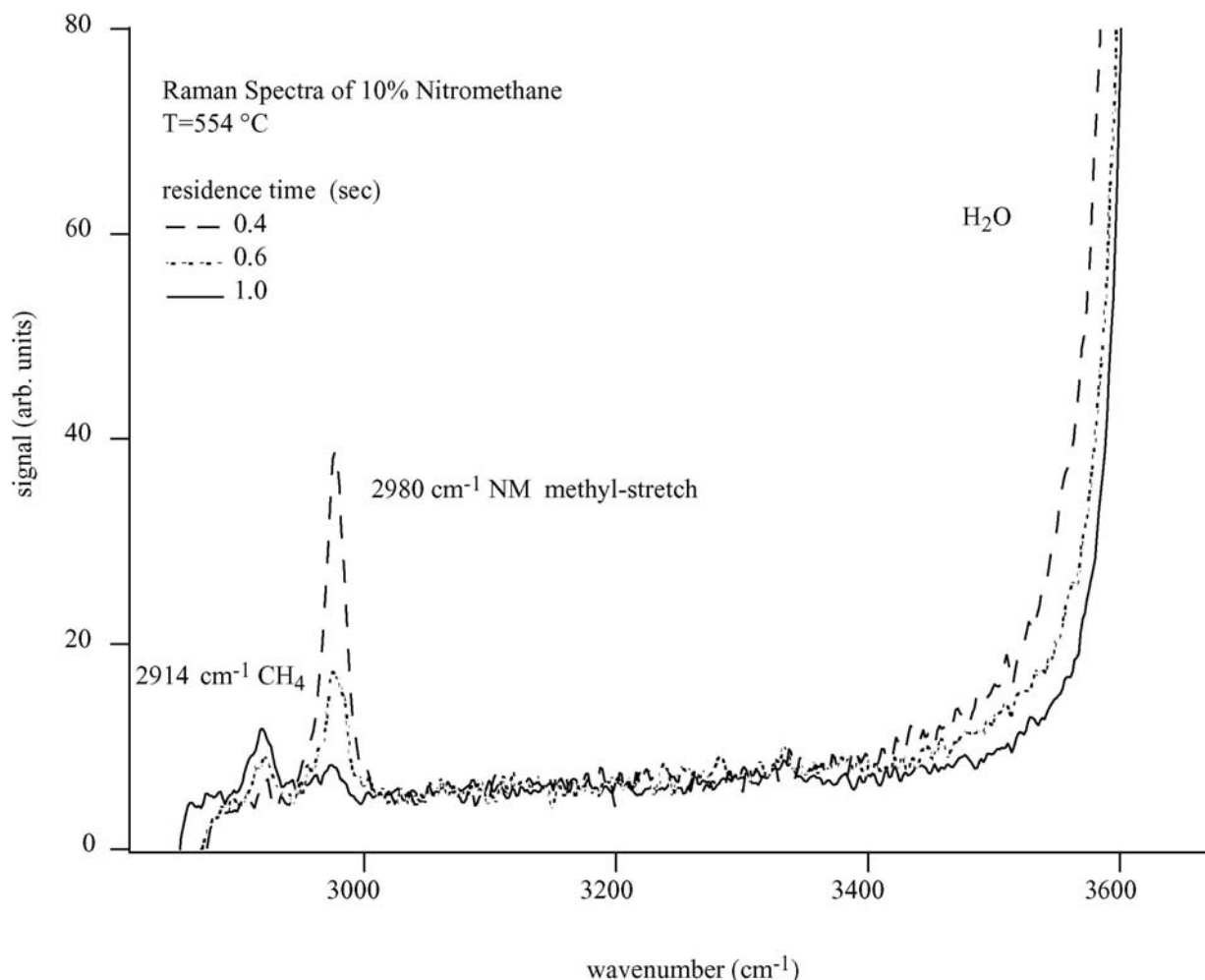


Figure 65. Raman spectra of 10% nitromethane in water at  $554^\circ\text{C}$  and 370 atm the region of the methyl stretching vibration

Figure 66 shows the time history of a 10% solution at two temperatures. At longer times, full destruction of the nitromethane, within experimental uncertainties, was observed.

Although the limited signal-to-noise ratio does not permit us to rule out non-exponential decay of the concentration, we can assign effective first-order rate constants for decomposition in four experiments. The rate constant for nitromethane decomposition determined from these optical measurements is combined with determinations from end product analysis of total

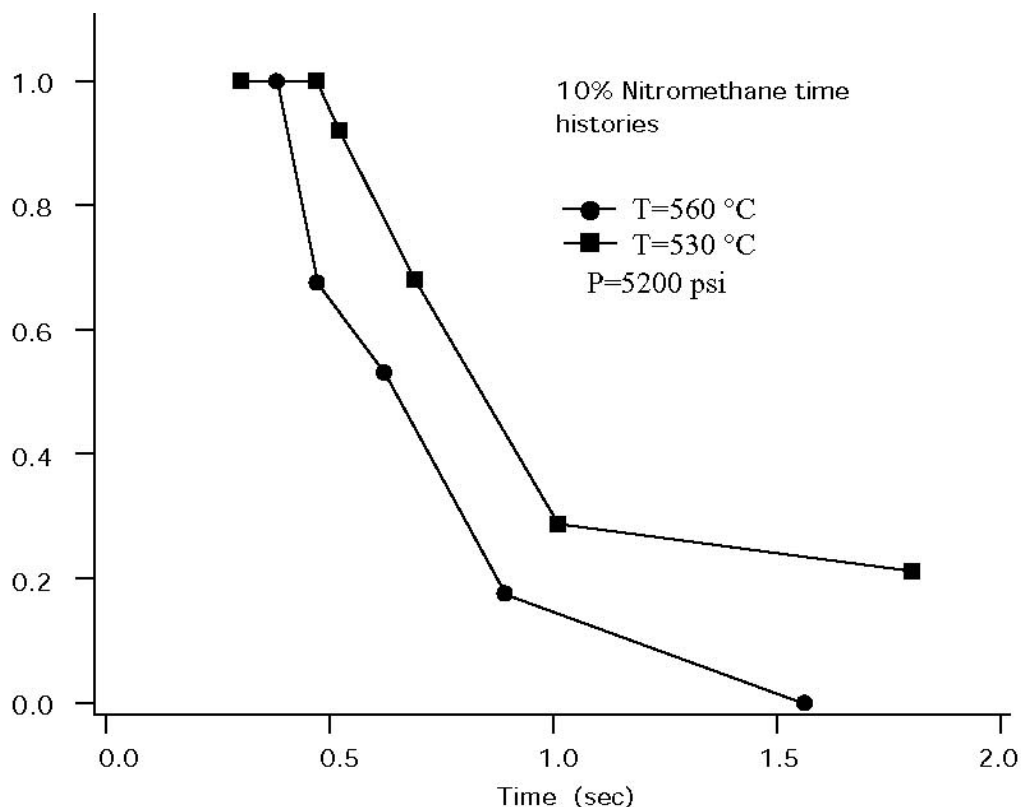


Figure 66. Decay of nitromethane Raman intensity as a function of Residence time in the optical cell.

organic carbon (TOC) from our flow reactor and results of sub-critical temperature experiments at SRI (Reference 40) (Figure 67). It is encouraging to note the good agreement, and fit to an Arrhenius expression, over a wide temperature range with diverse experimental setups.

Addition of hydrogen peroxide accelerated the nitromethane reaction rate. Three seconds residence time was sufficient for the destruction in mixtures of 10% nitromethane and twice stoichiometric  $H_2O_2$  at 280 °C and 3000 psi. In this case, methane was not an observed product.

### C. RAMAN MEASUREMENTS OF AMMONIUM PERCHLORATE (AP)

Raman spectroscopy followed the decomposition of AP in supercritical water. The optically accessible reactor (Figure 23, page 39) was configured as a batch reactor and coupled to a pressure intensifier with water used as a pressure-transfer fluid. Ammonium perchlorate solutions were prepared at a concentration of 100 g/L, which is about half the solubility limit at room temperature. Small samples (0.1 mL) were loaded into the reactor and heated to 550 °C.

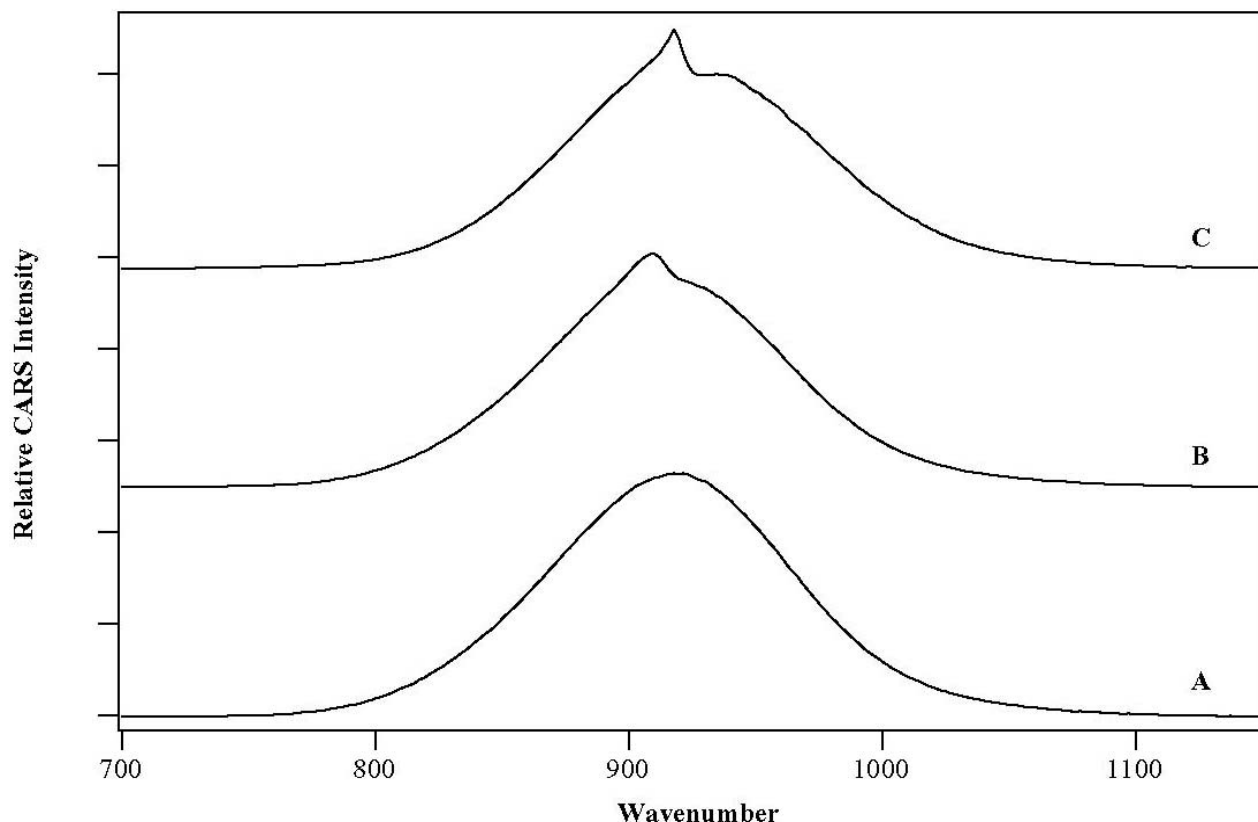


Figure 67. CARS spectra of NM in water at high pressure (348 atm). (A) Non-resonant water background; (B) Supercritical water (410 °C); (C) Subcritical water (20 °C).

Temperature, pressure and Raman spectra were recorded once every 10 seconds. At temperatures below the critical point of water, the perchlorate ion produced a strong Raman signal (the symmetric Cl–O stretch at  $974\text{ cm}^{-1}$ ). The Raman peak of the ammonium ion near  $3100\text{ cm}^{-1}$  could not be observed because it lies near the strong, broad O–H stretching peak of liquid water. Near the critical temperature ( $374\text{ °C}$ ), the Raman scattering from the perchlorate ion disappears and a feature at lower energy appears for about 10 seconds, after which it disappears. When the solution is cooled, the perchlorate signal does not reappear indicating that it has reacted. A fine black powder remains as a suspension in solution after the reaction. Analysis of this powder using inductively-coupled plasma atomic emission (ICP-AE) indicated that it contained large amounts of iron with trace amounts of other metals. These suggest that perchlorate ion reacts with the 316 stainless-steel reactor walls to form metal oxides.

#### D. MEASUREMENTS OF NITROMETHANE USING CARS

The CARS spectra of 5 percent nitromethane in water are shown in Figure 68. Shown in the figure are (a) the spectrum of pure water at 410 °C and 340 atm, the spectrum of the MN/water mixture at (b) 410 °C and 340 atm, and (c) room temperature and 340 atm. Spectrum (a) shows the contribution made by the nonresonant CARS generated by the water and by the diamond windows of the cell. This produces a large background "hump" in all of the spectra. The shape of the hump reflects the spectral profile of the broadband laser. The sharp feature in the center of the spectra (b) and (c) is due to the Raman band of nitromethane at  $917\text{ cm}^{-1}$ , which corresponds to the C–N stretching motion of the molecule.

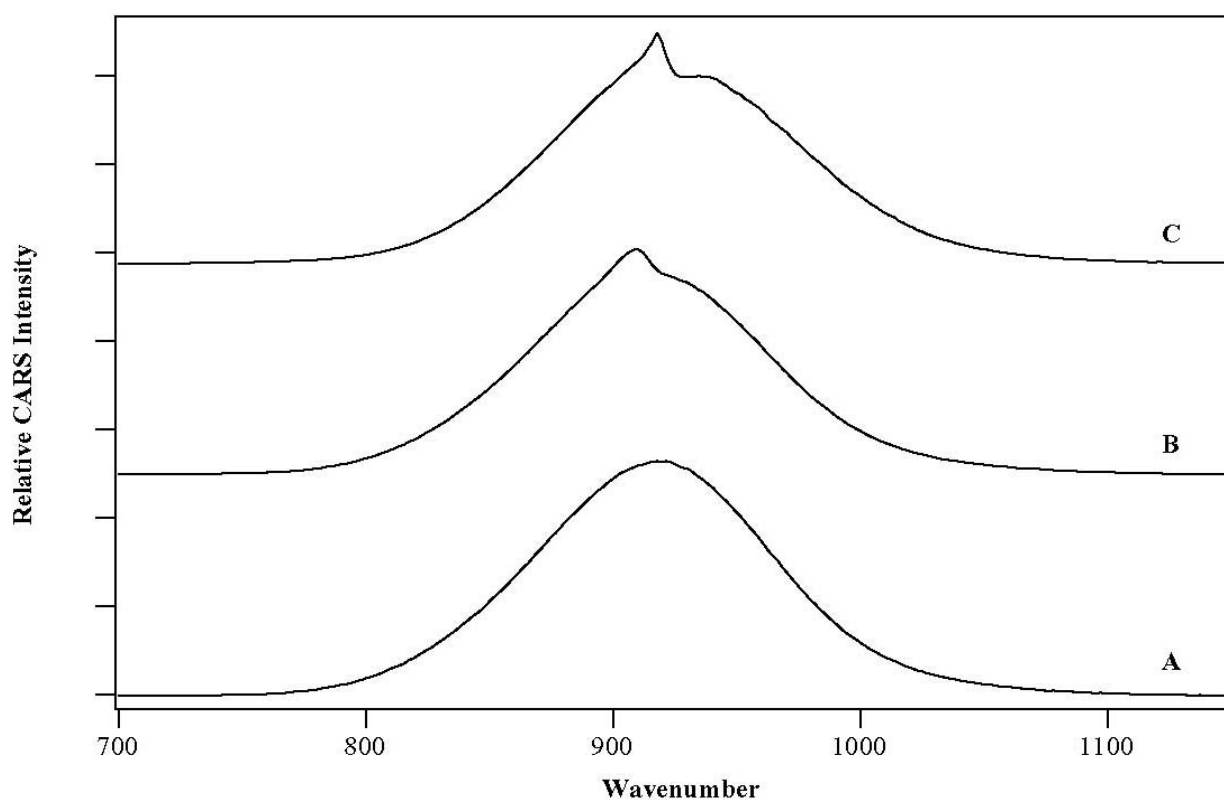


Figure 68. CARS spectra of NM in water at high pressure (348 atm). (A) Non-resonant water background; (B) Supercritical water (410 °C); Subcritical water (20 °C).

The most salient difference between the CARS spectra at room temperature and supercritical temperatures is the width of the spectrum, which increases from  $2\text{ cm}^{-1}$  at 20 °C to  $8\text{ cm}^{-1}$  at 410 °C. In the room-temperature liquid, the Raman spectrum of the molecule consists of a single, sharp vibrational transition. As the temperature increases, the density

decreases, and nitromethane becomes more of a gas-phase-like molecule that can rotate freely. The rotation gives rise to additional structure within the vibrational band. Although this additional structure cannot be resolved under these conditions, it appears as a broadening of the Raman spectrum. Hence, optical diagnostics of solute molecules in supercritical water can give information on the solvation environment.

Analysis of the observed CARS line shapes would be simplified considerably if the nonresonant contribution from the water solvent and the diamond windows were absent. It is possible to eliminate this contribution with a modification of the technique that involves rotating the polarizations of the input laser beams and using polarization filtering of the signal beam.

#### E. TRANSIENT GRATING EXPERIMENTS

Experiments were performed to demonstrate the feasibility of measuring thermal diffusion constants and the speed of sound on hydrothermal solutions using the transient grating technique. Thermal grating decay rates were measured for  $I_2$  dissolved in aqueous KI solutions. Figure 69 shows a typical thermal grating decay for a solution at 5040 psi and 400 °C, and a fringe spacing

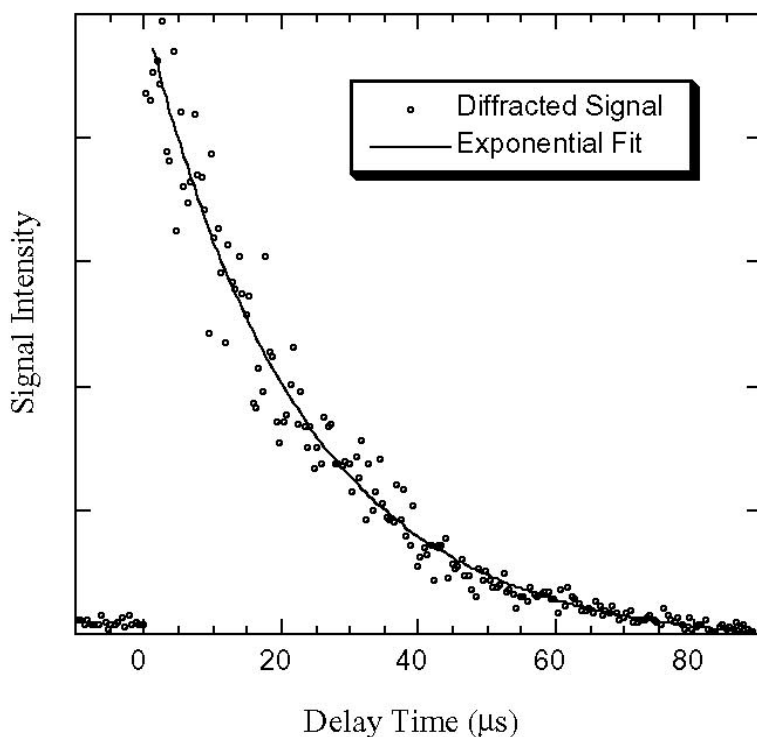


Figure 69. The thermal grating decay for an  $I_2$  + KI + water solution at 400 °C and 5040 psi. The line is the least-squares fit of the data. The grating fringe spacing is 16.1  $\mu\text{m}$ .

of  $13.5\ \mu\text{m}$ . The line is the least squares fit to an exponential function and has a lifetime of  $42.1 \pm 2.3\ \mu\text{s}$ , which corresponds to a thermal diffusivity  $(0.56 \pm 0.03) \times 10^{-3}\ \text{cm}^2\ \text{s}^{-1}$ . The thermal diffusivity of pure water under these conditions is  $0.69 \times 10^{-3}\ \text{cm}^2\ \text{s}^{-1}$ . Ultraviolet-transmitting diamond windows (Type I) would allow the technique to be applied to virtually any UV or visible light absorbing hydrothermal solution.

Figure 70 shows the grating signal resulting from acoustic waves generated in the same  $\text{I}_2 + \text{KI} + \text{water}$  solution at  $450\ ^\circ\text{C}$  and  $5060\ \text{psi}$ . The fringe spacing is  $13.5\ \mu\text{m}$  and the acoustic signal period is  $28.3\ \text{ns}$ . The measured speed of sound is  $477\ \text{m}\ \text{s}^{-1}$ . This measured speed is reasonable as the speed of sound of pure water under these conditions is  $505\ \text{m}\ \text{s}^{-1}$ . The fastest speed of sound that can be measured with the current 10-ns pulse width lasers is approximately  $1000\ \text{m}\ \text{s}^{-1}$ . Measurements of faster speeds requires larger fringe spacings, but a grating needs greater than about 20 fringes for efficient probe scattering, and the current diamond window aperture of  $600\ \mu\text{m}$  limits the feasible fringe spacing to less than about  $30\ \mu\text{m}$ .

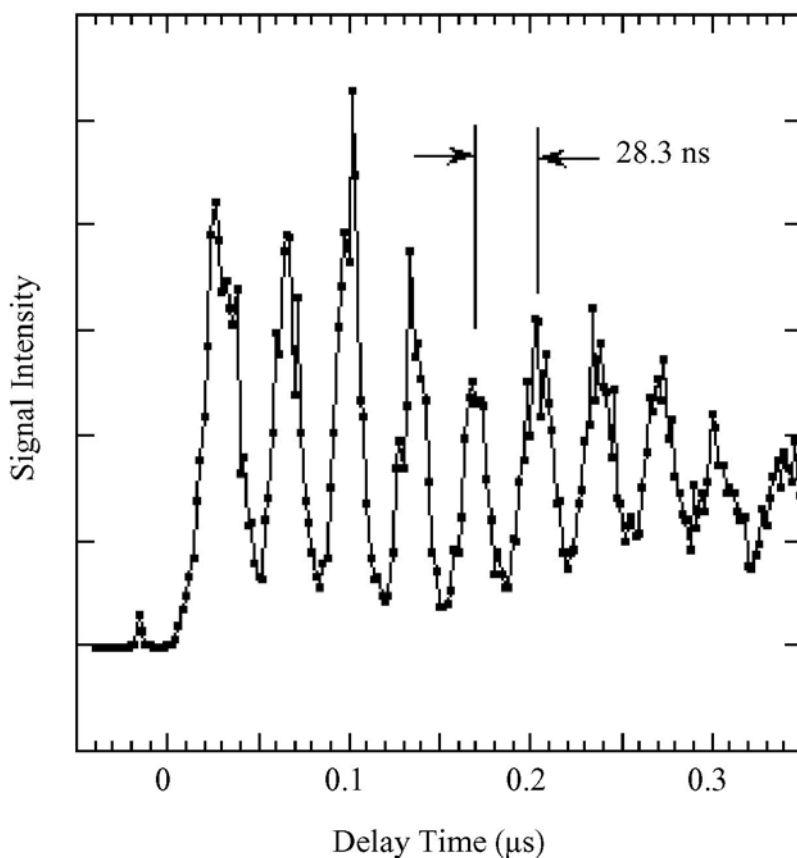


Figure 70. Transient grating signal from acoustic wave generated in a methanol/dye solution at  $450\ ^\circ\text{C}$  and  $5060\ \text{psi}$ . The grating fringe spacing is  $13.5\ \mu\text{m}$  and the acoustic signal period is  $28.3\ \text{ns}$ .

## SECTION VI

### THERMOCHEMISTRY OF ENERGETIC MATERIALS IN SUPERCRITICAL WATER

While supercritical water oxidation appears to have great potential as a way to dispose of energetic materials cleanly and safely, because of the nature of these materials, it is imperative to determine the heat released during the process. We used a commercial (Setaram 121) differential scanning calorimeter (DSC) to measure heats of reaction under supercritical conditions. We measured heats of decomposition for ammonium perchlorate (AP), neat and in aqueous solutions, using cells supplied with the DSC at supercritical conditions. Results are given in Table 44.

TABLE 44. HEAT OF DECOMPOSITION OF AP IN STAINLESS STEEL CELLS

Weight of AP (mg)	Melting Point (°C)	Temp. of Decomp. (°C)	Heat of Decomp. (cal/g)
Neat AP			
3.90	243	357	440
3.32	244	356	406
2.79	242	366	374
2.31	242	367	393
1.85	241	357	335
5.1M AP in aqueous solution			
0.6	--	251	2165
0.6	--	263	2448
0.6	--	253	2210
0.1M AP in aqueous solution			
0.176	--	333	2542
0.176	--	329	2547
0.176	--	334	2346
0.265	--	336	2130
0.352	--	343	2590



Neat AP melts at 242 °C and decomposes at 349–373 °C with heats of 334–440 calories per gram AP. The decomposition in aqueous solution exhibits different behavior. Solutions 0.1*M* in AP decompose at 329–343 °C with heats of 2130–2590 calories per gram AP. With 5.1*M* solutions of AP, a decrease in the temperature of decomposition to 251–263 °C is observed. However the measured heats of decomposition, 2164–2447 calories per gram AP, are similar to those for the 0.1*M* solutions. These results may indicate a strong influence of water on the energetics of decomposition of AP.

## SECTION VII

### REACTOR CORROSION

#### A. REACTOR METALLURGY AND CORROSION

One of the most critical issues affecting the practical implementation of SCWO processing to the treatment of energetic materials is reactor wear caused by corrosion. Corrosion of the Hastelloy C-276 reactor was not found to be a major problem with most of the energetic materials investigated. The exception was ammonium perchlorate (AP), which caused severe corrosion of C-276 and, under certain conditions, the 316-SS gold-lined reactor. However, corrosion by AP was reduced to acceptable levels in the gold-lined reactor by adding caustic to maintain a basic *pH*.

#### B. CORROSION CAUSED BY SCWO REACTIONS OF ENERGETIC MATERIALS

On occasion, we experienced mild to severe corrosion of experimental test apparatus. Corrosion reactions at the reactor wall may affect the reaction process under investigation, and in the extreme resulted in failure of pressure-containing components. Our experiences with corrosion caused by SCWO reactions of energetic materials are described in this section.

##### 1. Corrosion by SCWO of Ammonium Perchlorate (AP)

The only compound for which any reactor-dependent chemistry has been observed is AP. The destruction chemistry of AP in SCWO is unique among the energetic materials since AP has no carbon, and is a strong oxidant that contains chlorine. The chemistry is best described by the following equation:



The Cl is converted into  $\text{Cl}^-$ , formally reduced from  $7^+$  to  $1^-$ , and excess oxygen is produced in the reaction. The highly oxidizing nature of this reaction is evident by the strong oxidative corrosion of the Hastelloy C-276 reactor. The addition of reducing equivalents, in the form of a fuel such as a hydrocarbon, may improve the destruction of AP as well as reduce the reactor corrosion.

Corrosion problems with the Hastelloy C-276 reactor caused most of these reactions to be performed in the gold-lined reactor. Sodium hydroxide was added to the AP solutions in a 1:1 stoichiometry to ensure a net *pH* balance. However, we ran AP in the gold-lined reactor at both high and low *pH*. Significant corrosion was observed in acidic solutions of AP. At low *pH*, the oxidation of gold,  $\text{Au}^0 \rightarrow \text{Au}^{+3} + 3\text{e}^-$ , is activated. The oxidant could be  $\text{NO}_3^-$  produced in the decomposition of AP or the perchlorate itself. Gold complexes with chloride ion and dissolves as  $\text{AuCl}_4^-$ . The reactions are analogous to the well-known dissolution of gold in aqua regia. Raising the *pH* blocked this corrosion pathway was as shown in Table 45.

An interesting observation with the gold-lined reactor was a lower destruction efficiency for AP compared to that found for the Hastelloy C-276 reactor. We attribute this difference to the absence of reactions with the reactor walls in the case of the gold-lined reactor. The extensive corrosion of the Hastelloy C-276 reactor by AP reactions supports this conclusion.

TABLE 45. CORROSION PRODUCTS FOR SCWO OF AMMONIUM PERCHLORATE

Reactor Material	Au (ppm)	Cr (ppm)	Fe (ppm)	Mo (ppm)	Ni (ppm)
Hastelloy C-276	---	130.00	---	54.00	39.00
Gold-lined 316SS (acidic)	1622.00	3.36	65.38	---	55.04
Gold-lined 316SS (alkaline)	0	0.99	0.99	---	3.73

## 2. Corrosion by TNT, HMX, PETN and RDX

Corrosion products from the Hastelloy C-276 reactor are given in Table 46. No significant difference in DREs and products chemistry was observed for reactions of TNT, HMX,

TABLE 46. CORROSION PRODUCTS FOR SCWO OF EXPLOSIVES IN HASTELLOY C-276 ALLOY LINEAR REACTOR

Substrate	Cr (ppm)	Fe (ppm)	Mo (ppm)	Ni (ppm)
TNT	0.246	<0.02	0.095	<0.02
RDX	0.085	<0.01	<0.01	0.075
HMX	0.097	0.013	0.07	0.0375
PETN	<0.01	0.032	0.62	0.0572

PETN and RDX in the Hastelloy C-276 and the gold-lined reactors. We conclude from these observations that reactions with the Hastelloy C-276 and 316 stainless walls must not be significant for these energetic materials. The metals concentrations in the reactor effluent were just above background levels, corroborating the above conclusion.

### 3. Corrosion by Nitrate

Nitrates are formed when explosives are oxidized in supercritical water. As discussed in previous sections, the amount of nitrogen converted to nitrate and nitrite depends upon the substrate and the reaction conditions. A nitrate pyrolysis run was also conducted. At 525 °C and a 12.6-second residence time, a maximum nitrate conversion (to nitrite) of 36 percent was observed. No ammonia was detected from nitrate pyrolysis at 525 °C. In addition to analysis for carbon and nitrogen species, aqueous effluent and reactor rinse samples were also analyzed for sodium (present in the sodium nitrate feed) and corrosion products (Fe, Cr, Mo, and Ni). We recovered trace amounts of corrosion products in all experiments. While iron and nickel appeared only at sub-ppm levels in all experiments, chromium and molybdenum were present at higher concentrations in both effluent and rinsewater samples. At temperatures above 500 °C, these species have been recovered primarily in reactor rinsewater samples. These samples, which were yellow tinted, we believe contain the hexavalent forms of chromium ( $\text{CrO}_4^{=}$ ) and molybdenum ( $\text{MoO}_4^{=}$ ). These species likely deposited on the reactor walls as sodium salts. Sodium also precipitated substantially with carbonate species. These precipitation reactions were supported by ion balances performed on reactor rinse samples. Such balances were successful in predicting measured *pH* values to within one *pH* unit. Effluent concentrations of sodium, bicarbonate, chromium and molybdenum decreased with increasing temperatures, which indicated decreasing solubilities with increasing temperatures. The absence of iron and nickel in the rinse effluent indirectly suggests formation of an insoluble passive oxide film on the reactor surface. However, no metallographic examination was conducted to verify this.

### 4. Corrosion by Hydrazine

We also investigated the reactions of hydrazine with an oxidizer in SCW. We chose the nitrate anion as the oxidizer to simulate reactions of nitrogen tetroxide, since we expect to produce nitric and nitrous acid upon dissolution of  $\text{N}_2\text{O}_4$  in water. We expected the following reaction of hydrazine with nitrate:



We used a new Hastelloy C-276 reactor for this reaction, having the unique feature of vertical orientation, with the flow against gravity. This feature caused problems since one of the products of this reactions is NaOH as shown in the above equations. NaOH is molten above 300 °C and apparently forms a separate, molten alkaline salt phase at the concentrations we used (1000 ppm NaOH). This molten alkaline phase settled out in the bottom of the reactor, aided by gravity and produced severe corrosion in this part of the reactor, requiring rebuilding.

A reaction was also run using nitric acid as the source of nitrate oxidizer using the following assumed reaction stoichiometry:



With higher acid concentrations ( $\text{pH}=1$ ) we again experienced severe reactor corrosion leading to plugging. In this case the corrosion was confined to the preheater section of the reaction tube.

## C. CORROSION TESTING OF REACTOR MATERIALS

### 1. Introduction

Predicting corrosion rates for structural materials in high-temperature hydrothermal processing environments was not possible due to (1) a general lack of corrosion data at elevated temperatures and pressures, and (2) poor understanding of basic corrosion mechanisms in high-temperature supercritical dense-phase systems. The situation was further complicated by the sheer complexity of the substances proposed for treatment, the variety of possible corrosion mechanisms, and the wide range of operating pressures and temperatures and oxidizing/reducing environments under consideration.

Nevertheless, given the need to identify corrosion resistant materials for the construction of process equipment, we started a corrosion testing and evaluation program. We began to investigate the corrosion resistance provided by several alloys, hoping to gain a better understanding of the corrosion processes that are active in hydrothermal processing systems.

Corrosive attack may occur via a number of mechanisms that may act individually or in combination to render a particular material unsuitable for a particular process application. Nine of the more common corrosion attack mechanisms follow:

- 1) Uniform corrosion
  - a) electrochemical
  - b) direct attack (chemical reaction)
- 2) Pitting corrosion
- 3) Crevice corrosion
- 4) Galvanic corrosion of dissimilar metals
- 5) Stress corrosion cracking
- 6) Intergranular corrosion
- 7) Dealloying
- 8) Embrittlement
- 9) Corrosive wear.

The type of corrosion mechanism active in a particular location is strongly affected by the fluid phase or phases present. For hydrothermal processing systems, it is necessary to investigate corrosion mechanisms that might occur in the preheater and cooldown heat exchangers, as well as in the main process reactor. The preheater and cooldown heat exchangers will be exposed to phases ranging from a cool liquid/slurry at one end, to hot supercritical dense phase with the possible presence of molten salts at the other end. The cooler liquid regions perhaps favor ionic electrochemical attack, and the hotter regions perhaps favor gas-phase oxidation/direct attack.

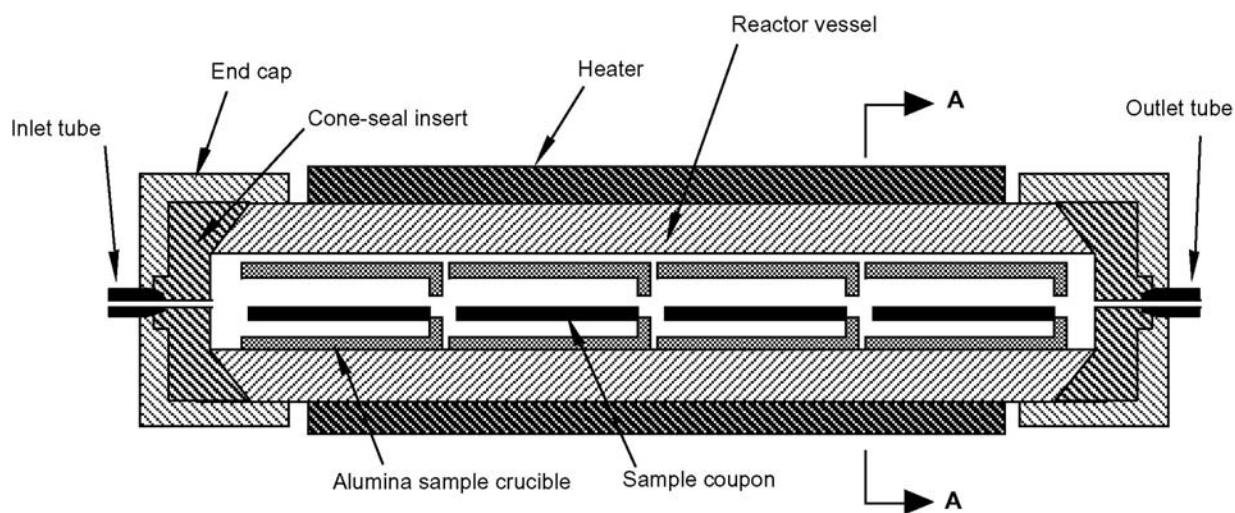
## 2. Discussion of Corrosion Testing Methods

### a. Coupon Testing

In view of the variety of available alloys and pure metals, the number of known corrosion mechanisms, and the many environmental factors affecting corrosion, our initial approach was to try to reduce the number of variables for study. We carried out a two-tiered investigation: First, the weight change caused by exposure to supercritical conditions was measured for a variety of sample coupons to investigate resistance to uniform corrosion and pitting corrosion. For these tests we exposed sample coupons to basic (NaOH) or acidic (HCl) solutions of increasing concentration. Second, those materials exhibiting resistance in these tests were short-listed for future, more rigorous investigation into resistance to other corrosion mechanisms. In subsequent testing, the test coupons could be so arranged as to simulate tensile/residual stresses, welds, crevices, and contact between dissimilar metals.

An extended coupon-testing program will be difficult to perform for two reasons. (1) It is necessary to construct an experimental apparatus that can contain high temperature, high pressure, and a variety of potentially highly corrosive substances in a safe and predictable manner for an extended period, and (2) reliability of delicate HPLC pumps and precision high-pressure pressure regulators will be poor due to the corrosive, non-homogeneous nature of the fluid media.

While we considered ways to build a safe and reliable test apparatus for the future, we assembled a temporary corrosion test apparatus as depicted in Figures 71 and 72,



(NOTE: Actual reactor holds 12 sample crucibles)

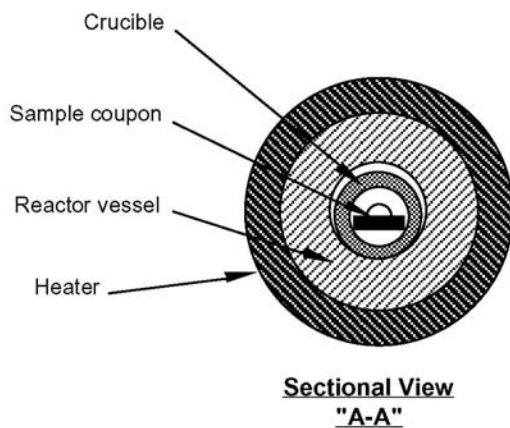


Figure 71. General arrangement of a SCWO corrosion test reactor.

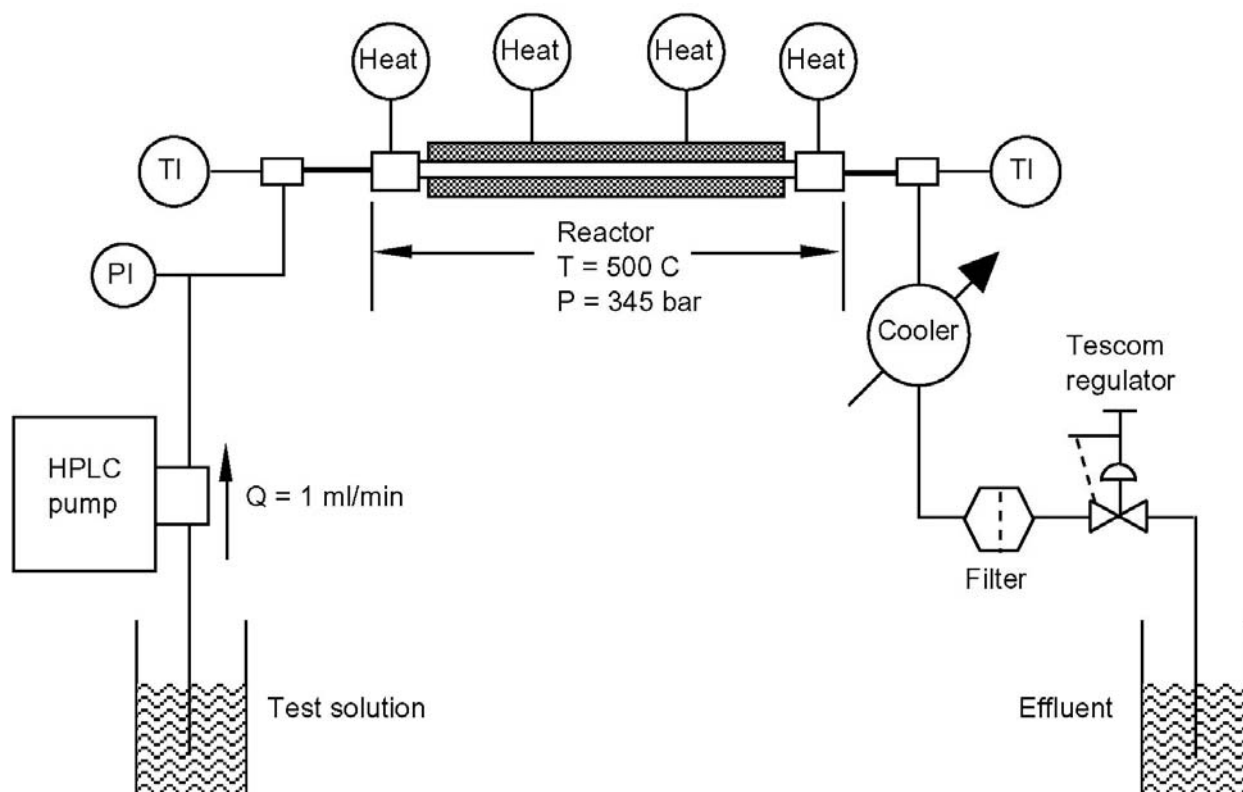


Figure 72. Flow Schematic of SCWO corrosion test loop.

and obtained sample coupons of a wide variety of alloys and pure metals. Our temporary apparatus included a 1/2 in. id x 20 in. long 316-SS tubular reactor vessel and 6,000-psi-rated Tescom regulator. Sample coupons were approximately 0.25 in. wide x 1.375 in. long x 0.0625 in. to 0.125 in. thick. As a safety precaution the high-temperature components were located behind a Lexan barrier in a limited access area. The nominal composition of alloys tested to date can be found in Table 47.

#### b. Corrosion by Basic Solutions

High concentrations of PEPs may be safely introduced into hydrothermal processing reactors by first hydrolyzing the material in a basic solution of NaOH. Base hydrolysis produces water-soluble materials that can be pumped to high pressure for hydrothermal processing. Due to the caustic nature of the hydrolysis products, there is a need to identify suitable corrosion-resistant structural materials for the reactor that will hold up in caustic environments. The required concentration of base has been observed to be as high as 1.0M. We decided to examine corrosion resistance to NaOH solutions of increasing concentration, without



TABLE 47. NOMINAL COMPOSITION OF TEST ALLOYS

Alloy	Cr %	Ni %	Mo %	Co %	W %	Fe %	Other	Test Status
Haynes alloy HR-160	28	37	0	29	0	2		NaOH test
Haynes alloy N	6	71	15	0.2	0.5	5	1.0% Si	NaOH test
Haynes alloy 230	22	57	2	5	14	3		NaOH test
Inconel 625	21	62	9	1	0	5	3.7% Cb	NaOH test
Hastelloy C-276	16	57	16	2.5	4	5	1.0% Mn	NaOH test
Al <sub>2</sub> O <sub>3</sub> -coated Ultimet	26	9	5	54	2	3		NaOH test
Haynes alloy 214	16	75	0	0	0	3	4.5% Al	
Haynes alloy 556	22	20	3	18	2.5	31		
Haynes alloy G-30	28	43	4	5	1.5	13	1.5% Mn	
Hastelloy C-22	22	56	13	2.5	3	3		
Haynes alloy HR-120	25	37	2.5	3	2.5	33		

the presence of an oxidizer. In view of the low concentrations of corrosion products previously observed with basic solutions, it was felt that the 316-SS reactor might allow testing for a reasonable period. Operational limitations imposed a maximum coupon exposure time of 5.0 hours. Based on this exposure time, sample coupon surface area, and maximum sensitivity of the precision laboratory balance, the corrosion rate resolution could be as low as 1.0 mils/year equivalent weight change. The results of these tests can be found in Table 48, as follows:

TABLE 48. AVERAGE COUPON WEIGHT CHANGE

	[Na <sup>+</sup> ],ppm	2.29	22.9	229	458
	Theoretical pH	10	11	12	12.3
Hastelloy C-276		-0.002%	0.023%	0.028%	0.046%
Haynes Alloy 230		0.005%	0.019%	0.046%	0.092%
Inconel 625		-0.006%	0.004%	0.026%	0.025%
Haynes Alloy HR-160		-0.003%	0.017%	0.000%	0.011%
Haynes Alloy N		0.009%	0.004%	-0.010%	0.050%
Al <sub>2</sub> O <sub>3</sub> -coated Haynes Ultimet		0.135%	0.046%	0.374%	0.430%

From the above it appears that the coupons tended to gain weight during the test. All coupons experienced an increasing weight gain with increasing  $[Na^+]$ , except for Haynes Alloy HR-160 and Haynes Alloy N. Comparison against Inconel 625 was considered important, as this alloy was the prime candidate for pilot-scale plant fabrication, although it is expensive and difficult to source in the required structural shapes.

Testing was interrupted twice due to reactor leakage. Disassembly and inspection of the inlet cone-seal insert revealed several fully-penetrating radial cracks. It is important to note that cracks occurred in both 316-SS and Hastelloy C-276 inserts. As cracking occurred shortly after switching from deionized water to NaOH solution of  $pH$  13, we believe the cracks were caused by the concentrated NaOH environment. Out of concern for the integrity of the 316-SS reactor, we limited testing to  $pH < 13$ .

During each test we periodically measured the  $pH$  of the test solution and effluent. We noticed that the  $pH$  of the effluent during the test never achieved the same value as the test solution  $pH$ , and that flushing the system with deionized water prior to cooldown/shutdown caused a sharp increase in effluent  $pH$ . We concluded that the NaOH was largely insoluble in water at test conditions, and was separating out as a molten NaOH phase at the bottom of the reactor vessel. Consequently, we could not determine what fluid phase (or phases) the coupons were exposed to. In view of this, we believe that the chosen experimental design was not suitable for corrosion testing under (potentially) multi-phase supercritical conditions. However, the test apparatus was adequate for corrosion testing under single-phase subcritical conditions.

#### c. Static Corrosion Test Apparatus

We designed an alternate test apparatus for testing under all conditions, including multi-phase supercritical conditions. This apparatus is depicted in Figure 73. In this design, instead of using sample coupons, we fabricated replaceable 3/8-in. od x 18-in. long tubular reactors from a variety of candidate alloys. Tube id was designed to produce a tensile stress at the inner wall near to the maximum ASME-allowable tensile stress for the test temperature and pressure. The system was designed to allow testing to 1,000 bar and 550 °C. By making the reactor tube itself out of the candidate material, we avoided the experimental problems associated with multi-phase segregation, and at the same time permitted investigation of the materials resistance to a far wider and more realistic range of corrosion mechanisms. At some future time, the reactor tubes will be charged with the actual waste or waste simulant at

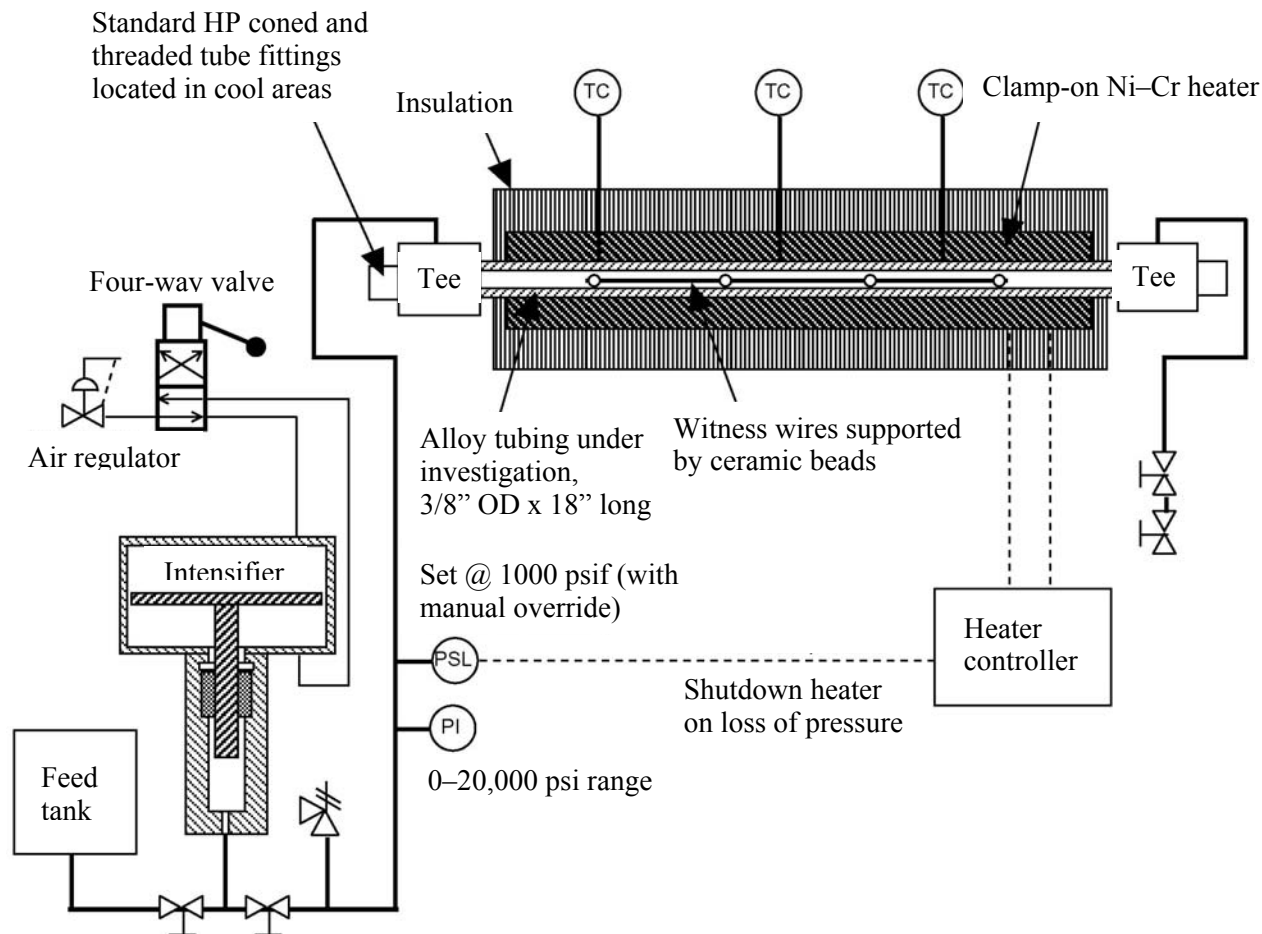


Figure 73. "Static" corrosion test reactor.

design temperatures and pressures, and held at these conditions for extended periods of up to several weeks, or until tube failure. To avoid problems associated with pump reliability and plugging of pressure regulators, we plan to maintain static pressure via an intensifier. If desired, the air pressure to the intensifier and the reactor temperature can be cycled for fatigue testing. We can also conduct extended testing with difficult-to-handle wastes, such as slurries, that would otherwise present pumping and plugging problems, which are difficult to address at the small scale. The design allows the periodic recharging of the system with fresh fluid. We will also be able to insert unstressed witness wires of various advanced materials and noble metal alloys which are being considered for unstressed internal system components, such as liners and sensor elements. Upon completion of the specified test period, the reactor tube will be removed and sectioned for comprehensive metallographic examination.

## SECTION VIII

### SALT SOLUBILITY STUDIES

#### A. INTRODUCTION

The solubility and phase behavior of compounds formed by base hydrolysis of propellants containing metallic aluminum is an important aspect of the treatability of such propellants in a hydrothermal system. Solubility depends in a complex way on the *temperature*, *pressure*, and overall *composition* (number and concentration of species). Salt solubility generally increases with increasing temperature; exceptions are salts—*e.g.*, carbonates—that exhibit retrograde solubility behavior. The temperature of a hydrothermal processing system is determined by maximizing the destruction efficiency of the hydrolyzed propellant components (which generally occurs at higher temperatures) while minimizing corrosion and other unwanted reactions (nitrate formation). Unfortunately, temperature-dependent solubility data from the literature do not generally extend to high enough temperatures to be in the "hydrothermal" range. Another difficulty is that the optimum hydrothermal processing temperature may be less than the liquid–vapor critical temperature ( $T_c$ ) of the solution, which adds the complexity of multi-phase behavior. Prediction of salt behavior for multi-phase conditions requires solubility data in both aqueous and vapor phases. Pressure determines the density of the hydrothermal medium, which in turn greatly influences salt solubilities; increasing the pressure increases the density, which in general increases salt solubility. Finally, salt solubility is determined by the solution composition. Base-hydrolyzed propellants are complex, multicomponent solutions containing a wide variety of ionic species. A reasonable approach to handling this complexity, however, is to focus on the solubility behavior of those components that are highest in concentration in the hydrolyzed propellant and/or are expected to be least soluble, based on knowledge of solubility at lower temperatures. Data for selected two- and three-component systems should prove valuable for predicting the behavior of a multicomponent system. We therefore chose to study the phase and solubility behavior of the two major components expected to be the least soluble of the products of base hydrolysis of aluminum-bearing propellants. These are 1) aluminates from the reaction of aluminum with strong base, and 2) carbonates from the base hydrolysis and subsequent hydrothermal oxidation of the organic components of the propellant.

## B. PRODUCTS OF BASE HYDROLYSIS OF ALUMINUM-BEARING PROPELLANTS

### 1. Composition of Aluminum-Bearing Propellants

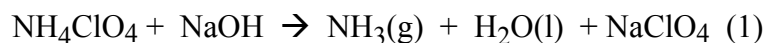
CYH is a typical aluminum-bearing propellant. The composition on a weight basis is approximately as follows:

ammonium perchlorate ( $\text{NH}_4\text{ClO}_4$ )	- 11%
aluminum	- 21%
energetic materials	- 68%.

The energetic materials are HMX, nitrocellulose, and nitroglycerin. We hydrolyzed a small amount of solid CYH in concentrated sodium hydroxide solution at room temperature, followed by heating to the boiling point for 30 minutes, after which no further reaction was evident (Reference 41). No attempt was made to analyze the gases evolved during the reaction, but the remaining solution was analyzed by ion chromatography. The products relevant to the solubility studies are discussed below. Our studies of the solubilities of these products under hydrothermal conditions assumed that the solution produced in the base hydrolysis step is hydrothermally processed without further treatment, for example to alter the *pH* or remove the aluminum.

### 2. Products of Ammonium Perchlorate Hydrolysis

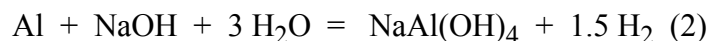
Ammonium ions react with strong base to produce ammonia and water:



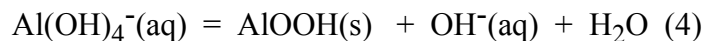
Since the solution was boiled in the last phase of base hydrolysis, most of the ammonia produced left the solution as a gas. The perchlorate ion does not react with base under hydrolysis conditions, so the net effect was to convert ammonium perchlorate into sodium perchlorate, which is a highly soluble salt.

### 3. Products of Aluminum Hydrolysis

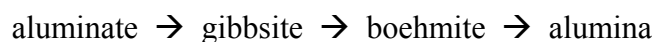
Under oxygenated conditions of base hydrolysis aluminum metal oxidizes to the  $3^+$  oxidation state. The presence of excess hydroxide causes the subsequent formation of "aluminate" ions, sometimes written as  $\text{AlO}_2^-$ , but more properly written as  $\text{Al}(\text{OH})_4(\text{H}_2\text{O})_2^-$ . We will abbreviate aluminate ions as  $\text{Al}(\text{OH})_4^-$ .



Sodium aluminate is highly soluble in water at room temperature, particularly in solutions of high  $p\text{H}$ , since high  $p\text{H}$  suppresses the formation of the insoluble compounds gibbsite,  $\text{Al(OH)}_3$ , and boehmite,  $\text{AlOOH}$ .



It was important to maintain high  $p\text{H}$  since Tikhonov (Reference 42) reports that, at low  $p\text{H}$ , the aluminum hydroxide gradually converts into boehmite at room temperature, and boehmite converts into alumina ( $\text{Al}_2\text{O}_3$ ) above 600 °C. [The above discussion is somewhat oversimplified since  $\text{Al(OH)}_3$  and  $\text{AlOOH}$  each have two isomers]. The reaction sequence



would cause severe plugging problems in a flow reactor because the last three species are insoluble at low  $p\text{H}$ . A much more favorable situation exists at high  $p\text{H}$ . Apps and Neil (Reference 43) measured equilibrium constants for reactions (3) and (4) between 0 and 350 °C. They found gibbsite and boehmite to be highly soluble in basic solutions, with solubility increasing with temperature along the vapor saturation curve. Extension to temperatures above the critical temperature of water is not straightforward, however. The presence of dissolved salts raises the liquid–vapor critical temperature of the solution, so that multi-phase behavior is possible at temperatures well in excess of 374 °C. Also, the dielectric strength of water decreases dramatically with increasing temperature and decreasing density above  $T_c$ . Therefore, salt solubilities are expected to decrease with increasing temperature, regardless of whether the system is a liquid, vapor, or supercritical fluid. Data in the literature are nonexistent for the system of interest above 350 °C. New experimental data are required to ascertain whether aluminum salts will stay in solution during hydrothermal processing.

#### 4. Products of Energetic Materials Hydrolysis

The carbon products of hydrolysis of CYH were mostly acetate and formate ions, with a small amount of carbonate and several less-abundant, unidentified species. Most of the nitrogen evolved as gas ( $\text{NH}_3$ ,  $\text{N}_2\text{O}$  and  $\text{N}_2$ ); the remaining nitrogen was in the form of nitrite

and nitrate anions. Slightly less than half of the carbon and nitrogen were accounted for in the solution, the rest presumably having left as gaseous species.

The carbon- and nitrogen-containing species resulting from base hydrolysis are not the most stable products possible; they reflect the fact that base hydrolysis was carried out at relatively low temperature, and equilibrium was not reached due to kinetic considerations. In studies of hydrothermal oxidation of organics at LANL (Reference 44), incomplete oxidation to form species such as acetate, oxalate, and formate ions is often observed at temperatures below 400 °C. At temperatures above 400 °C, however, oxidation of these anions to carbonate is virtually complete in a few seconds or less. Under these conditions, nitrite ions are effective oxidizing agents, the nitrogen ending up as either N<sub>2</sub> or N<sub>2</sub>O. At slightly higher temperatures, nitrate ions are similarly good oxidizing agents. The conclusion is that base hydrolysis of CYH propellant, followed by hydrothermal oxidation, will convert all of the organic carbon into either neutral species (gases) or carbonate anions, while all of the organic nitrogen will end up as neutral species or possibly as unreacted nitrite and nitrate anions. Nitrites and nitrates are in general highly soluble and are not expected to precipitate under hydrothermal conditions.

## C. PHASE BEHAVIOR UNDER HYDROTHERMAL PROCESSING CONDITIONS

### 1. Basic Aluminate and Carbonate Solutions

Having determined that aluminate and carbonate are the species most likely to produce precipitates in the hydrothermal processing of base-hydrolyzed CYH propellant, we turned our attention to the phase behavior of basic sodium aluminate and sodium carbonate solutions. It is well known that the liquid–vapor critical temperature of a solution of a nonvolatile salt in water is higher than that of pure water (374 °C). For example, Urusova (Reference 45) found that a 2.9*M* solution of NaOH had a critical temperature of 450 °C. A study by Marshall and Jones (Reference 46) showed that the elevation of the critical temperature for solutions of many common salts is in the range of 25–65 °C for 1.0*M* solutions. Because a base-hydrolyzed propellant solution is expected to have a large excess concentration of sodium hydroxide, together with a large amount of aluminate and other dissolved salts, it is likely that the liquid–vapor critical temperatures will exceed 450 or even 500 °C. Hydrothermal processing will probably take place at a temperature in the 400–500 °C range; that is, processing may take place at subcritical temperatures, unless the feed solution is diluted to avoid this possibility. The number of phases that the system can partition into will be determined by whether the system is above or below its critical temperature.

## 2. Solutions Below the Liquid–Vapor Critical Temperature

In a hydrothermal process, a solution initially at room temperature would be pumped at high pressure into a heated reactor. As temperature increases at constant pressure, density (hence dielectric constant) decreases and salts may become less soluble. [Some salts exhibit retrograde solubility behavior; that is, their solubility decreases with temperature even at constant density.] If solubility limits are exceeded, solids or molten salts will separate from the aqueous phase. As temperature continues to increase, the vapor pressure of the solution may exceed the applied pressure, and a vapor phase will appear. Since the solubility of the salt in the (less dense) vapor phase will be less than that in the aqueous phase, the aqueous phase will become more and more concentrated in salt (unless it is already saturated, in which case more solid or molten salt will separate out). If the vapor pressure of the remaining solution is higher than the applied pressure when the maximum temperature is reached, the aqueous phase will disappear entirely, leaving a solid- or molten-salt phase incorporating a small amount of water, and a vapor phase consisting mostly of water with some dissolved salt. The existence of solid- or molten-salt phases will degrade the performance of the reactor by causing plugging and excessive corrosion. The following conditions should be met to avoid these problems: 1) the solubility limits in the aqueous phase should not be exceeded; and 2) the applied pressure must be greater than the vapor pressure of the aqueous phase so that no vapor phase can form.

## 3. Solutions Above the Liquid–Vapor Critical Temperature

If the conditions outlined in the previous section have been met at the point in the reactor where the solution is just below the critical temperature, the system is a single homogeneous aqueous phase. As the temperature increases beyond  $T_c$ , the system changes smoothly and continuously to a supercritical fluid with all salts still in solution. As temperature continues to increase at constant pressure, however, density (hence salt solubility) decreases, and again solids or molten salts may separate out. Thus, even at supercritical temperatures, it is necessary to keep the pressure (density) high enough to keep the salts in solution.

It is clear that several kinds of experimental data are required to design a hydrothermal reactor for aqueous salt solutions:

- 1) vapor pressure vs. temperature
- 2) critical temperature
- 3) salt solubility in liquid, vapor and supercritical fluid as a function of temperature and pressure.



In the following sections we discuss experimental results pertaining to each of the above categories for basic carbonate and aluminate solutions.

#### D. SOLUBILITY AND PHASE EQUILIBRIA MEASUREMENTS

##### 1. Experimental Techniques for the Study of Solubility and Phase Behavior

Two experimental approaches have been employed to study phase behavior and solubility in hydrothermal systems. One approach uses an optical cell to observe the behavior of static solutions as they are heated under high pressure. By decreasing the applied pressure at constant temperature, phase changes (crystallization of solids, appearance of molten salts, vapor-liquid equilibria) can be observed visually or by their effect on the optical transmission of the cell. The other approach uses a packed-bed flow tube to measure salt solubilities. Solutions initially at room temperature are pumped at high pressure into a heated packed bed, after which they are cooled and passed through a pressure letdown valve. If the salt concentration entering the packed bed exceeds the solubility at the final temperature and pressure, salt will precipitate in the bed and the solution exiting the cell will be saturated with salt. Inductively coupled plasma spectroscopy and acidimetric titration analysis of the effluent stream gives a direct measurement of salt concentration and hence solubility. This method probably works best for salts that separate out as solids rather than molten salts, since molten salts may partially or completely flow out of the packed bed and be redissolved in the cooldown section. Since both sodium aluminate and sodium carbonate have very high melting points, they will separate out as solids. Sodium hydroxide, on the other hand, is molten at the temperatures used in this study. In principle, the packed-bed method works for sub- or supercritical temperatures, and for any pressure, with one possible exception. If the temperature is subcritical and the pressure is in the two-phase liquid-vapor (or liquid-liquid) region, there is no direct method for distinguishing what fraction of the fluid is in each phase, and so the solubility cannot be found unambiguously in either phase.

The optical cell, measuring 1 in. x 2 in. x 2 in., was fabricated from a commercial four-way 1/4-in. high-pressure tubing cross (Hi-P) made of Inconel 625 alloy. The optical axis was in the direction orthogonal to both pairs of tube fittings on the cross. Diamond windows were pressed into cone-shaped depressions in the bottom of wells that were machined into the faces of the cross. Thin (0.003 in.) gold washers between the diamonds and the cell walls allowed the faceted diamonds to make a pressure-tight seal. The diamonds were squeezed into place with pusher blocks made from Inconel 718. Spring washers, also made of Inconel 718,

were used to compensate for the difference in thermal expansion between diamond and Inconel, keeping nearly constant pressure on the pusher blocks as the cell is heated up. Fluid was conveyed into and out of the cell by Inconel 625 tubing connected to two of the ports of the cross. A third port housed a type K thermocouple, used for temperature control, which was inserted in close proximity to the region of the cell near the windows. The fourth port on the cross was plugged. The cell was able to operate at temperatures up to 600 °C and pressures up to 1200 atm.

Phase changes in the cell were monitored by two coaxial optical systems. A white-light source entered the cell from the left. On the right, a lens formed a magnified image of one of the diamond windows on a color CCD camera. By means of a beam splitter, light from a helium–neon (HeNe) laser was passed through the cell from right-to-left, and another beam splitter was used to deflect the transmitted HeNe beam to a photodiode. The CCD camera was equipped with a blue filter to block scattered laser light, and the photodiode was equipped with a bandpass filter to discriminate against white light. The CCD camera output allowed visual observation of phase changes, which could be seen in several ways. When solid precipitates from solution, crystals could be seen growing on the window or dropping out of the bulk of the solution. A salt at a temperature above its melting point was sometimes observed to separate out as a molten liquid blob. When vapor–liquid equilibrium was established, density gradients were seen propagating across the liquid phase, and sometimes bubbles were seen. The laser diagnostic is particularly sensitive to the appearance of a vapor phase. When the pressure above an aqueous phase was lowered until a vapor phase appears, the laser transmission through the cell dropped abruptly, allowing the vapor pressure to be determined accurately and reproducibly.

Solubility studies of sodium aluminate and sodium carbonate were also performed in a packed-bed flow apparatus, shown schematically in Figure 74. Primary features of the apparatus included a preheat section followed by a packed bed, in which salt precipitation occurred, and then a 100- $\mu$ m-high temperature filter to capture precipitates. The packed bed consisted of a microreactor constructed from 6 in. of 1 in. od (0.5 in. id) Inconel 625 tubing with cone closures at each end. The internal volume of the microreactor was 19 mL and was packed with 0.25 in. to 0.5 in. pieces of 0.3125 in. od Inconel 625 high pressure tubing. Similarly, the high-temperature filter was constructed of Inconel 625 and housed four 0.75-in.-diameter 316 stainless steel sintered filter discs. All tubing in the hot sections of the apparatus was constructed from 0.25-in. od C276 high-pressure tubing.

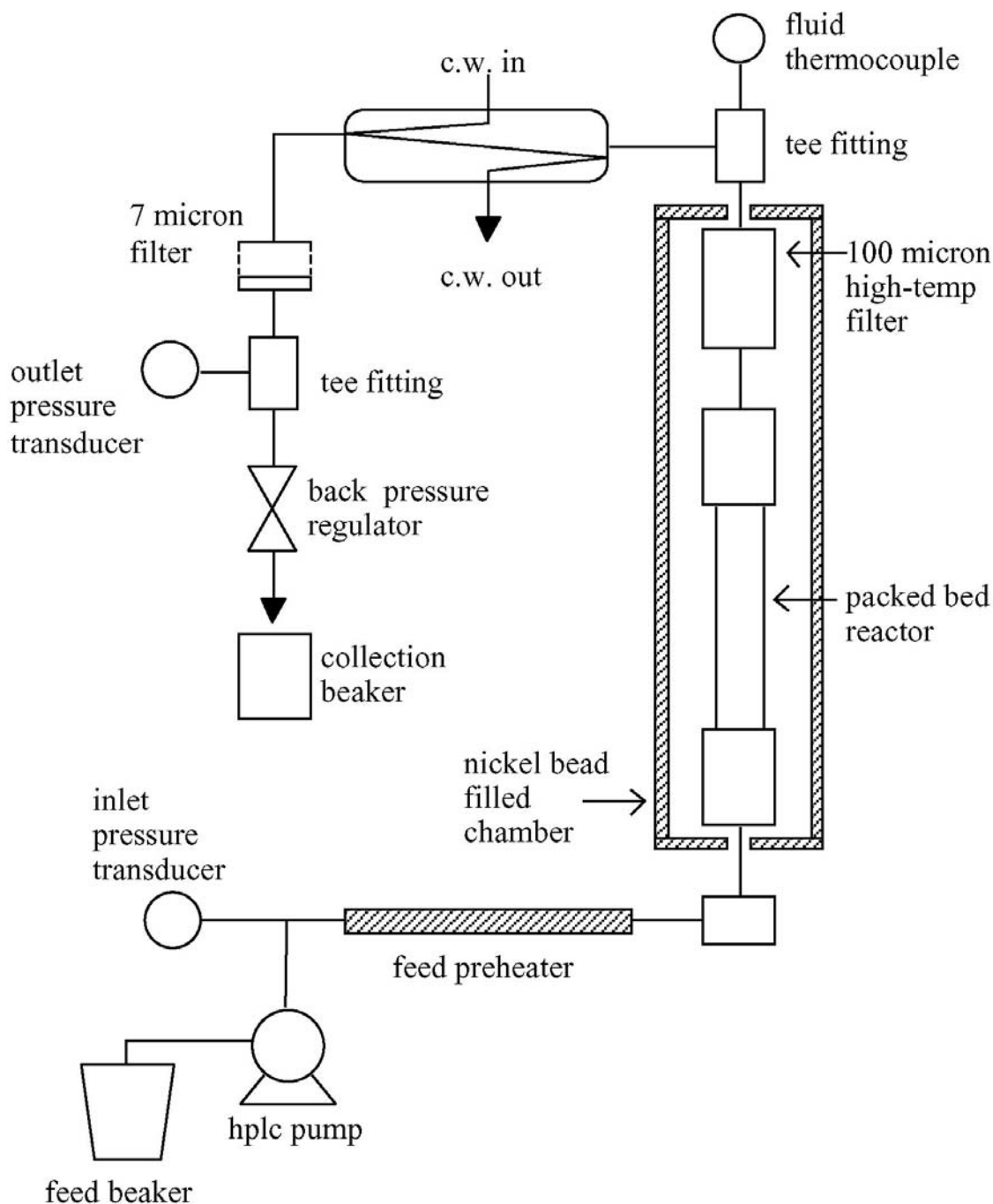


Figure74. Packed-bed flow apparatus for salt solubility studies.

The preheat section consisted of 0.6 m of C276 high-pressure tubing, surrounded by cylindrical brass clamshell heaters. Heating wire was wound on the brass, and current was supplied to the heating wire with variable transformers. Heat was generated by resistive heating of the wire, which was conducted through the brass to the preheater tubing. The packed bed and

the high-temperature filter were heated to the desired temperature by heating wire wound inside an 18-in. section of 3-in. od stainless steel tubing. The packed bed and filter were positioned inside the 3-in. od stainless tube, and the void spaces were filled with 0.1-in. diameter nickel beads. The heat generated in the heating wire was conducted through the nickel beads to the packed bed and filter, and the desired temperature was maintained by regulating the current through the heating wire with microprocessor temperature controllers. A chilled water countercurrent heat exchanger following the high temperature filter reduced the temperature of the effluent stream to near ambient. Pressure reduction was accomplished with a spring-loaded, backpressure-regulating valve.

Nine type K thermocouples monitored the temperature at various positions on the apparatus. A thermocouple in contact with the fluid stream at the exit of the high-temperature filter provided the temperature at which solubility measurements were made. This represented the highest temperature achieved by the fluid in the apparatus. Transducers measured pressures immediately following the feed pump and just prior to pressure letdown. Salt solutions were fed to the system using a high-performance liquid chromatography pump.

Solubility experiments were conducted by heating the apparatus with pressurized deionized water. When the fluid temperature at the exit of the filter reached the desired experimental value, the influent was switched to the feed salt solution. After allowing the system to flush with the feed salt solution for 15–20 minutes, the effluent was collected in vials with zero headspace for 2–3 hours. Generally, 5–7 samples were collected during each experiment, and temperature and pressure data were recorded every 5 minutes. After the last sample vial was filled, all heaters were turned off and a recirculating water rinse was initiated. This water rinse served to collect electrolytes and corrosion products that precipitated at high temperature, and that again became soluble as the reactor cooled to ambient conditions.

## 2. Optical Cell Studies of Basic Aluminate and Carbonate Solution Solubilities

A series of solutions with varying aluminate or carbonate concentrations were made in 1.0M sodium hydroxide solutions. The choice of unit molarity for sodium hydroxide was somewhat arbitrary but reflects the fact that hydroxide is present in excess in the products of base hydrolysis of propellants, and the fact that hydroxide ion has a large effect on aluminate and carbonate solubility. The solutions that were tested are listed in Table 49.

TABLE 49. SOLUTION COMPOSITION (MOLAR CONCENTRATIONS OF SUBSTITUENTS) FOR SOLUBILITY STUDIES

sodium aluminate	sodium carbonate	sodium hydroxide
0.5		1.0
2.0		1.0
	0.1	1.0
	0.2	1.0
	0.3	1.0
	0.5	1.0
	1.0	1.0

Aluminate solutions were studied at temperatures of 375, 400, 425, 450, and 475 °C. The experiments consisted of heating the solutions up to the desired temperature at high initial pressure, followed by lowering the pressure until a phase change was observed. In all cases except for the most-dilute aluminate solution at the highest temperature, the solutions displayed normal vapor–liquid equilibria. No precipitates were observed as long as the systems were in the liquid phase. For the 0.5M aluminate solution at 475 °C, no vapor–liquid phase transition was observed; instead, a solid phase was seen to separate out when the pressure dropped to about 7700 psia. The vapor pressure data are summarized in Table 50.

TABLE 50. VAPOR PRESSURES FOR SODIUM ALUMINATE SOLUTIONS IN 1.0 MOLAR SODIUM HYDROXIDE

$T$ (°C)	$P_v$ (psia)	
	0.5 molar aluminate	2.0 molar aluminate
375	2930	2844
400	4011	3826
425	5203	5254
450	6597	7018
475	supercritical	8751

We concluded that sodium aluminate is highly soluble in basic solutions at sufficiently high pressures, whether or not the solutions are above their critical temperatures.

Aluminate is therefore not expected to contribute to reactor plugging in hydrothermal treatment of base-hydrolyzed aluminum-bearing propellants.

Carbonate solutions in 1.0*M* sodium hydroxide behaved differently from aluminate solutions heated up under high pressure (typically 10,000 psia in these experiments). For the more-concentrated solutions, crystals started to grow before the final temperature was reached, making the cell partially opaque. For the more-dilute solutions, the experiments could be done in the normal way, but the normal vapor–liquid phase transition was not observed as the pressure was lowered. Instead, a molten salt phase (and sometimes a solid phase) appeared to separate out. The pressure at which this phase change occurred could not be reproducibly observed with our optical diagnostics. In most cases it was not even clear whether the system was above or below the liquid–vapor critical temperature. Therefore, the experiment was done in a different manner. Starting with a dilute (0.1*M*) carbonate solution, the cell was heated up to 475 °C at a pressure of 10,000 psia. Very little precipitate was seen during heatup and no crystals grew on the window under these conditions. Carbonate concentration was then increased in steps and the experiment repeated, until crystal growth was observed during heatup. In this way it was estimated that sodium carbonate solubility in 1.0*M* NaOH at 475 °C and 10,000 psia is between 0.3 and 0.5*M*. Solubility increased with increasing pressure and/or decreasing temperature (retrograde temperature behavior).

Since it was likely that the sodium hydroxide concentration influences sodium carbonate solubility, we next ran a series of tests in which carbonate concentration was kept fixed at 0.7*M* and sodium hydroxide concentration was increased in steps, starting at 0.7*M*. As in the previous tests, the solutions were heated to 475 °C while held at 10,000 psia pressure. The results were dramatic, and showed that hydroxide has a large, positive influence on carbonate solubility. At hydroxide concentrations of 0.7, 1.4, and 2.8*M*, solid sodium carbonate was seen to crystallize out of solution during the heatup phase, much as in the previous tests. At higher hydroxide concentrations, however, the behavior was qualitatively different. The solution remained as a single-phase liquid throughout the heatup period, with no precipitation of sodium carbonate evident. When the pressure was lowered, the liquid appeared to boil at a pressure of approximately 7500 psia, but no sodium carbonate precipitate was observed. At the intermediate hydroxide concentration of 4.2*M*, the most interesting behavior occurred. Again, a single-phase solution resulted at 475 °C and 10,000 psia. When the pressure was dropped to about 9040 psia, however, the system segregated into two liquid phases with a clear horizontal line separating them. Again, no solid carbonate precipitate was observed. It appeared that the upper of the two liquid phases was mostly aqueous, while the lower behaved as a sodium hydroxide "melt," albeit

with a large amount of water in it, since it occupied a significant fraction of the cell volume. A high solubility of sodium carbonate in the melt phase would account for the observation that sodium carbonate precipitated from the solutions low in hydroxide, but not from those high in hydroxide. [The use of the word "melt" is descriptive only; for example, in a 5.6*M* sodium hydroxide solution, there are still almost 10 molecules of water for each molecule of NaOH.]

### 3. Summary of Solubility and Phase Behavior Studies at High Density

The solubility of sodium carbonate in dense, high-*pH*, subcritical liquids has been shown to vary strongly with temperature, pressure, and composition. Thus, precipitation and reactor plugging due to carbonate may be of concern in a system treating base-hydrolyzed propellant. The addition of excess hydroxide creates a "melt" phase in which carbonate solubility is dramatically enhanced. However, there is a range of pressures over which the melt phase can coexist with an aqueous phase. It would appear to be prudent to operate a reactor at high enough pressure to avoid the coexistence of two liquid phases. At a temperature of 475 °C, a pressure on the order of 10,000 psia would be required.

Sodium aluminate was found to be highly soluble in basic solutions at hydrothermal temperatures and pressures; there was no concern that aluminates from base-hydrolyzed propellants would precipitate as long as the pressure of the system exceeded the saturation vapor pressure of the solution.

Hydrothermal processing of concentrated electrolytes has been shown to require that reactors operate at very high pressure to ensure solubility and single-phase behavior. High-pressure equipment is more costly and more subject to corrosion than equipment operating at moderate pressures. An alternative is to dilute the solutions to be processed, which allows the salts to remain soluble at lower pressures during hydrothermal processing. To evaluate the tradeoffs between high- and moderate-pressure processing, we undertook a study of salt solubilities at hydrothermal temperatures and pressures in the range of 4000–8000 psia. We now turn our attention to solubilities measured in these low-density supercritical fluids.

### 4. High-Temperature, Low-Density Salt Solubility Studies in the Packed-Bed Flow Apparatus

Several measurements were made to determine sodium aluminate and sodium carbonate solubility in supercritical sodium hydroxide solutions as a function of temperature and pressure. The feed salt solutions for these experiments were made in 0.1*M* NaOH, to which was

added a lesser quantity of either sodium aluminate or sodium hydroxide. Once again the choice of 0.1M NaOH was arbitrary but in this case was selected so that supercritical behavior could be achieved at the temperatures studied (400–475 °C). [Recall that as discussed previously, the critical temperature of 2.9M NaOH is elevated to 450 °C. However, based on experimental observation, the critical temperature of a 0.1M molar NaOH solution is less than 400 °C.]

Carbonate and hydroxide concentrations were determined by acidimetric titration and aluminum and sodium concentrations were determined by inductively coupled plasma spectroscopy. With the determined concentrations of all species in effluent samples the solubility of sodium aluminate and sodium carbonate were calculated. Solubility values were derived from effluent concentrations of aluminate and carbonate, rather than sodium, because additional sodium was added (NaOH) to the feed solutions. The calculated solubility values represent the quantity of sodium aluminate or sodium carbonate that was soluble in the supercritical fluid phase after exiting the high-temperature filter.

Table 51 shows the results of the packed-bed flow apparatus solubility studies and confirms that, as anticipated, the supercritical-phase solubility of these electrolytes is very low (< 3 g/kg) at these relatively moderate pressures. Temperatures and pressures were determined from the averages of 6–30 readings during the course of the experiment. Reported solubilities are the averages from analysis of 5–7 samples collected during each run. The reported uncertainties are given as two times the estimated standard deviations.

TABLE 51. SUPERCRITICAL-PHASE SOLUBILITY OF SODIUM ALUMINATE AND SODIUM CARBONATE IN 0.1 MOLAR SODIUM HYDROXIDE

electrolyte	temperature (°C)	pressure (psia)	solubility (mg/kg)
sodium aluminate	399.7 ± 2.6	5045 ± 34	201 ± 34
	424.9 ± 2.6	5112 ± 123	182 ± 38
	450.1 ± 1.8	5025 ± 48	75 ± 12
	475.5 ± 1.8	5026 ± 57	59 ± 6
	450.2 ± 0.5	6800 ± 158	1530 ± 82
	450.3 ± 0.2	7926 ± 312	2284 ± 68



## E. CONCLUSIONS AND RECOMMENDATIONS

Presently, the available solubility data for sodium aluminate and sodium carbonate cover a very small part of the range of temperature, pressure and overall composition that are possible. At the highest pressures, the data are semiquantitative; only lower bounds on solubility may be established. A few general conclusions are obvious, however. First, the pressure (and its effect on the density and phase) has an enormous effect on salt solubility. Solubilities at 450 °C and 5000 psia are typically on the order of grams/kg H<sub>2</sub>O or less, while at 450 °C and 10,000 psia solubilities are on the order of 100 grams/kg H<sub>2</sub>O or more. Second, excess sodium hydroxide can have an enormous effect on solubility, presumably by the creation of a "melt" phase. This effect was particularly pronounced for sodium carbonate. The data strongly suggest that hydrothermal processing of base-hydrolyzed propellants should be carried out in concentrated solutions at high pressure, despite the increased cost and increased corrosion rates that might be encountered.

The packed-bed apparatus has been upgraded and is capable of bridging the gap between the low- and high-pressure data now available. It is recommended that quantitative solubility measurements for the various components of base-hydrolyzed propellants be extended into the high-pressure regime. The effect of excess hydroxide on the solubilities should be carefully examined. These studies would provide data for the design of a demonstration unit for hydrothermal processing of actual base-hydrolyzed propellant solutions.

## SECTION IX

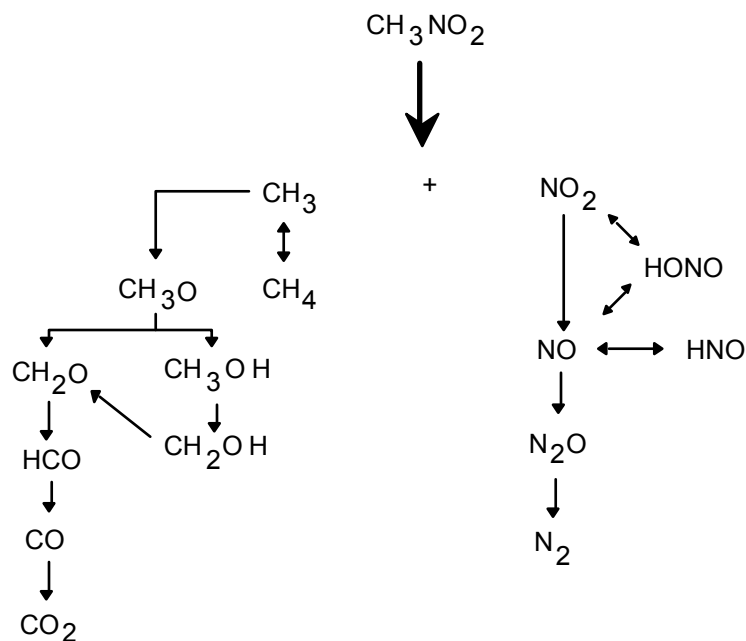
### THEORY AND MODELING

#### A. INTRODUCTION

Design of an actual hydrothermal processing reactor system requires knowledge that includes rates of the pertinent chemical reactions, thermodynamics of the reactant–product–solvent system, and dynamics of fluid flow in the system. Such knowledge provides input to a process model used to optimize design with respect to performance and/or cost, depending on the desired objectives. In this section we report significant progress in the areas of required knowledge, and in preliminary process modeling for optimization of performance/cost.

#### B. MODELING OF NITROMETHANE REACTION KINETICS

We have had an ongoing interest in kinetic modeling of reactions in supercritical water, as this should provide insight into the chemical mechanisms and how they compare with those of the gas and liquid phases. Constructing a detailed elementary reaction network for nitromethane, however, is not a simple task, due to the size of the molecule and the many possible chemical intermediates formed by the four atoms C, H, N, and O. An attempt to develop such a mechanism has been made by Dr. Carl Melius of Sandia National Laboratories (Livermore, California), who was motivated by a desire to model the detonation of pure nitromethane at ambient conditions (Reference 47). We have adapted this reaction mechanism for use in high-pressure water to simulate the decomposition that occurs under the conditions used in our experiments (550 °C, 330 atm, 0.4 percent nitromethane in water, ~2-s reaction time). Many of the reaction rate values were taken from the combustion literature. Where appropriate, reaction rate constants were set to their high-pressure limits; in some cases, fall-off estimates were used (Reference 48). In a few cases, reactions with water were added because of their importance at high water densities. Apart from these modifications, however, the reaction mechanism is essentially a gas-phase mechanism, with no attempt to account for molecular clustering or other possible "nonideal" effects that may be important in supercritical water. The resulting mechanism includes 44 chemical species and 214 reversible chemical reactions. The overall reaction scheme is depicted below. For several of the chemical species, properties and reactivity are not known, and were estimated by Melius using his quantum chemistry techniques.



Reaction scheme for nitromethane (after Melius)

The results of the model calculations, both with and without additional oxidizer, are shown in Figure 75. At 550 °C in supercritical water without oxidizer, destruction of the nitromethane occurs in about one second, in excellent agreement with the experimental results described in Section III.E of this report. The model predicts that major products will be NO and CO, with smaller amounts of CH<sub>4</sub>, CH<sub>3</sub>OH, N<sub>2</sub>O, CH<sub>2</sub>O, and H<sub>2</sub>. The products N<sub>2</sub> and CO<sub>2</sub> are predicted to form on a longer time scale (seconds to minutes) by further reduction of NO and oxidation of CO. When an excess of hydrogen peroxide is added to the reaction mixture (10 moles of H<sub>2</sub>O<sub>2</sub> to 1 mole of nitromethane), the reaction is predicted to proceed about 10 times faster. The carbon is oxidized completely to CO<sub>2</sub>. Nitric oxide (NO) is still the principal nitrogen product, but NO<sub>2</sub> is formed as a secondary product, rather than N<sub>2</sub>O. This occurs because the conversion of NO<sub>2</sub> into NO is slowed by the excess oxygen, and production of the intermediate species HONO from NO<sub>2</sub> becomes an important pathway (see the reaction scheme above).

Experimentally, when no oxidizer was added, N<sub>2</sub>O was observed in higher amounts than NO, and no methanol or formaldehyde were observed. When oxidizer was added, carbon dioxide was the major carbon product. With some disagreements, then, model predictions and experimental data show qualitative parallels. This agreement is encouraging, considering the preliminary nature of the reaction mechanism used in the calculations. The results demonstrate the valuable predictive capability of this type of calculation, especially in understanding why

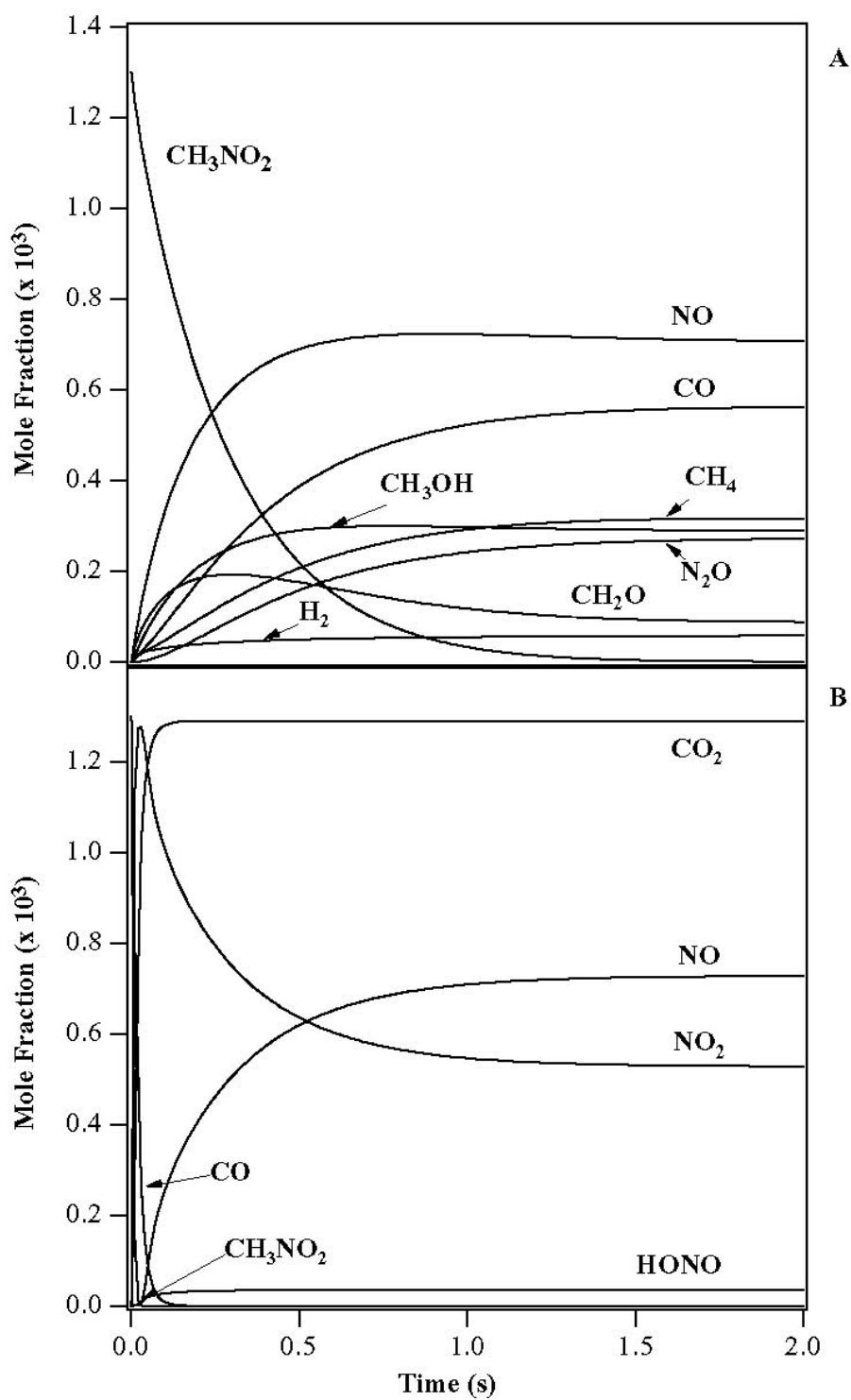


Figure 75. Calculated species profiles for decomposition of nitromethane in supercritical water (A) at 550 °C, 330 atm and 0.4% v/v NM in water; (B) as (A), with addition of H<sub>2</sub>O<sub>2</sub> at a 10:1 molar ratio to NM

different products form under different conditions. Additional work on the reaction mechanism is needed and may produce closer agreement with the observations.

### C. STEADY-STATE OXIDATION OF H<sub>2</sub> IN SUPERCRITICAL WATER

The combustion of hydrocarbons in supercritical water produces the initial products H<sub>2</sub> and CO, which are further decomposed into H<sub>2</sub>O and CO<sub>2</sub> in complete combustion. Since the oxidation of H<sub>2</sub> involves perhaps the simplest kinetics, it is very important to understand this reaction mechanism in supercritical water. Furthermore, there is a large body of experimental data for H<sub>2</sub> oxidation (Reference 49) with which we can compare the steady-state kinetic theory.

Oxidation of H<sub>2</sub> in supercritical water is different from normal oxidation at atmospheric pressure. Normal oxidation occurs at high temperature >1000°C, where the chain-branching reactions  $\text{H}_2 + \text{O}^\cdot \rightarrow \text{OH}^\cdot + \text{H}^\cdot$  and  $\text{H}^\cdot + \text{O}_2 \rightarrow \text{OH}^\cdot + \text{O}^\cdot$  dominate (Reference 50). However, in supercritical water the temperature is too low to activate this reaction and instead the three-body reaction  $\text{H}^\cdot + \text{O}_2 + \text{H}_2\text{O} \rightarrow \text{HO}_2^\cdot + \text{H}_2\text{O}$  occurs.

Experiments show (Reference 49) that the global reaction for oxidation of H<sub>2</sub> in supercritical water,  $2\text{H}_2 + \text{O}_2 \rightarrow 2\text{H}_2\text{O}$ , does not depend on O<sub>2</sub> concentration as would normally be expected. This remarkable fact can be explained by a steady-state analysis of the detailed reaction kinetics, which is described herein.

In Table 52 we show the seven primary reactions for H<sub>2</sub> oxidation in supercritical water and their rates. The first four reactions are the fastest. At steady state (for times of several seconds or longer) the first two reactions occur at twice the rate of the next two reactions. This greatly simplifies the determination of the steady state concentrations because this equality of rates gives the following relations:

$$k_1[\text{H}_2][\text{OH}^\cdot] \sim k_2[\text{H}^\cdot][\text{O}_2][\text{H}_2\text{O}] \quad (1)$$

$$k_2[\text{H}^\cdot][\text{O}_2][\text{H}_2\text{O}] \sim 2k_3[\text{HO}_2^\cdot]^2 \quad (2)$$

$$k_3[\text{HO}_2^\cdot]^2 \sim k_4[\text{H}_2\text{O}_2] \quad (3)$$

$$k_1[\text{H}_2][\text{OH}^\cdot] \sim 2k_4[\text{H}_2\text{O}_2]. \quad (4)$$

TABLE 52. PRIMARY REACTIONS FOR OXIDATION OF H<sub>2</sub> IN SUPERCRITICAL WATER

$$k_i = AT^b e^{-(E/RT)}$$

Reaction	Rate constant	log <i>A</i>	<i>b</i>	<i>E</i> (kJ/mole)
1. 2H <sub>2</sub> + 2OH → 2H <sub>2</sub> O + 2H	<i>k</i> <sub>1</sub>	8.33	1.51	14.35
2. 2H + 2O <sub>2</sub> + 2M → 2HO <sub>2</sub> + 2M	<i>k</i> <sub>2</sub>	16.50	0.00	-4.18
3. HO <sub>2</sub> + HO <sub>2</sub> → H <sub>2</sub> O <sub>2</sub> + O <sub>2</sub>	<i>k</i> <sub>3</sub>	12.93	0.00	17.62
4. H <sub>2</sub> O <sub>2</sub> → OH + OH	<i>k</i> <sub>4</sub>	14.47	0.00	202.55
5. HO <sub>2</sub> + OH → H <sub>2</sub> O + O <sub>2</sub>	<i>k</i> <sub>5</sub>	16.16	-1.00	0.00
6. HO <sub>2</sub> + H <sub>2</sub> O → H <sub>2</sub> O <sub>2</sub> + OH	<i>k</i> <sub>6</sub>	12.85	0.0	146.48
7. H <sub>2</sub> O <sub>2</sub> + H <sub>2</sub> O → HO <sub>2</sub> + H <sub>2</sub> O	<i>k</i> <sub>7</sub>	12.85	0.0	5.98

Because of these relations, the first four reactions in Table 52 produce as many intermediate species (H<sup>•</sup>, OH<sup>•</sup>, HO<sub>2</sub><sup>•</sup>, and H<sub>2</sub>O<sub>2</sub>) as are consumed, resulting in the net global reaction 2H<sub>2</sub> + O<sub>2</sub> → 2H<sub>2</sub>O.

Equations (3) and (4) above give rate relations among the three species OH<sup>•</sup>, HO<sub>2</sub><sup>•</sup>, and H<sub>2</sub>O<sub>2</sub> which do not depend on O<sub>2</sub> concentration. Also, in Table 52 the remaining three reactions (5–7) involve only these three radicals and do not depend on O<sub>2</sub>. Therefore, at steady state the three species OH<sup>•</sup>, HO<sub>2</sub><sup>•</sup>, and H<sub>2</sub>O<sub>2</sub> cannot depend on O<sub>2</sub> concentration. This result has been demonstrated in experiments (Reference 49). Furthermore, the first relation above shows that the H<sup>•</sup> concentration is inversely proportional to O<sub>2</sub> concentration.

Solving the steady-state equations for zero-time derivatives of the four intermediate radicals, one derives the global steady-state rate for H<sub>2</sub> oxidation:

$$d[H_2]/dt = -9.77 \times 10^{10} [H_2O]^{2/3} [H_2]^{2/3} T \exp(-232,390/RT), \quad (5)$$

where  $R = 8.31 \text{ J/mole-K}$ ,  $T$  is the temperature in kelvins, and the concentrations are in moles/cm<sup>3</sup>. In Figure 76 we compare the steady-state rate calculated from Eq. (5) with the experimental data in Reference 49 using the values  $[\text{H}_2] = 10^{-6} \text{ moles/cm}^3$  and  $[\text{H}_2\text{O}] = 4.25 \times 10^{-3} \text{ moles/cm}^3$ . Note that the steady-state analysis gives an upper limit to the oxidation rate. This is because there is an induction time for the reaction to reach steady state, which decreases with increasing temperature. At 500 °C the induction time is about 50 seconds whereas at 600 °C it is less than 1 second. The data in Figure 76 were collected at times less than 15 s so the measured rate at 500 °C is well below the steady state value. The theoretical activation energy of 232 kJ is very close to the global steady state energy of 244 kJ found by Holgate (Reference 51). The theoretical value was derived directly from the individual rates given in Table 52.

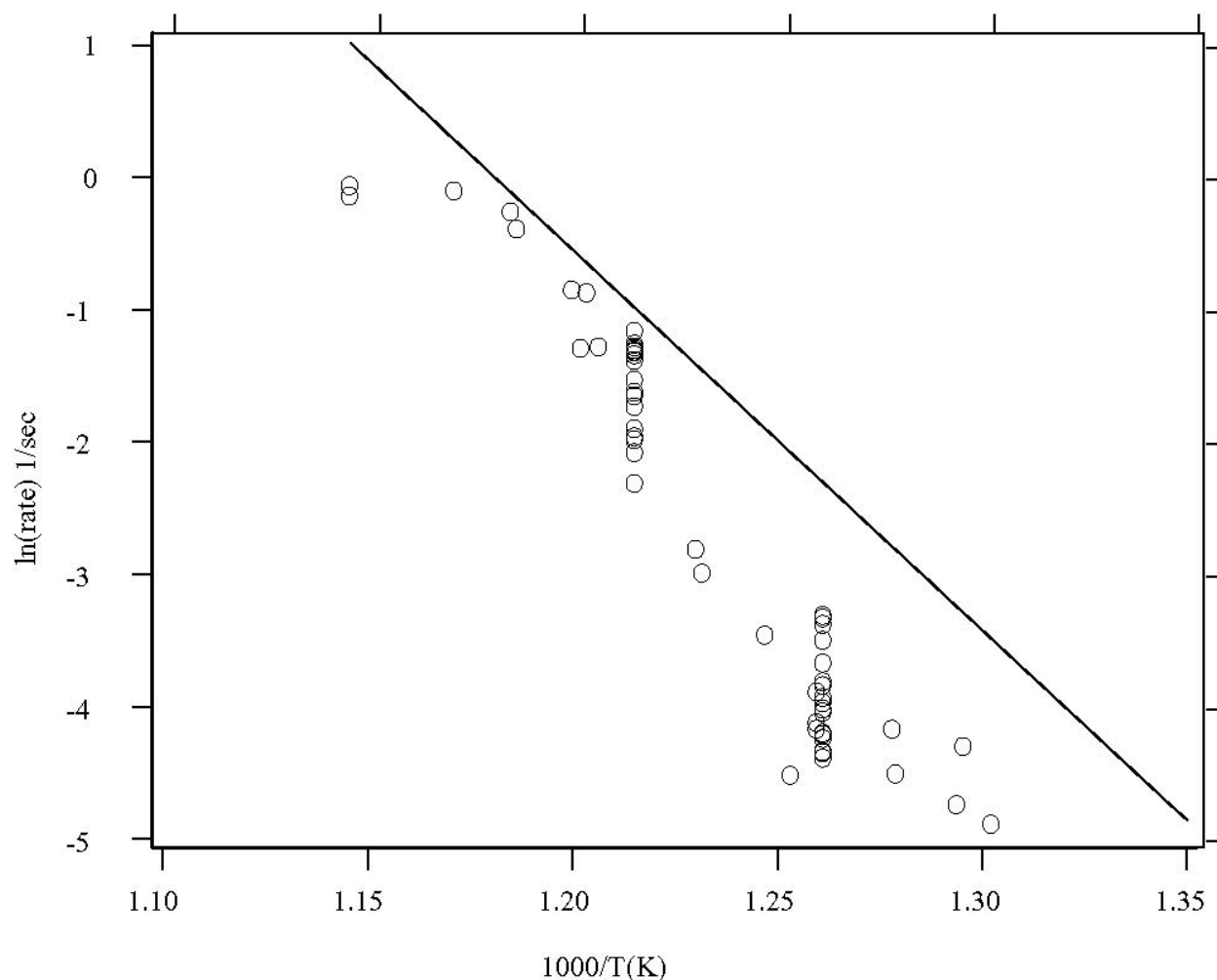


Figure 76. Comparison of theoretical steady-state oxidation rate of hydrogen with experiment.

The hydrogen oxidation rate above does not depend on  $O_2$  concentration but it does depend on the  $2/3$  power of the  $H_2$  concentration. This is also consistent with experiment. In Figure 77 we show the data from Figure 76 at  $550\text{ }^\circ\text{C}$  where we plot  $[H_2]/[H_2]_0$  vs time where  $[H_2]_0$  is the initial concentration of  $H_2$ . The data are shown for three different initial concentrations. The three curves shown for the three initial concentrations are found by solving equation (5) involving the  $2/3$  power law. Note that we can fit the data by assuming one induction time of two seconds for all the data.

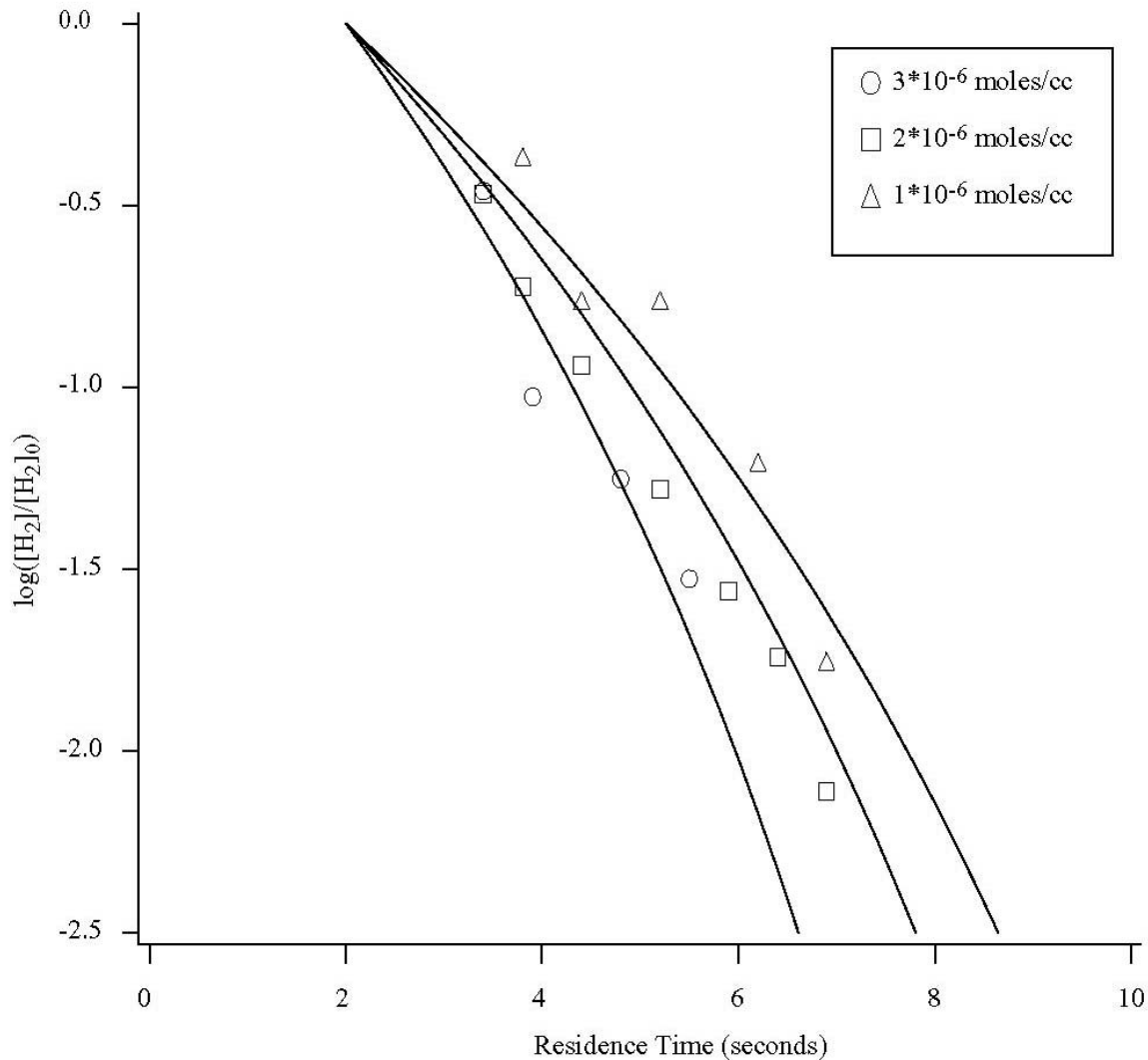


Figure 77. Comparison of theoretical steady-state decay of hydrogen concentration  $\log([H_2]/[H_2]_0)$  with experiment for three concentrations.

In conclusion, we have explicitly derived the steady-state activation energy for the oxidation of  $H_2$  in supercritical water and have shown that the oxidation does not depend on the



oxygen concentration but depends on the  $2/3$  power of the hydrogen concentration, in agreement with experimental results. The analysis given here illustrates the simplifications that result whenever steady-state approximations are valid. Clearly, in future studies of more-complex reaction systems, exploration of potential steady-state regimes is highly desirable.

#### D. MODELING OF CLUSTER DISTRIBUTIONS IN SUPERCRITICAL WATER

The distributions of cluster sizes in water vapor at temperatures below the critical point and in the fluid above the critical point were calculated using equilibrium constants obtained from a thermodynamic model for water clusters. The model uses information such as the enthalpy of vaporization of water, the experimental bond strength of the dimer, a combination of Debye and Einstein temperatures that reproduces the heat capacity of ice, and the theoretical structures and energies of a few small clusters. The calculations were checked by comparing to measured water properties such as density and volume of the saturated steam and densities of the supercritical water. To make the comparisons, we developed an equation of state, a modification of the van der Waals equation of state, that relates pressure, temperature and density in terms of the cluster distribution. Cluster distributions for a variety of temperatures above and below the critical point were calculated at a pressure of 246 bar. At low temperatures the calculations with a finite number of clusters (20) show an increased stability above a cluster size near four. If much larger clusters are included, most of the water molecules are found in the largest cluster, *i.e.*, liquid water. Near the critical temperature (647.3 K) the number of molecules in each cluster size is roughly the same. Well above the critical temperature (900 K) the cluster size distribution monotonically decreases.

#### E. MODELING TOOLS FOR SOLVATION FREE ENERGIES IN HYDROTHERMAL SYSTEMS

It has been demonstrated that a dielectric continuum model provides a physically sound approximate description of solvation free energies of charged and polar solutes in complex solutions including aqueous solutions, (Reference 52). Adaptation of these models for application to supercritical aqueous solutions should assist in developing a predictive molecular description of ion-pairing phenomena, corrosion and scale formation, chemical reactivity in solution, and equation-of-state modeling. These tools should unify the elementary information required by the Advanced Process Simulator for Engineering (ASPEN) computer code, provide new information to fill the gaps within available experimental results, and produce physically

sound extrapolations of experimental results into thermodynamic regimes not easily studied experimentally.

The physical idea of the dielectric continuum model is that the molecular medium external to a solute of interest is idealized as a dielectric continuum. The technical difficulty in applying the model is the solution of a known partial differential equation, the Poisson equation for continuous media. We have written and validated a boundary element computer code to solve this equation and thus evaluate solvation free energies, (Reference 53–56). The molecular information required for the solute molecule is (i) the dielectric response of the solvent; (ii) the molecular geometry of the solute; (iii) molecular charge distribution of the solute; and (iv) van der Waals radii used in defining the internal volume of the solute. The code that was written is applicable to arbitrary specification of these parameters and therefore applies to general complex solute molecules for which current alternative molecular theories can be applied.

As an initial validation of this approach, we studied the solvation free energy of the acetamide molecule ( $\text{CH}_3\text{CONH}_2$ ) in aqueous solution near the triple point of the solvent. This example was chosen because experimental results and alternative molecular theoretical results were available for comparison, (Reference 57). The input information was taken from that previous theoretical study to provide the clearest comparison. The dielectric model predicted -0.47 eV for the solvation free energy (the excess, or interaction part of the chemical potential of the solute). The experimental result is -0.50 eV. The previous molecular theoretical calculation predicted -0.45 eV for the same quantity. Of that latter value, -0.39 eV was regarded as due to classical electrostatic forces. That distinction is not available for the experimental result or the model prediction. In this test, the model was clearly successful in predicting the solvation free energy of moderately complex solute in aqueous solution.

A second validation calculation studied the solvation free energies of alkali–chloride ion pairs in liquid water. Such information can teach us about the likelihood of encounter of charged groups in solution and thus about chemical reaction rates in solution. These particularly simple examples were, however, chosen because of the availability of molecular theoretical information with which to compare our model results. The results for calculated solvation free energies as a function of interionic distance (the so-called *potential of mean force*) are shown in Figure 78. These results depend crucially on our ability to achieve sufficient computational resolution to extract free energetic changes of tens of meV ( $1 \text{ eV} = 23.06 \text{ kcal/mol}$ ). The results shown are in surprisingly good qualitative agreement with the results of reliable molecular theoretical calculations. For the case of  $\text{Na}^+ \cdots \text{Cl}^-$  ion pair, the potential of mean force shows a free

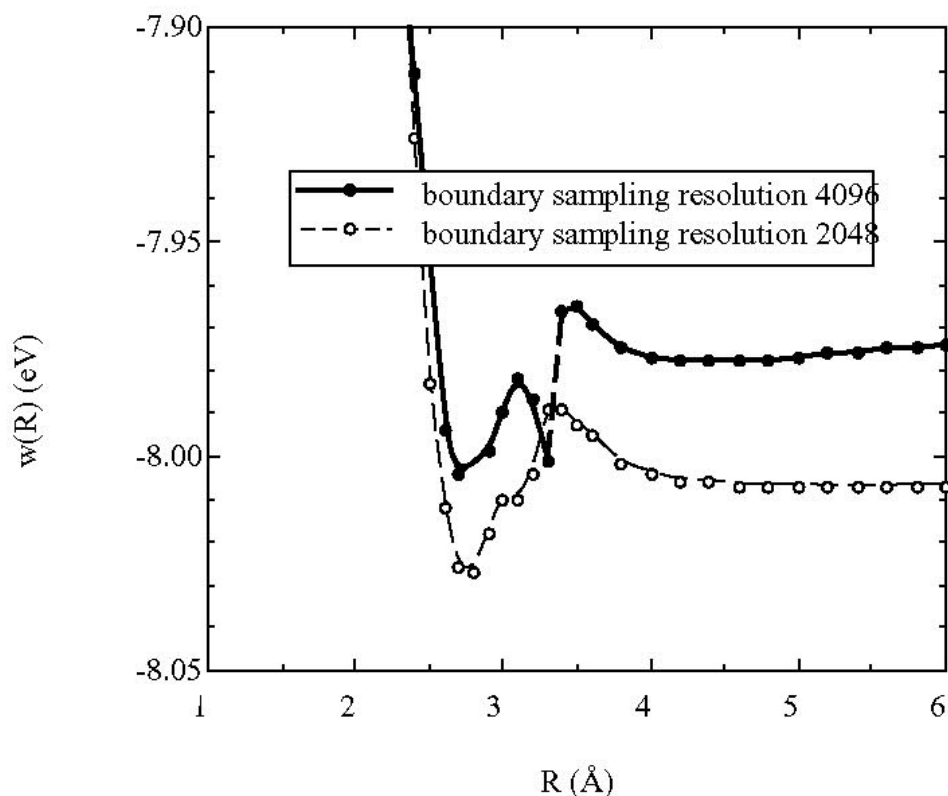


Figure 78. Potential of average force,  $w(R)$ , for  $\text{Na}^+ \cdots \text{Cl}^-$  ion pair in water at the water triple point according to the continuum dielectric model. The upper curve was obtained with a much higher-resolution calculation

energetic barrier at approximately 3.2 Å to ion contact at about 2.5 Å. For conditions near the triple point of water this contact ion pair is “metastable,” as is expected physically since close ion pairs are expected to be rare under such conditions. The model results are in remarkable qualitative agreement with available molecular information; the level of quantitative agreement, though quite reasonable, is currently being scrutinized with the objective of refining the parameterization of the model. In this way, we expect to be able to produce the most reliable predictions with this model approach.

With these validation efforts in view, our next application was to the solvation free energy of the carbonate anion ( $\text{CO}_3^{2-}$ ) in water as a function of temperature. Carbonate is a solute of interest in hydrothermal processing because it is the product of complete carbon oxidation. The molecular geometric parameters and partial charges necessary for the solvation free energy calculations were acquired from an electronic structure calculation by Joel Kress\*. Figure 79

\*Personal communication with Joel Kress of the Theoretical Division at Los Alamos National Laboratory

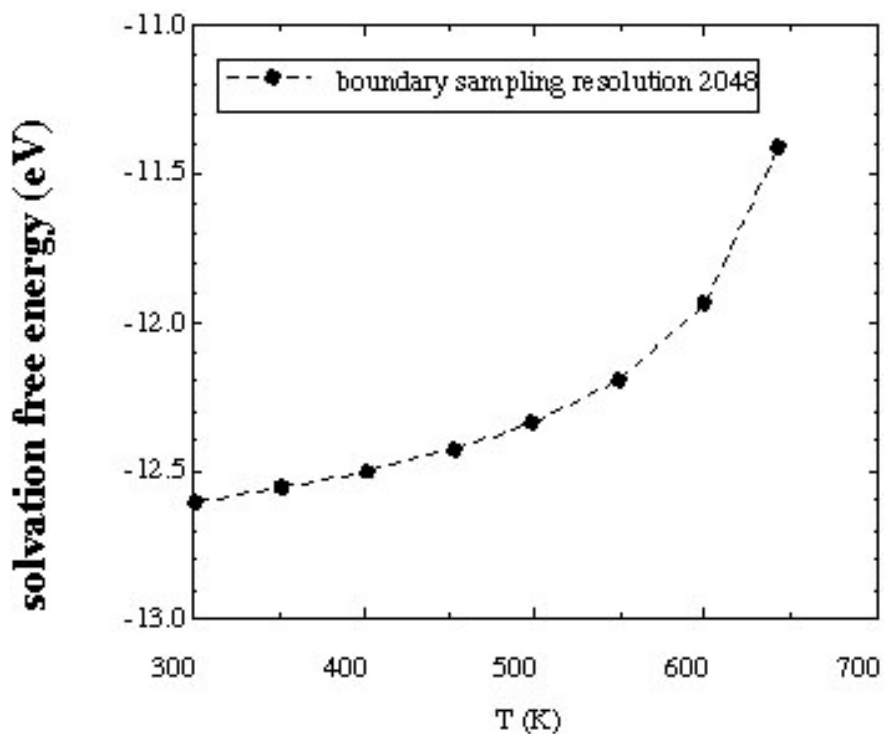


Figure 79. Solvation free energy of the carbonate anion,  $\text{CO}_3^{2-}$ , in water along with the coexistence curve as a function of temperature from the triple point to the critical point.

shows as the solid circles the results for that solvation free energy at thermodynamic states on the water *liquid-vapor* coexistence curve for temperatures between the triple temperature and the critical temperature of water. We expect these results, together with calculations in progress for complexes of the carbonate ion with the sodium ion, to be helpful in predicting concentrations of the various possible complexes of this type.

Finally, we have applied our code to the problem of encounter of a  $\text{Cl}^-$  ion in aqueous solution with a metal wall. In this case the wall effects are incorporated naturally into the dielectric continuum by assigning the static dielectric constant of the metal to be infinite,  $\epsilon = \infty$ . We expect that close contact would be required for efficient electron transfer and hence efficient corrosion. Subsequent study of how these barriers change with thermodynamic state progressing into supercritical regions should provide insight into the rates of corrosion of reactor walls.

## F. REACTOR DESIGN TO MINIMIZE WALL CORROSION

### 1. Basic Concept

One of the major concerns in designing a reactor for the supercritical water oxidation of wastes is the corrosion that occurs on the reactor walls, seriously shortening the lifetime of the reactor. Given the wide array of wastes, ranging from organics to fuel propellants, that can be treated with this process, it is clearly desirable to lessen or eliminate the corrosion problem to enhance its utility.

Corrosion of reactor walls can be caused either by the waste stream, oxidizers, reaction products, or a combination of all three. In practice, it is found that having the oxygen–supercritical water mixture in contact with the walls is a less serious problem than having the waste stream and reaction products in contact with the walls. The reason for this is that the walls can be passivated by electrochemical means against corrosion from the oxidizing stream.

Clearly, the simplest way to deal with the problem is to prevent the waste stream and the reaction products from ever reaching the reactor walls. With this in mind, we can think of a tubular flow reactor. In this reactor, a mixture of supercritical water and oxygen is fed in and flows downstream continuously at a low velocity, *e.g.*, 1 cm/s. The waste stream is then fed in along the axis of the tube in the form of a spray. In the case of a gaseous stream, which is the one we shall consider here, the "spray" will consist of vapor bubbles. These vapor bubbles are of course surrounded by the mixture of supercritical water and oxygen. Given the small dimensions of the bubble (the order of micrometers), it takes a minuscule amount of time (milliseconds) for the vapor to mix with the ambient stream. In this manner, the waste stream mixes well with the oxidizing stream. If the tube is long enough to allow the reaction to proceed to completion, and if the tube is sufficiently wide to prevent the mixed reacting stream from coming in contact with the walls before it leaves the tube, then we will have significantly reduced the corrosion problem.

### 2. Design Considerations

Typical flow speeds ( $u_f$ ) are on the order of 1 cm/s. Residence times for the supercritical water oxidation of wastes are typically tens of seconds,  $\tau_r \sim 60$  s. Thus the length  $L_t$  of the tube we shall need is of the order of  $u_f \tau_r \sim 60$  cm. In a time  $\tau_r$ , the lateral diffusion (the diffusion constant being  $\sim 10^{-3}$  cm<sup>2</sup> s<sup>-1</sup>) will have an extent  $R_t \sim (D \tau_r)^{1/2} \sim 0.3$  cm. On the

other hand, the spray that is injected along the axis will have an angular extent  $\theta$ . In a distance  $L_t$ , this translates to a radius of  $\theta L_t \sim 3$  cm. This latter number defines the radius of the tube we shall need.

These considerations give us an idea of the dimensions of the tube reactor we need. Later, we shall show that detailed calculations change these numbers somewhat. The changes are primarily due to the fact that in our flow reactor, there are concentration gradients that cause the reaction to proceed at nonuniform rates within the reactor.

The physical picture we have from these considerations is a narrow jet issuing into the center of a cylindrical tube, mixing with the surrounding, flowing oxidizer–supercritical water mixture, and flowing downstream while spreading laterally in a plume as the oxidizing reaction proceeds. We have depicted this in Figure 80.

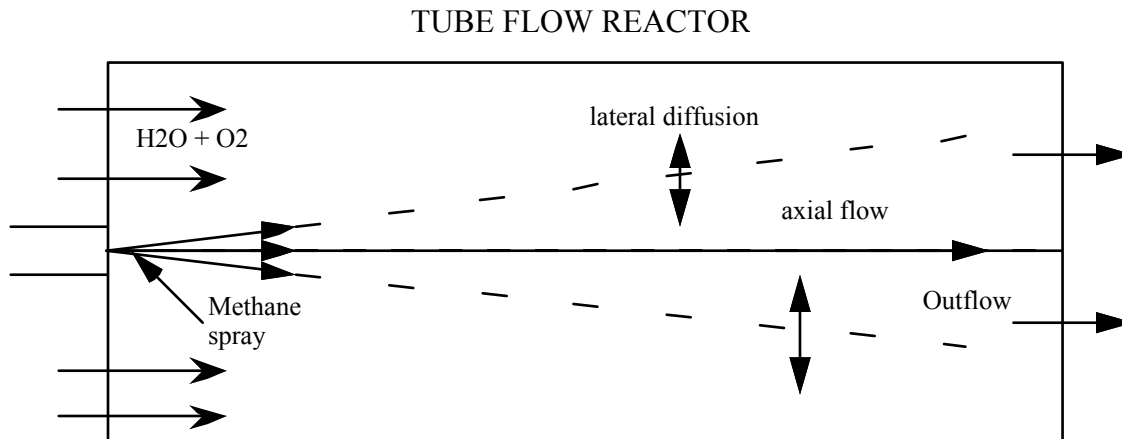


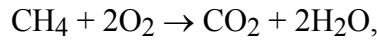
Figure 80. Conceptual set-up of the reactor geometry.

### 3. Numerical Calculations

As mentioned in the previous two sections, the idea is to avoid corrosion by shaping the reacting flow in our reactor such that it does not touch the walls. We have performed numerical simulations of such flows using KIVA-II. This is a Fluid Dynamics code to simulate low-speed reactive flows, using a semi-implicit method for advancing in time. While this code is a state-of-the-art tool designed to handle primarily internal combustion engines, it has options for inflow and outflow boundary conditions that allow it to be utilized for our purposes.

As an example of reactive flows confined to the neighborhood of the axis of the tube, we have used methane (CH<sub>4</sub>) to simulate the waste stream. Methane is known to cause the carburization of refractory metals according to the reaction CH<sub>4</sub> (gas) → C(diss) + 2H<sub>2</sub>. As such, methane serves as an example of a stream that can have deleterious effects on the walls of a reactor. The oxidation of methane in our reactor served to show that by having a confined reactive flow, the reactants as well as the products, along with the very high temperatures that are achieved during exothermic reactions, are not transported to the walls, thereby reducing the likelihood of corrosion.

The global reaction mechanism we used is



with the reaction rate given by Webley and Tester: (Reference 58)

$$\frac{d[\text{CH}_4]}{dt} = -A \exp\left(-\frac{E_a}{RT}\right) [\text{CH}_4] [\text{O}_2]^{2/3},$$

where  $A = 10^{11.4} \text{ (mol/L)}^{-0.65}/\text{s}$ ,  $E_a = 408.8 \pm 85.4 \text{ kJ/mol}$ , in the temperature range 450–550°C.

The simulations were performed for a tube 10 cm (diameter) x 25 cm (length). The procedure we followed is to start a flow of oxygen (O<sub>2</sub>) and supercritical water (H<sub>2</sub>O) into the reactor until all the transients die out and a steady state is reached. At that point we noticed that the velocity pattern was almost uniform, with a narrow boundary layer developed along the walls. The boundary layer increases in width with the distance downstream. This is exactly what one would expect from a uniform flow past a flat plate. We estimated the thickness of the boundary layer expected from a uniform flow past a flat plate, and found it agreed reasonably well with the numerical results. Had we done the calculation for a longer tube, the boundary layer would have eventually enveloped the entire width of the tube.

Once steady state was reached, we turned on a (gaseous) spray of methane (0.1 g/s), which is well mixed with the surrounding flow of oxygen (mass fraction 10%) and supercritical water (mass fraction 90%) at a density of 0.2 g/cm<sup>3</sup>. We have done the simulations at sufficiently high temperatures that the water can essentially be treated as a perfect gas. This not

only aids in the equation of state to be used, but also ensures a higher rate of destruction (oxidation) of methane. We kept the walls at a constant temperature of 837 kelvin.

Figure 81 shows the  $\text{CO}_2$  concentration profile about 12 s after the methane spray has been turned on. At this point we have not reached a steady-state. We see the beginnings of a flame/blow-torch. The temperature is significantly higher in the central core region where chemical reactions are taking place. One might expect that since the central core region has a higher temperature than the surrounding gas, we would have a Rayleigh–Bensard instability. We note that while this might occur on a very short time scale, we are looking at the reaction zone on the time scale of seconds. This is many orders of magnitude more than the acoustic transit time across the reaction zone. On this sort of a time scale, one can safely expect the pressure to have equilibrated throughout the reaction zone, thereby damping out any instability.

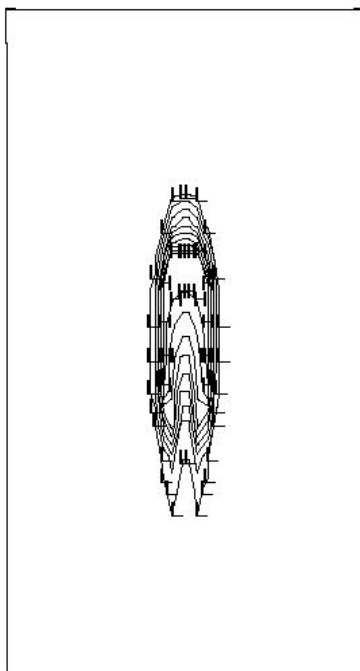


Figure 81. Contours of  $\text{CO}_2$  (product) concentration 12 s after the spray of methane was turned on. Steady state has not been reached.

Figure 82 shows the  $\text{CO}_2$  concentration profile about 31 s after the methane spray has been turned on. We have now reached a steady state. The density contours show a definite dip near the axis. In the contours of the mass fractions of the chemical species, we notice that the methane forms a core around which the other species appear to form a halo. We will show in the



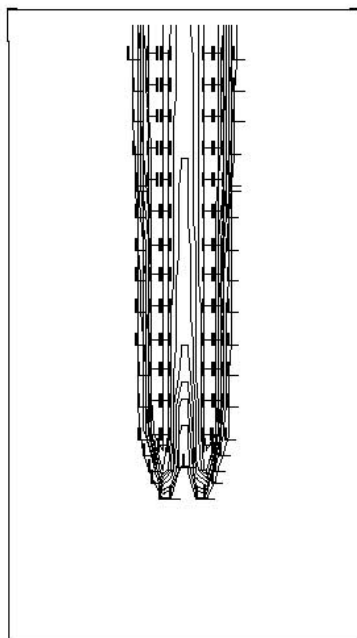


Figure 82. Contours of CO<sub>2</sub> (product) concentration after steady state has been reached (31s).

next section how one can understand this behavior in terms of a self-similar model for the flame structure in our reactor.

In all the contours, we see that the methane stream and the reaction products never touch the walls. This happened just as we had planned. For this “test” length of reactor tube, we find that the destruction of methane is about 20%. Thus, if we had a tube of about 125 cm, we would have had complete destruction. We have not made a simulation of a reactor of this length, due to the significant computer time required. However, we did halve the length of the tube to 12.5 cm, and found that the destruction is very nearly halved. Based on these numerical results, we project that a tube of about 150 cm length and a radius of about 10 cm would be sufficient to achieve close to 100% destruction, without the flow reaching the walls of the reactor.

## G. PROCESS EVALUATION AND OPTIMIZATION

### 1. Objective

Several laboratory-scale versions and a few bench-scale versions of the SCWO process existed at the time of this study. Los Alamos National Laboratory (LANL) used plant

design techniques to evaluate the SCWO process and to guide supporting experimental work. To reduce the number of experiments required, we compared several design and operating scenarios for full-scale SCWO plants. Undesirable design and operating conditions were identified, and values were taken at optimal or near-optimal points identified by these simulations.

The tool used for this work was the ASPEN (Advanced System for Process ENgineering) computer code, which is normally used for designing chemical plants and refineries. The ASPEN code can produce mass and energy balances for an entire plant flowsheet. The code has many built-in unit operations that can be integrated to form process flowsheets. It also has a large database of thermophysical properties and many options for estimating vapor–liquid equilibria and phase behavior. The ASPEN code is one of the few commercial simulators that can model solids-handling processes.

Based on actual experiments, several simple schemes representing the LANL experimental set-up were analyzed using ASPEN. One set of experiments with methyl ethyl ketone as a surrogate waste provided the basis for six full-scale plant designs. Analyzed on the basis of capital and operating costs, the data indicate which cost factors weigh heaviest on the SCWO process and provide information for finding the optimal plant design and operating conditions.

## 2. The ASPEN Code

The ASPEN code is an extremely large, flexible computer program that acts as a process flowsheet simulator. It provides building blocks that can be combined to build modules that represent portions of refineries, chemical plants, and waste disposal processes. These building blocks include unit operations such as pumps, reactors, heat exchangers, and distillation columns.

The ASPEN code provides a thermodynamic database for equilibrium calculations and energy balances. It easily handles normally tedious plant calculations such as recycle matching and provides an accurate material balance for the plant. Other calculations that ASPEN performs are chemical equilibrium calculations (minimization of Gibbs free energy), flash calculations, and pump, turbine, and compressor calculations. This code also establishes design specifications; that is, the engineer can specify a process condition such as stream temperature at a given point in the process and a variable to be manipulated such as a component of the feed stream. The code manipulates the variable (the concentration of the specified

component in the feed stream) until the process condition (stream temperature) matches the desired temperature, and can also do equipment sizing and cost analysis.

The ASPEN code has a large, built-in database of physical thermodynamic properties. It also contains correlations and models for the prediction of physical and thermodynamic properties. These correlations are given for both pure components and mixtures. Predicting physical properties of fluid mixtures is not straightforward unless the mixtures are ideal, which is seldom the case. A package of models that applies to a particular class of components is called a system option or SYSOP. Los Alamos National Laboratory's version of ASPEN features 12 SYSOPs. The physical property models in each SYSOP are for the fugacity coefficient, enthalpy, Gibbs free energy, entropy, volume or density, viscosity (no solid correlation), thermal conductivity, diffusivity (no solid correlation), and surface tension (liquid correlation only). Of these models, the fugacity coefficient correlation is probably the most important. The version of ASPEN used in this work was ASPEN/SP, a product of Simulation Sciences of Denver, Colo.

### 3. Modeling Results

One purpose of this study was to provide heat and material balance information for a commercial-scale (20,000 gallons per day) SCWO waste-processing unit. This study gives insight into SCWO process optimization and potential plant scale-up problems. It also provides information to experimentalists about the relationship of their experiments to the overall plant problem so they can make their experiments more meaningful.

The study was subdivided into two problem sets based on two types of plant design. Problem Set 1 dealt entirely with commercially configured plants. In addition to a supercritical water oxidation reactor, plant flowsheets included peripheral equipment that a commercial plant would require to perform complete waste destruction, including heat exchangers, pumps, turbines, compressors and knock-out vessels. All problems in Problem Set 2 were based on a plant configuration closely resembling a scaled-up version of one LANL experimental reactor. This plant had a compressor and a pump, but the reactor essentially emulated an electrically heated tube. Problem Set 1 provided insight into the issues of full-scale plant design, construction and operation. Problem Set 2 provided feedback for the experimentalists. Problem Set 2 also provided screening for a large set of problems that will be run later in the Problem Set 1 mode, which is more difficult to set up and run. The ASPEN computer code simulated the plant designs at steady-state operation to provide heat and material balance information for both problem sets.

Problem Set 1 was subdivided into plants that extracted energy as a byproduct and plants that extracted no energy. Plants with no energy extraction furnish the more realistic models because the process conditions used for the energy extraction turbines in the models may be too severe for current commercial turbines. The comparative studies were originally intended to provide incentive for development of those turbines, at least for the higher concentration of hydrocarbons in water. In Problem Set 1, methyl ethyl ketone was used as a surrogate to simulate hydrocarbon-based chemicals such as paint thinner. In this problem set, two times the stoichiometric amount of pure oxygen was used as the oxidant. The calculations showed it is impractical to use this much oxygen in practice; future experiments will be more meaningful if they reflect this information. Six runs were calculated, two each (one with energy extraction and one without) for 2, 10, and 20 wt% methyl ethyl ketone in water.

Several preliminary conclusions can be drawn from the results of Problem Set 1:

- Energy extraction does not pay when the plant feed contains only a small amount of usable energy. In this case, 2 wt% methyl ethyl ketone in water provides a small amount of usable energy. This situation holds for mixtures of other energy-rich compounds such as hydrocarbons in water. Energy extraction is only slightly better (821 kW input versus 879 kW input) than with no extraction. Both cases require net energy input.
- Destruction of hazardous waste solutions containing only 2 wt% methyl ethyl ketone or its heat equivalent in water probably will not be economical. These cases require large heat transfer areas for the reactors—over 10 times that of the 10 wt% methyl ethyl ketone case (based upon heat transfer rates of  $8.1 \times 10^6$  BTU/hr for the 2 wt% case versus  $0.64 \times 10^6$  BTU/hr for the 10 wt% case). Water waste solutions with low heat values require large energy inputs to keep the reaction going, and large energy inputs normally require large heat transfer areas.
- If energy extraction is not the goal, the 10 wt% methyl ethyl ketone case appears to be a good choice. It requires little energy input and a small heat exchange area. If energy extraction is the goal, one can get about as much energy out of the 10 wt% energy extraction case as must be put into the 10 wt% nonextraction case. This level of energy extraction does not justify the extra equipment costs.

Note that the above analyses depend strongly upon the heating value per pound of the waste.

Conclusions that may be drawn from the results of Problem Set 2 are as follows:

- Pumping liquid oxygen to process pressures requires less energy than compressing gaseous oxygen to process pressures. How much less energy depends on pump efficiency. A small penalty is paid in energy input and heat exchange area to heat and vaporize the cold liquid.
- Air costs more to compress and heat because more inert gas is present. The effect of heating the inert gas will be different in systems when a greater weight percent of organic matter is present in the feed.
- The difference between methyl ethyl ketone and the other organics comes from different molecular weights and heating values. Another difference between the methyl ethyl ketone cases and the other organics is the difference in the amount of oxygen required to meet the  $1.1 \times$  stoichiometric requirement. This difference affects the compression costs.

#### 4. Conclusions

In addition to the information obtained from this study, mass and energy balances were computed that allow designers to size, specify, and select equipment (or at least anticipate scale-up problems) for these plants. We developed a framework that will allow us to continue efforts to determine optimum operating conditions. We also have a framework on which to build better cost analyses. Even though the cost analysis presented here is preliminary, it provides a first step in the search for optimal plant configurations and operating conditions.

Important things we learned from this study include the following:

- We should use a higher weight percentage of organic matter as a base case. The 2 wt% organic base case has a high operating cost.
- Energy extraction is not economical at 20 wt% methyl ethyl ketone (or equivalent hydrocarbon) and below. The calculation trends indicate that above 20%, energy extraction may have an economic payoff.

- With the current set of plant designs, purchased oxygen represents the most expensive single operating cost. Using two times stoichiometric oxygen is too expensive and probably unnecessary. The costs of manufacturing oxygen on site will be studied next as an alternative to purchasing.
- In general, operating costs represent a larger share of overall costs than capital equipment costs. Of the capital equipment costs, equipment such as pumps, compressors, and turbines represent a bigger investment than the capital costs of reactors and heat exchangers. We should keep these points in mind as we try to improve the process.

## SECTION X

### CONCLUSIONS

#### A. SCWO CHEMISTRY

In general the chemistry of oxidation of energetic materials in supercritical water is very similar to that found previously for other classes of organics. We have established conditions for which the hydrocarbon elements of all the energetic compounds investigated thus far are completely oxidized to  $\text{CO}_2$  and  $\text{H}_2\text{O}$ . The temperature, residence time and oxidant concentration necessary to achieve complete oxidation vary, depending on the nature of the energetic material. Our results indicate that complete oxidation is always achievable using excess oxidant and operating the linear reactor at 600 °C (11-s residence time). Reasonable carbon balances are obtained for all the energetic materials investigated under these conditions, including PETN, HMX, TNT, RDX, NQ, NM, NG and UDMH. Most of the carbon is detected as  $\text{CO}_2$ , with some small fraction remaining in solution as inorganic carbon ( $\text{CO}_3^{2-}$  or  $\text{HCO}_3^-$ ). The exception is NQ, which produces large quantities of inorganic carbon.

The conditions that produce these results were deliberately "extreme" to ensure complete oxidation. In many cases we have not adequately explored the dependence of the chemistry on oxidant concentration and temperature to determine optimum conditions. Minimization of oxidant concentration is particularly important since the oxidant represents a large fraction of the process cost and if present in excess may enhance corrosion or cause the formation of undesirable products. Furthermore, we have very few data for one variable, the reactor residence time. Less-extreme conditions (*e.g.*, lower temperatures and 1:1 oxidant stoichiometries) may be sufficient to achieve complete oxidation given longer residence times.

Without added oxidant, products of incomplete oxidation were often observed, including CO,  $\text{CH}_4$  and HCN. These products are highly undesirable because of their toxicity and/or flammability. Therefore a necessary part of process control is online analysis for the detection of products of incomplete oxidation in the event of loss of oxidant or other such failure. The criteria necessary for online analysis are ppm sensitivity, specificity for multiple components of complex mixtures and rapid (seconds) response. The gaseous effluent diagnostics used in this work, FTIR and mass spectroscopy, meet these criteria and are thus suitable for this purpose.

The nitrogen chemistry of energetics is considerably more complicated, varying widely depending on the nature of the starting material. The nitrogen is always distributed among a group of products,  $N_2$ ,  $N_2O$ ,  $NO_2^-$ , and  $NO_3^-$ , having formal oxidation states of N varying from 0 to +5. For most of these reactions, quantitative data have been obtained for all products except  $N_2$ . The latter is implicated as the major N product in many of the reactions by elimination of other possible products. Qualitative data (MS and GC) indicate  $N_2$  production in the case of NM, NQ, and TNT. The production of  $N_2$  has been quantified in the reactions of  $N_2H_4$  and UDMH using gas chromatography.

No obvious correlation exists between the nitrogen content or the type of nitrogen groups (*e.g.*,  $NO_2$  or  $NH_2$  groups) of a particular energetic material and the distribution of nitrogen products ( $N_2$ ,  $N_2O$ ,  $NO_2^-$  and  $NO_3^-$ ). It is possible, however, to vary the distribution of products in the different oxidation states by varying the temperature and the oxidant concentration. The clearest example of this variability is  $NO_x^-$  production in the reactions of TNT. When a large excess of oxidant is employed at 600 °C, a significant fraction of the initial N (74 percent) is converted into  $NO_x^-$ . This fraction is much less (12 percent) for a small (fivefold) excess of oxidant and yet complete oxidation of the carbon still occurs. The same trend is observed for the oxidation of RDX with excess  $H_2O_2$  (10 percent  $NO_3^-$ ) and with oxygen balance (no  $NO_3^-$ ). These results indicate that significant control over the oxidation chemistry is possible through the precise tuning of reaction parameters.

The type of oxidant can also have a dramatic effect on the nitrogen product distribution. A case in point is hydrazine. The use of  $H_2O_2$  as oxidant produces primarily  $N_2$  and only trace amounts of nitrate, nitrite and  $N_2O$ . Nitrate was also explored as an oxidizer since  $N_2O_4$  is usually used as the oxidizer for hydrazine in liquid-fueled rockets and it disproportionates into nitric and nitrous acids when dissolved in water. In contrast to the  $H_2O_2$  case, substantially different nitrogen chemistry is observed with either  $HNO_3$  or  $NaNO_3$  oxidizer; the primary products are  $N_2$  and  $N_2O$ . Experiments with isotopically labeled  $HNO_3$  indicate that the  $N_2O$  is produced from the combination of an NO group of  $NO_3$  with an N from  $H_2N_4$ . Clearly the reaction with  $H_2O_2$  is cleaner, although  $N_2O_4$  (or  $NO_3$ ) would also be an effective oxidizer for both hydrazine and UDMH.

The destruction chemistry of AP in SCW is unique among the energetic materials since AP has no carbon and is a strong oxidant. The chemistry is best described by the following equation:





Conditions have been determined for which 99.6 percent of the  $\text{ClO}_4^-$  is destroyed. The Cl is converted into  $\text{Cl}^-$ , formally reduced from  $7^+$  to  $1^-$ , and excess oxygen is produced in the reaction. Further evidence for the highly oxidizing nature of this reaction is provided by the strong oxidative corrosion of the C-276 and 316 stainless reactors. The addition of reducing equivalents, in the form of a fuel such as a hydrocarbon, may improve the destruction of AP as well as reduce reactor corrosion. The nitrogen is distributed between  $\text{N}_2$  and  $\text{N}_2\text{O}$ , with no formation of higher oxides or  $\text{NO}_x^-$ . In contrast to thermal decomposition of solid AP, no harmful products such as  $\text{Cl}_2$  or  $\text{NOCl}$  are formed in the SCWO reactions.

## B. INCREASING THROUGHPUT OF EXPLOSIVES

A critical issue in scaling up SCWO treatment of energetic materials to enable a practical process is introduction of significant quantities of explosives into the reactor. We have examined three potential approaches to this problem. The least attractive approach appears to be pre-dissolving the explosive in an organic co-solvent. While convenient for introducing large concentrations of explosives, the co-solvent is partially oxidized in the process, creating numerous byproducts that must subsequently be separated and processed. This disadvantage could be overcome by using a co-solvent that is inert to oxidation, such as supercritical  $\text{CO}_2$ . We have found, however, that many explosives and propellant components are only very slightly soluble in  $\text{SCCO}_2$ .

A second approach we have explored is to introduce high concentrations of energetics as aqueous slurries. Results on the thermal decomposition of aqueous slurries of TATB suggest somewhat unpredictable behavior. The source of this unpredictability is not presently known; however, we suspect that it may be a mixing problem that leads to self-heating and faster reactions. These experiments have been limited to a static batch reactor with no attempt to stir or agitate the slurry. Experiments with a double base propellant (NG/NC) and with pure HMX gave more predictable results. In both of these cases it was found that water significantly moderated the decomposition compared to the dry material and also modified the product distribution.

We also attempted to pump slurries mechanically, which may prove to be the greatest hazard associated with their handling. We designed and constructed a slurry-pumping reactor that can be operated remotely at a firing site. We have pumped slurries of a simulant, melamine,

and an actual explosive, HMX. We find that the most critical factor in successful slurry pumping is the particle size. With our reactor design, it was necessary to use particle sizes less than 50  $\mu\text{m}$  to avoid accumulation and plugging of the reactor. Modeling studies indicate that a combination of larger reactor pipe diameter and faster flow rates would allow the use of larger particle size.

Finally, the most promising approach appears to be pretreatment of the energetic material to increase its solubility in water. Our effort focused on degradation of the explosive via base-catalyzed hydrolysis at elevated temperatures. These reactions produce water-soluble products that are further processed in SCW to achieve complete destruction of the energetic material and its hydrolysis byproducts. This approach has been successfully demonstrated for NQ, NC, NG, TNT, HMX, RDX and propellants including PBX 9404 and class 1.1 aluminum-containing formulations (CYH). We have processed large amounts (up to 500-g pieces) at low temperatures ( $< 150\text{ }^{\circ}\text{C}$ ) and pressures ( $< 60\text{ psi}$ ) to produce water-soluble, nonexplosive products. We find that one mole of base is consumed per mole of  $\text{NO}_x$  groups in the explosives. For class 1.1 propellant formulations, additional base is consumed in reactions with the Al and AP. We find that 1 mole of base is consumed for each mole of Al and AP. Because this approach allows the processing of large concentrations, we have demonstrated very high destruction efficiencies of the starting materials. In most cases, the final products of the combined hydrolysis/SCWO process are identical to those obtained with SCWO alone.

### C. REACTOR CORROSION

One of the most critical issues for practical application of an SCWO process to the treatment of energetic materials is reactor wear caused by corrosion. Corrosion of the C-276 reactor by most of the energetic materials does not appear to be a problem. The exception is AP, which caused severe corrosion of the C-276 and 316 stainless reactors. For laboratory-scale reactors, this problem was solved by the use of a gold liner in the SCW region, which reduces corrosion to acceptable levels.

### D. SALT SOLUBILITY

Efficient hydrothermal processing of PEPs requires high starting concentrations, which results in the formation of high salt concentrations. Information regarding the solubility behavior of salts formed in hydrothermal processing is essential to control plugging, corrosion, phase behavior and the chemistry related to these processes. The salts produced in hydrothermal

processing that were of primary concern are carbonates and aluminates. Carbonates formed from the oxidation of carbon at  $pH$  5 or greater (carbonate is also referred to as TIC or inorganic carbon in this report). Aluminates formed from the base hydrolysis of class 1.1 propellants. The solubilities of these species are highly dependent on pressure and temperature (which determine density). For example, at 450 °C, doubling the pressure from 5000 psia to 10,000 psia increases the solubility more than 100fold. The solubility of aluminates is easily controllable using  $pH$ . Under most hydrothermal processing conditions aluminates are highly soluble and should not present any processing difficulties. Carbonates are much less soluble and tend to plug the reactors. Our results indicate that carbonate solubility is significantly enhanced at high pressures ( $< 10,000$  psia) and at high sodium hydroxide concentrations, presumably due to the creation of a melt phase. Our results suggest that it is possible to control the solubility of carbonates to prevent plugging and other harmful effects by operating at high pressure and hydroxide concentration.

## REFERENCES

1. Timberlake, S. H., Hong, G. T., Simson, M., and Modell, M., *SAE Technical Paper 820872*, 12th Intersociety Conference on Environmental Systems, San Diego, California, July 1982.
2. Thomason, T. B. and Modell, M., "Supercritical Water Destruction of Aqueous Wastes," *Haz. Waste*, **1**(4), 453, 1984.
3. Johnston, J. B., Hannah, R. E., Cunningham, V. L., Daggy, B. P., Sturm, F. J., and Kelly, R. M., *Bio/Technology*, **6**, 1423, 1988.
4. Thomason, T. B., Hong, G. T., Swallow, K. C., and Killilea, W. R., "The MODAR Supercritical Water Oxidation Process," *Innovative Hazardous Waste Treatment Technology Series, Volume 1: Thermal Processes*, H. M. Freeman, ed., Lancaster, Pennsylvania, Technomic Publishing Co., pp. 31–42, 1990.
5. Modell, M., "Gasification and Liquefaction of Forest Products in Supercritical Water," US Patent 4,338,199, 6 July 1982.
6. Modell, M., "Supercritical Water Oxidation," *Standard Handbook of Hazardous Waste Treatment and Disposal*, H. M. Freeman, ed., New York: McGraw–Hill, pp. 8.153–8.168, 1989.
7. Stone and Webster Engineering Corporation, *Assessment and Development of an Industrial Wet Oxidation System for Burning Waste and Low-Grade Fuels*, final report, DOE Contract No. DE-FC07-88ID12711, 1989.
8. Modell, M., *Treatment of Pulp Mill Sludges by Supercritical Water Oxidation*, final report, DOE Contract No. FG05-90CE40914, 1990.
9. Saul, A. and Wagner, W., "A Fundamental Equation for Water Covering the Range from the Melting Line to 1273 K at Pressures up to 25,000 MPa," *J. Phys. Chem. Ref. Data*, **18**, 1537–1565, 1989.

10. Schumacher, J. C., *Perchlorates: Their Properties, Manufacture and Use*, New York, Reinhold Publishing Corporation, 1960.
11. Castegnaro, M., Brouet, I., Michelon, J., Lunn, G., and Sansone, E. B., "Oxidative Destruction of Hydrazines Produces *N*-Nitrosamines and Other Mutagenic Species," *Am. Ind. Hyg. Assoc. J.*, **47**, 360–364, 1986.
12. Weast, R.C., *CRC Handbook of Chemistry and Physics*, CRC Press, Inc., Cleveland, 1978.
13. Michel, K. W. and Wagner, H. G., *Tenth Symposium (International) on Combustion*, p. 353, The Combustion Institute: Pittsburgh, 1965.
14. Eberstein, I. J. and Glassman, I., *Tenth Symposium (International) on Combustion*, p. 365, The Combustion Institute: Pittsburgh, 1965.
15. Stein, S. E., Benson, S. W., and Golden, D. M., *J. Catalysis*, **44**, 429, 1976.
16. McHale, E. T., Knox, B. E., and Palmer, H. B., *Tenth Symposium (International) on Combustion*, p. 341, The Combustion Institute: Pittsburgh, 1965.
17. Meyer, E., Olschewski, H. A., Troe, J., and Wagner, H.G., *Twelfth Symposium (International) on Combustion*, p. 345, The Combustion Institute: Pittsburgh, 1969.
18. Genich, A. P., Zhirnov, A. A., and Manelis, G. B., *Zh. Fiz. Khim. (Engl. Transl.)*, **48**, 416, 1974.
19. Kerr, J. A., Sekhar, R. C., and Trotman–Dickenson, A. F., *J. Chem. Soc. B*, 3217, 1963.
20. Miller, J. A. and Bowman, C. T., *Prog. Energy. Combust. Sci.*, 287, 1989.
21. Guelachvili, G. and Rao, K.N., *Handbook of Infrared Standards*, Academic Press, Inc., Orlando, 1986

22. Durand, R., *Proc. Minnesota Intl. Hydraulics Conf.* pp. 89–103, 1953; Durand, R.; Condolios, E., *Proc. of a Colloq. on the Transport of Coal*, National Coal Board, London, 1953.
23. Spells K. E., *Trans. Inst. Chem. Engineers, London*, **33**, 78–84, 1955.
24. Cairns R. C., et al., *British Chemical Engineering*, **5**, 849–856, 1960.
25. Urbanski, T., *Chemistry and Technology of Explosives, Volume I*, Pergamon Press, New York, 1964.
26. Urbanski, T., *Chemistry and Technology of Explosives, Volume II*, Pergamon Press, New York, 1965.
27. Urbanski, T., *Chemistry and Technology of Explosives, Volume III*, Pergamon Press, New York, 1967.
28. Urbanski, T., *Chemistry and Technology of Explosives, Volume IV*, Pergamon Press, New York, 1984.
29. Miles, F. D., *Cellulose Nitrate*, Interscience Publishers, New York, 1955.
30. Fessenden, R. J. and Fessenden, J. S., *Organic Chemistry*, Willard Grant Press, Boston, 1979.
31. Jones, W. H., *J. Am. Chem. Soc.*, **76**, 829, 1954.
32. Epstein, S. and Winkler, C. A., *Can. J. Chem.*, **29**, 731, 1951.
33. Hoffsommer, J. C., Kubose, D. A., and Glover, D. J., “Kinetic Isotope Effects and Intermediate Formation for the Aqueous Alkaline Homogeneous Hydrolysis of 1,3,5 - Triaza-1,3,5-Trinitrocyclohexane,” *J. Phys. Chem.*, **81**, 380–385, 1977.
34. Durig, J. R., Bush, S. F., and Mercier, E. E., *J. Chem. Phys.*, **44**, 4238, 1966.
35. Langseth, A., *Z. Physik*, **77**, 60, 1932.

36. Herzberg, G., *Infrared and Raman Spectra of Polyatomic Molecules*, Van Nostrand Reinhold, p. 295, New York, 1945.
37. Cutler, A. H., Antal, M. J., and Jones, M., *Ind. Eng. Chem. Res.*, **27**, 691, 1988.
38. Tsang, W., *Int. J. Chem. Kinet.*, **10**, 41, 1978.
39. Melius, C. F., Bergan, N. E., and Shepard, J. E., *23rd Symposium (International) on Combustion*, pp. 217–223, The Combustion Institute: Pittsburgh, 1990.
40. Jayaweera, I., Njuyen, L.K., and Ross, D.S., *Destruction of Energetic Compounds on Soil and in Water by Reductive Hydrothermal Systems*, 1330-24, SRI Report, Menlo Park, California, July, 1992.
41. Buntain, G., et.al., "Destruction of Waste Energetic Materials Using Base Hydrolysis," *LA-UR Report 93-1527*, Los Alamos National Laboratory, 1993. Also submitted to 1993 Incineration Conference, Knoxville, Tennessee, May 3–7, 1993.
42. Tikhonov, V.N., *Analytical Chemistry of Aluminum*, John Wiley and Sons, New York, pp. 6–8, 1973.
43. Apps, John A. and Neil, John M., "Solubilities of Aluminum Hydroxides and Oxyhydroxides in Alkaline Solutions", *Chemical Modeling of Aqueous Systems II*, Melchior and Basset, eds., American Chemical Society, Washington, D.C., pp. 414–428, 1990.
44. Robinson, J., et.al., "Destruction of Nitrates, Organics, and Ferrocyanides by Hydrothermal Processing," presentation to the Waste Management Symposium, 1993, February 28–March 4, Tucson, Arizona.
45. Urusova, M.A., "Phase Equilibria in the Sodium Hydroxide–Water and Sodium Chloride–Water Systems at 350–550°C," *Russian Journal of Inorganic Chemistry*, **19**(3), 450, 1974.

46. Marshall, W.L. and Jones, E.V., "Liquid–Vapor Critical Temperatures of Aqueous Electrolyte Solutions," *J. Inorg. Nucl. Chem.*, **36**, 2313, 1974.
47. Melius, C.F., "Thermochemical Modeling: II. Application to Ignition and Combustion of Energetic Materials," *Chemistry and Physics of Energetic Materials*, ed. S.N. Bulusu, pp. 21–78, Kluwer, Boston, 1990.
48. Tsang, W., and Hampson, R.F., "Chemical Kinetic Data Base for Combustion Chemistry. Part 1. Methane and Related Compounds," *J. Phys. Chem. Ref. Data*, **15**, 1087, 1986.
49. Holgate, H.R. and Tester, J.W., "Fundamental kinetics and mechanisms of hydrogen oxidation in supercritical water," *Combust. Sci. Technol.*, **88**, 369, 1993.
50. Yetter, R.A., Dryer, F.L., and Rabitz, H., "A Comprehensive Reaction Mechanism For Carbon Monoxide/Hydrogen/Oxygen Kinetics," *Combust. Sci. Technol.*, **79**, 97, 1991.
51. H.R. Holgate, "Oxidation Chemistry and Kinetics in Supercritical Water: Hydrogen, Carbon Monoxide, and Glucose," Dissertation, Dept of Chemical Engineering, Massachusetts Institute of Technology, 1992.
52. Honig, B., Sharp, K., and Yang, A.–S., "Macroscopic Models of Aqueous Solutions: Biological and Chemical Applications," *J. Phys. Chem.*, **97**, 1101, 1993.
53. Zauhar, R. J., and Morgan, R. S., "A New Method for Computing the Macromolecular Electric Potential," *J. Mol. Biol.*, 186, 815, 1985; Zauhar, R. J., and Morgan, R. S., "The Rigorous Computation of the Molecular Electric Potential," *J. Comp. Chem.*, **9**, 171, 1988.
54. Rashin, A. A., and Namboodiri, K., "A Simple Method for the Calculation of Hydration Enthalpies of Polar Molecules with Arbitrary Shapes," *J. Phys. Chem.*, 91, 6003, 1987; Rashin, A. A., "Hydration Phenomena, Classical Electrostatics, and the Boundary Element Method," *ibid.*, **94**, 1725, 1990.



- 55. Yoon, B. J., and Lenhoff, A. M., "A Boundary Element Method for Molecular Electrostatics with Electrolyte Effect," *J. Comp. Chem.*, 11, 1080, 1990.
- 56. Juffer, A., Botta, E. F. F., van Keulen, B. A. M., van der Ploeg, A., and Berendsne, H. J. C., "The Electric Potential of a Macromolecular in a Solvent: a Fundamental Approach," *J. Comp. Phys.*, 97, 144, 1991.
- 57. Bash, P. A. , Singh, Langridge, R., and Kollman, P. A., "Free Energy Calculations by Computer Simulation," *Science*, 236, 564, 1987.
- 58. P. A. Webley and J. W. Tester, "Oxidation of Methane in Supercritical Water," *Energy and Fuels*, 5, 411, 1991.